UNIVERSITÀ DEGLI STUDI DI TRIESTE
XXXVI CICLO DEL DOTTORATO DI RICERCA IN FISICA

# Measurement of top-quark-pair and $Z$-boson production cross sections and their ratio in $pp$ collisions at $\sqrt{s} = 13.6$ TeV with the ATLAS detector

Settore scientifico disciplinare: **FIS/01 FISICA SPERIMENTALE**

DOTTORANDO:
**GIOVANNI GUERRIERI** Giovanni Guerrieri

COORDINATORE:
**PROF. FRANCESCO LONGO** Francesco Longo

SUPERVISORE DI TESI:
**DR. MICHELE PINAMONTI**

CO-SUPERVISORE DI TESI:
**DR. GIANCARLO PANIZZO** Giancarlo Panizzo

ANNO ACCADEMICO 2022/2023

# Abstract

This thesis presents one of the first measurements performed by the ATLAS collaboration using proton–proton collisions at the centre-of-mass energy of 13.6 TeV, employing 29 $\text{fb}^{-1}$ of data collected in 2022 at the Large Hadron Collider. The analysis aims at extracting, for the first time with Run 3 data at 13.6 TeV, the inclusive top-quark-pair production cross-section $\sigma_{t\bar{t}}$, the fiducial $Z$-boson production cross-section $\sigma^{\text{fid.}}_{Z\to\ell\ell}$, and their ratio in the dilepton channel. The top-quark-pair production cross-section is measured using events with an opposite-charge electron-muon pair and $b$-tagged jets, and corresponds to:

$$\sigma_{t\bar{t}} = 850 \pm 3(\text{stat.}) \pm 18(\text{syst.}) \pm 20(\text{lumi.})\ \text{pb}.$$

Additionally, the ratio of the $t\bar{t}$ and the $Z$-boson production cross sections is measured, where the $Z$-boson contribution is determined for inclusive $e^+e^-$ and $\mu^+\mu^-$ events in a fiducial phase space:

$$\sigma^{\text{fid.}}_{Z\to\ell\ell} = 743.6 \pm 0.2\ (\text{stat.}) \pm 11\ (\text{syst.}) \pm 16\ (\text{lumi.})\ \text{pb},$$
$$R_{t\bar{t}/Z} = 1.145 \pm 0.003(\text{stat.}) \pm 0.021(\text{syst.}) \pm 0.002(\text{lumi.}).$$

The relative uncertainty on the ratio is reduced compared to the $t\bar{t}$ cross-section, thanks to the benefits deriving from the cancellation of several systematic uncertainties. The measured cross sections, as well as their ratio, are consistent with the Standard Model prediction using the PDF4LHC21 PDF set.

# Contents

# Introduction

The Standard Model (SM) of particle physics serves as the prevailing framework for our understanding of the fundamental constituents of the Universe. Developed over the past decades through rigorous theoretical formulation and extensive empirical validation, the SM encapsulates the interactions between elementary particles via three of the four fundamental forces: electromagnetism, the weak force, and the strong nuclear force. High-energy particle colliders like the Large Hadron Collider (LHC) [1] at CERN (Conseil Européen pour la Recherche Nucléaire) offer unique opportunities to probe the robustness of the SM and to search for phenomena that could signify physics beyond the Standard Model (BSM). The LHC is currently the world's most powerful particle accelerator, operating at a centre-of-mass energy of 13.6 TeV. In July 2012, the last missing piece of the SM, the Higgs Boson, was observed [2, 3] independently by the two multi-purpose experiments at the LHC: ATLAS [4] and CMS [5].

Despite its overwhelming success in predicting and describing a plethora of phenomena, the SM is not without limitations. For instance, it does not incorporate the fourth fundamental force, gravity, as described by General Relativity, nor does it offer an explanation for the disparity between the quarks' masses.

Among the quarks, the top quark stands as a notable representative of some intricacies within the SM, also hinting at potential pathways to explore the unresolved issues; it is the heaviest known elementary particle, and its large coupling to the Higgs boson suggests a particularly important role in the SM. The top quark was discovered in 1995 by the CDF [6] and DØ [7] Collaborations at the Fermilab Tevatron $p\bar{p}$ collider. Its short lifetime causes the top quark to transfer all of its properties to the decay products, making it a unique particle compared to others in the SM.

## Motivation and structure of the thesis

In the Summer of 2022, the LHC resumed its physics operations, entering the third run of physics data acquisition. The LHC Run 3 is characterised by a small energy increase with respect to the previous run, from $\sqrt{s}$ =13 to $\sqrt{s}$ =13.6 TeV, accompanied by improvements in both the accelerator and the experiments. The ATLAS detector has received a number of upgrades, both in its hardware and software components. All of these upgrades are designed to withstand the more challenging conditions expected after the High-Luminosity upgrade of the LHC.

The analysis reported in this thesis uses the first dataset available from Run 3, offering crucial insights into validating the functionality of the upgraded detector and reconstruction software. To ensure a quick and reliable feedback at the beginning of a new physics run, fast physics measurements of known processes are highly beneficial. The top quark pair production is an accessible, well-known process within the SM. The measurement of the top quark pair production cross section represents one of the best scenarios to benchmark the performance of the ATLAS detector. Events featuring a pair of opposite-charge leptons (electrons or muons), several jets and $b$-tagged jets are considered. The choice of the dilepton channel allows to reduce the sensitivity to uncertainties related to $b$-tagging and jets. However, carrying out a measurement in the early stages of a physics run implies having a significant impact from the possibly limited knowledge of the integrated luminosity. To mitigate the considerable uncertainty on luminosity, the ratio of the top quark pair to the $Z$-boson production cross sections is presented. This approach enables the mutual cancellation of not only luminosity-related uncertainties but also various other uncertainties, thereby enhancing the precision of the measurement. Furthermore, given that the dynamics of top quark pairs and $Z$-boson production are largely influenced by different parton distribution functions, the ratio of these cross-sections at a specific centre-of-mass energy exhibits considerable sensitivity to the gluon-to-quark parton distribution function ratio [8].

To obtain a consistent and robust study on the ATLAS detector performance in Run 3, the same measurement is performed three times, employing three different datasets, gathered in different periods of 2022. The author of this thesis took part in all the measurements, significantly contributing to almost every aspect of the analysis, as well as in the writing of the internal supporting notes, and of the paper that is based on them. Given the nature of the analysis, the author believes that three words aptly capture the essence of the measurements presented in this work: accuracy, speed, and momentum. It constitutes one of the first measurements published by the ATLAS collaboration in Run 3, and it is the result of a collaborative endeavour involving nearly all the experiment's working groups.

This thesis is structured as follows: Chapter 1 provides an overview on the SM, focusing on its gauge structure and on the overall physics reach of the theory. Chapter 2 specifically addresses the top quark physics, highlighting its production mechanisms, its properties, and summarising the previous measurements performed by both the ATLAS and CMS collaborations. In Chapter 3, the design and performance of the LHC accelerator complex, together with the ATLAS detector, are presented. Special consideration is given to the upgrades performed on the ATLAS detector since the last run of data acquisition. Chapter 4 presents the experimental procedures employed in the reconstruction, identification and isolation of the physics objects used in the measurement, highlighting the updates. Chapter 5 discusses in depth the strategy employed in the measurement, and the statistical procedures adopted to extract the results. This chapter also provides a chronological summary of publications pertinent to the analysis, tracing their development over time. Chapter 6 includes the description of the simulated Monte Carlo samples utilised in the analysis to model signal and background events. Chapter 7 explores comprehensively the dataset used in the measurement, as well as the event selection employed. Chapter 8 delves into the description of the theoretical predictions for the ratio of the $t\bar{t}$ and $Z$-boson production cross sections. Chapter 9 elaborates on the sources of systematic uncertainties affecting the measurement. Chapter 10 presents the experimental results obtained for the individual cross sections, as well as for the ratio measurement. Finally, the conclusions of this thesis, alongside with an outlook for the future of Run 3 in ATLAS, is provided in Chapter 11.

# Chapter 1

# The Standard Model

The SM of elementary particles represents the current state of knowledge regarding the fundamental constituents of the Universe and their ways of interacting. This theory is founded on two essential principles: gauge theories that are rooted in the $SU(3)_c \otimes SU(2)_L \otimes \mathrm{U}(1)_Y$[1] gauge group, which provide a comprehensive depiction of both strong and electroweak interactions, along with the mechanism of Spontaneous Symmetry Breaking (SSB). These gauge theories provide a well-defined mechanism for adding interaction terms to the free-particle Lagrangian through the exploitation of local transformations depending on four-position coordinates. The aim of the SM is to provide a unified theoretical description of the three fundamental interactions (strong, weak, and electromagnetic, the last two being united in a single Electroweak (EW) interaction), which are predominant at the particle physics scales[2].

The model successfully describes the interaction between the fundamental spin-$\frac{1}{2}$ constituents of matter, called fermions, through the exchange of spin-1 gauge bosons. Fermions, obeying Fermi-Dirac statistics, are classified into leptons and quarks, whereas bosons are governed by Bose-Einstein statistics. Among the five elementary bosons, four are spin-1 *vector bosons*, and one is a spin-0 *scalar boson*; the properties of bosons are further described in the next sections.

The fermion sector is organised into three generations, as shown in Figure 1.1. Out of the 3 × 4 elementary fermionic building blocks of matter (together with their anti-matter counterparts), six are charged or neutral leptons. The charged ones $(e^-, \mu^-, \tau^-)$ are able to undergo both electromagnetic and weak interactions, while neutral leptons $(\nu_e, \nu_\mu, \nu_\tau)$ called neutrinos, are solely subject to the weak force. Each lepton is assigned a quantum number called lepton flavour [10]. Its exact conservation in every process involving leptons accidentally follows from gauge invariance and the assumption that neutrinos are massless. However, due to the observation of

---

[1] In this notation, $c$ denotes the colour charge, while $L$ and $Y$ respectively represent the action of the $SU(2)$ Lie algebra on left-handed chiral fields and the weak hypercharge $Y = 2(Q - T_3)$[9]; here, $Q$ is the electric charge and $T_3 = \frac{1}{2}\sigma_3$ is the third component of the isospin, which is a quantum number of the weak interaction.

[2] The gravitational force cannot yet be included in the framework of the SM at present.

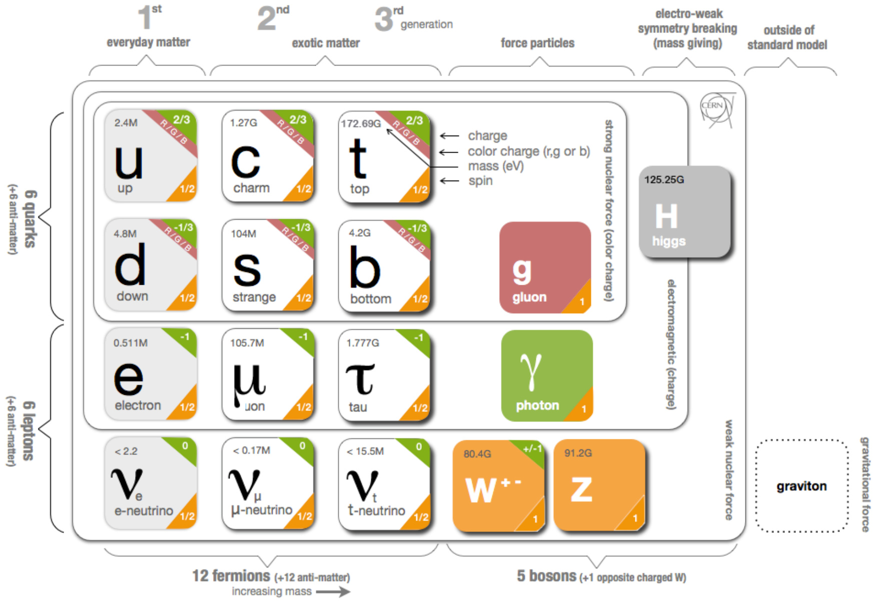

Figure 1.1: Overview of the elementary particles and fields in the Standard Model. Figure taken from [15]. Adapted the top quark mass according to [16] and the Higgs boson mass according to [17].

neutrino oscillations [11–13], the conservation law of this quantum number is in fact only a very good approximation [3].

The remaining six elementary fermions are the so-called quarks [14]. Quarks exist in six flavours, up ($u$), down, ($d$), charm ($c$), strange ($s$), top ($t$) and bottom ($b$); they carry a fractional charge, expressed in units of the positron charge. In addition to the flavour quantum number, quarks are also characterised by a colour state (blue, red or green); this quantum number causes the quarks to be confined in colour-neutral bound states called hadrons. This concept will be further described in Sec. 1.1.3.

The SM also describes the interactions between particles via the three previously mentioned forces; all these interactions are mediated by the exchange of gauge bosons. The forces are described with a Quantum Field Theory (QFT) that is based on a Lie algebra stating the symmetry of the interactions, and are explained in the following sections.

The Lagrangian of the SM can be constructed by requiring it to be gauge-invariant, local, and renormalisable. It can be divided in several parts:

$$\mathcal{L}_{\text{SM}} = \mathcal{L}_{\text{gauge}} + \mathcal{L}_{\text{fermions}} + \mathcal{L}_{\text{Higgs}} + \mathcal{L}_{\text{Yukawa}} \tag{1.1}$$

---

[3] Total lepton and baryon numbers are, separately, exactly and accidentally conserved, so far, from experimental constraints on the proton decay lifetime.

The first term describes gauge fields and their self-interactions, while the second term represents fermions and their interplay with corresponding gauge fields; both of these subjects are further discussed in Section 1.1. The third term concerns the Higgs field and its self-interactions; together with the fourth term, it is responsible for the SSB, a process responsible for the creation of mass of the elementary particles, as reported in Sec. 1.2. Finally, the fourth term outlines the interactions of fermions with the Higgs field. Crucial for the generation of mass for fermions, this term's implications are studied in Section 1.3.

## 1.1 Gauge theories

A pivotal advancement in constructing the SM involved the formulation of a method to derive interaction theories from theories without interaction within the framework of QFT.

### 1.1.1 Quantum electrodynamics

The concept of gauge invariance arises from the necessity for the Lagrangian to be independent of the phase of complex-valued fields.[18]. The formulation of this symmetry principle goes back to the electromagnetism, where the physical **E** and **B** fields are obtained from the scalar and vector potentials, respectively $\phi$ and **A** and do not change under the transformations

$$\phi \to \phi' = \phi - \frac{d\chi}{dt} \qquad \text{and} \qquad \mathbf{A} \to \mathbf{A} = \mathbf{A} + \nabla\chi$$

or, in 4-vector notation:

$$A_\mu \to A'_\mu = A_\mu + \partial_\mu \chi. \tag{1.2}$$

In relativistic quantum mechanics, the gauge invariance of electromagnetism is related to a local phase transformation that must leave the physics unmodified:

$$\psi(x) \to \psi'(x) = \hat{U}(x)\psi(x) = e^{iq\chi(x)}\psi(x) \tag{1.3}$$

where the phase $\chi(x)$ can potentially assume different values at all points in space-time; if $\chi(x)$ is not constant in the whole space-time, this is the case of a *local* phase invariance. To the contrary, if $\chi(x) = \chi$ the phase invariance is *global*.

The Maxwell equations in their covariant form for a free electromagnetic (EM) field are written as:

$$\partial_\mu F_{\mu\nu} = 0\,, \text{ with } F_{\mu\nu} = \partial_\mu A_\nu - \partial_\nu A_\mu \tag{1.4}$$

where the EM field strength tensor $F_{\mu\nu}$ is gauge invariant (if a global phase transformation is considered). Consequently, the Maxwell field equations are both gauge-invariant and Lorentz-covariant. The EM Lagrangian Density (referred to as Lagrangian from now on) is then given by:

$$\mathcal{L}_{\text{EM}} = -\frac{1}{4} F_{\mu\nu} F^{\mu\nu} \tag{1.5}$$

Similarly, the expression of the Dirac Lagrangian of a fermion requiring the invariance under a global $U(1)$ symmetry is[4]:

$$\mathcal{L}_{\mathrm{D}} = \overline{\psi}(x)(i\gamma^{\mu}\partial_{\mu} - m)\psi(x) \tag{1.6}$$

In (1.6), the Dirac spinor $\psi(x)$ is defined as $\psi(x) = (\psi_1(x), \ldots, \psi_4(x))^T$, while $\overline{\psi}(x)$ is the complex-valued $\psi(x)$ such that $\overline{\psi}(x) = \psi^{\dagger}(x)\gamma^0$, $m$ is the fermion mass and $\gamma^{\mu}$ the Dirac matrices.

To the contrary, for a local phase transformation $\mathcal{L}_{\mathrm{D}}$ has to be modified by coupling the Dirac field to the Maxwell field in order to preserve invariance:

$$\mathcal{L}_{\mathrm{D,EM}} = \overline{\psi}(x)[i\gamma^{\mu}D_{\mu} - m]\psi(x) \tag{1.7}$$

where the partial derivative has been substituted by the *gauge covariant derivative* following the definition:

$$\partial_{\mu} \longrightarrow D_{\mu} = \partial_{\mu} - ieA_{\mu} \tag{1.8}$$

In (1.8), $A_{\mu}$ is interpreted as the field corresponding to a *massless gauge boson*. The existence of a gauge field which couples to Dirac particles in exactly the same way as the photon implies a fundamental statement: quantum electrodynamics (QED), including Maxwell equations can be obtained demanding the invariance of physics under a local $U(1)$ transformation.

The complete gauge invariant QED Lagrangian is therefore given by:

$$\mathcal{L}_{\mathrm{QED}} = -\frac{1}{4}F_{\mu\nu}F^{\mu\nu} + \overline{\psi}(x)[i\gamma^{\mu}D_{\mu} - m]\psi(x) \tag{1.9}$$

where the *interaction term* is defined by

$$\mathcal{L}_{\mathrm{int}} = e\overline{\psi}\gamma^{\mu}A_{\mu}\psi$$

### 1.1.2 Electroweak interaction

The local gauge invariance principle can be applied to include weak interactions in the gauge invariant Lagrangian formalism. The EW theory [19–21] unifies the EM interaction and the weak interaction through the $SU(2)_L \otimes U(1)_Y$ group, which includes both charged and neutral currents. The charged currents change the flavour of the left-handed fermion fields, whereas neutral currents conserve the flavour. In the notation $SU(2)_L$, the subscript $L$ denotes that the weak isospin current interacts solely with left-handed fermions; this is a direct consequence of the hypothesis that parity is not conserved[5] in weak interactions [22]. The correctness of this hypothesis has been proved experimentally [23], leading to the conclusion that parity must be *maximally violated*. Maximal parity violation is accomplished by introducing a *vector minus*

---

[4] The set of all transformations $\hat{U} = e^{iq\chi(x)}$ such as (1.3), constitute the unitary Abelian group $U(1)$.

[5] This statement implies that the Lagrangian might be a pseudoscalar.

*axial* $(V - A)$ structure of the weak theory; this implies right-handed and left-handed spinors defined as:

$$\begin{aligned}\psi_R &= P_R\psi = \frac{1}{2}(1+\gamma^5)\psi \\ \psi_L &= P_L\psi = \frac{1}{2}(1-\gamma^5)\psi\end{aligned} \tag{1.10}$$

In (1.10), $P_{R,L}$ are the *chirality operators*, and $\gamma^5$ is the product of the Dirac matrices. Hence, fermions are characterised as of left-handed doublets of quarks $q^i_L$ and leptons $\ell^i_L$, along with right-handed singlets of quarks $u^i_R(d^i_R)$ and leptons $\ell^i_R(\nu^i_R)$:

$$\begin{aligned} & q^i_L = \begin{pmatrix} u \\ d \end{pmatrix}_L \begin{pmatrix} c \\ s \end{pmatrix}_L \begin{pmatrix} t \\ b \end{pmatrix}_L ; \qquad && \ell^i_L = \begin{pmatrix} e \\ \nu_e \end{pmatrix}_L \begin{pmatrix} \mu \\ \nu_\mu \end{pmatrix}_L \begin{pmatrix} \tau \\ \nu_\tau \end{pmatrix}_L ; \\ & u^i_R = u_R, c_R, t_R; && d^i_R = d_R, s_R, b_R; \\ & \ell^i_R = e_R, \mu_R, \tau_R; && \nu^i_R = \nu^e_R, \nu^\mu_R, \nu^\tau_R; \end{aligned} \tag{1.11}$$

In doublets, both neutrinos and up-type quarks $(u, c, t)$ carry a weak isospin value of $T_3 = +\frac{1}{2}$. Conversely, charged leptons and down-type quarks $(d, s, b)$ possess a weak isospin of $T_3 = -\frac{1}{2}$. As a result, members of the same doublet hold identical hypercharges: leptons hold $Y = -1$, while quarks carry $Y = \frac{1}{3}$. This hypercharge is inferred from the multiplication of the two symmetry groups.

The $SU(2)_L \otimes U(1)_Y$ gauge group is incompatible with mass terms for either the gauge bosons or fermions without causing a violation of gauge invariance. To incorporate the observed masses, spontaneous electroweak symmetry breaking (EWSB) is employed at energies around the mass scale of the $W$ and $Z$ bosons. This process, often referred to as the "Higgs mechanism" [24–26], includes the introduction of an $SU(2)_L$ doublet of complex scalar fields $\phi = (\phi^+, \phi^0)^T$. As demonstrated in Section 1.2, when the neutral component achieves a non-zero vacuum expectation value, the symmetry of $SU(2)_L \otimes U(1)_Y$ breaks down to $U(1)_{\text{QED}}$. This breakdown imparts mass to the three electroweak gauge bosons, $W^\pm$ and $Z^0$, while the photon remains massless. This process preserves the electromagnetic symmetry $U(1)_{\text{QED}}$. The residual degree of freedom from the scalar doublet produces an additional scalar particle, known as the Higgs boson.

### 1.1.3 Quantum Chromodynamics

The SM section that accounts for strong interactions between quarks is called Quantum Chromodynamics (QCD). Similarly to QED, QCD interactions are mediated by eight massless gluons corresponding to the eight generators of the $SU(3)_c$ local gauge symmetry. The single charge of the QED is replaced by "colour" charges *r, g* and *b* which correspond to three orthogonal states in $SU(3)_c$ space.

The development of QCD began with the *Eightfold Way* classification of baryons and mesons [27], followed by the introduction of the hadron quark content [14, 28]. The study of this inner structure, achieved through the Deep Inelastic Scattering (DIS) [29] technique, has led to the formulation of the *Parton Model* [30].

The quarks' dynamics is generated by a colour symmetry [31] in the SU$(3)_c$ symmetry group; this framework is a non-Abelian gauge theory, so that the interaction mediators can carry colour charge themselves and couple to each other.

At large momentum scale $Q^2 \gg 1$ (GeV/$c$)$^2$ the coupling $\alpha_s$ diminishes, a phenomenon termed *Asymptotic freedom* [32], implying that quarks and gluons are weakly coupled. To the contrary, $\alpha_s$ is large for small values of $Q^2$: as a result, quarks are bounded in the so-called *colour confinement*. This fact has the important experimental consequence that quarks produced in high energy particle interactions manifest themselves as collimated streams of hadrons called *jets*[6].

The Lagrangian that describes the strong interaction is given by:

$$\mathcal{L}_{\text{QCD}} = -\frac{1}{4} G^a_{\mu\nu} (G^{\mu\nu})_a + \sum_{k=1}^{n_f} \overline{\psi}_k \, i\gamma^\mu (D_\mu - m_k) \psi_k, \tag{1.12}$$

where the index $k$ stands for the flavour of the quark. The covariant derivative $D_\mu$ is defined as:

$$D_\mu = \partial_\mu - i g_s T_a G^a_\mu \tag{1.13}$$

while $G^a_{\mu\nu}$ represents the gluon field (with $a = 1 \ldots 8$):

$$G^a_{\mu\nu} = \partial_\mu G^a_\nu - \partial_\nu G^a_\mu + g_s f^{abc} G^b_\mu G^c_\nu. \tag{1.14}$$

The terms $f^{abc}$ are the structure constants of $SU(3)_c$ and $T_a$ are the eight $SU(3)_c$ generators ($T^a = \frac{1}{2}\lambda^a$, where $\lambda^a$ are the Gell-Mann matrices) undergoing the commutation relation $[T^a, T^b] = i f^a_{bc} T^c$. The Lagrangian in (1.12) has a built-in exact colour gauge symmetry, meaning that the gluon fields are massless. $\mathcal{L}_{\text{QCD}}$ can be summarised as the contribution of three different parts:

$$\mathcal{L}_{\text{QCD}} = \mathcal{L}_{\text{G}} + \mathcal{L}_{\text{q}} + \mathcal{L}_{\text{int}}, \tag{1.15}$$

where $\mathcal{L}_{\text{G}} = -\frac{1}{4} G^a_{\mu\nu}(G^{\mu\nu})_a$ is the massless gluon field term, $\mathcal{L}_{\text{q}} = \sum_{k=1}^{n_f} \overline{\psi}_k \, i\gamma^\mu (\partial_\mu - m_k)\psi_k$ represents the massive quark fields and the interaction between quark currents and gluon fields is encoded in $\mathcal{L}_{\text{int}} = J^\mu_a G^a_\mu$ with $J^\mu_a = \alpha_s \sum_{k=1}^{n_f} \overline{\psi}_k \, \gamma^\mu T^a \psi_k$.

---

[6] The energy and direction of a jet are correlated to the energy and direction of its parent quark. The process by which the quark evolves into a jet is called *hadronisation*, and consists of a parton shower, which can be perturbatively calculated, and a fragmentation process, which is a non-perturbative process modelled using Monte Carlo (MC) techniques. The treatment of jets is further inspected in Section 4.3.

## 1.2 Spontaneous Symmetry Breaking and Higgs Mechanism

A Lagrangian is composed of two parts. The first part involves the derivatives of the fields, which is referred to as the kinetic term. The second part, called the potential, is expressed in terms of the fields themselves.

Within the EW framework, the Higgs mechanism is incorporated in the $SU(2)_L \otimes \mathrm{U}(1)_Y$ local gauge symmetry. Let's consider two complex scalar fields arranged in a weak isospin doublet:

$$\phi = \begin{pmatrix} \phi^+ \\ \phi^0 \end{pmatrix} = \frac{1}{\sqrt{2}} \begin{pmatrix} \phi_1 + i\phi_2 \\ \phi_3 + i\phi_4 \end{pmatrix} \tag{1.16}$$

which is subject to a potential of the form:

$$V(\phi) = \frac{1}{2}\mu^2 \phi^\dagger \phi + \frac{1}{4}\lambda(\phi^\dagger \phi)^2; \tag{1.17}$$

the corresponding Lagrangian is:

$$\mathcal{L}_{\text{Higgs}} = (\partial_\mu \phi)^\dagger (\partial^\mu \phi) - V(\phi). \tag{1.18}$$

The quadratic term in the field can be interpreted as a mass term, while the $\phi^4$ term is identified as self-interactions of the scalar field.

A distinction arises from the sign of $\mu^2$. Specifically, $\lambda$ must be positive to ensure the potential is bounded from below. However, $\mu^2$ can be either positive or negative, which leads to different shapes of the potential. When $\mu^2 < 0$, $V(\phi)$ exhibits a set of degenerate minima satisfying:

$$\phi^\dagger \phi = \frac{v^2}{2} = -\frac{\mu^2}{2\lambda}.$$

The no longer unique choice of the potential minimum (called *vacuum state*) produces a *spontaneous symmetry breaking* of the Lagrangian.

Since it is necessary that after SSB the neutral photon remains massless, the minimum of the potential must correspond to a non-zero vacuum expectation value (VEV), $v$, only for $\phi^0$:

$$\langle 0 | \phi | 0 \rangle = \frac{1}{\sqrt{2}} \begin{pmatrix} 0 \\ v \end{pmatrix}. \tag{1.19}$$

The fields can then be expanded around the minimum as follows:

$$\phi(x) = \frac{1}{\sqrt{2}} \begin{pmatrix} \phi_1(x) + i\phi_2(x) \\ v + \eta(x) + i\phi_4(x) \end{pmatrix}. \tag{1.20}$$

As described before, after the SSB a massive scalar field and three massless gauge Goldstone[7] bosons appear. These Goldstone bosons are absorbed by the gauge fields corresponding to the $W^\pm$ and $Z^0$ bosons, providing them with the longitudinal polarisation states necessary for acquiring mass.

Through the "gauging away" of the Goldstone fields the doublet can be written in the unitary gauge:

$$\phi(x) = \frac{1}{\sqrt{2}} \begin{pmatrix} 0 \\ v + h(x) \end{pmatrix} . \tag{1.21}$$

Herein lies the essence of the *Higgs mechanism*: the Goldstone fields are removed from the Lagrangian while the mass terms of gauge bosons and the Higgs particle itself arise. More than forty years after its prediction, a particle consistent with the Higgs boson was discovered [2, 3], thus completing the SM framework.

### 1.2.1 Bosons masses

The bosons mass terms previously mentioned can be identified by correcting the Lagrangian of (1.18) such that it is gauge invariant under the $SU(2)_L \otimes \mathrm{U}(1)_Y$ symmetry group. This is achieved by replacing the partial derivative with the appropriate covariant term:

$$\partial_\mu \rightarrow D_\mu = \partial_\mu + ig_W \mathbf{T} \cdot \mathbf{W}_\mu + ig' \frac{Y}{2} B_\mu ;$$

here, the gauge field $B_\mu$ couples with $Y$, $\mathbf{T}$ are the three generators of the $SU(2)_L$ symmetry[8], and $\mathbf{W}_\mu$ are the three weak gauge fields.

The expression of $(D_\mu \phi)^\dagger (D^\mu \phi)$ where $\phi$ is a Higgs doublet [9] expressed in the unitary gauge as in (1.21) is:

$$\begin{aligned} (D_\mu \phi)^\dagger (D^\mu \phi) =& \left| \left( \partial_\mu - ig_W \frac{\tau^k}{2} W^k_\mu - i \frac{g'}{2} B_\mu \right) \phi \right|^2 = \\ =& \frac{1}{2} (\partial_\mu h)(\partial^\mu h) + \frac{1}{8} g_W^2 (W^{(1)}_\mu + iW^{(2)}_\mu)(W^{(1)\mu} - iW^{(2)\mu})(v+h)^2 \\ & \frac{1}{8} (g_W W^{(3)}_\mu - g' B_\mu)(g_W W^{(3)\mu} - g' B^\mu)(v+h)^2 . \end{aligned} \tag{1.22}$$

---

[7] According to the Goldstone theorem, for every independent transformation of the symmetry group that does not preserve the fundamental state, a massless particle originates in the spectrum of field excitations; this particle takes the name of Goldstone boson.

[8] In this notation, $\mathbf{T} = \frac{1}{2}\sigma$, where $\sigma$ are the Pauli matrices.

[9] This particular doublet is such that the lower component is neutral and has $I_W^{(3)} = -\frac{1}{2}$; thus, it has hypercharge $Y = 1$. Furthermore, the dependence on $x$ of $\phi$ is neglected in the notation.

Since the bosons masses are given by the terms in (1.22) which are quadratic in the boson fields, in the Lagrangian the mass terms for the $W^{(1)}$ and $W^{(2)}$ fields will be:

$$\frac{1}{2}m_W^2 W_\mu^{(k)} W^{(k)\mu} \quad \text{with} \quad k = 1, 2$$

This means that:

$$m_W = \frac{1}{2} g_W v \tag{1.23}$$

Taking now the terms which are quadratic in the $W^{(3)}$ and $B$ fields, one gets:

$$\frac{v^2}{8}(g_W W_\mu^{(3)} - g' B_\mu)(g_W W^{(3)\mu} - g' B^\mu) = \frac{v^2}{8}\begin{pmatrix} W_\mu^{(3)} & B_\mu \end{pmatrix}\begin{pmatrix} g_W^2 & -g_W g' \\ -g_W g' & g'^2 \end{pmatrix}\begin{pmatrix} W_\mu^{(3)} \\ B_\mu \end{pmatrix}, \tag{1.24}$$

where the matrix containing the coefficients $g_W$ and $g'$ is called *mass matrix* **M**.

Here the physical boson fields are obtained by computing the basis in which the mass matrix is diagonal, so after solving the characteristic equation $\det(\mathbf{M} - \lambda I) = 0$, the expression of (1.24) becomes:

$$\frac{v^2}{8}\begin{pmatrix} A_\mu & Z_\mu \end{pmatrix}\begin{pmatrix} 0 & 0 \\ 0 & g_W^2 + g'^2 \end{pmatrix}\begin{pmatrix} A_\mu \\ Z_\mu \end{pmatrix}, \tag{1.25}$$

where $A_\mu$ and $Z_\mu$ are physical fields corresponding to the eigenvectors of **M** which are summarised below, together with their eigenvalues:

$$Z_\mu = \frac{g' W_\mu^{(3)} + g_W B_\mu}{\sqrt{g_W^2 + g'^2}} \quad \text{with} \quad m_Z = \frac{v}{2}\sqrt{g_W^2 + g'^2} \tag{1.26}$$

$$A_\mu = \frac{g' W_\mu^{(3)} - g_W B_\mu}{\sqrt{g_W^2 + g'^2}} \quad \text{with} \quad m_A = 0. \tag{1.27}$$

The parameters which regulate the EWSB of the SM are the two coupling constants $g_W$ and $g'$, together with the parameters $\lambda$ and $\mu$ of (1.17), whose values are computed from the experimentally measured masses of the gauge and Higgs bosons [17] to be $\lambda \simeq 0.129$ and $|\mu^2| \simeq (88.8 \text{ GeV})^2$.

The mass of the Higgs boson, $m_H$, and the VEV are connected via parameters of the potential, $\mu$ and $\lambda$:

$$m_H = \sqrt{\frac{\lambda}{2}} v \tag{1.28}$$

$$v = \sqrt{\frac{\mu^2}{\lambda}}. \tag{1.29}$$

## 1.3 The Yukawa mechanism and the fermions masses

Regarding fermions, the SM operates on the families of left-handed doublets and right-handed singlets of quarks and leptons; however the fact that the SU$(2)_L$ group acts only on the left-handed part of fermions constitutes an issue concerning their mass. In fact, the mass-related term $-m(\overline{\psi}_L\psi_R + \overline{\psi}_R\psi_L)$ that appears in the QED Lagrangian in (1.9) is not gauge invariant, since it couples both the left-handed and right-handed components. A new interaction called *Yukawa interaction* is then introduced, to mediate the coupling between the Higgs field and massless fermions via a coupling constant $y$.
The corresponding piece of the Lagrangian is:

$$\mathcal{L}_\mathrm{Y} = -\Gamma_u^{ij}\overline{q}_L^i\epsilon\phi^* u_R^j - \Gamma_d^{ij}\overline{q}_L^i\phi d_R^j - \Gamma_e^{ij}\overline{\ell}_L^i\phi e_R^j + h.c^{10}, \tag{1.30}$$

where $\Gamma_u, \Gamma_d, \Gamma_e$ are $3 \times 3$ complex Yukawa matrices (in family space) of the up- and down-type quarks, respectively, and $i, j$ are the generation labels. Following the same operation of "gauging away" previously shown in (1.21), the physical states are obtained by diagonalising the Yukawa matrices in order to obtain the diagonal mass matrices for $f = u, d$:

$$m_f = y_i\frac{v}{\sqrt{2}}, \tag{1.31}$$

where $y_i$ is the Yukawa coupling for the i-th fermion mass eigenstate.
Since these matrices introduced in (1.30) do not need to be diagonal, mixing between different fermion generations is allowed. In the quark sector, the mixing between the *weak eigenstates* of the down-type quarks $d'$, $s'$ and $b'$, and the corresponding mass eigenstates $d$, $s$ and $b$, is described by the Cabibbo-Kobayashi-Maskawa (CKM) matrix [33, 34]:

$$\begin{pmatrix} d' \\ s' \\ b' \end{pmatrix} = \begin{pmatrix} V_{ud} & V_{us} & V_{ub} \\ V_{cd} & V_{cs} & V_{cb} \\ V_{td} & V_{ts} & V_{tb} \end{pmatrix} \begin{pmatrix} d \\ s \\ b \end{pmatrix}. \tag{1.32}$$

As per convention, only the down-type quarks undergo mixing, while the up-type mass matrix remains diagonal. The coupling strength of the $W^\pm$ boson to physical up- and down-type quarks are determined by the matrix elements.

This unitary matrix contains diagonal entries close to unity, while the off-diagonal entries are roughly 0.2 between the first and second generation, about 0.04 between the second and third, and even smaller when transitioning from the first to the third generation [17].

The matrix element $V_{tb}$ is indirectly constrained by the unitarity of the CKM matrix, assuming three quark generations (and by directly measuring the single top production cross-section, see

---

[10] $\epsilon = i\sigma_2$ is the total antisymmetric tensor in two dimensions, related to the second Pauli matrix $\sigma_2$, required to ensure each term is separately electrically neutral.

Section 2.1.1). The value is very close to 1: $|V_{tb}| > 0.999$ at a 90% confidence level (C.L.). Therefore, the top quark in the SM predominantly couples to bottom quarks, which influences both the top quark production, suppressing the electroweak single top production mechanisms relative to pair production (see Section 2.1.1), and its decay, facilitating the isolation and reconstruction of top events by focusing on the presence of $b$-quark jets in the final state (see Section 4.5).

Assuming that neutrinos are massless, no such mixing occurs in the lepton sector. However, experimental evidence shows that neutrinos possess mass, leading to the introduction of an analogous leptonic mixing matrix, the Pontecorvo-Maki-Nakagawa-Sakata (PMNS) matrix [35]. For the purposes of this thesis, any lepton sector mixing has no impact, thus a massless neutrino SM formulation is adopted.

In summary, the SM is a unitary, renormalisable theory, capable of perturbatively calculating processes at high energies. It includes 18 parameters that must be derived from measurements:

- 9 Yukawa couplings for the fermion masses,
- 4 parameters for the CKM mixing matrix,
- 3 coupling constants $\alpha_s$, $g_W$, $g'$ for $SU(3)_c$, $SU(2)_L$, and $U(1)_Y$, respectively,
- 2 parameters from EWSB: $v$ and $m_H$.

At currently accessible energy scales, the SM successfully models the interactions of fundamental fermions and gauge bosons. Its predictions have been corroborated with high precision at recent colliders (SPS, LEP, Tevatron, and LHC).

## 1.4 Beyond the Standard Model

Despite the undeniable success of the SM in predicting a plethora of phenomena, as also shown in Figure 1.2 for what concerns LHC measurements, it does not account for several observed aspects of the Universe. Evidence of non-baryonic matter that does not partake in electromagnetic interactions, often referred to as *dark matter*, is one such phenomenon outside the design limits of the SM [36]. Moreover, the occurrence of baryogenesis in the early Universe necessitates the violation of baryon numbers, a process not accommodated within the SM's scope [37]. Furthermore, evidence [38] for dark energy, an unknown form of energy that accelerates the Universe's expansion, is also beyond the SM's explanatory capacity.

Given these limitations, numerous theoretical models that extend beyond the Standard Model (BSM) have been proposed to elucidate these unexplained phenomena. Prominent among these is Supersymmetry (SUSY) [39–42], a theoretical construct that to every fermion in the SM associates a bosonic counterpart, and conversely, to every boson associates a fermionic counterpart. These partner particles differ in spin by half a unit. Additionally, supersymmetry implies the existence of a second Higgs doublet. It is theorised that the new particles with colour charge, such as the gluinos ($\tilde{g}$) and top squarks ($\tilde{t}$) — the supersymmetric counterparts of the gluon and top quark, respectively — should have masses around 1 TeV. This feature addresses one of the most critical unknowns of the SM, whenever this is thought as a low energy limit of some additional UV completion: the so-called *hierarchy problem*. This problem pertains to the question of why the Higgs boson is substantially lighter than the scale at which radiative corrections are significant [43]:

$$\Delta m_H = \frac{|\lambda_f^2|}{8\pi^2}\Lambda_{\mathrm{UV}}^2 + \dots \tag{1.33}$$

where $\lambda_f$ is the coupling between the Higgs field and a fermion, and $\Lambda_{\mathrm{UV}}$ represents the typical mass scale of the UV completion, which is e.g. the Plank mass for gravity. A boson partner to the top quark would stabilise the Higgs boson mass against these large corrections, provided its mass is close to the electroweak symmetry breaking energy scale.

Another popular way of investigating BSM physics is through models featuring flavour-changing neutral currents (FCNCs), which the SM prohibits at the tree level due to the Glashow-Iliopoulos-Maiani (GIM) suppression [44]. This suppression is evident in the rarity of processes like top quark decays to a quark and a neutral boson, $t \to Xq$, ($X = g, Z, \gamma$ or $H$; $q = u$ or $c$). However, several BSM theories predict an enhanced FCNC rate, potentially observable in experiments. For instance, in models with multiple Higgs doublets or those incorporating additional quark families, FCNC effects can be significantly magnified.

Each of these BSM theories provides predictions for a vast number of properties that precise measurements within the SM framework can either exclude or constrain.

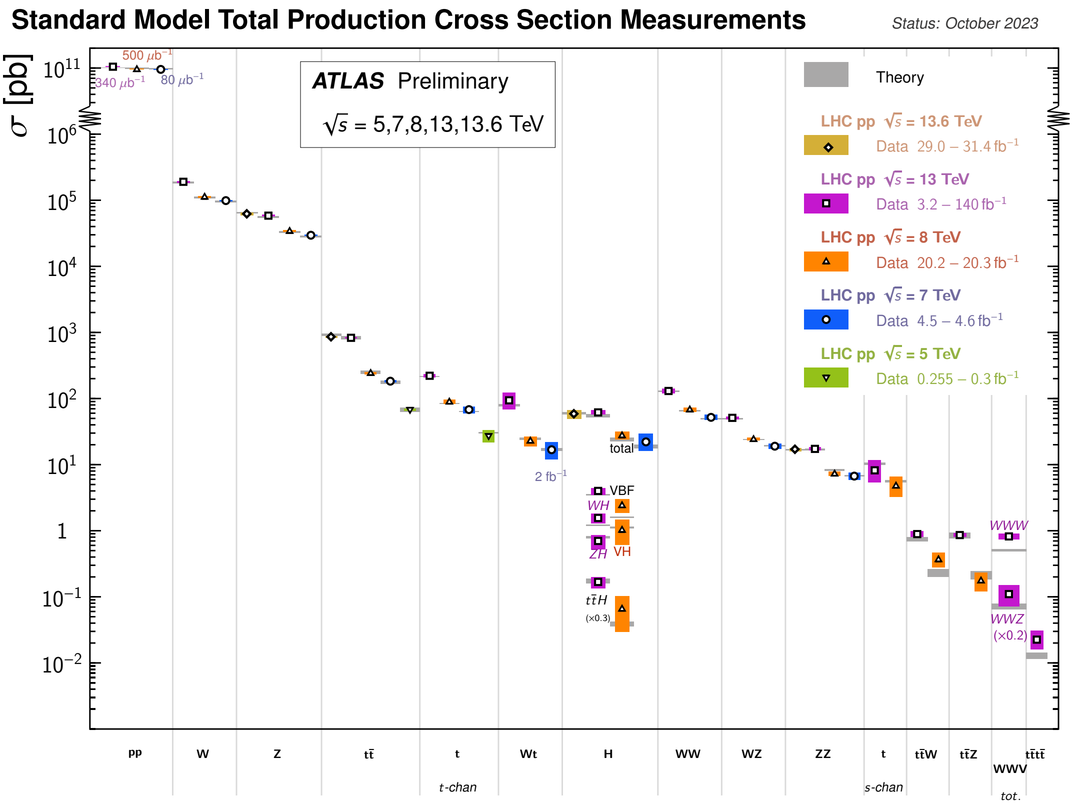

Figure 1.2: Summary of several Standard Model cross-section measurements performed by ATLAS at the LHC. The measurements are corrected for branching fractions, compared to the corresponding theoretical expectations. Figure taken from [45].

# Chapter 2

# The top quark, the $Z$-boson, and their properties

## 2.1 The top quark

Historically, the observation of charge-parity (CP)-violation in neutral $K$-mesons [46] posed a significant challenge to the SM, which, at the time, accommodated only two generations of quarks and leptons. The proposed solution involved the inclusion of a third generation of fermions, which was yet to be observed. With the inclusion of the third quark generation, the quark mixing matrix expanded from a $2 \times 2$ matrix with a single parameter, to a $3 \times 3$ matrix, defined by four parameters. The addition of these degrees of freedom allowed for an intrinsic complex phase, potentially leading to $CP$-violating terms [34]. This theoretical shift became even more appealing following the discovery of a third-generation lepton, the $\tau$ lepton [47].

Upon detecting a third-generation quark, often referred to as the bottom[1] quark [47], it was logically anticipated that its weak isospin partner, the top quark, would exist. This assumption was confirmed in 1995, when the top quark was eventually discovered by the CDF [6] and DØ [7] Collaborations at the Fermilab Tevatron $p\bar{p}$ collider.

The top quark is the heaviest known elementary particle of the SM. Its large mass, around 172.5 GeV, and consequently the top-Higgs Yukawa coupling $y_t \sim 1$, suggest that the top quark plays an important role in the spontaneous symmetry breaking mechanism. The top quark mean lifetime is approximately $\tau_t \sim 10^{-25}$s [17]; it decays before hadronising, thus transferring all of its properties to the decay products.

---

[1] Sometimes, the name *beauty* is used.

### 2.1.1 Top quark production

At hadron colliders, and within the SM, the top quark is predominantly[2] produced via two classes of processes: top quark pairs ($t\bar{t}$), via the strong interaction, or single-top production, through the electroweak interaction.

#### Hard scattering in proton-proton collisions

In the study of particle interactions, such as those involving proton-proton or electron-proton collisions, the proton is considered as mainly composed of three *valence* quarks ($uud$), that dictate its quantum numbers and carry the most of its momentum. Alongside valence quarks, there are *sea* quarks and gluons, that carry the remaining part of the momentum of the proton. Together, the constituents of the proton are called *partons*. When two protons collide, a hard interaction occurs between their partons; soft interactions involving the remainder of the hadron constituents produce many low energy particles which are largely uncorrelated with the hard collision. In the centre-of-mass frame, in which protons are moving relativistically, the momentum of the parton is nearly collinear with the momentum of the proton. Thus, the colliding objects can be ideally visualised as streams of partons, each one carrying a fraction $x_i$[3] of the longitudinal momentum of its parent hadron. As a result, hadronic collisions can be *factorised* [48] into parton collisions weighted by *parton distribution functions* (PDFs), describing the probability for the $i-th$ parton to carry $x_i$. The cross-section, $\sigma$, of each process can be calculated by harnessing the factorisation properties of hadrons and producing an expression composed of a non-perturbative term, described by PDFs, and a perturbative part:

$$\sigma(pp \to X) \sum_{i,j=q,\bar{q},g} \int_{4m^2}^{s} d\hat{s}\hat{F}_{ij}(\hat{s}, s, \mu_F)\hat{\sigma}_{ij\to X}(\hat{s}, m^2, \mu_f^2, \mu_r^2) \tag{2.1}$$

where $X$ represents a generic final state, $s$ is the square of the $pp$ centre-of-mass energy, $\hat{\sigma}_{ij\to X}$ is the partonic cross-section. The factorisation scale, $\mu_f$, is a term that separates the non-perturbative and the perturbative part, represented by the renormalisation scale $\mu_r$. $\hat{F}_{ij}$ is the partonic density, expressed as

$$\hat{F}_{ij} = \frac{1}{s}\int_{\hat{s}}^{s} \frac{ds'}{s'} f_{i/p}\left(\mu_f^2 \cdot \frac{s'}{s}\right) f_{j/p}\left(\mu_f^2 \cdot \frac{s'}{s}\right) \tag{2.2}$$

in which $f_{i(j)/p}$ represents the initial state of a parton $i(j)$ in a proton $p$, and $\hat{s}$ is the square of the partonic centre-of mass energy. Typically, the factorisation scale is considered together with the appropriate scale for the renormalisation of the perturbative cross-section, given that both parameters are arbitrary. This common scale, $\mu$, is usually taken to be similar to the energetic scale of the investigated process; for instance, when measuring the $t\bar{t}$ cross section, $\mu$ is equal

---

[2] The SM accounts also for combination of the dominant processes listed, as four-top and three-top production. However, for the purpose of this thesis, the cross section of these processes can be considered negligible.

[3] The quantity $x_i$ is often referred to as Bjorken-$x$.

to the top quark mass, $\mu_r = \mu_f = m_t$; an exact calculation would not depend on these scales. However, these scales affect finite-order calculations and must be taken into account as sources of uncertainty in the theoretical predictions. In this thesis, these uncertainties are generally estimated by bounding the predictions using two sets of calculations, considering an independent variation of the renormalisation and factorisation scales in the ME by factors of 0.5 and 2. Further details are provided in Section 9.

### Top quark pair production

In proton-proton collisions, the majority of top quark pair production originates from strong interactions. Nonetheless, a minor contribution also comes from electroweak processes. At leading order (LO), two main processes can be distinguished: quark-antiquark ($q\overline{q}$) annihilation and gluon-gluon ($gg$) fusion, as illustrated in Figure 2.1. The relative contribution to the production, whether due to the annihilation process or fusion, depends on the colliding objects and properties. In proton-antiproton ($p\overline{p}$) collisions at energies close to the kinematic threshold, both quark and antiquark can be valence quarks. Therefore, the contribution from the $q\overline{q} \rightarrow t\bar{t}$ process can prevail, as in the case of the Tevatron collider. In $pp$ colliders like the LHC, antiquarks can only come from the quark sea, therefore gluon fusion dominates the production. At higher energies, the $gg \rightarrow t\bar{t}$ process dominates for both $p\overline{p}$ and $pp$ collisions, as the gluon density increases with the energy.

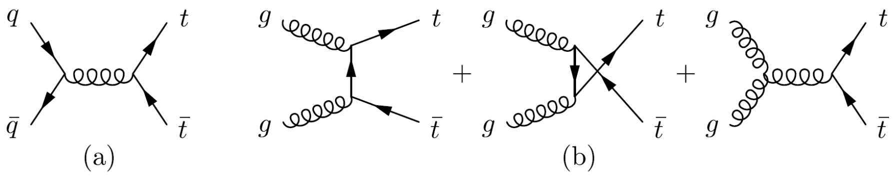

Figure 2.1: Feynman diagrams of the LO processes for $t\bar{t}$ production: (a) quark-antiquark annihilation ($q\overline{q} \rightarrow t\bar{t}$) and (b) gluon-gluon fusion ($gg \rightarrow t\bar{t}$).

In this thesis, the Top++ 2.0 [49] program is employed to calculate the $t\bar{t}$ cross-section; the predictions [50–55] are computed at next-to-next-to-leading order (NNLO) with next-to-next-to-leading resummation of logarithmic soft gluon terms (NNLL). The theoretical predictions estimation is further described in Chapter 6. The uncertainties on the predictions originate from variations of renormalisation and factorisation scales, as well as from an uncertainty from the PDF. Experimental checks of the theoretical predictions for $\sigma_{t\bar{t}}$ show that all observed values agree within their uncertainties with these predictions, as summarised in Figure 2.2.

### Single-top production

Top quarks can be produced as single particles through the EW interaction involving the $tWb$ vertex. Three production models exist, regulated by the virtuality[4] $Q^2$ of the $W$-boson:

---

[4] See Section 1.1.3.

- ***s*-channel**
  A virtual space-like ($Q^2 > 0$) $W$-boson interacts with a $b$-quark inside the proton; production in the $t$-channel is the dominant source of single top quarks at the LHC. Figure 2.3 (a) illustrates the Feynman diagrams corresponding to this process.

- ***t*-channel**
  This channel, also called $t\bar{b}$ production, corresponds to a Drell-Yan process, in which a time-like $W$-boson with $Q^2 \leq (m_t + m_b)^2$ is produced by the fusion of two quarks belonging to an $SU(2)$-isospin doublet. This process is displayed in Figure 2.3 (b)

- ***tW*-channel**
  The top quark is produced in association with a real ($Q^2 = m_W^2$) $W$-boson. Figure 2.3 (c) illustrates the Feynman diagram corresponding to this process.

In this work, cross-section predictions in the $s$-channel are calculated at next-to-leading order (NLO) in QCD with the HATHOR 2.1 [65, 66] program. The predicted cross-sections in the $t$-channel are calculated with the MCFM program [67] at NNLO in QCD. In the $tW$ channel, predictions are computed at NLO in QCD with the addition of third-order corrections of soft-gluon emissions by resumming NNLL terms [68]. The top quark mass is set to 172.5 GeV for all channels, and the PDF4LHC21 PDF set [69] is used.

Both the ATLAS and the CMS collaboration have extensively measured single-top production across the three channels [70–85] covering all the processes at $\sqrt{s}$ = 7, 8 TeV, and some at 5.02

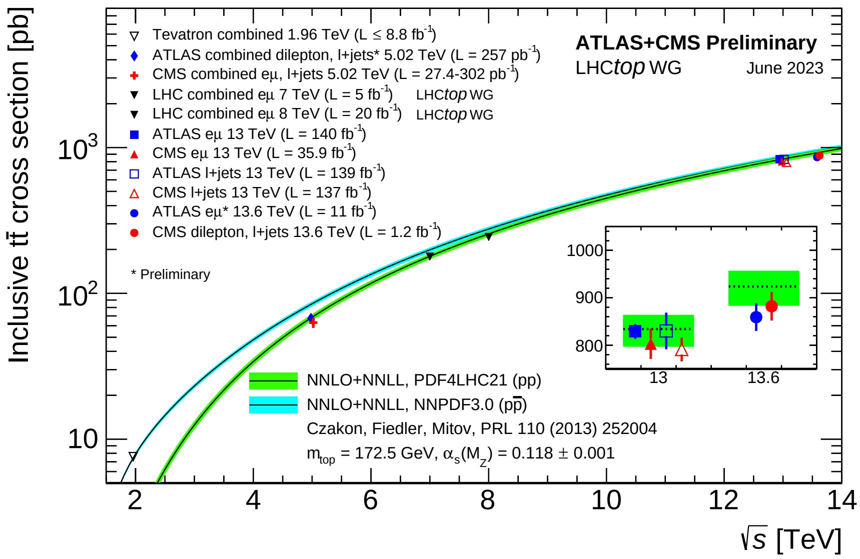

Figure 2.2: Summary of LHC and Tevatron results [56–63] for the top quark pair production cross-section measurements as a function of the centre-of-mass energy compared to the theoretical prediction [55]. Both theory and experimental results assume $m_t$ = 172.5 GeV. The figure is taken from [64].

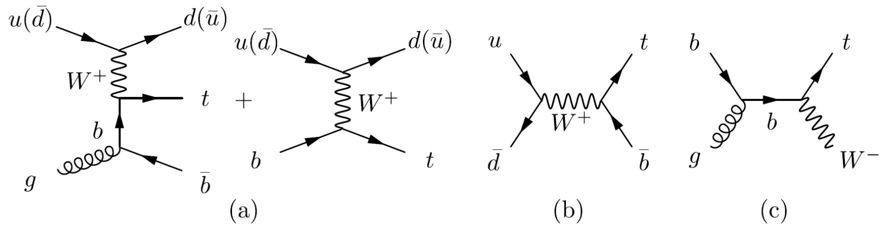

Figure 2.3: Feynman diagrams of the LO processes for single-top production: (a) $s$-channel, (b) $t$-channel and (c) associated $tW$ production.

and 13 TeV. The results are summarised in Figure 2.4.

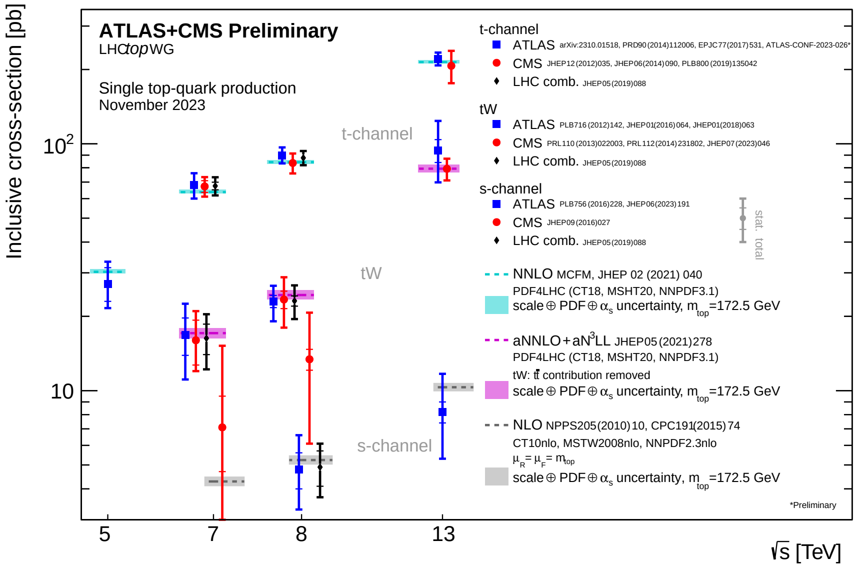

Figure 2.4: Summary of ATLAS, CMS and combined measurements of the single top production cross-sections in various channels as a function of the center of mass energy. The measurements are compared to theoretical calculations based on NLO QCD, NLO QCD complemented with NNLL resummation and NNLO QCD ($t$-channel only). The figure is taken from [64].

## 2.1.2 Top quark decay

As discussed before, the top quark decays via the weak interaction, with a mean life shorter than the typical timescale of the hadronisation processes, producing a $W$-boson and a down-type quark, $t \to W^+q(\bar{t} \to W^-\overline{q})$. The flavour of the produced quark is determined by the CKM matrix. Assuming its unitarity and considering three generations of quarks, the predominant matrix element responsible for the top quark decay is $|V_{tq}| \simeq |V_{tb}| = 0.999142^{+0.000018}_{-0.000023}$ [86]. This coupling allows to consider the top quarks as decaying essentially only into a $W$-boson and a $b$-quark. The $W$-boson decays in about $1/3$ of the cases into a charged lepton ($e$, $\mu$ or $\tau$ ) and a neutrino, with all the three lepton flavours being produced at equal rate. In the remaining $2/3$ of the cases, the $W$-boson decays into a quark-antiquark pair, and the abundance of a given pair is instead determined by the magnitude of the relevant CKM matrix element. Specifically, the CKM mechanism suppresses the production of $b$-quarks as $|V_{cb}| \simeq 1.7 \times 10^{-3}$. Therefore, the hadronic $W$-boson decay can be considered as a clean source of light quarks. Experimentally, a $t\bar{t}$ pair decay can be characterised by the subsequent decays of the $W$-bosons into the following channels (see Figure 2.5).

**All-hadronic or fully hadronic**[5] ($t\bar{t} \rightarrow W^{+}bW^{-}\overline{b} \rightarrow \overline{q}q'b\, q''\overline{q}'''\overline{b}$): representing ~4/9 of all the $t\bar{t}$ decays, in this channel both $W$-bosons decay hadronically into quarks. Thus, six jets characterise the event: two $b$-jets from the top quark decay and four light jets from the $W$-boson decay. This process suffers from a large multijet background, which is quite difficult to model, leading to a lower signal-to-background ratio. Moreover, matching reconstructed jets to the original partons produced in the $t\bar{t}$ decay constitutes a significant challenge, due to the high combinatorial nature of the background. This complication, combined to the fact that the experimental resolutions of jets are broader compared to charged leptons, impacts directly the computation of variables like reconstructed invariant masses.

**Dilepton or fully leptonic** ($t\bar{t} \rightarrow W^{+}bW^{-}\overline{b} \rightarrow \ell^{+}\nu b\, \ell^{-}\overline{\nu}\overline{b}$): enclosing ~1/9 of all the $t\bar{t}$ decays, this channel is characterised by the leptonic decay of both the $W$-bosons into a charged lepton, and a related neutrino. This mode yields an extremely pure sample of top quark events; moreover, because it involves only two jets, the measurement has reduced uncertainties originating from reconstruction of jet kinematics. On the other hand, this process suffers both from poor statistics, and by the presence of two neutrinos that remain undetected.

**Single-lepton or Semileptonic**[6] ($t\bar{t} \rightarrow W^{+}bW^{-}\overline{b} \rightarrow \ell^{+}\nu b\, q\overline{q}'\overline{b}$ or $t\bar{t} \rightarrow W^{+}bW^{-}\overline{b} \rightarrow \overline{q}q'b\, \ell^{-}\overline{\nu}\overline{b}$): encompassing ~4/9 of all the $t\bar{t}$ decays, in this process one $W$-boson decays hadronically into two quarks and the other decays leptonically into a charged lepton and a corresponding neutrino. The presence of a single high $p_{\mathrm{T}}$[7] lepton and of four or more jets (two of them coming from $b$-quarks) allows to suppress the multijet and the $W$+jet backgrounds respectively. This set of features grants the single-lepton channel a larger signal-to-background ratio compared to the all-hadronic channel, and higher branching ratio compared to the dilepton channel. Moreover, the presence of a single neutrino simplifies its reconstruction process, being it the only source of missing energy.

$W$-boson decays involving $\tau$ leptons are generally not directly measurable due to the short lifetime of the leptons $\tau_{\tau} = 2.9 \times 10^{-13}$s [17]. In these processes, the $\tau$ lepton decays 62.96% [17] of the times hadronically, into a $\tau$ neutrino and one or more hadrons. In the remaining cases, either an electron or a muon, and two neutrinos are produced. Usually, analyses do not consider

---

[5] Sometimes, this channel can be also called *all-jets*.

[6] Sometimes, this channel can be also called *lepton+jets* ($\ell$+jets).

[7] A particle's $p_{\mathrm{T}}$, is defined as the projection of the particle momentum ($p$) on the plane orthogonal to the $z$ axis. See Section 3.2.1.

leptonically decaying taus in either the dilepton or single-lepton channel; nevertheless, these decays are implicitly included in the events considered. Analyses involving the identification of a hadronically decaying $\tau$ are treated apart.

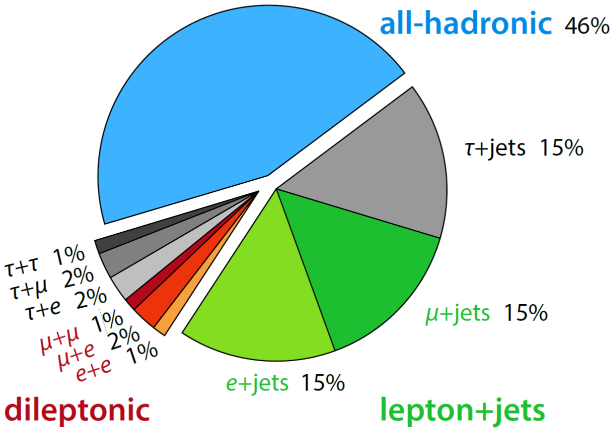

Figure 2.5: Top quark pair branching fractions.

### 2.1.3 Top quark mass

There are a number of free parameters within the SM[8], and the top quark mass happens to be one of them. It cannot be calculated from first principles, therefore precise measurements of $m_t$ provide a crucial benchmark for the consistency of the EW parameters in the SM [87–89]. Moreover, the measurement of $m_t$ has significant implications for understanding the stability of the electroweak vacuum, and it plays a crucial role in our knowledge of the early stages of the universe [90]. The mass of the top quark has been measured in the experiments conducted at both the Tevatron and the LHC, involving various energies and both $t\bar{t}$ and single-top production channels [16, 91–106]. Among the various results, the world combination of the top quark measurements reports $m_t^{\text{world}} = 172.69 \pm 0.30$ GeV [17], whereas the ATLAS and CMS combination from 2023 yields $m_t^{\text{ATLAS+CMS}} = 172.52 \pm 0.33$ GeV [107].

The investigation of the top quark mass is a vital element of experimental physics, one of the most relevant aspects of which is the precise determination of the parameters being experimentally measured. Direct estimations employ the reconstruction of invariant mass from the decay products of the top quark, and then comparing the distribution observed in data with predictions obtained using different $m_t$ values as input parameter in the simulation of the full process, including non-perturbative effects. Such direct measurements are usually considered possessing an intrinsic theoretical uncertainty of the order of $\Lambda_{QCD}$ related to the inclusion of non-perturbative effects in the predictions, even if the argument is still under debate in the theory community[9] [109, 110]. To

---

[8] The complete list of the free parameters of the SM is summarised in Section 1.3.

[9] Recent studies suggest that the implementation of EW corrections in computing $m_t$ could help in understanding the scale-dependent top quark masses obtained from the LHC and Tevatron data [108].

avoid these interpretation issues, so-called "indirect" top-quark mass measurements are performed by estimating $m_t^{\text{pole}}$[10] via the top-quark production cross-section dependence on it [112–117]. Another possible strategy is to exploit purely leptonic distributions, avoiding the hadronisation issue, and achieving a theoretically cleaner measurement of $m_t^{\text{pole}}$ [118]. Currently, the most precise estimate of the pole-mass with indirect measurements is $m_t^{\text{pole}} = 170.5 \pm 0.8$ GeV [116].

In this thesis, unless stated otherwise, a top quark mass of 172.5 GeV is adopted for the cross-section calculations and the Monte Carlo samples. This approach aligns with the recommendations of the LHC Top Physics Working Group [119] and maintains consistency with the previous analyses using Run 2 data [8, 120].

## 2.2 The $Z$-boson

The discovery of the $Z$-boson, along with the discovery of the $W$-boson, was achieved in 1983 by the joint efforts of the UA1 and UA2 collaborations at the S$p\bar{p}$S collider at CERN [121–123]. These events represent the culmination of a series of accomplishments that began in 1973, with the observation of Neutral Currents; immediately afterwards, the charm quark was discovered in 1974, the tau lepton in 1975, and the bottom quark in 1977. The combination of these experimental milestones and the theoretical breakthrough represented by the renormalisation of the Gauge Theory has outstandingly solidified the SM as an experimentally successful theory.

The $Z$-boson serves as one of the most effective tools for investigating the features of the SM with unprecedented accuracy, as demonstrated by the experimental campaigns at the Large Electron-Positron Collider (LEP) [124], the Stanford Linear Collider (SLC) [125], and hadron colliders.

### 2.2.1 $Z$-boson properties

The $Z$-boson lineshape parameters, such as the mass ($m_Z$), the total width ($\Gamma_Z$) and the partial widths ($\Gamma_{f\bar{f}}$), have been determined from an analysis of the production cross sections of fermionic final states starting from $e^+e^-$ collisions, constituting arguably the most significant achievement of LEP. The shape of the cross-section around the $Z$ peak, $\sigma(s)$, can be estimated through an analytic expression:

$$\sigma(s) = \sigma^0_{f\bar{f}} \frac{s\Gamma_Z^2}{(s - m_Z^2)^2 + \frac{s^2}{m_Z^2}\Gamma_Z^2}, \tag{2.3}$$

where $\sigma^0_{f\bar{f}}$ represents the cross-section of the $e^+e^- \to f\bar{f}$ process at $\sqrt{s} = m_Z$. Currently, the most up-to-date values [17] for the $Z$-boson mass and total width are:

$$m_Z = 91.1876 \pm 0.0021 \text{ GeV},$$
$$\Gamma_Z = 2.4955 \pm 0.002 \text{ GeV}.$$

---

[10] The top quark pole mass $m_t^{\text{pole}}$, corresponds to the definition of the mass of a free particle [111].

On the other hand, the pole cross section can be described as a function of the $Z$-boson partial widths:

$$\sigma^0_{f\bar{f}} = \frac{12\pi}{m_Z^2}\frac{\Gamma_{ee}\Gamma_{f\bar{f}}}{\Gamma_Z^2}. \tag{2.4}$$

In terms of total width, the decay of the $Z$-boson can be expressed as:

$$\Gamma_Z = N_\nu\Gamma_\nu + 3\Gamma_{ee} + \Gamma_{\text{hadrons}}, \tag{2.5}$$

where $N_\nu$ is the number of neutrino families. Experiments at LEP determined $N_\nu$ to be $2.9840 \pm 0.0082$, in agreement with the three observed generations of fundamental fermions [126]. Figure 2.6 displays the predicted cross-sections for different numbers of generations around the $Z$ peak.

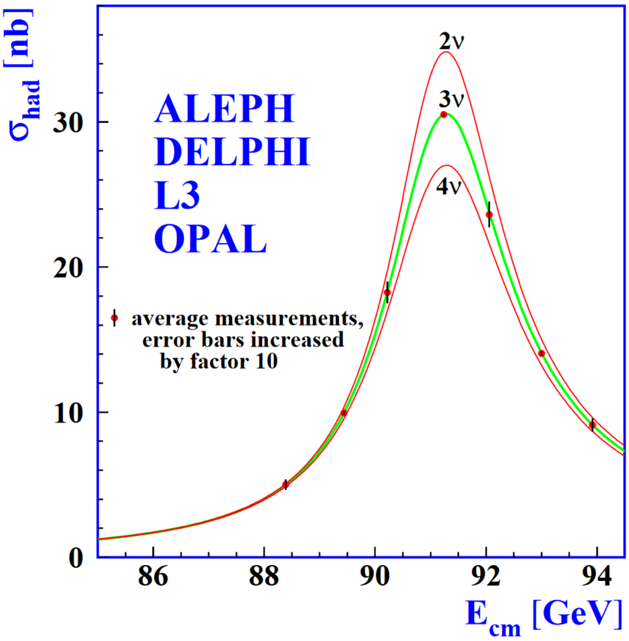

Figure 2.6: Measurements of the hadron production cross-section around the $Z$-boson resonance. The curves indicate the predicted cross-section for two, three and four neutrino species with SM couplings and negligible mass. Figure taken from [126].

More recent studies [127, 128] have applied corrections to the LEP results, including the effect of correlated luminosity systematics, and used an improved cross-section calculation to obtain $N_\nu = 2.9963 \pm 0.0074$.

### 2.2.2 $Z$-boson production

The dominant contribution to the $Z$-boson at the LHC is given by the neutral-current *Drell-Yan* process [129]. The annihilation of a quark-antiquark pair leads to the creation of a $Z$-boson (or a virtual photon), consequently decaying in a pair of high transverse momentum[11] fermions. At the LHC, measuring the $Z$-boson decaying into leptons is preferred because of clearer signals, reduced backgrounds, and enhanced energy and momentum resolution. Figure 2.7 reports a representative LO Feynman diagram for the Drell-Yan process, with leptons in the final states.

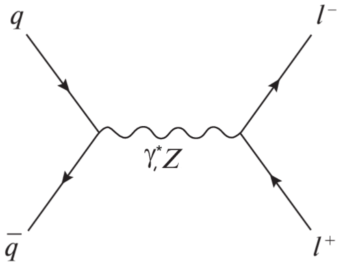

Figure 2.7: Leading order Feynman diagram for the lepton pair production in the Drell-Yan process.

As shown in Figure 2.8, at NLO the production of a $Z$-boson occurs alongside a jet. This process includes both an electroweak vertex and a strong interaction vertex.

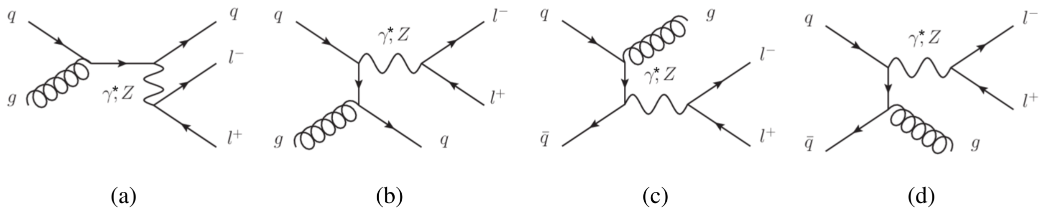

Figure 2.8: NLO Feynman diagrams for the lepton pair production in the Drell-Yan process.

The NLO Drell-Yan process enables the examination of perturbative QCD across a broad range of kinematics and varying jet multiplicities. A high level of precision can be achieved in these studies, helping to refine the PDFs, which represent a primary source of uncertainty in modeling final states with multiple partons.

Since its discovery, several measurements of the $Z$-boson cross-section have been performed with $p\bar{p}$ collisions by the CDF and D0 collaborations, at the centre-of-mass energies of $\sqrt{s} = 1.8$ TeV and $\sqrt{s} = 1.96$ TeV [130, 131], as well as with $pp$ collisions at the LHC by the ATLAS and CMS experiments [132–142].

### 2.2.3 $Z$-boson early measurements at the LHC

The generation of $Z$-bosons at hadron colliders is characterised by a large production rate and provides a distinct signature, thanks to the high transverse momentum leptons in the final state.

---

[11] For the definition of transverse momentum, see Section 3.2.1.

These characteristics, together with its well-known properties, such as precise mass and decays, make the $Z$-boson a “standard candle” in the SM, a vital benchmark tool for detector calibration and alignment in hadron collider physics.

In early stages of data-taking, such as the ones described in this thesis, when experimental conditions change, including shifts in the centre-of-mass energy or modifications to the detector configuration, measuring the $Z$-boson is often one of the first steps [143].

As further described in Section 4, several detector calibrations rely on the precise knowledge of the $Z$ peak energy, such as the lepton reconstruction. Moreover, the monitoring of the luminosity can be enhanced by using the counts of reconstructed $Z \rightarrow \ell\ell$ events, or $Z$ *counting technique* [144]. Exploiting the knowledge of $Z$-boson phenomenology ensures that detectors are correctly calibrated and functioning as intended, paving the way for more complex and less well-known analyses.

Moreover, it is usually beneficial to exploit the high precision attainable in the $Z$-boson measurements to enhance analyses that would be otherwise challenging during the initial phases of data collection. For instance, as presented in Section 5, by calculating the ratio between the top quark pair cross-section and the $Z$-boson cross-section, it is possible to mutually cancel several sources of systematic uncertainty and become sensitive to the gluon-to-quark PDF ratio. Several measurements have been conducted by the ATLAS collaboration at $\sqrt{s}$ =7,8, and 13 TeV in order to probe gluon PDFs in different Bjorken-$x$ regions [8].

# Chapter 3

# The Large Hadron Collider and the ATLAS Detector

## 3.1 The Large Hadron Collider

The Large Hadron Collider (LHC) [1] is a two-ring-hadron accelerator, the largest and most powerful existing at the moment. It is situated at CERN, a particle physics research site located on the border between France and Switzerland, near the city of Geneva. It is in operation since 2008, and it is the last addition to the CERN's accelerator complex. The LHC is housed in a 27.7-kilometre tunnel, originally built for the LEP machine between 1984 and 1989, buried around 50 to 175 m underground. The tunnel is divided into eight straight sections and eight arcs, and lies on a plane inclined at 1.4° towards the Lèman lake. Along the perimeter of the tunnel there are four points in which the LHC major experiments are located: points 1 and 5 host ATLAS and CMS, while points 2 and 8 are respectively assigned to ALICE [145] and LHCb [146]; the layout of the experimental caverns is shown in Figure 3.1. Two link tunnels, each approximately 2.5 km long, connect the LHC with the CERN accelerator group that acts as an injector [147]; the structure of the facility is shown in Figure 3.2.

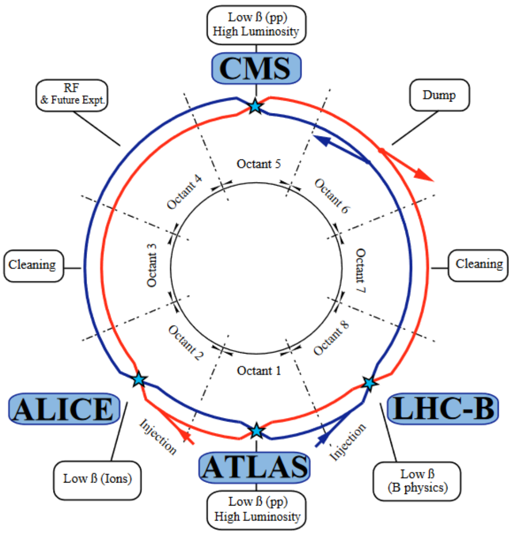

Figure 3.1: Location of the LHC pits and of the major experiments. © CERN.

The injection strategy is described in the following: protons are firstly accelerated into the LINAC

(LINear ACcelerator) to ~ 0.05 GeV, then the PSB (Proton Synchrotron Booster) increases their energy up to 1.4 GeV. The Proton Synchrotron (PS) accelerates protons up to 26 GeV, and finally, the Super Proton Synchrotron (SPS) provides further acceleration to 450 GeV. At this point the proton beams are injected in the LHC main ring. The beam is composed of bunches of approximately 1.2 to $1.4 \times 10^{11}$ protons, and the total designed number of bunches is 2808. These bunches travel in ultra-high-vacuum at an energy of 6.8 TeV. In order to focus the beam, 392 magnetic quadrupoles are distributed along the ring, while the particles' trajectory is kept stable by 1232 14-meters-long superconductive dipoles with NbTi windings that produce a 8.4 T magnetic field. The magnetic system is immersed into a bath of superfluid Helium and cooled to an operating temperature of 1.9 to 4.5 K.

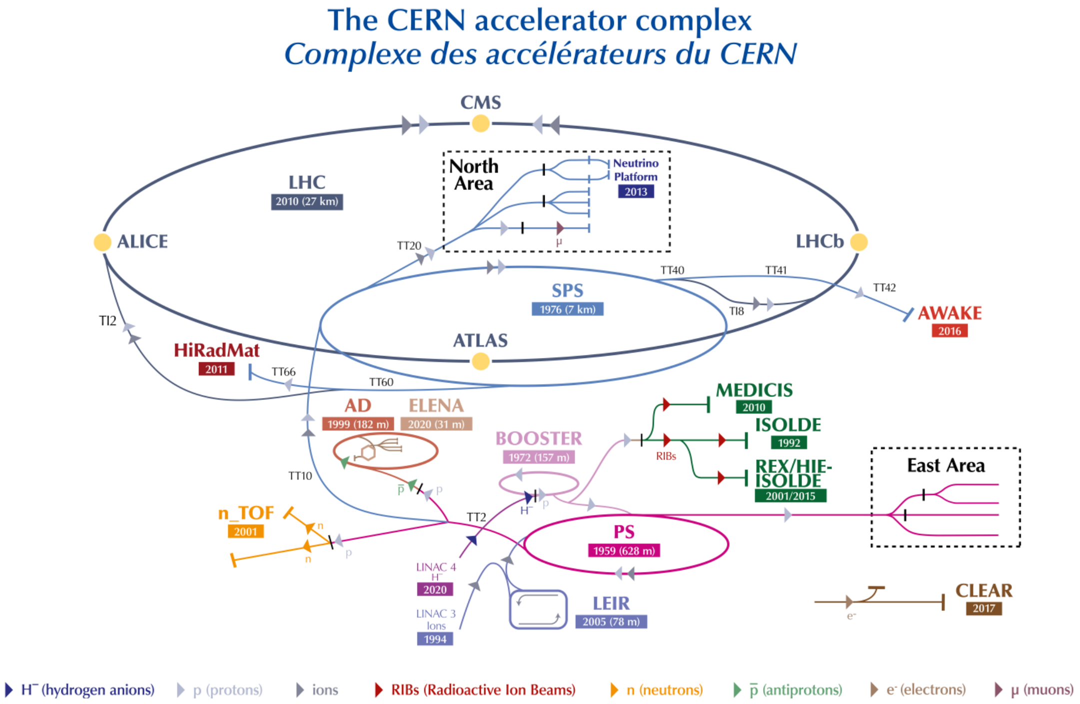

Figure 3.2: The CERN injection complex together with the ensemble of active experiments. © CERN.

Below the main features and purposes of the four main experiments at the LHC are reported:

- **ALICE** (A Large Ion Collider Experiment) is a detector focused on heavy ion collisions. It studies strongly interacting particles at extreme energy densities; the result of the collision between high energy lead ions provides a specific state of matter called *quark-gluon plasma*, in which the quark confinement is temporarily violated. These extreme conditions recreate the ones present just after the Big Bang, allowing the test of many key features of QCD like confinement or the chiral-symmetry restoration problem.

- **ATLAS** (A Toroidal Lhc ApparatuS) is a general multi-purpose detector optimised to study high-energy $pp$ collisions in order to test the SM as well as eventually explore BSM physics. An accurate description of the detector is provided in Section 3.2.
- **CMS** (Compact Muon Solenoid) is the other multi-purpose detector at CERN. It is smaller than ATLAS, and consists of a cylinder 15 m wide and 21 m long (against the 25x44 m of ATLAS) positioned at the diametrically opposite spot with respect to ATLAS. The two detectors are based on different technologies and materials, but investigate the same phenomena.
- **LHCb** (Large Hadron Collider beauty) focuses on investigating the differences between the matter and antimatter distribution in the universe. The detector is designed to study the forward propagating collision debris rather than the transversely travelling ones; a sophisticated tracking system, together with a particle identification (PID) system, allows the investigation of the decay products of the quarks produced in the LHC.

Collisions at the LHC occur every 25 ns, which corresponds to a rate of 40 MHz; the centre-of-mass energy of these collisions is designed to be 14 TeV at the present state of the accelerator[1]; the quantity that measures the ability of a particle accelerator to produce the required number of interactions is called the luminosity:

$$\mathcal{L} = \frac{dN}{dt} \cdot \frac{1}{\sigma},$$

where $\sigma$ is the cross section for the considered process and $\frac{dN}{dt}$ represents the number of events per second. For gaussian shaped beams colliding head on the luminosity assumes the expression [148]:

$$\mathcal{L} = \frac{N_1 N_2 f_r N_b}{4\pi \Sigma_x \Sigma_y} \tag{3.1}$$

where $N_1$ and $N_2$ are the numbers of particles per bunch, $N_b$ is the number of bunches, $f_r$ is the rate of collisions and $\Sigma_x$ and $\Sigma_y$ are respectively the horizontal and vertical profiles of the LHC beams. To express the amount of collected data, the *integrated luminosity* $L = \int \mathcal{L} dt$ is introduced and measured in $\text{b}^{-1}$, where b stands for *barn*, such that 1 b=100 $\text{fm}^2 = 10^{-24}$ $\text{cm}^2$. The cumulative luminosity delivered to the ATLAS detector during stable beams of $pp$ collisions over time is shown in Figure 3.3.

On September 10th, 2008, the first single beams were measured at the LHC. After a few successes, LHC operation was suspended due to a major breakdown occurred to the superconducting magnets composing the accelerator, their mountings, and the vacuum pipe. After more than a year of technical work, the LHC resumed its program on November 20th, 2009. A few days later, an energy of 1.18 TeV per beam was successfully reached, making the LHC the most powerful accelerator to date.

---

[1] The maximum energy reached up to now is 13.6 TeV, achieved during Run 3.

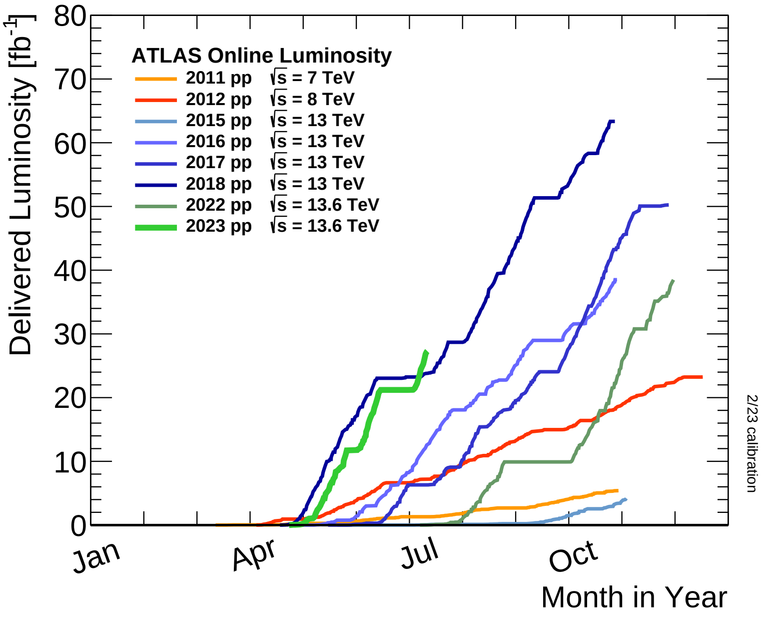

Figure 3.3: Cumulative luminosity versus day delivered to ATLAS during stable beams and for high energy $pp$ collisions. Figure taken from [149].

During 2011, the LHC ran its operations at a center-of-mass energy of 7 TeV; during this period, both the ATLAS and CMS detectors captured about 5 fb$^{-1}$ of data. The LHC recommenced activities on April 5th, 2012, producing its first collision with stable beams at a center-of-mass energy of 8 TeV. This operation continued until the end of 2012, culminating in the first run (Run 1) of the LHC program before the planned extended shutdown (LS1) began. Both the CMS and ATLAS detectors managed to record approximately 20 fb$^{-1}$ of proton-proton collision data at a center-of-mass energy of 8 TeV, enough to allow the discovery of the Higgs boson.

The LHC resumed stable beam conditions on June 3rd, 2015, marking the onset of the second run (Run 2) of data collection. This time, an unprecedented energy of 6.5 TeV per beam was achieved, leading to a center-of-mass energy of 13 TeV. Proton-proton collisions at a center-of-mass energy of 13 TeV were gathered over the years 2016, 2017, and 2018, resulting in an aggregate total integrated luminosity of around 140 fb$^{-1}$.

On April 22nd, 2022, after the second long shutdown period (LS2), the LHC became operational again with a new maximum beam energy of 6.8 TeV, and it officially commenced its Run 3 physics season on July 5th, 2022. The data taking is expected to last until the end of 2025, corresponding to a delivered integrated luminosity of 250 fb$^{-1}$.

Finally, the LHC complex is programmed to undergo a significant upgrade, entering the *high luminosity* (HL) stage; the HL-LHC is expected to deliver a levelled instantaneous luminosity of $\mathcal{L} \sim 5 \times 10^{34}\text{cm}^{-2}\text{s}^{-1}$ and an annual integrated luminosity of approximately 250 fb$^{-1}$ to reach a total dataset of 3000 $\text{fb}^{-1}$.

## 3.2 The ATLAS Detector

The ATLAS experiment represents one of the largest science collaborations, involving several thousand physicists, engineers, technicians and students. It has provided and still provides some of the most crucial contributions to the understanding of the actual physics phenomenology, as well as the chance to test the predictions of theoretical models such as the SM.

The ATLAS detector is cylindrical and covers nearly the entire solid angle around the collision point[2]. The dimensions of the detector are 25 m in height and 44 m in length, with an overall weight of approximately 7000 t. It is located into the LHC "Pit 1", 100 m underground. Figure 3.4 depicts the structure of the ATLAS detector.

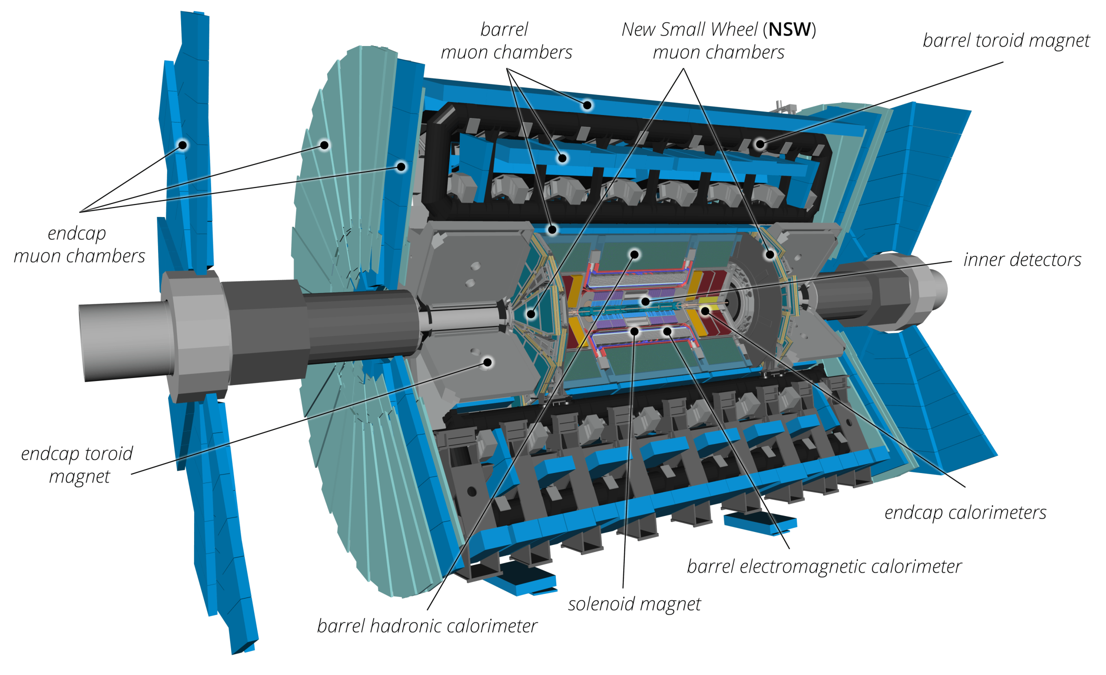

Figure 3.4: Cut-away view of the ATLAS detector with its main subcomponents. Figure taken from [150]

ATLAS, along with all other LHC detectors, needs to satisfy a set of general requirements dictated by the nature of the investigated collisions:

- Fast radiation-hard electronics and sensors which also grant high detector granularity in order to minimize overlapping events.

---

[2] The coordinate system adopted by ATLAS is described in Section 3.2.1.

- Optimal angular acceptance: largest possible azimuthal angle and pseudorapidity coverage.
- Precise charged-particle momentum resolution and track-reconstruction efficiency.
- Very good electron and photon identification and measurements; full coverage hadronic calorimetry for jets and missing energy measurements.
- Good muon identification and momentum resolution.
- Highly efficient trigger system for low transverse-momentum objects. Good background rejection.

The caveats listed above are nicely satisfied by the ATLAS detecting subsystems.The physical subsystems of the detector are the *Inner Detector*, responsible for tracking of particles and vertex identification, the *Calorimeters*, which are crucial for energy measurements of photons, electrons, hadrons and jets, and the *Muon systems*, needed to precisely reconstruct muon momenta. The individual sub-detectors are further described in the following sections. A magnet system is combined to the detector components, and consists of two different devices: a thin 2 T superconducting solenoid surrounding the Inner Detector cavity and three large superconducting toroids disposed with an eight-fold azimuthal symmetry around the calorimeters. These components are integrated with the Trigger and Data Acquisition System and the Computing facility.

The LHC was designed to deliver a luminosity of $\sim 10^{34}$ cm$^{-2}$ s$^{-1}$, at a centre-of-mass energy of $\sqrt{s} = 14$ TeV with about 25 interactions per bunch crossing. The ATLAS detector, as described in [4], was configured to comply with the requirements. However, the LHC operating conditions differed from expectations; in particular, the instantaneous luminosity surpassed the design one, reaching a maximum value of $\mathcal{L} \sim 2.1 \times 10^{34}$cm$^{-2}$s$^{-1}$ during Run 2. There were on average 33.7 interactions per bunch crossing[3] during Run 2, with a peak value of over 60 interactions per bunch crossing recorded in 2017 and 2018. Despite the harsher conditions, the ATLAS detector performed well; performance and analysis methods were adapted to optimise the experiment's physics reach in Run 2. Subsequently, the detector underwent a major upgrade, called "Phase-I Upgrade", with the aim of improving the subsystems and their electronics in order to withstand the Run 3 conditions of $<\mu>\sim 50$ (and at maximum 60) interactions per bunch crossing, and maintain the lowest achievable trigger thresholds, enabling the continued broad physics program planned for Run 3 [150].

Almost all components of the ATLAS detector were upgraded over time; a detailed description of the state of the art at the beginning of Run 3 can be found in Ref. [150]. In this thesis, only the introduction of new detector elements or major upgrades to the structure of an existing sub-detector will be reported.

---

[3] The number of interactions per bunch crossing, or "pile-up", refers to the situation in which two colliding bunches give rise to multiple interaction vertices. The average number of vertexes represents a fundamental feature of the colliding beams and it is noted with the symbol $\mu$.

### 3.2.1 Coordinate system

To rigorously describe the detector components and the particles emerging from collisions, it is necessary to introduce an appropriate coordinate system and nomenclature. The ATLAS experiment uses a right-handed coordinate system with its origin at the nominal interaction point (IP) in the centre of the detector and the $z$-axis along the beam pipe. The $x$-axis points from the IP to the centre of the LHC ring, and the $y$-axis points upwards. A spherical coordinate system is used with the azimuthal angle $\phi$ defined on the $x - y$ plane, and the polar angle $\theta$ measured from the $z$-axis. The rapidity, $y$:

$$y = \frac{1}{2} \ln \left( \frac{E + p_{\mathrm{L}}}{E - p_{\mathrm{L}}} \right) \tag{3.2}$$

where $p_{\mathrm{L}}$ represents the longitudinal momentum, is often used instead of $\theta$, as the rapidity difference $y_1 - y_2$ is invariant under Lorentz boosts alongside the beam axis. In case of massless particles, the pseudorapidity, $\eta$, is used:

$$\eta = -\ln \tan \frac{\theta}{2}. \tag{3.3}$$

Moreover, it is common to define the distance $\Delta R_{ij}$ between two particles $i, j$ in the pseudorapidity-azimuthal angle space:

$$\Delta R_{ij} = \sqrt{(\eta_i - \eta_j)^2 + (\phi_i - \phi_j)^2} \tag{3.4}$$

Other relevant variables are listed below:

- Transverse Momentum ($p_{\mathrm{T}}$): fraction of the particle momentum ($p$) on the plane orthogonal to the $z$ axis.
- Transverse Energy ($E_{\mathrm{T}}$): fraction of the particle energy ($E$) on the plane orthogonal to the $z$ axis.
- Missing Transverse Energy ($E_{\mathrm{T}}^{\mathrm{miss}}$): fraction of energy on the plane orthogonal to the $z$ axis, which cannot be traced back to a specific particle but is expected due to energy conservation in the transverse plane.

### 3.2.2 The Inner Detector

The ATLAS tracking system, typically referred to as the Inner Detector (ID), aims to achieve the momentum and vertex resolution requirements imposed by the benchmark physics processes. The ID consists of three fine-granularity different components: a Pixel Detector [151], a Semiconductor Tracker (SCT) [152] and a Transition Radiation Tracker (TRT) [153].

At inner radii, silicon pixel and microstrip layers ensure optimal pattern-recognition efficiency; the outer shell of the detector comprises TRT gaseous straw tubes elements interleaved with polymer fibres (barrel) and foils (endcaps) to create transition radiation. A cut-away view of the ID layout is given in Figure 3.5.

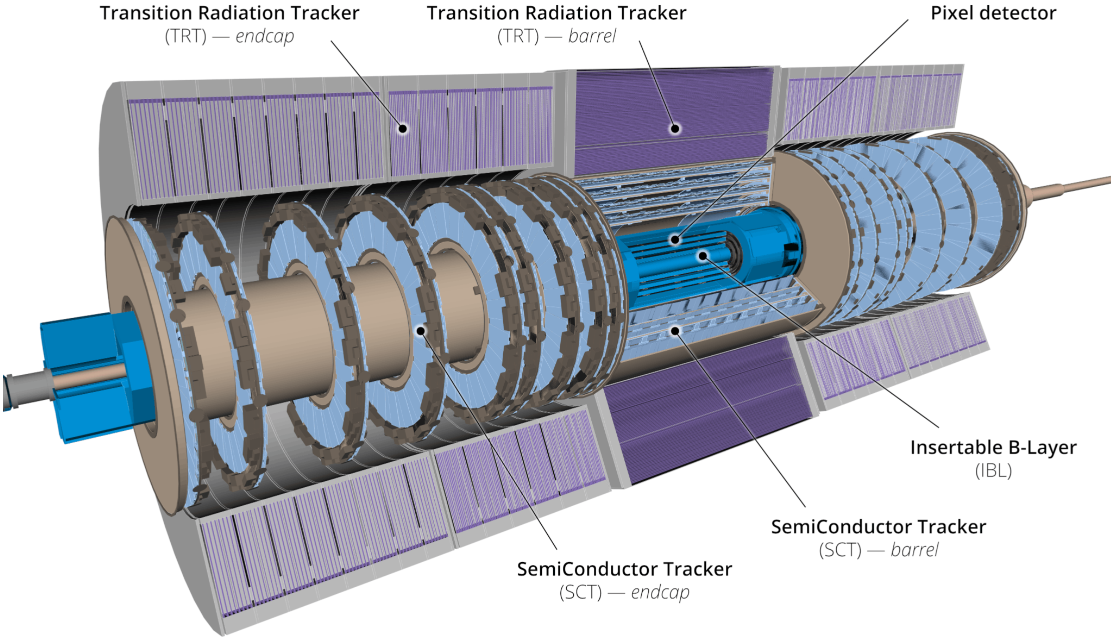

Figure 3.5: Cut-away view of the Inner Detector with its main subcomponents. Figure taken from [150]

The ID is designed to grant hermetic and robust space measurements for charged particles with $p_{\mathrm{T}}$ above a precise threshold[4] and within a pseudorapidity acceptance range $|\eta| < 2.5$. Two of the major issues concerning the fabrication of the ID components are the high-radiation environment due to collisions and the temperature regime at which the sensors are required to operate. There is, therefore, a mandatory trade-off between low-cost radiation-tolerant materials and optimal detector performance, along with repeated low-temperature (from -20°C to 20°C) tests. Figure 3.6 presents a detailed depiction of the Inner Detector components.

## Pixel Detector

The pixel detector consists of 1744 silicon pixel modules concentrically arranged in three barrel layers. Two end-caps, each with three disks, are combined with the barrel to optimise the geometrical acceptance. Each module contains 47232 pixels, covering an area of 16.4 mm×60.8 mm; it is read out by 16 hard-radiation front end chips which are bump-bonded to the sensor, providing 46080 readout channels per single module, ~80 millions in total [150].

Between 2012 and 2014 a new type of device, called Insertable B-Layer (IBL) [154–156], was commissioned and installed between the existing Pixel detector and the beam-pipe. It is composed of 14 carbon fiber staves, each one tilted by 14° and measuring 2 cm×64 cm. The IBL barrel is

---

[4] Specifically 0.5 GeV, even if it is possible to measure transverse momenta down to 0.1 GeV in *ad hoc* studies.

designed to surround the collision point covering a $|\eta| < 3$ interval[5], at an average distance of $\sim$33 mm with respect to the beam pipe. Each carbon stave is equipped with a cooling system and 32 silicon sensors bump-bonded with front-end chips, for a total of $\sim$12 millions of pixel cells.

The detection principle is based on the production of an electron-hole pair in the charge-depleted region of the silicon sensor when a charged particle hits it. Since several pixels can be activated by a single track, normally the result of the detection is a cluster whose center represents the hit position of the particle. During Run 2, the IBL achieved a spatial resolution of $\lesssim 10\,\mu$m [157]. The Pixel detector and the IBL cover a radial distance ($r$) of $r < 122.5$ mm.

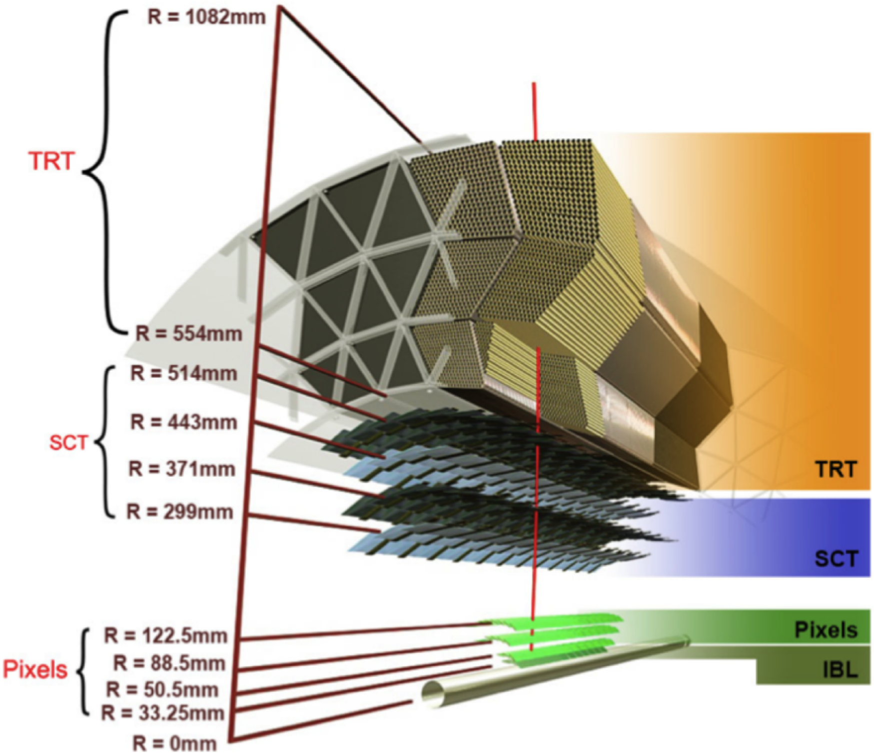

Figure 3.6: Structure of the ID barrel system, showing the beam pipe, the IBL, Pixel, SCT and TRT with their relative sub-apparatus. Figure taken from [150]

## SemiConductor Tracker

The sensitive elements of this detector cover radial distances of $299 < r < 514$ mm. The 4088 modules of silicon strips sensors are organised in four barrel layers, with two end-caps of nine disks each. The strips in the barrels, approximately parallel to the beam axis, are formed by attaching two pairs of daisy-chained sensors back-to-back at a stereo angle of 40 mrad. This operation

---

[5] During Run 2, the IBL has been kept operational in the tracking coverage region of $|\eta| < 2.5$.

results in 768 strips of 12 cm in length. Typically, the detection provides eight strip measurements (four space-points) for particles originating from the beam-interaction region [158].

While the detection is based on the same principle as of the Pixel module, the SCT further extends the tracking volume to radial distances, playing an important role in measuring the transverse momenta of charged particles.

#### Transition Radiation Tracker

The fundamental elements of the TRT detector are 4 mm diameter gas-filled Polyimide drift (straw) tubes. Like the other ID components, the TRT consists of a barrel and two end-caps. The barrel part houses 52544 straws, while each end-cap contains 122880 radially aligned straws, each 370 mm in length and oriented towards the beam axis. In total, the system consists of about 300000 straws, read out by  350000 channels of electronics [159]. The TRT's volume occupancy and pseudorapidity acceptance are designed to ensure that particles traverse at least 30 straws, thus providing additional information based on the photon emission of particles in materials with varying refractive indices. The transition radiation may be emitted by highly relativistic charged particles as they traverse a material boundary. The soft X-rays produced can be absorbed by the atoms in the gas mixture, leading to significantly higher readout signals. The TRT achieves 130 µm resolution for charged particle tracks with $|\eta| < 2$ and $p_{\mathrm{T}} > 0.5$ GeV. This detector spans an area within the range $563 < r < 1066$ mm.

#### Performance of the ID detector in Run 3

During Run 2, the Pixel detector accumulated a significant amount of radiation damage at the location of IBL, which required a careful tuning of the detector operating parameters in order to minimise its impact on the performance in the reconstruction of charged particle tracks. Figure 3.7(a) shows the IBL performance in terms of fraction of track between Run 2 and Run 3. Moreover, in Run 2 the LHC delivered high instantaneous luminosity and pileup conditions that were far in excess of the original SCT design goals. Radiation damage in SCT will continue to evolve in Run 3, but with a trend that is well modelled, as presented in Figure 3.7(b). The average hit occupancy of the TRT straws will be significantly higher in Run 3 than in previous runs. The track occupancy in the TRT, defined as the hit occupancy in straws in the path of a track of interest, is expected to be 50% higher than in Run 2. Thanks to the improvements to the TRT reconstruction software, a good performance is expected [150].

### 3.2.3 Calorimeters

The ATLAS calorimeter system is made up of a series of devices with complete $\phi$ symmetry around the beam axis and the ID, covering a total pseudorapidity of $|\eta| < 4.9$. The function of this apparatus is to measure the energy deposited by particles passing through it. It also acts as a shielding agent for the outer components of ATLAS (e.g. limiting punch-through[6] into the muon

---

[6] If some of the hadron shower remnants reach the muon system, they may be misreconstructed as muons, causing the "punch-through" effect.

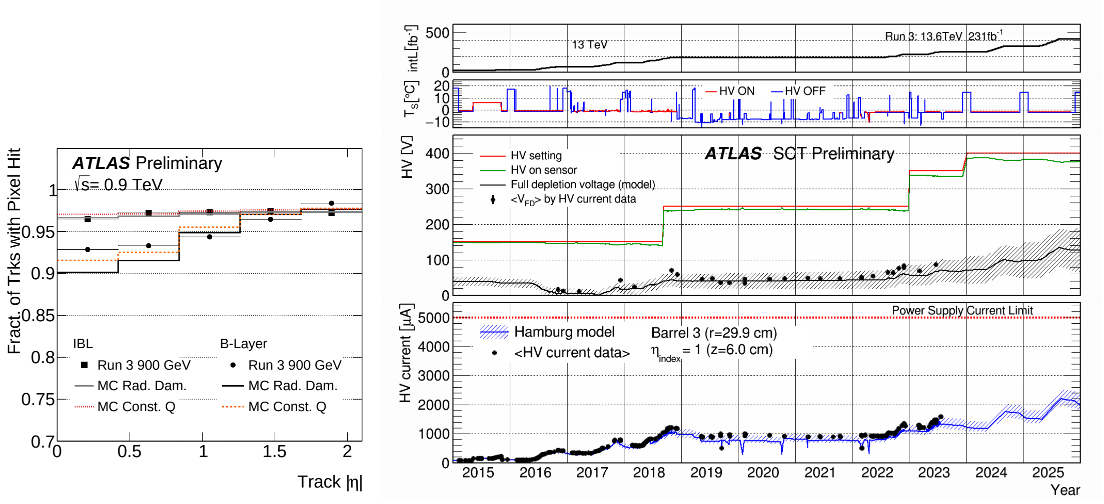

(a) (b)

Figure 3.7: (a) the average fraction of tracks with an associated hit in the IBL and B-Layer as a function of the track pseudorapidity, $\eta$, comparing the Run 3 900 GeV data to MC (IBL) and the Run 2 data (B-Layer). The fraction is computed for fraction of selected tracks with $p_\mathrm{T} > 1.0$ GeV, $|\eta| < 2.1$ and pixel hits in the two neighbouring layers having an associated hit in the layer under study. (b) the projection for the module high voltage (HV) for the central Barrel 3 modules from 2015 to the end of 2025. (top) Integrated luminosity. (2nd) time profile of the sensor temperature. The red line indicates the expected temperature rise due to bulk-heating by leakage current. (3rd) the HV setting (red), actual HV values on the sensor (green) and the full depletion voltage (black) estimated by the Hamburg model. he black points show measurements obtained from I-V scans. (bottom) Evolution of leakage current using the Hamburg model (blue line) compared to data (black points). Hashed areas indicate model uncertainties which do not include (unknown) errors of the luminosity to fluence conversion factors. Figures taken from [160, 161].

system).

The Calorimetry apparatus shown in Figure 3.8 consists of two sampling technologies: Liquid Argon (LAr) [162] for the electromagnetic calorimeters, together with all the endcap and forward calorimeters, and scintillating Tiles [163] for hadron calorimetry in the central region. The sampling principle involves the presence of two detector layers that alternate in regular intervals: the absorber, in which high-energy particles are converted into two or more particles with correspondingly less energy, and the emitter, thanks to which the emitted particles are detected as currents. The LAr calorimeter resolution is usually parameterized as

$$\frac{\sigma_E}{E} = \frac{a}{\sqrt{E}} \oplus \frac{b}{E} \oplus c, \tag{3.5}$$

where $a$ is the stochastic term, $b$ the noise term, $c$ the constant term, and the symbol $\oplus$ indicates the sum in quadrature. The energy scale and energy resolution of Monte Carlo simulation are calibrated by comparing $Z \to ee$ data and simulation. The resulting corrections are then verified with $Z \to ee\gamma$ and $Z \to \mu\mu\gamma$ data. The Run 2 calibration, as shown in Figure 3.9(a), results in an agreement with precision $\leq 0.5\%$ [164, 165].

The resolution of the Tile calorimeter is defined as

$$R^{\sigma^{\text{raw}}} = \frac{a'}{\sqrt{E}} \oplus b', \tag{3.6}$$

where $a'$ describes the fluctuations on the number of particle produced in the showers, and $b'$ describes the non-uniformity of the cell response. The comparison between the measured energy of particles and the predictions of the simulation program used in ATLAS to simulated jets produced in proton-proton collisions during Run 2 is shown in Figure 3.9(b).

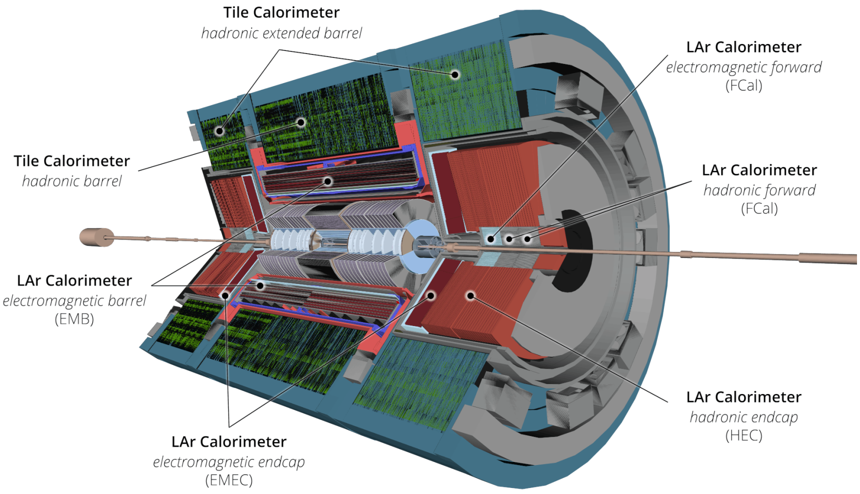

Figure 3.8: The layout of the ATLAS calorimeters. Figure taken from [150]

The system is designed to provide effective containment for electromagnetic and hadronic showers, thereby the total thickness of the EM components exceeds 22-24 radiation lengths $X_0$ [7], nominally $> 22\ X_0$ in the barrel and $> 24\ X_0$ in the end-caps. Then $\sim 9.7$ (10) interaction lengths[8] $\lambda$ are sufficient for the containment and resolution of high energy jets in the barrel (end-caps). Considering an additional support of 1.3 $\lambda$, the total thickness results in 11 $\lambda$, ensuring the additional feature of good $E_{\text{T}}^{\text{miss}}$ measurements.

## LAr Electromagnetic Calorimeter

LAr Electromagnetic Calorimeter (ECal) is composed of two main subsystems, the first of which is the Electromagnetic Barrel (EMB) calorimeter. It is formed by two half barrels, separated by a 4 mm gap in correspondence of the IP ($z = 0$). A vacuum vessel encases the barrels, composed

---

[7] The radiation length, $X_0$, is defined as a distance on which an electron reduces its energy by a factor $e^{-1}$ due to bremsstrahlung.

[8] The interaction length, $\lambda$, is the mean distance travelled by a hadronic particle before undergoing an inelastic nuclear interaction.

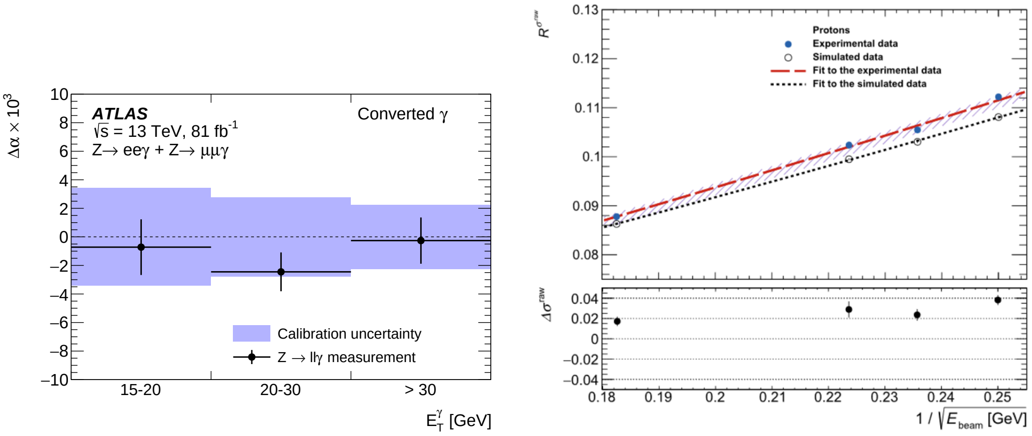

(a) (b)

Figure 3.9: (a) Residual photon energy scale factors for converted photons from $Z \rightarrow ee\gamma$ and $Z \rightarrow \mu\mu\gamma$ data as a function of the photon transverse energy after calibration with $Z \rightarrow ee$ data. (b) Energy resolution normalized to incident beam energy, $R^{\sigma^{\text{raw}}}$, measured (blue circles) and predicted by Monte Carlo simulation (black circles) as a function of $1/\sqrt{E}$ obtained in the case of proton beams. The experimental uncertainties include statistical and systematic effects combined in quadrature. Only statistical uncertainties affect simulated results. Figures taken from [164, 166].

of accordion-shaped kapton electrodes and lead absorber plates interlaid with liquid Argon. The LAr Electromagnetic End-Cap (EMEC) comprises two independent concentric wheels and possesses a relatively coarser lateral granularity compared to the rest of the acceptance. The outer wheel disposes of 768 plates of electrodes and spans a pseudorapidity range of $1.4 < |\eta| < 2.5$, while the inner one has 256 plates and a range of $2.5 < |\eta| < 3.2$; moreover, the amplitude of the accordion waves scales with the radius. A presampler detector is deployed in the region of $|\eta| < 3.2$ to account for the energy lost by electrons and photons upstream of the calorimeter. The presampler consists of an active LAr layer of thickness 11 mm (5 mm) in the barrel (end-cap) region.

### LAr Hadronic End-cap Calorimeter

The LAr Hadronic End-cap Calorimeter (HEC) consists of two independent wheels per end-cap with an outer radius of 203 cm, covering the pseudorapidity range of $1.5 < |\eta| < 3.2$, positioned back to back to the EM end-caps and sharing the same LAr cryostat. The first wheel is constructed using 25 mm copper plates, while the second one employs 50 mm plates as a cost-saving measure. The HEC wheels consists of 32 identical wedge-shaped modules, assembled with fixtures at the periphery and at the central bore. The total depth of the hadronic section amounts $10\lambda$.

### LAr Forward Calorimeter

In ATLAS, the LAr Forward Calorimeter (FCal) is incorporated into the end-cap cryostat, with its front face situated approximately 470 cm from the IP. Although this positioning presents challenges in managing radiation, it offers a distinct advantage in terms of uniform calorimetric coverage, including reduced radiation background levels in the muon spectrometer. The FCal is 9.5-10$\lambda$ long, and consists of three modules in each end-cap: the first, made of copper, is optimised for electromagnetic measurements, while the other two, made of tungsten, measure predominantly the energy from hadronic interactions. The front face of this detector is backed up 120 cm with respect to the EM calorimeter front face, calling for a high density calorimeter. A lower density would significantly increase the pile-up seen in the end-cap calorimeter, especially in the farthest wheel from the IP which is otherwise rather protected.

For Run 3, significant upgrades were made to the LAr systems on the trigger side [167], including the introduction of the LAr Trigger Digitizer Board (LTDB). This component is designed and constructed to transmit the higher-granularity trigger signals off the detector, where they are read out and processed by a completely new readout system. The new layout of the LAr readout system is shown in Figure 3.10.

### Hadronic Tile Calorimeter

The Tile calorimeter is made out of plastic scintillating tiles and a laminate of steel plates, and is placed directly outside the EM calorimeter envelope; it consists of a barrel ($|\eta| < 1.0$) and two additional extended barrels ($0.8 < |\eta| < 1.7$), divided azimuthally into 64 modules. A 60 cm gap, necessary for the Liquid Argon and ID electronics, cables, and services, separates the barrel and the extended barrels. To maximise the active material volume of the calorimeter, part of the gap houses a continuation of the extended barrel, referred to as the Intermediate Tile Calorimeter (ITC): this add-on critically enhances the sampling of electromagnetic showers, where the normal detection is compromised by the inert materials of the cooling system walls and the ID's electronics. The radial extent of the Tile apparatus, organised in three layers of varying thickness, ranges from an inner radius of 228 cm to 425 cm, resulting in 9.7$\lambda$ at the outer edge of the tile-instrumented region. The scintillator tiles and steel absorbers are read out with approximately 10000 photo-multiplier tubes (PMTs).

## 3.2.4 Muon spectrometer

The ATLAS Muon Spectrometer (MS) [168] is designed for excellent resolution at large transverse momentum. Its aim is to detect charged particles exiting the barrel and end-cap calorimeters and to measure their momentum. The detection of muons is achieved through the usage of different proportional chambers consisting of a series of wires or cathode strips surrounded by a gas-filled chamber. When a charged particle passes through the chamber, it ionises the gas along its path, causing positive ions to drift towards the cathode and electrons towards the anode. In the immediate vicinity of the anode, electrons are accelerated by the associated high potential fields,

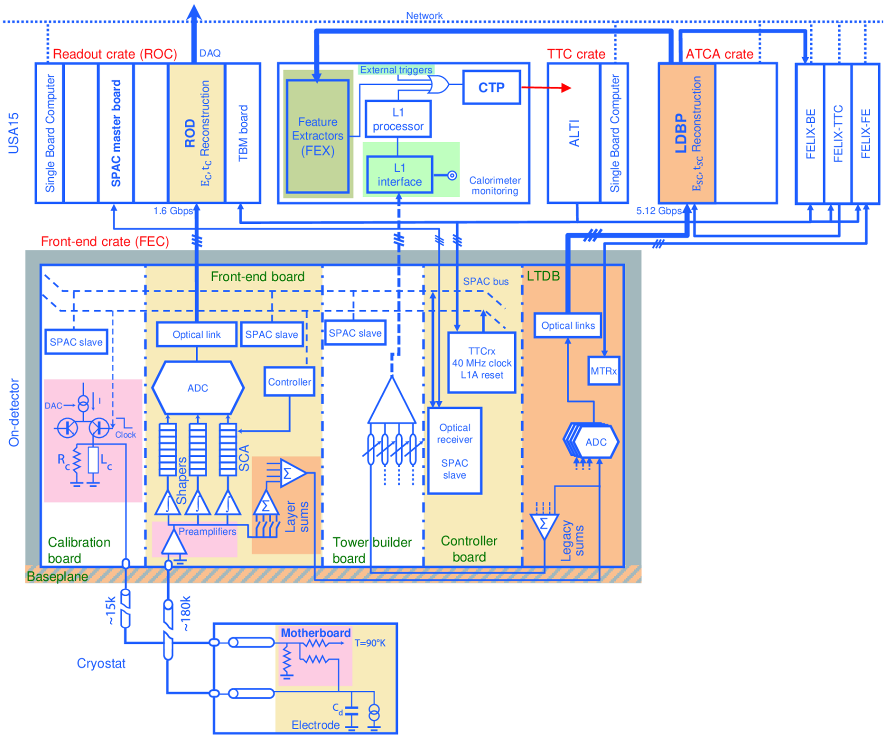

Figure 3.10: The schematic block diagram of the Run 3 LAr readout electronics architecture. In this representation, the LAr ionisation signal proceeds upwards, through the front-end crates mounted on the detector to the off-detector electronics. The elements added during LS2 are highlighted in orange. This diagram is valid for the electromagnetic calorimeters, where only the very minimal boards shown at the bottom of the diagram are located inside the cryostats; the HEC and FCal have additional electronics inside the endcap cryostats. Figure taken from [150].

causing further ionisation by collision with gas molecules. The resultant avalanche of electrons caused by this “gas multiplication” effect is discharged at the anode and measured by the counter electronics.

The detector is sensitive within the pseudorapidity region $|\eta| < 2.7$; within this acceptance, the granularity for 1 TeV tracks is better than 15%, resulting in a 75 µm resolution over a 500 µm trail. The detector performance is based on the magnetic bending of muon tracks in the superconducting air-core toroid magnets, instrumented with approximately 4000 tracking chambers plus a separate triggering system. The magnetic deflection in the $|\eta| < 1.4$ range is provided by the barrel toroid, while for $1.6 < |\eta| < 2.7$ the tracks are diverted by two magnets located at both ends of the barrel toroid. In the $1.4 < |\eta| < 1.6$ gap (transition region), the magnetic deflection is provided by a combination of barrel and end-cap fields; this configuration results in a field mostly orthogonal to the muon trajectories. Figure 3.11 reports a cut-away view of the apparatus indicating different muon spectrometer sub-detectors.

The detection in the barrel region is achieved by three layers of chambers around the $z$-axis, while in the transition and end-cap region the chambers are installed in planes perpendicular to the

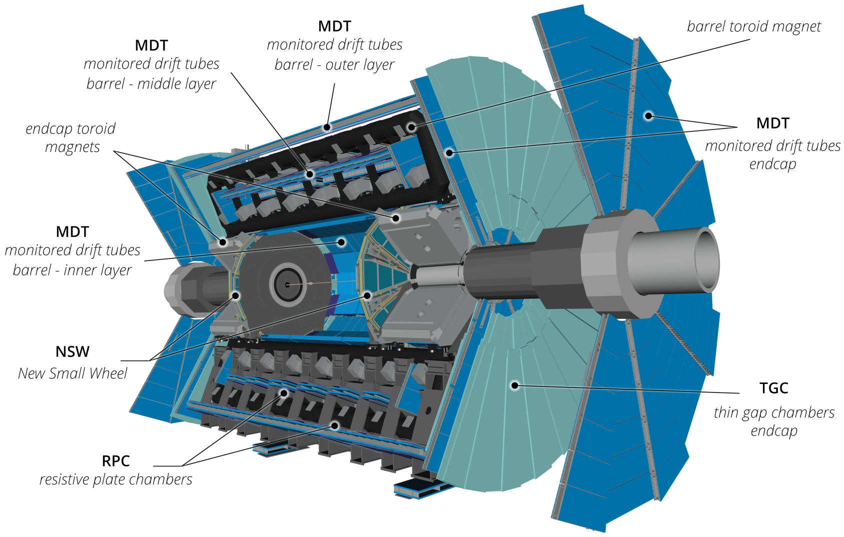

Figure 3.11: Cut-away view of the muon spectrometer system. Figure taken from [150]

beam, still in three layers.

### Muon Chambers

As described in Section 3.2.7, the Muon system features a so-called Level-1 trigger [169], as well as participating in the High Level Trigger. The purpose of the Level-1 trigger is to look for large transverse momentum muons by reconstructing tracks that point approximately to the IP, covering a pseudorapidity range $|\eta| < 2.4$. In order to achieve the selection requirements, two types of chambers are deployed:

- **Resistive Plate Chamber (RPC)**: Three layers of RPCs are housed in the barrel and operate in avalanche mode. The RPCs use two gas volumes and provide the low-$p_T$ threshold trigger in the first two layers; the third one contributes to the high-$p_T$ threshold trigger.
- **Thin Gap Chamber (TGC)**: TGCs are installed in the end-cap regions, and consist of multi-wire chambers operated in saturated mode. Three multi-layers of TGCs are present to accomplish Level-1 trigger, while additional chambers are used in the inner region to increase the tracking efficiency.

The trigger chambers for the muon spectrometer serve a threefold purpose: to provide bunch-crossing identification, to provide well-defined $p_T$ thresholds, and to measure the muon spatial coordinate. Once the triggering events have been located, their momentum and coordinate is measured by a set of two precision chambers:

- **Monitored Drift Tube (MDT) chamber**: the MDTs are multi-layer tubes chambers which provide in almost all the detector precision measurements of muon momentum. MDTs can sustain high rates while maintaining little sensitivity to space charge and a good spatial resolution (50 µm).

- **Cathode Strip Chamber (CSC)**: the CSCs are high granularity devices used in the end-cap region. These multi-wire proportional chambers with segmented cathode readout have a track resolution on the bending plane of 60 µm *per layer*. For Run 3, the CSC gas system was repurposed to supply the Micromegas (see next section) detectors with a new gas mixture.

#### The New Small Wheel

Over the last years, a set of upgrades focusing chiefly on the endcap regions were performed. In particular, each small wheel was replaced by a New Small Wheel (NSW). This detector operates in a high-background radiation region[9], using two chamber technologies: small-strip TGC (sTGC) detectors, and Micro-MEsh GAseous Structure (Micromegas) detectors.

Both the detectors can be used for triggering and provide precision tracking capabilities, with ultimate resolutions in the bending direction of the order of 100 µm. The resolution in the Micromegas detectors is due to the very fine strip pitch (less than 0.5 mm), whereas sTGCs (with a strip pitch of 3.2 mm) rely more on charge sharing. Thus, the coordinate resolution in the azimuthal direction is significantly improved and the sTGC-Micromegas chamber technology combination, provides a fully redundant detector system for tracking, both for the trigger and offline analysis. This detector configuration grants a robust, fast, high-resolution performance for the HL-LHC, as well as meeting the immediate requirements of Run 3. The results shown in this thesis do not include the contribution of the NSW for the data taking, since the detectors are still in a commissioning phase.

### 3.2.5 Magnetic System

The layout of the magnetic system [170] comprises three components producing a field in the range from 0.5 to 2 T.

- **The Central Solenoid** [171], which is aligned with the beam axis and provides an axial magnetic field for the inner detector, while minimising the radiative thickness in front of the barrel electromagnetic calorimeter.

- **The Barrel Toroid** [172], consists of eight super-conducting coils, assembled radially and symmetrically with respect to the beam axis. The overall size of the barrel toroid system as installed is 25.3 m in length, with inner and outer diameters of 9.4 m and 20.1 m, respectively.

---

[9] In this region, detected hit rates could potentially increase to as much as 20 kHz/cm$^2$ in the small region closest to the beamline, at the upper-limit estimate of HL-LHC luminosity of $\mathcal{L} \sim 7.5 \times 10^{34}\text{cm}^{-2}\text{s}^{-1}$.

- **The end-cap Toroid** [173], is formed by eight superconducting coils, closed in a cryogenic vessel that is 5 m wide and 11 m in diameter, located between the first and the second station of tracking chambers. Each coil contains two double type windings, lodged in a cryostat.

### 3.2.6 Forward detectors and luminosity measurements

The ATLAS Forward detectors [174] are a set of four detectors installed along the LHC beampipe, at different distances from the IP. These detectors exploit the information carried by particles that the rapidity coverage of the ATLAS central detector misses. One of the main purposes of the ATLAS forward systems is to achieve a precise measurement of the collected luminosity. To perform such a measurement [175], knowledge of the LHC $< \mu >$, the number of bunches $n_b$, the revolution frequency of the bunches $f_r$, and the production cross-section of inelastic interactions, $\sigma_{\text{inel.}}$, is necessary. Then the Luminosity estimate can be calculated as:

$$\mathcal{L} = n_b \frac{< \mu > f_r}{\sigma_{\text{inel.}}}. \tag{3.7}$$

To achieve the measurement of the online luminosity (and its uncertainty), ATLAS employs three subdetectors:

- **LUCID (LUminosity measurement using a Cherenkov Integrating Detector)**: it is designed for high-precision measurement of the luminosity delivered to the ATLAS experiment by the LHC, both in real time and, with final calibrations and a more refined analysis, for offline reconstruction and physics analyses. It was upgraded for Run 2, and the LUCID 2 [176, 177] detector is used also in Run 3. The detector is composed of two arms placed symmetrically at about ±17 m on either side of the ATLAS IP. The PMT detector is formed by four groups of four PMTs each, arranged symmetrically around the beampipe. The quartz entrance window of each PMT is used as a Cherenkov radiator.

- **Zero Degree Calorimeters (ZDC)**: ZDCs play a central role in the ATLAS heavy ion physics program; their purpose is to measure the energy of “spectator” neutrons which do not take part in any hadronic process during the collision of nuclei. The aim is to determine the impact parameters when the nuclei do not overlap completely. Located at 140 m from the nominal IP, the detector protects one of the LHC beamline dipoles. It is composed of four modules on each side; each module is composed of 1.1 nuclear interaction lengths of tungsten plates (11 plates, each of 1 cm thickness) interleaved with a row of 1.5 mm-diameter quartz rods. Light produced by Cherenkov radiation from shower products is transported up to the top of the detector, into a PMT.

- **ALFA (Absolute Luminosity For ATLAS)**: located at ±240 m from the IP, it is operated during special runs for elastic cross-section and diffraction studies at $\beta^*$ [10] values from 11 m to 2.5 km.

---

[10] The $\beta$ function describes the single-particle betatron motion around the central orbit, and in particular the variation of the transverse beam envelope along the beam trajectory [178]. $\beta^*$ is the value of the $\beta$ function at the IP, and

Additionally, *van der Meer* scans [179] are performed to estimate the horizontal(vertical) profiles $\Sigma_x(\Sigma_y)$ of the LHC beams. Therefore, eq. (3.7) can be brought back to eq. (3.1); with this method, it is possible to calculate the luminosity without the knowledge of the total inelastic cross-section.

The fourth forward detector is the **ATLAS Forward Proton (AFP)**: it consists of four detector stations, two on either side of the ATLAS IP at ±205 m (near stations) and ±217 m (far stations). It is used to identify events in which one or two protons emerge intact from the proton-proton collisions, allowing to study the soft and hard diffractive events at low luminosities.

### 3.2.7 Trigger and Data Acquisition System (TDAQ)

The LHC produces an average of 1 billion interactions per second, resulting in a data volume of 60 Terabytes per second. As only a small fraction of this data is relevant for physics studies, selective triggering is indispensable. Moreover, to avoid an excessive dead time, the trigger should be able to analyse event data at a rate of 40 MHz. To meet the analysis requirements ATLAS employs a two-level trigger:

- The **First Level trigger (L1)** [169] exploits the calorimetric information and, as previously mentioned, the dedicated muon triggers (RPCs, TGCs, and NSW). The system consists of of the Level-1 Calorimeter (L1Calo) and Level-1 Muon (L1Muon), alongside the Muon-to-Central Trigger Processor Interface (MUCTPI), the Level-1 Topological Processor (L1Topo) and the Level-1 Central Trigger Processor (CTP). Additionally, the inputs from other subsystems are considered; specifically, these subsystems are the Minimum Bias Trigger Scintillators (MBTS) [180], the LUCID-2 Cherenkov counter, and the AFP, ALFA and ZDC detectors. The readout of the detector allows a 100 kHz accept rate, with a maximum latency of 2.5 $\mu$s. The L1 trigger searches for high transverse-momentum muons, electrons, photons, jets, and $\tau$-leptons decaying into hadrons, as well as large missing and total transverse energy. The L1 trigger also defines one or more Regions of Interest (RoI), which are then passed to the HLT trigger.
- The **High Level Trigger (HLT)** [181] is software-based, and meant to further reduce the rate of data: the selection is seeded by the RoI information provided by the L1 trigger over a dedicated data path. The full-granularity information from the calorimeters and the muon and tracking systems is exploited to provide refined energy and momentum resolution for selections, as well as precision tracking for particle identification. The reconstruction sequence employs several selection applications, called processing units (PUs), designed to make decisions within a few hundred milliseconds. The trigger menus are designed to reduce the data flow to a few kHz, with a latency of the order of $10^2$ ms. The target rate

---

indicates how squeezed the beams are at the IP, by giving the distance along the beam direction after which the $\beta$ function (the transverse beam size) has been multiplied by a factor of 2 ($\sqrt{2}$) compared to its value at the IP. A large $\beta^*$ indicates wide and almost parallel beams, a small $\beta^*$ indicates narrow, but divergent beams. During Run 3, $\beta^*$ is typically around 30 cm for the ATLAS IP.

achieved in Run 2, about 1 kHz, whereas in Run 3, the performance of this trigger is set to approximately 3 kHz.

Figure 3.12 reports a flowchart of the TDAQ system. The trigger and data acquisition system are integrated into a complex network of control and data processing units, comprising the TDAQ architecture. The TDAQ was partially upgraded for Run 3, introducing a new set of data routers and commodity servers to further improve the flexibility of the infrastructure [182].

The output is then stored in the CERN Tier-0 computing centre of the worldwide ATLAS Grid [183, 184]. Tier 0 is the CERN Data Centre, which distributes the raw data and the reconstructed output to Tier 1s, and reprocesses data when the LHC is not running. Tier 1 consists of 13 computer centres around the world large enough to store LHC data. Finally, data is sent to Tier 2s, typically universities and other scientific institutes that can store sufficient data and provide adequate computing power for specific analysis tasks. Individuals can access the Grid through local (or Tier 3) computing resources, which can consist of local clusters in a university department.

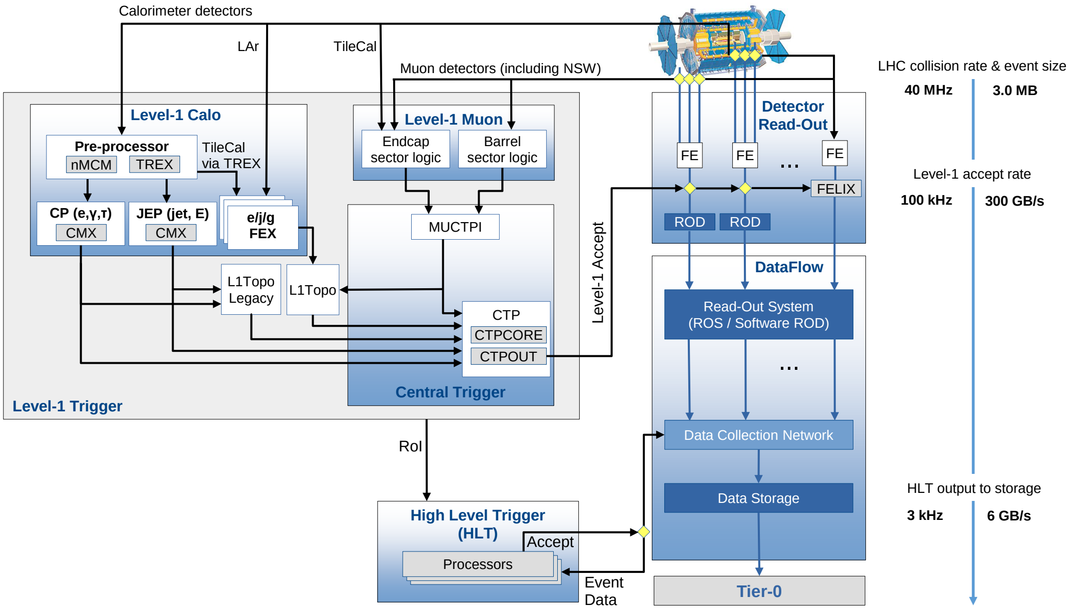

Figure 3.12: Schematic overview of the Trigger and DAQ system at the beginning of Run 3. Figure taken from [150].

# Chapter 4

# Physics objects definition

A surprisingly vast variety of particles is produced after a collision at the LHC; however, most of these collision products decay almost immediately and do not reach the detector. To the present knowledge, there are only 15 *long lived particles*[1], corresponding to a lifetime of $\tau c > 500\,\mu\mathrm{m}$ [17]. Of these, six are quite rare, being the charged and neutral $B$ and $D$ mesons, the $\Lambda_c$ baryon, and the $K^0_\mathrm{S}$.

The remaining 9 are: proton, neutrons, electrons, muons, neutrinos, photons, pions, kaons, and the $K^0_\mathrm{L}$. The ATLAS detector, described in Section 3.2, is designed to identify and directly measure the properties of protons, neutrons, pions, kaons, electrons, muons, photons, and jets [2]; additionally, the $E_\mathrm{T}^\mathrm{miss}$ information is exploited to extrapolate the properties of neutrinos or other BSM particles that are not expected to interact with the detector. Figure 4.1 depicts different particles and their identification inside the ATLAS detector. A candidate particle or jet that has been identified and reconstructed by the detector, is called *physics object*.

As further presented in Chapter 6, data is typically compared with the simulation of the physics processes involved in the measurement, produced via Monte Carlo generators. In the simulation, different steps are considered to produce physics objects; the stage involving hard processes or scattering, is referred to as *parton level* or *truth level*. Despite the implication of the name, the particles produced include not only partons but also leptons and photons. Next, coloured objects can emit more particles through QCD and QED radiation, hadronising to form bound objects. This configuration is called the *particle level*. Finally, when these particles traverse the detector, they interact with its material, leaving behind specific signatures. This is called the *detector level* or *reconstruction level*. The detector level is the only stage that can actually be observed in an experiment; both parton and particle level objects are available only through

---

[1] No distinction between particles and antiparticles will be made from this point on, unless otherwise stated.

[2] Hadronically decaying $\tau$-leptons are sometimes included in the physics objects detectable by ATLAS. However, since they decay before being detected, these particles are normally reconstructed by relying on the configuration of the jets produced by the decay.

simulation. The software utilised by the ATLAS collaboration, which performs this whole simulation infrastructure, is called *Athena* [185, 186].

This chapter presents the methods and recommendations[3] adopted by ATLAS in the Run 3 to characterise the physics objects mentioned above, highlighting the specific requirements implemented in the analysis presented in this thesis. In the early stages of data taking, most of the calibrations were not available with Run 3 data; therefore, Run 2 data recommendations were used. Because of this, and as further described in Section 5.1, the results presented in this thesis were subjected to several updates over time. For each subject discussed in this chapter, a concise historical overview of modifications and updates is provided, where applicable. This is done to maintain a record of the conditions of analysis throughout the early data collection period of Run 3.

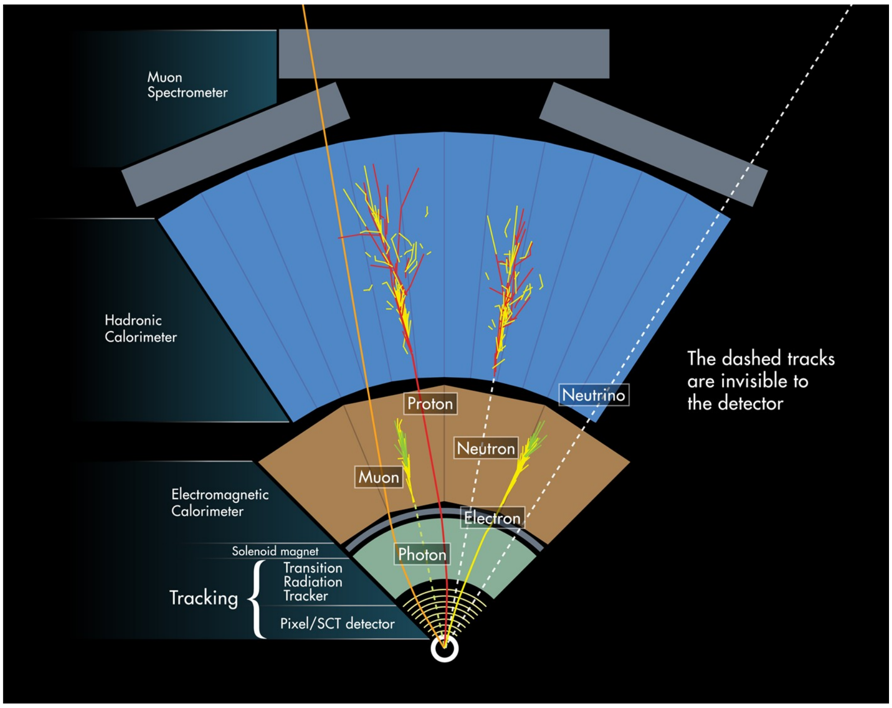

Figure 4.1: A demonstration of particle reconstruction within the ATLAS detector. © CERN.

## 4.1 Electrons

Electrons passing through the ATLAS detector leave a track in the ID and then deposit almost all their energy in the ECal [187, 188]. Therefore, the reconstruction of an electron candidate is

---

[3] The term "recommendations" refers to the set of best practices provided by dedicated working groups to the whole collaboration, regarding the reconstruction and calibration of physics objects.

based on localised clusters of energy deposits found within the ECal, typically $E_{\mathrm{T}} > 2.5$ GeV, that is successively matched in the $\eta \times \phi$ space to charged-particle tracks identified in the ID with $p_{\mathrm{T}} > 0.5$ GeV. The tracks associated to an electron candidate need to be compatible with the primary vertex of the hard scattering and satisfy the requirements on the impact parameters: $d_0/\sigma_{d_0} < 5$ and $|z_0 \sin\theta| < 0.5$ mm[4], where $\sigma_{d_0}$ is the $d_0$ uncertainty. Figure 4.2 illustrates the identification and reconstruction of an electron candidate. Because of the structural limitations of the ID, only electron candidates satisfying $|\eta| < 2.47$ are considered. Additionally, the "crack" region between the barrel and the end-cap detector $1.37 < |\eta| < 1.52$, is excluded as well. In this thesis, electron candidates are required to have $p_{\mathrm{T}} > 27$ GeV. To correct for the discrepancies, *scale factors* (SFs) are derived and applied to the simulated events; the SFs are expressed as ratios of efficiencies in data vs MC, as illustrated in the following sections. For reconstruction, SFs are set to 1 with a conservative uncertainty. Additionally, electron trigger SFs are derived from Run 3 data. Finally, the electron momentum scale and resolution is measured in $Z \to ee$ events and is checked in $J/\psi \to ee$ and in events with a radiative $Z$ decay [189].

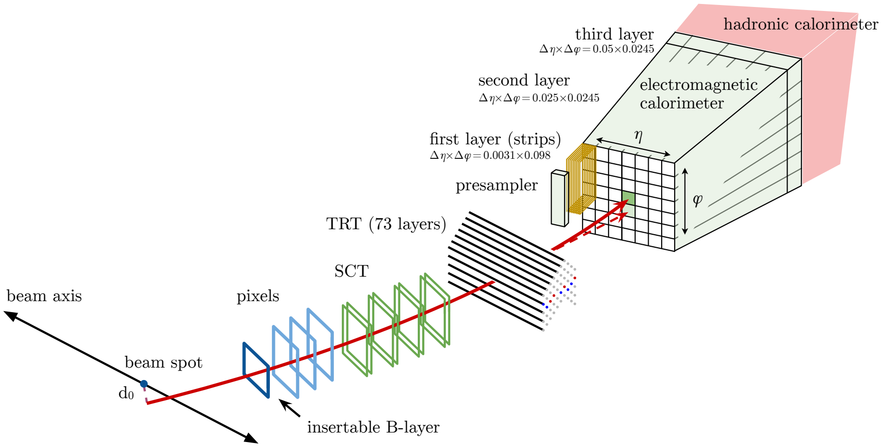

Figure 4.2: Schematic illustration of the path of an electron through the detector. The solid red trajectory shows the path of an electron, while the dashed red trajectory indicates the path of a photon produced by the interaction of the electron with the material of the tracking system. Figure taken from [188].

### 4.1.1 Electron identification

Leptons emerging from the hard scattering process of a collision are typically referred to as "prompt", or "real" leptons. The definition of prompt lepton can be of three different kinds: Born, bare and dressed. Born leptons are defined as "leptons prior to QED final-state radiation (FSR)", whereas bare leptons correspond to "leptons after QED FSR". On the other hand, for dressed leptons, a cone or a jet algorithm can be used to cluster all photons around the direction of the

---

[4] $d_0$ is the distance of closest approach of the track to the primary vertex point, in the $r$—$\phi$ projection and $|z_0|$ is the $z$-coordinate of the track at the point of closest approach to the global $z$-axis.

bare lepton, forming a lepton after partial QED radiation recovery. In this procedure, all photons not from hadrons decays are used [190].

Not all the reconstructed electron candidates are "prompt", or "real" electrons. Semileptonic decays of $b$- and $c$-quarks, photon conversions and jets with large electromagnetic energy can give rise to "non-prompt and fake" electrons. To reject this kind of backgrounds, ATLAS employs a likelihood-based algorithm (LH) [188]. This is a multivariate technique that evaluates several input variables simultaneously. For each electron candidate, likelihoods for the signal ($\mathcal{L}_\mathrm{S}$) and background ($\mathcal{L}_\mathrm{B}$) are combined into a single discriminant, $d_\mathcal{L}$:

$$d_\mathcal{L} = \frac{\mathcal{L}_\mathrm{S}}{\mathcal{L}_\mathrm{S} + \mathcal{L}_\mathrm{B}} \qquad \text{with } \mathcal{L}_{\mathrm{S(B)}}(\vec{x}) = \prod_{i=1}^{n} P_{\mathrm{S(B)},i}(x_i) \tag{4.1}$$

where $\vec{x}$ is the vector of the discrimination variables, and $P_{\mathrm{S(B)},i}(x_i)$ represents the value of the signal probability density function of the $i$-th variable evaluated at $x_i$.

To cover the various required prompt-electron signal efficiencies and corresponding background rejection factors, three fixed values of the LH discriminant are used to define the *Loose*, *Medium* and *Tight* operating points. The *Tight* working point (WP) is used for the results shown in this thesis. This choice is driven by the ability to achieve increased purity through stricter requirements, since the analysis is not constrained by statistics. The same reasoning can be applied to the isolation WP choice in the next section.

Identification SFs for electrons have been measured with the *tag-and-probe method*[5], similarly to Refs. [164, 188], using the *Z-mass normalisation method* only, using Run 2 data reprocessed with the Run 3 software release. Figure 4.3 shows identification efficiencies as a function of the electron $p_\mathrm{T}$ and pseudorapidity $\eta$, considering $Z \to ee$ events with the tag-and-probe method.

The identification efficiency estimation is expected to further improve with the usage of Run 3 data, alongside the combination between $J/\Psi \to ee$ *measurement*, the $Z$-*isolation* and the $Z$-mass normalisation methods [191].

### 4.1.2 Electron isolation

Electron candidates are further subjected to an isolation requirement, designed to separate prompt electrons from other background processes. The typical signature of prompt electrons is represented by little activity, both in the calorimeter and in the ID, in an area of $\eta \times \phi$ surrounding the candidate object. Therefore, the isolation variables used for reconstructed electrons are:

- **Track-based isolation variable**, $p_\mathrm{T}^\mathrm{varcone30}$: it is computed by summing the transverse momentum $p_\mathrm{T}$ of selected tracks, within a cone centred around the electron track direction, excluding the electron track itself: $\Delta R = \min(0.3, 10)\ \mathrm{GeV}/p_\mathrm{T}$.

---

[5] In the tag-and-probe method, one object is required to have a strict selection criterion and is used to identify given events - *tag*. The other object is selected with a looser criterion and is used to study the efficiency of that selection method - *probe*.

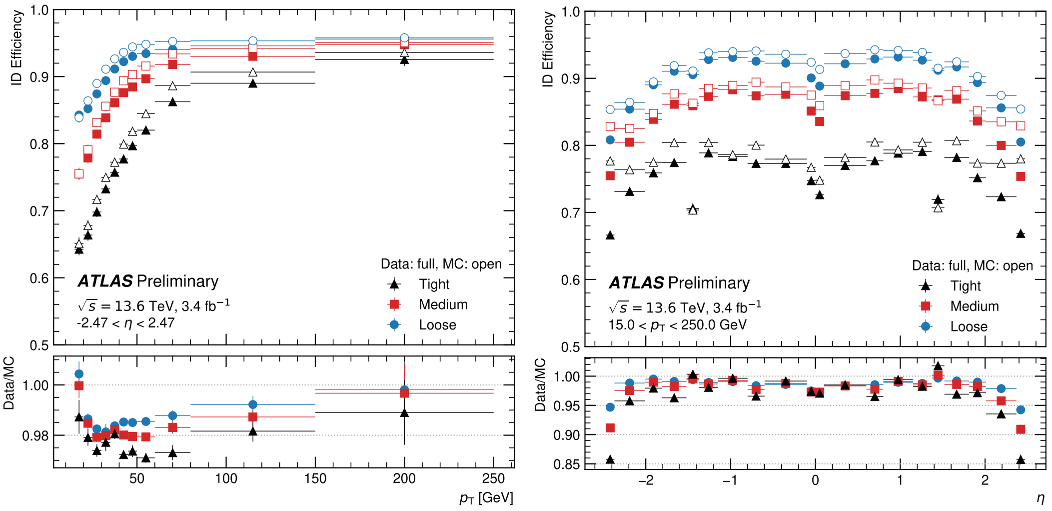

(a) (b)

Figure 4.3: Electron identification efficiencies in $Z \to ee$ events as a function of $p_{\mathrm{T}}$ integrated over the full pseudo-rapidity range (a), and as a function of pseudo-rapidity $\eta$ for electrons with transverse momentum $15 < p_{\mathrm{T}} < 250$ GeV (b). The efficiencies are shown in data and MC for three WPs based on a likelihood approach: Loose (blue points), Medium (red points) and Tight (black points). The data used was recorded in 2022 from $pp$ collisions at $\sqrt{s} = 13.6$ TeV, corresponding to an integrated luminosity of 3.4 fb$^{-1}$. For both plots, the bottom panel shows the data-to-simulation ratios. The total statistical and systematic uncertainty are included in the error bars. Figure taken from [192].

- **Calorimeter-based isolation variable**, $E_T^{\text{cone20}}$: it is built by summing the transverse energy of topological clusters in a cone of size $\Delta R = 0.2$ around the electron, after subtracting the contribution from the energy deposit of the electron itself.

The isolation criteria are defined calculating the ratio of the track- or calorimeter-based variables to the transverse momentum of the electron ( $p_{\mathrm{T,TTVA}}^{\text{varcone30}}/p_{\mathrm{T}}$, $E_T^{\text{topocone20}}/p_{\mathrm{T}}$), where the subscript “TTVA” stands for *track-to-vertex association* and indicates that the track was used in the vertex fit, or satisfies $|\Delta z_0 \sin\theta| < 3$ mm.

Five different WPs are extrapolated: *HighPtCaloOnly, Loose_VarRad, Tight_VarRad, TightTrackOnly_VarRad*, and *TightTrackOnly_FixedRad*.

In this thesis, the *Tight_VarRad* WP, corresponding to $E_T^{\text{cone20}}/p_{\mathrm{T}} < 0.15$ and $p_{\mathrm{T,TTVA}}^{\text{varcone30}}/p_{\mathrm{T}} < 0.04$, is used. Electron isolation SFs are set to 1 with conservative uncertainty. Figure 4.4 shows isolation efficiencies on the full Run 2 dataset, adopting the *Tight* identification WP.

Isolation efficiencies are expected to significantly improve with the usage of Run 3 data, alongside the updated pile-up subtraction for the calorimeter isolation.

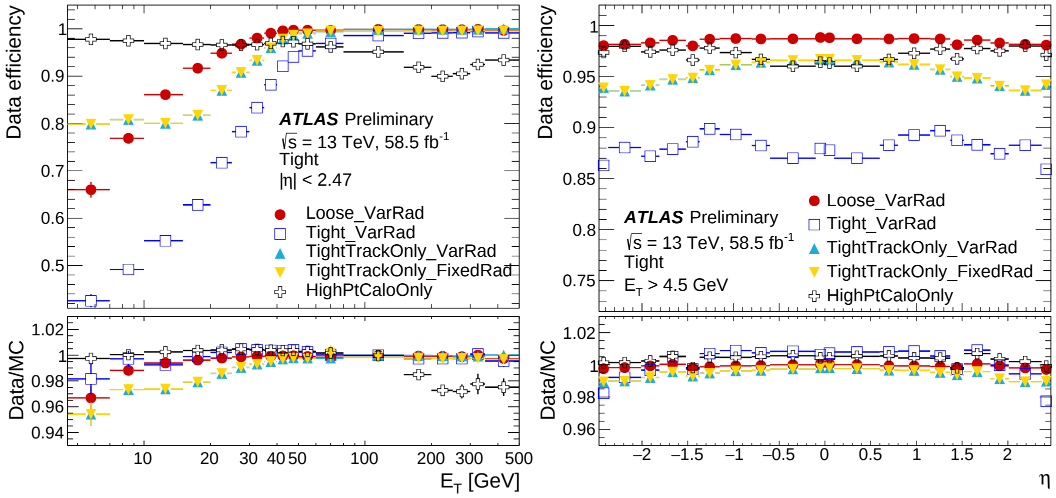

(a)

(b)

Figure 4.4: Electron isolation efficiencies in $Z \to ee$ events as a function of the electron transverse energy $E_{\mathrm{T}}$ (a) and as a function of pseudo-rapidity $\eta$ (b). The electrons are required to fulfill the Tight selection from the likelihood-based electron identification. For both plots, the bottom panel shows the data-to-simulation ratios. The total uncertainties are shown, including the statistical and systematic components. Figure taken from [193].

## 4.2 Muons

Being minimum ionising particles (MIP), muons are not stopped in the calorimeter; they are reconstructed and identified using the information from the ID and from the MS as well as the calorimeters [194, 195]. The reconstruction proceeds according to five main strategies, leading to the corresponding muon *types*: combined (CB), inside-out combined (IO), muon-spectrometer extrapolated (ME), segment-tagged (ST), and calorimeter-tagged (CT).

For this thesis, CB muons are used; muon tracks are first reconstructed independently in the ID and MS. Subsequently, the information from the subdetectors is refitted globally to form the muon tracks, taking into account the energy loss in the calorimeters. In the ID, muons are reconstructed like any other charged particle. Muon reconstruction in the MS starts with a search for hit patterns inside each muon chamber to form segments. The muon reconstruction efficiency is measured from $Z \to \mu\mu$ and $J/\Psi \to \mu\mu$ events, and it is close to 99% for $|\eta| < 2.5$ and $p_{\mathrm{T}} > 5$ GeV [195]. SFs for reconstruction and muon momentum scale and resolution corrections are calculated using Run 3 data. Trigger SFs are also measured in Run 3, using various data taking periods, and are applied to the MC simulation reflecting the relative luminosity of the individual periods. For the muon triggers, the SFs depend on muon $\eta$, $\phi$ and the simulated run number as to match the conditions of the data.

### 4.2.1 Muon identification

Muon candidates are identified as prompt muons by applying specific criteria, which help distinguish them from muons resulting from the decay of pions and kaons. Candidates originating from the decay of charged hadrons in the ID can typically be identified by the poor fit quality of the combined track and the discrepancy between the momentum measurements in the ID and the MS. To further differentiate muons produced in the hard scattering from those originating from semi-leptonic decays, particularly within hadronic jets, isolation requirements are set, adopting specific thresholds on the impact parameters $d_0$ and $z_0$. Unlike the process for identifying electrons, muon identification relies on a non-multivariate, cut-based selection, consisting of applying specific thresholds or "cuts" to different variables or parameters associated with the physics object. Three levels of identification selections are provided: *Loose, Medium*, and *Tight*. Each level has increasingly stringent criteria, improving the power to reject pion and kaon decays. A significant drop in efficiency can be observed in the *Medium* and *Tight* WPs because of the acceptance losses in the region at $\eta \sim 0$, where the MS is only partially equipped with muon chambers. In this thesis, the *Medium* WP is used; muon identification SFs are computed relying on Run 3 data. Figure 4.5 shows identification efficiencies computed on the full 2022 dataset.

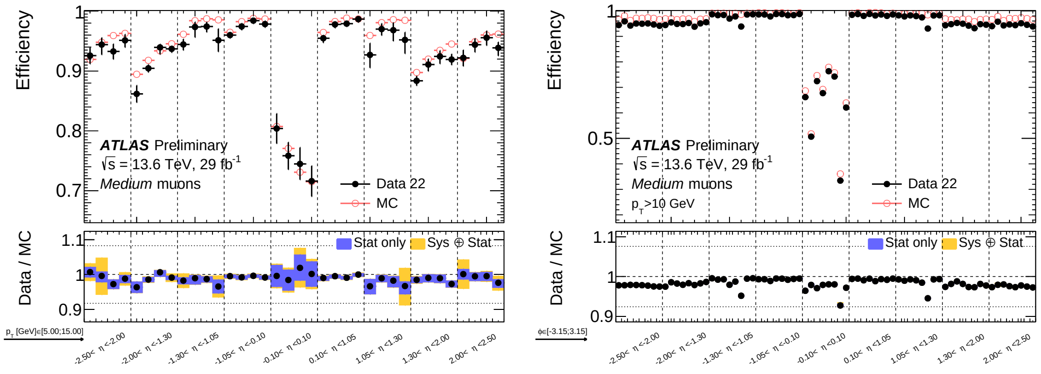

(a) (b)

Figure 4.5: Reconstruction and identification efficiency for muons with $p_T$ between 5 and 15 GeV satisfying the Medium quality criteria, measured in $J/\Psi \to \mu\mu$ events as a function of the $\eta$ and $p_T$ of the muons (a) and in $Z \to \mu\mu$ events as a function of the $\eta$ and $\phi$ of the muons (b). Black dots indicate the efficiency measured in data while red circles indicate the prediction by the simulation. The errors on the efficiencies are statistical. The bottom panel shows the ratio between the result in data and simulation, with statistical (blue) and the combination of statistical and systematic uncertainties (yellow). Figure taken from [196].

### 4.2.2 Muon isolation

The evaluation of detector activity around the muon candidate, addressed as *muon isolation*, is an effective technique for detecting non-prompt muons inside jets. Just as with electrons, the isolation algorithm can be developed using variables that represent the level of activity close to the candidate object. In this thesis, the *Tight_VarRad* isolation WP is used, defined as in Section 4.1.2. SFs are computed relying on Run 3 data.

For both muon identification and isolation, a notable improvement is expected with the usage of the updated Run 3 dataset and a refined estimate of contributions from pile-up and the underlying event.

## 4.3 Jets

The process of jet reconstruction typically involves aggregating energy deposits in topologically connected calorimeter cells [197] of the calorimeters to form what is known as *topological-clusters* or *topo-clusters*. These clusters serve as input for jet reconstruction algorithms. In the analysis presented in this thesis, the anti-$k_t$ [198] jet algorithm is used, as implemented in the FastJet [199, 200] software package.

### 4.3.1 The anti-$k_t$ jet algorithm

The anti-$k_t$ algorithm combines energy clusters from the calorimeters based on a distance parameter $d_{ij}$ between clusters $i$ and $j$:

$$d_{ij} = \min\left(p_{\mathrm{T},i}^{2p}, p_{\mathrm{T},j}^{2p}\right)\frac{\Delta R_{ij}^2}{R^2} \tag{4.2}$$

where the *radius parameter* $R$ is set to 0.4, the exponent[6] $p$ is equal to $-1$, and $\Delta R_{ij}$ is the angular distance[7] between two objects.

The anti-$k_t$ algorithm entails two crucial properties that incentivise its use at hadron colliders. It prioritises the clustering of hard jets rather than soft ones. This leads to simpler calibrations, since just one parameter, $R$, is sufficient to describe the shape of the corresponding reconstructed jets. Furthermore, the anti-$k_t$ algorithm is invariant with respect of the emission of a soft or collinear particle. This property is called infrared and collinear (IRC) safety [203], where the term “infrared” is referred to a soft particle.

### 4.3.2 Jet reconstruction and calibration

Three types of jets are identified, according to the type of input provided to the jet-reconstruction algorithm:

---

[6] Varying the $p$ exponent implies employing different algorithms similar to the anti-$k_t$: with $p = 1$, the $k_t$ [201] algorithm is obtained, whereas $p = 0$, results in the Cambridge-Aachen algorithm [202].

[7] The angular distance $\Delta R_{ij}$ between two objects $i$ and $j$ is defined as the angular distance between the two energy barycentres $\Delta R_{ij} = \sqrt{(\eta_i - \eta_j)^2 + (\phi_i - \phi_j)^2}$.

- **Topo jets** [204]: these objects are built using only calorimeter-based energy information derived from the origin-corrected EM scale[8] topo-clusters.

- **Particle-Flow (PFlow) jets** [205]: PFlow[9] jets exploit the information from both the ID and calorimeter systems. Specifically, the energy deposited in the calorimeter is subtracted from the observed topo-clusters and replaced by the momenta of the tracks that are matched to those topo-clusters. PFlow jets exhibit improved energy and angular resolution, reconstruction efficiency, and pile-up stability compared to calorimeter jets.

- **Truth jets**: these jets are reconstructed using simulated, stable final-state particles, excluding muons, neutrinos, and products of pile-up interactions.

The energy deposited in the calorimeters originates from EM interactions only; therefore, a jet energy must be extracted solely from the EM information. A set of calibrations are applied to reconstructed jets in order to match the jet energy of the corresponding simulated truth jets. A series of sequential calibrations are applied [206], all aiming at correcting the jet four-momentum, by scaling its $p_{\mathrm{T}}$, energy and mass. Below, the set of calibrations is briefly described:

- **Pile-up corrections**: this correction aims to remove the excess energy due to additional proton-proton interactions within the same (in-time) or nearby (out-of-time) bunch crossings. These corrections consist of two components: a correction based on the jet area and transverse momentum density of the event, and a residual correction derived from MC simulation.

- **Absolute Jet Energy Scale (JES) calibration**: the absolute JES calibration corrects the jet so that it agrees in energy and direction with truth jets from dijet MC events.

- **Global Sequential Calibration (GSC)**: this correction improves the jet $p_{\mathrm{T}}$ resolution and associated uncertainties by removing the dependence of the reconstructed jet response on observables constructed using information from the tracking, calorimeter, and muon detector systems.

- **Residual *in-situ* calibration**: this operation is performed on data to correct for remaining differences between data and MC simulation. It is derived using well-measured reference objects, including photons and $Z$-bosons.

Furthermore, a precise knowledge of the Jet Energy Resolution (JER) is crucial for several detailed measurements of the SM jet production, including measurements and studies of the properties of the SM particles that decay to jets, as well as searches for physics beyond the SM involving jets. The JER estimate is typically derived using the *dijet balance* technique [207].

---

[8] The EM scale origin correction points the jet back to the primary event vertex, instead of the nominal center of the ATLAS detector, ensuring that the energy measurements are accurate and correspond to the true energy of the particles involved.

[9] Since both Topo and PFlow jets are usually reconstructed using topo-clusters at the EM scale, they can be also referred to as EMTopo/EMPFlow jets.

Finally, even though the pile-up is subtracted in the calibrations mentioned above, its activity can still mimic jets, especially low-$p_{\mathrm{T}}$ ones. To correct the contribution of pile-up activity misidentified as jets from the hard scattering, a likelihood-based discriminant named *jet-vertex-tagger* (JVT) was employed during Run 2 [208]. In Run 3, the JVT algorithm has been replaced by an artificial neural-network-based discriminant (NNJVT).

Due to their enhanced performance, and in compliance with the recommendations provided by the dedicated working group, PFlow jets are employed in this thesis. The jet calibration (including all the corrections listed in Section 4.3.2), is derived from Run 2 data and MC, reprocessed in the Run 3 analysis framework. Since the NNJVT algorithm was not calibrated at the time of writing, no corrections are applied and a large uncertainty is added on the efficiency.

After the calibration, jet candidates are required to have $p_{\mathrm{T}} > 30$ GeV and $|\eta| < 2.5$. To suppress pile-up jets, the NNJVT algorithm is used for jets with $p_{\mathrm{T}}$ below 60 GeV.

Several improvements are expected in jet-related studies by adopting Run 3 data to perform the calibrations.

## 4.4 Missing transverse energy

There are particles, such as neutrinos, that do not interact with the detector material, thus escaping direct detection. However, exploiting the momentum conservation law, they can be detected indirectly. In fact, since the parton transverse momentum can be considered to be exactly zero, the total transverse momentum of all the collision products, including those that are measured and those that escape direct detection, can be assumed to be zero. Therefore, the measurement of a non-zero *missing transverse momentum*, whose magnitude is often referred to as missing transverse energy, $E_{\mathrm{T}}^{\mathrm{miss}}$, suggests the presence of one or more undetected particles.

Such $E_{\mathrm{T}}^{\mathrm{miss}}$ is calculated combining the information from the ID, the calorimeters and the MS [209], by building a vectorial sum of all the calibrated physics objects (leptons, jets associated to the primary vertex, etc.) projected in the transverse plane, and adding a term to account for good quality soft tracks not associated to any of those physics objects, resulting in:

$$E_{\mathrm{T}}^{\mathrm{miss}} = \left| - \sum_{\text{muons}} \vec{p_{\mathrm{T}}}^{\mu} - \sum_{\text{electrons}} \vec{p_{\mathrm{T}}}^{e} - \sum_{\text{photons}} \vec{p_{\mathrm{T}}}^{\gamma} - \sum_{\tau} \vec{p_{\mathrm{T}}}^{\tau} - \sum_{\text{jets}} \vec{p_{\mathrm{T}}}^{\text{jets}} - \sum_{\text{soft trks}} \vec{p_{\mathrm{T}}}^{\text{trk}} \right| \tag{4.3}$$

Energy deposits in the calorimeters and tracks are matched to reconstructed objects in an order chosen to minimise double-counting of elements. The order used for $E_{\mathrm{T}}^{\mathrm{miss}}$ reconstruction starts with muons, electrons, followed by photons, then hadronically decaying $\tau$-leptons, jets and finally the track soft term [210].
The $E_{\mathrm{T}}^{\mathrm{miss}}$ reconstruction performance is derived by comparing $E_{\mathrm{T}}^{\mathrm{miss}}$ distributions in data and

MC simulations for the same final state selection [211]. The analysis presented in this thesis does not utilise the information provided by the reconstruction of $E_{\mathrm{T}}^{\mathrm{miss}}$; therefore, no calibrations are applied.

## 4.5 Identification of $b$-jets

The top quark decays into a $W$-boson and a $b$ quark practically 100% of the times; it is therefore crucial to correctly identify a jet originating from a $b$ quark in all studies involving a top quark. The identification of $b$-jets, and their discrimination from $c$-jets and light-flavour jets[10], is called $b$-tagging.

The characteristics of $b$-jets are related to the properties of the $B$-hadrons they contain. Specifically, their large lifetime ($\tau_b \sim 1.5$ ps) [17] and high decay multiplicity (on average ~ 5 charged particles), allow for the formation of a quite recognisable topology that involves at least one *secondary vertex*, separated by a macroscopic distance from the *primary* one, as illustrated by Figure 4.6. In addition, approximately 20% of $B$-hadron decay products contain an electron or a muon. Due to the large mass of the $b$ quark ($m_b \sim 4.5$ GeV), these decay products can have relatively large transverse momentum. These features, alongside other discriminating variables, are incorporated in the $b$-tagging algorithms.

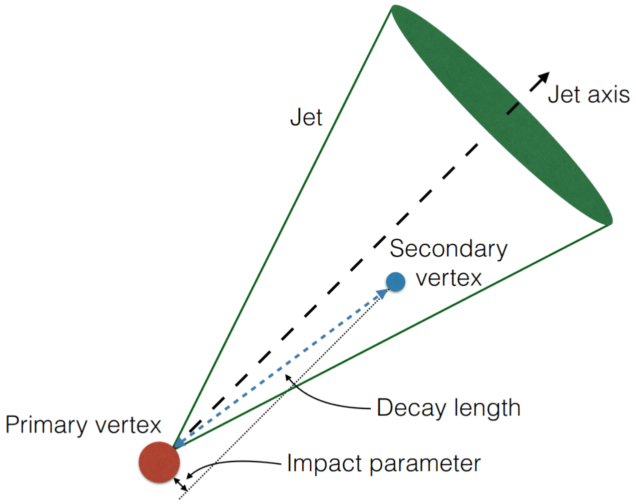

Figure 4.6: Illustration of the production of a secondary vertex, with its associated $b$-jet. Figure taken from [212].

In this thesis, the DL1d algorithm [213, 214], which is based on artificial neural networks (NN), operates at the 77%-efficiency[11], to identify $b$-tagged jets. The recommendations provided

---

[10] Light jets are characterised by the hadronisation of light quarks, such as $u$, or $d$.

[11] An efficiency of 77% means that in a MC sample of $t\bar{t}$ events, 77% of true $b$-jets pass the selection requirements.

reported the same the $b$-tagging SFs uncertainties for all the efficiencies. Thus, the 77% efficiency was chosen as a reasonable tradeoff between the number of true $b$-jets selected and the amount of statistics accumulated[12]. The DL1d neural network has a multidimensional output corresponding to the probabilities for a jet to be a $b$-jet, a $c$-jet or a light-flavour jet. The topology of the output consists of a mixture of fully connected hidden and Maxout layers [215].

The NN input variables include jets and tracks related features:

- Jet kinematics ($p_{\mathrm{T}}$ and $\eta$);
- A likelihood-based combination of the transverse and longitudinal impact parameter significances, implemented in the IP3D algorithm [216] that is based on a likelihood ratio where the impact parameters of the track are compared to simulated $b$- and light-flavour hypotheses;
- Identification of secondary (and tertiary) vertices through the algorithms SV0 and SV1 [217].
- Reconstruction of the $b$- and $c$-hadron decay chains to identify their topology, implemented in the JetFitter algorithm [218].

These input variables have been optimised to provide the best separation power between the signal, corresponding to $b$-jets, and the background, represented by $c$- and light-jets. The final output discriminant includes the $b$-jet, $c$-jet and light-flavour jet probabilities. The performance of DL1d at the start of Run 3, compared to the previous tagger, DL1r [219], used in Run 2, is shown in Figure 4.7.

The $b$-efficiency is measured using $t\bar{t}$ dilepton events [221] to get corrections to the efficiency of tagging a true $b$-jet. The details regarding the extraction of $b$-efficiency SFs are further inspected in Appendix I. No dedicated correction is applied for $c$- and light-flavour jets.

The $b$-tagging performance is expected to greatly improve throughout Run 3; a refined estimate of the efficiency SFs, and eventually a newer tagger, the so called GN1 tagger [222], will significantly improve the overall performance.

## 4.6 Overlap removal

*Overlap removal* (OR) addresses the topics of duplication, where the reconstruction of a single physical object results in two distinct objects, and isolation, which involves the treatment of two separate yet close objects [223]. To remove any double counting or ambiguity, the OR procedure is employed with the aim of correctly identifying the true physical objects. The following steps are applied in sequence:

---

[12] Moreover, as further explained in the next chapters, the analysis is designed to be insensitive to the $b$-tagging efficiency, since the choice of efficiency is primarily reflected in the fitted value of the $\epsilon_b$ parameter. Additionally, varying the $b$-tagging efficiency might cause a variation of the statistical uncertainty in the fit, but since the measurement is largely dominated by the systematic uncertainties, this effect would be negligible.

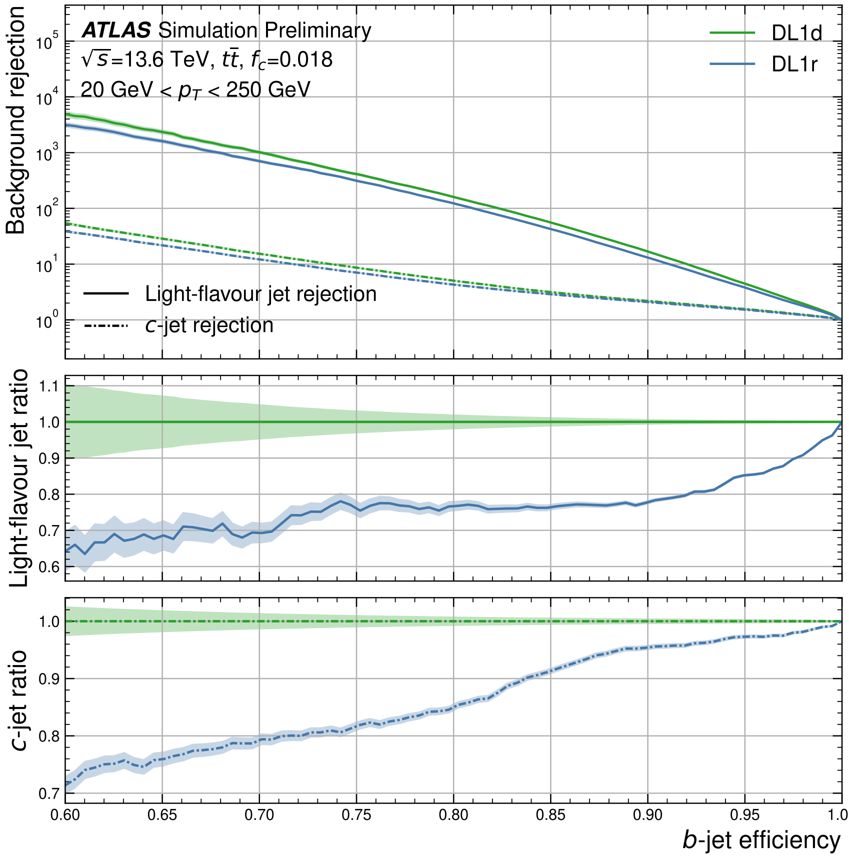

Figure 4.7: The light-flavour jet (solid line) and $c$-jet (dashed line) rejection for the latest DL1r and DL1d algorithms. The taggers are re-optimised on reprocessed Run 2 simulation. The x-axis corresponds to the $b$-jet efficiency, while the y-axis corresponds to the background rejection in the upper panel. The middle panel shows the ratio of the light-flavour jet rejection while the lower panel shows the ratio of the $c$-jet rejection. The statistical uncertainties on the rejection are calculated using binomial uncertainties and are indicated as shaded bands. Figure taken from [220].

1. Any calorimeter-tagged muon found to share a track with an electron is removed.
2. Any electron found to share a track with a muon is removed, as the electron can be misidentified as a photon radiated by the muon.
3. Any jet found within a $\Delta R$ of 0.2 from an electron is removed. This step is necessary because energy deposits in the EM calorimeter are used in jet reconstruction irrespective of the electron reconstruction result.
4. Any electron subsequently found within $\Delta R$ of 0.4 from a jet is removed. In this case, the electron is assumed to be the product of a semi-leptonic decays of heavy-flavour hadrons.
5. Any jet with less than three tracks associated to it found within $\Delta R$ of 0.2 from a muon is removed. This is because such a low track multiplicity can be compatible with radiation effects from the muon.
6. Any jet with less than three tracks associated to it, which has a muon inner-detector track ghost-associated[13] to it, is removed.
7. Any muon subsequently found within $\Delta R$ of 0.4 from a jet is removed. As before, in this case the muon is considered as a product of a semi-leptonic heavy-flavour hadron decay.
8. Any tau found within a $\Delta R$ of 0.2 from a *Loose* electron is removed.
9. Any tau found within a $\Delta R$ of 0.2 from any type of muon with $p_{\mathrm{T}}$ greater than 2 GeV is removed; it should be noted that if the tau $p_{\mathrm{T}}$ is greater than 50 GeV, it will only be removed if it is found to overlap with a combined-type muon.
10. Any jet found within a $\Delta R$ of 0.2 from a tau is removed.
11. Any photon found within a $\Delta R$ of 0.4 from an electron or a muon is removed, as the photon could be a radiative product of the lepton.
12. Any jet found within $\Delta R$ of 0.4 from a photon is removed. Similarly to the electrons case, the reconstruction of jets is independent of the photon reconstruction.

## 4.7 Time evolution of physics objects recommendations

### 4.7.1 Electrons

Below, a summary of the upgrades on the electron recommendations is provided starting from the beginning of Run 3 (July 2022).

---

[13] Ghost-association is a technique used to define the jet area by making use of infinitely soft particles, called “ghosts” [224].

- **July - December 2022**: preliminary recommendations and calibrations are provided for reconstruction, identification, isolation and trigger. In particular, since the tool dedicated to the calculation of the trigger SFs was not available in the Run 3 software suite at the time of writing, a custom implementation is used. The detailed description of the procedure is provided in Appendix F.
- **January - March 2023**: update of the electron trigger SFs using Run 3 data.
- **April - June 2023**: update of the momentum scale corrections.

### 4.7.2 Muons

Muon recommendations were progressively updated and naturally evolving with the amount of data that were being collected and analysed.

- **July - December 2022**: preliminary recommendations evaluated on early Run 3 data are provided. Muon trigger SFs are estimated using the procedure provided in Appendix F.
- **January - March 2023**: prescriptions for identification, isolation, trigger, momentum scale/resolution corrections and SFs are provided. Corrections are extracted from 12 $\text{fb}^{-1}$ of Run 3 data.
- **April - June 2023**: update related to trigger SFs and momentum scale/resolution recommendations.

### 4.7.3 Jets

- **July - December 2022**: calibrations used in Run 2 are employed, JVT algorithm employed.
- **January - March 2023**: prescriptions for Run 3 as presented in Section 4.3; upgrade to NNJVT algorithm.
- **April - June 2023**: update on jet reconstruction prescription.

### 4.7.4 Flavour tagging

- **July - December 2022**: preliminary prescriptions are provided: SFs set to 1, with conservative uncertainties on the $b$-tagging and $c$- and light-mistagging rates, respectively, 10%, 20% and 40%. The corrections accounting for different MC generators used in Run 2 are applied also for Run 3 samples. A detailed comparison between Run 2 vs Run 3 MC SFs is presented in Appendix G.
- **January - March 2023**: recommendations for flavour tagging are updated and efficiencies are calibrated using $\sim$ 12 $\text{fb}^{-1}$ of Run 3 data.

# Chapter 5

# Analysis strategy

The aim of the analysis presented in this thesis is two-fold. The first goal is to provide an extensive validation of the new detector components, reconstruction methodologies, and software used in the third run of the LHC. This validation is carried out by providing data-to-MC comparisons for various kinematic distributions in a relatively pure sample of $t\bar{t}$ events, in the dilepton final state.

The second and the main goal of the analysis is to measure the inclusive $t\bar{t}$ cross-section, $\sigma_{t\bar{t}}$, in the above-mentioned final state. A cross-section ratio of $t\bar{t}$ to $Z$-boson production, denoted as $R_{t\bar{t}/Z}$, is provided with the goal of reducing experimental uncertainties, primarily those related to luminosity. Moreover, given that the $t\bar{t}$ and $Z$-boson production dynamics are driven to a large extent by different PDFs, the ratio of these cross-sections at a given centre-of-mass energy has a significant sensitivity to the gluon-to-quark PDF ratio [225, 226]. Finally, the measurement of the $Z$-boson cross-section, $\sigma^{\text{fid.}}_{Z\to\ell\ell}$, defined in a fiducial phase space characterised by kinematic selection requirements that follow closely those applied to data events, is provided.

Three channels are defined using electrons and muons of opposite electric charge: $ee$, $\mu\mu$ and $e\mu$. For the same-flavour channels ($ee$, $\mu\mu$), the reconstructed invariant mass of the lepton pair, $m_{\ell\ell}$, is required to be close to the $Z$-boson mass: these channels constitute a very pure sample, with ~99.5% of events originating from $Z$-boson production. In the opposite-flavour channel ($e\mu$), the well-established technique of "$b$-tag counting" is exploited (as presented in Ref. [59]), consisting in a simultaneous extraction of the $t\bar{t}$ cross-section and the $b$-jet identification efficiency. In this analysis, this $b$-tag counting method is modified to be suitable for a profile-likelihood approach that facilitates combinations with the single-lepton channel and the $Z$-boson measurements. Section 5.1 reports a concise summary of the various results published during Run 3. A detailed description of the procedure used to extract the cross-sections is provided in Section 5.2.

## 5.1 Results chronology

The results presented in this thesis are divided into three parts: a primary measurement, and two preliminary analyses, each corresponding to distinct periods of the early Run 3 at the LHC. A brief overview of the measurements, alongside with a preliminary study conducted at the very beginning of the data taking, is presented below. Furthermore, Table 5.1 provides a summarised comparison of the strategies; a more in-depth discussion of the varying procedures implemented across the three publications will be provided as necessary in the ensuing chapters.

### 5.1.1 Preliminary studies - 790 pb$^{-1}$ of 2022 data

The first studies on the detector and software performance were presented at the “15th International Workshop on Top Quark Physics” (TOP2022) conference, in September 2022 [227]. Data were collected from August 6th to August 8th, 2022; the dataset corresponds to three LHC fills, specifically 8102, 8103, and 8106. The comparison of data and prediction in the electron-muon final state provides a valuable input to validate the functionality of the detector and the reconstruction software which went through a number of upgrades during LS2.

### 5.1.2 ATLAS-CONF-2022-070 - 1.2 fb$^{-1}$ of 2022 data

The first measurement of the inclusive $t\bar{t}$ production cross-section, a fiducial $Z$-boson production cross-section and their ratio is performed using 1.2 fb$^{-1}$ of data collected by the ATLAS detector at the centre-of-mass energy of 13.6 TeV [228]. The data correspond to four different LHC fills, recorded between August 6th and August 9th, 2022. The LHC fill 8112 was added to the previous set. This first set of results was presented as a poster at the “152nd LHCC Meeting” (LHCC2022), in November 2022.

### 5.1.3 ATLAS-CONF-2023-006 - 11.3 fb$^{-1}$ of 2022 data

This result [229] represents a midterm milestone for the analysis effort, and a refined estimation of the $t\bar{t}$ production cross-section, of the fiducial $Z$-boson production cross-section and of the ratio between the two using 11.3 fb$^{-1}$. A number of features are improved in the analysis, including a significant reduction of the luminosity uncertainty, and several updates on physics objects reconstruction and calibrations. These results were presented at the “57th Rencontres de Moriond 2023" (Moriond2023) conference, in March 2023.

### 5.1.4 Primary measurement - 29 fb$^{-1}$ of 2022 data

This measurement is the main result of this thesis. As in the previous analyses, it includes the estimate of the $t\bar{t}$ production cross-section and of the $t\bar{t}/Z$ cross-sections ratio; additionally, the measurement of the fiducial $Z$-boson cross-section is provided by using a different fir strategy, as further described in Section 5.2.3. [230]. The analysis exploits the full 2022 dataset, enabling a significant validation of Run 3 data; moreover, this study presents an opportunity to refine the recommendations and features associated with the physics objects. These results were presented at the “European Physical Society Conference on High Energy Physics 2023" (EPS-HEP2023) conference, in August 2023.

<table>
<tr><th>Feature</th><th colspan="2">ATLAS-CONF-2022-070</th><th colspan="2">ATLAS-CONF-2023-006</th><th colspan="2">Primary measurement</th></tr>
<tr><td colspan="7"><b>Analysis strategy</b></td></tr>
<tr><td>Fit setup</td><td colspan="2">Two separate fits; the first to measure $\sigma_{t\bar{t}}$ ($e\mu$ channel), the second to extract $\sigma_{Z\rightarrow\ell\ell}^{m_{\ell\ell}>40}$, $R_{t\bar{t}/Z}$ and $\epsilon_b$ ($e\mu$, $ee$ and $\mu\mu$ channels)</td><td colspan="2">Two separate fits in the $e\mu$, $ee$ and $\mu\mu$ channels; the first to compute $\sigma_{t\bar{t}}$ and $\sigma_{Z\rightarrow\ell\ell}^{\text{fid.}}$, the second to extract $R_{t\bar{t}/Z}$ and $\epsilon_b$</td><td colspan="2">Added third fit to measure $\sigma_{Z\rightarrow\ell\ell}^{\text{fid.}}$ from $ee$ and $\mu\mu$ channels only.</td></tr>
<tr><td colspan="7"><b>Fiducial treatment of the $Z$-boson</b></td></tr>
<tr><td>Phase space definition</td><td colspan="2">$66 < m_{\ell\ell} < 116$ GeV, extrapolated to $m_{\ell\ell} > 40$ GeV with $Z \rightarrow \ell\ell$</td><td colspan="2">lepton $p_{\text{T}} > 27$ GeV, lepton $|\eta| < 2.5$, $66 < m_{\ell\ell} < 116$ GeV for $Z \rightarrow \ell\ell$</td><td colspan="2">Unchanged</td></tr>
<tr><td>Acceptance corrections</td><td colspan="2">Not applied</td><td colspan="2">Applied</td><td colspan="2">Updated</td></tr>
<tr><td>Cross-section prediction</td><td colspan="2">$\sigma(Z)^{m_{\ell\ell}>40} = 2182^{+20}_{-25}(\text{scale}) \pm 37(\text{PDF})$ pb</td><td colspan="2">$\sigma(Z)^{\text{fid.}} = 741 \pm 4(\text{int.})^{+3}_{-4}(\text{scale}) \pm 14(\text{PDF})$ pb</td><td colspan="2">$\sigma(Z)^{\text{fid.}} = 746 \pm 0.7(\text{int.})^{+3}_{-5}(\text{scale}) \pm 21(\text{PDF})$ pb</td></tr>
<tr><td colspan="7"><b>Objects definition</b></td></tr>
<tr><td>Electrons</td><td colspan="2">$TightLH$ ID, $Tight\_VarRad$ Isol.</td><td colspan="2">Updated trigger scale factors</td><td colspan="2">Unchanged</td></tr>
<tr><td>Muons</td><td colspan="2">$Medium$ ID, $Tight\_VarRad$ Isol.</td><td colspan="2">Updated trigger scale factors</td><td colspan="2">Unchanged</td></tr>
<tr><td>Jets</td><td colspan="2">k-nearest neighbour based JVT</td><td colspan="2">Neural network based JVT</td><td colspan="2">Unchanged</td></tr>
<tr><td>Flavour tagging</td><td colspan="2">DL1d tagger</td><td colspan="2">Updated $b$-tagging calibrations</td><td colspan="2">Unchanged</td></tr>
<tr><td colspan="7"><b>Theoretical prediction for $R_{t\bar{t}/Z}$</b></td></tr>
<tr><td>PDF sets used</td><td colspan="2">PDF4LHC21</td><td colspan="2">PDF4LHC21(including $m_t$ variations), CT18, CT18A, MSHT20, NNPDF4.0, ATLASpdf21, ABMP16</td><td colspan="2">Updated predictions</td></tr>
<tr><td colspan="7"><b>Data</b></td></tr>
<tr><td>Integrated luminosity</td><td colspan="2">1.2 fb$^{-1}$ of 2022 data</td><td colspan="2">11.3 fb$^{-1}$ of 2022 data</td><td colspan="2">29 fb$^{-1}$ of 2022 data</td></tr>
<tr><td colspan="7"><b>MC samples</b></td></tr>
<tr><td></td><td><b>Generator</b></td><td><b>Theory prediction</b></td><td><b>Generator</b></td><td><b>Theory prediction</b></td><td><b>Generator</b></td><td><b>Theory prediction</b></td></tr>
<tr><td>Single-top</td><td>PP8</td><td>NLO+NNLL</td><td colspan="2">Unchanged</td><td>Unchanged</td><td>Updated</td></tr>
<tr><td>$t\bar{t} + V$</td><td colspan="2">Not included</td><td colspan="2">Not included</td><td>Sherpa</td><td>From MC</td></tr>
<tr><td colspan="7"><b>Systematic uncertainties</b></td></tr>
<tr><td>Electrons</td><td colspan="2">ID, Isol., Reco., momentum/scale resolution</td><td colspan="2">Updated systematic model</td><td colspan="2">Updated scale uncertainties</td></tr>
<tr><td>Muons</td><td colspan="2">ID, Isol., TTVA, momentum/scale resolution</td><td colspan="2">Updated systematic model</td><td colspan="2">Updated momentum/scale and trigger uncertainties</td></tr>
<tr><td>Jets</td><td colspan="2">JES, JER, JVT uncertainties</td><td colspan="2">Updated systematic model</td><td colspan="2">Updated jet reconstruction</td></tr>
<tr><td>Flavour tagging</td><td colspan="2">SFs=1, uncertainties for $b$-tagging, $c$- and light-mistagging set at 10%, 20% and 40%</td><td colspan="2">SFs estimated on Run 3 data, uncertainties unchanged</td><td colspan="2">Unchanged</td></tr>
<tr><td>Top $p_{\text{T}}$ reweighting</td><td colspan="2">Not estimated</td><td colspan="2">Estimated</td><td colspan="2">Estimated</td></tr>
<tr><td>$Z$-boson modelling</td><td colspan="2">Scale uncertainties</td><td colspan="2">Corrected with acceptance effects</td><td colspan="2">Updated</td></tr>
<tr><td>Luminosity</td><td colspan="2">10%</td><td colspan="2">2.2%</td><td colspan="2">Unchanged</td></tr>
<tr><td>Pileup</td><td colspan="2">Variation of average $\mu$ by 3% in simulation (Run 2)</td><td colspan="2">Variation of average $\mu$ by 4% in simulation</td><td colspan="2">Unchanged</td></tr>
<tr><td>$t\bar{t} + V$ normalisation</td><td colspan="2">Not included</td><td colspan="2">Not included</td><td colspan="2">Set at 50%</td></tr>
<tr><td colspan="7"><b>Additional uncertainties</b></td></tr>
<tr><td>Top mass dependence</td><td colspan="2">Not estimated</td><td colspan="2">Not estimated</td><td colspan="2">Estimated</td></tr>
</table>

Table 5.1: Comparison of the main features characterising the measurements presented in this thesis. Only elements that were updated at least once over time are shown.

## 5.2 Statistical treatment

### 5.2.1 Profile-likelihood

The profile-likelihood approach offers an efficient way to integrate the statistical model as well as all the sources of the systematic uncertainties in the likelihood function itself. Following the maximum-likelihood principle, the best estimates for the parameters of interest (POIs) in a certain model can be obtained by maximising such likelihood function with respect to these POIs as well as a set of nuisance parameters (NPs), associated with systematic uncertainties. The likelihood, $L$, can be schematically written as follows:

$$L\left(\vec{n}|\mu, \vec{\theta}\right) = \prod_{i \in \mathrm{bin}} \mathrm{Pois}\left(n_i|\mu S_i(\vec{\theta}) + B_i(\vec{\theta})\right) \times \prod_{j \in \mathrm{NP}} G\left(\theta_j\right), \tag{5.1}$$

where $\vec{n}$ is the data vector, and $n_i$ represents the data yields in each bin. The notation $\vec{\theta}$ denotes the NPs, that affect the number of signal events $S_{i,r}$ as well as the number of background events $B_i$. Finally, $\mu$ is the signal strength, which is the parameter of interest in the likelihood and it represents the ratio of the measured signal cross-section over the predicted one. The terms “Pois” and $G$, represent the Poisson and Gaussian distributions, respectively. The Gaussian terms act as constraints on the NPs associated with systematic uncertainties, parametrising the prior knowledge on the parameters controlling systematic effects[1]. In addition to the parameter of interest and the nuisance parameters, unconstrained nuisance parameters, $\vec{k}$, can be added to the likelihood, typically as multiplicative factors, or “normalisation factors” (NFs) to certain signal or background model components, to be extracted from the data at the same time of the POIs. The full form of the likelihood can be found in the *HistFactory* reference [231].

Internally, the systematically-varied histograms provided are compared to the nominal histograms considering the total yield difference; this approach takes the name of normalisation [2]. For each bin, the product of an exponential and polynomial of 6-th order is used; the polynomial is needed to have a smooth transition for the function and its first and second derivative between the up and down variations. The normalisation effect is controlled by the parameter $\theta$. This results in a Gaussian constraint for the shape component and an approximate log-normal constraint for the normalisation component, which prevents an unphysical negative normalisation.

The likelihood from Eq. 5.1 is maximised to obtain the best-fit values for all the parameters as well as their uncertainty. The maximisation of the likelihood, or rather, the minimisation of

---

[1] For the *gamma* terms, representing the MC statistical uncertainty, the constraint term is Poissonian — in Bayesian statistics this would result in Gamma function posterior distribution, hence the name.

[2] More generally a second component is taken into account, and includes a pure shape effect, where the total yield of the variation is forced to match the nominal prediction. Then, for each bin, the shape variation is interpolated and extrapolated using a linear interpolation. Since in this thesis the fit is performed on single bins, no shape component is considered.

the negative logarithm of the likelihood, exploits the MINUIT framework [232], adopting the MIGRAD minimisation method. Such minimisation can be summarised as follows:

1. Fix the parameters to a certain value, $x$.
2. Compute the gradient $\nabla$ in a given point, assuming that the Hessian matrix corresponds to unity.
3. Along the direction of the gradient, find the value $\alpha$ such that $-\log L(x - \alpha V \times \nabla)$ is minimum. In the previous expression, $V$ represents the covariance matrix of the parameters, or the inverse of the Hessian matrix.
4. Repeat the operation until the estimated distance to the minimum (EDM) is sufficiently small. The EDM is typically defined as $EDM = \nabla^{\mathrm{T}} V \nabla$.

This procedure provides also the correlation matrix between the NPs, since it can be trivially extracted from the covariance matrix $V$. The post-fit uncertainties for both POIs and NPs can be derived from the diagonal elements of the covariance matrix, which is the inverse of the symmetric Hessian matrix. For this reason, the estimated uncertainties are symmetric. To accommodate a more precise determination of the uncertainties, allowing them to be also asymmetric, the MINOS algorithm [232] is employed.

### 5.2.2 $b$-tag counting method and profile-likelihood

The $b$-tag counting method has proven to be an effective method of measuring the cross-section of the $t\bar{t}$ process in the dilepton decay channel due to its low sensitivity to systematic uncertainties [59]. The method requires to select events with opposite-sign electron and muon pairs and counting the number of those that have exactly one $b$-tagged jet ($N_1$) and exactly two $b$-tagged jets ($N_2$).

The two event counts satisfy the tagging equations:

$$
\begin{aligned}
N_1 &= L\sigma_{t\bar{t}}\epsilon_{e\mu}2\epsilon_b\,(1 - C_b\epsilon_b) + N_1^{\mathrm{bkg}}, && (5.2)\\
N_2 &= L\sigma_{t\bar{t}}\epsilon_{e\mu}C_b\epsilon_b^2 + N_2^{\mathrm{bkg}}, && (5.3)
\end{aligned}
$$

where $L$ is the integrated luminosity, $\sigma_{t\bar{t}}$ is the sought after $t\bar{t}$ production cross-section, and the $b$-jet efficiency $\epsilon_b$ is the efficiency to reconstruct and $b$-tag a jet originating from the fragmentation of a $b$ quark coming from a top-quark decay in $t\bar{t}$ events. $\epsilon_{e\mu}$ is the efficiency for a $t\bar{t}$ event to pass the opposite sign $e\mu$ selection, $C_b$ is a tagging correlation coefficient that is close to unity, and $N_{1(2)}^{\mathrm{bkg}}$ is the number of background events with one (two) $b$-tagged jets.

The correlation factor, $C_b$, is defined as $C_b = \epsilon_{bb}/\epsilon_b^2$, where $\epsilon_{bb}$ represent the probability to reconstruct and tag both $b$-jets. The deviation of $C_b$ from unity is caused by kinematic correlations of the two $b$-jets produced in a $t\bar{t}$ event and the kinematic dependence of the $b$-tagging probability. The correlation factor can be rewritten as:

$$C_b = \frac{4N^{t\bar{t}}_{\geq 0} N^{t\bar{t}}_{2}}{\left(N^{t\bar{t}}_{1} + 2N^{t\bar{t}}_{2}\right)^2}, \tag{5.4}$$

where $N^{t\bar{t}}_{\geq 0}$ is the number of selected $e\mu$ events without any requirements on jet or $b$-tagging. The $C_b$ parameter is estimated using the MC simulation; in this thesis, using 29 fb$^{-1}$ of data, $C_b = 1.0068$.

Although the $b$-tagging technique is powerful, it does not allow for direct implementation in the standard profile-likelihood tools. This is evident from the Eq. 5.2 which does not have the usual form of signal strength (normalisation) times the predicted number of events due to the presence of the free parameter $\epsilon_b$. The equations have to be adapted to make them suitable for a profile-likelihood fit. The first step is to rewrite the signal prediction part using $L\sigma_{t\bar{t}}\epsilon_{e\mu} = \mu N^{t\bar{t}}_{\geq 0}$, where $\mu$ is the signal strength and $N^{t\bar{t}}_{\geq 0}$ is the number of $t\bar{t}$ events passing the lepton selection without any requirement on jets.

The Eq. 5.2 can then be reinterpreted as:

$$\begin{aligned} N_1 &= \mu 2\epsilon_b N^{t\bar{t}}_{\geq 0} - \mu 2\epsilon_b^2 C_b N^{t\bar{t}}_{\geq 0} + N_1^{\text{bkg}} \\ N_2 &= \mu C_b \epsilon_b^2 N^{t\bar{t}}_{\geq 0} + N_2^{\text{bkg}}. \end{aligned}$$

These equations now have the standard form of product between free parameter and prediction, which makes them suitable for a profile likelihood fit.

Moreover, it is possible to rewrite the equations in order to make it more suitable for an implementation in the HistFactory formalism, where data counts in a certain set of bins are compared with expectations obtained as a sum of predictions for a number of different signal or background processes, obtained from MC simulation, possibly multiplied by normalisation factors (NFs) and modified by systematic effects.

Exploiting Eq. 5.4 to expand the $C_b$ term yields:

$$\begin{aligned} N_1 &= M_a + M_b + N_1^{\text{bkg}} \\ N_2 &= M_c + N_2^{\text{bkg}}, \end{aligned}$$

where

$$
\begin{aligned}
M_a &= 2\mu\epsilon_b N^{t\bar{t}}_{\geq 0}, \\
M_b &= -8\mu\epsilon_b^2 N^{t\bar{t}}_{\geq 0} A, \\
M_c &= 4\mu\epsilon_b^2 N^{t\bar{t}}_{\geq 0} A, \\
A &= N^{t\bar{t}}_{\geq 0} N^{t\bar{t}}_2 / \left(N^{t\bar{t}}_1 + 2N^{t\bar{t}}_2\right)^2 .
\end{aligned}
$$

Further simplifying the equations leads to:

$$
\begin{aligned}
N_1 &= \mu\epsilon_b H_a - \mu\epsilon_b^2 H_b + N_1^{\mathrm{bkg}} \\
N_2 &= \mu\epsilon_b^2 H_c + N_2^{\mathrm{bkg}},
\end{aligned}
\tag{5.5}
$$

where $H_a, H_b, H_c$ are one-bin histograms prepared before they are passed to the fit. Specifically:

$$
\begin{aligned}
H_a &= 2N^{t\bar{t}}_{\geq 0}, \\
H_b &= 8\left(N^{t\bar{t}}_{\geq 0}\right)^2 N^{t\bar{t}}_2 / \left(N^{t\bar{t}}_1 + 2N^{t\bar{t}}_2\right)^2 , \\
H_c &= 4\left(N^{t\bar{t}}_{\geq 0}\right)^2 N^{t\bar{t}}_2 / \left(N^{t\bar{t}}_1 + 2N^{t\bar{t}}_2\right)^2 .
\end{aligned}
\tag{5.6}
$$

Using the histograms presented in Eq. 5.5 provides a convenient way to interface the counting method to the standard profile-likelihood tools.Additionally, systematic uncertainties affect the MC predictions for $N^{t\bar{t}}_{\geq 0}$, $N^{t\bar{t}}_1$ and $N^{t\bar{t}}_2$, therefore are simply propagated to the one-bin histograms $H_{a,b,c}$. To properly deal with the statistical uncertainty on these predictions, due to the limited number of simulated events used to obtain them (referred to as MC statistical uncertainty in the following), three systematic variations for each of the predictions $H_{a,b,c}$ are defined, by shifting $N^{t\bar{t}}_{\geq 0}$, $N^{t\bar{t}}_1$ and $N^{t\bar{t}}_1$ up and down by one standard deviation, obtained as the square root of the sum over the selected event squared weights. Meanwhile, the standard approach is used for the background MC statistical uncertainties.

### 5.2.3 Practical implementation of the individual cross-sections and ratio fits

A total of three fits are used for the extraction of the results. The fit setups are organised as follows:

1. **Individual $t\bar{t}$ and $Z$-boson cross-sections**: in the $e\mu$ channel, the procedure outlined in Section 5.2.2 is employed for the $e\mu$ events. Events from the $ee$ and $\mu\mu$ channels are also used in this fit. The extension of the $t\bar{t}$ cross-section measurement to the $ee$ and $\mu\mu$ channels is performed in order to account for the correlations between the $t\bar{t}$ and the $Z$-boson POIs. Thus, the output of the first fit is:

  - the signal strength for the $t\bar{t}$ production;
  - the signal strength for the $Z$-boson production;
  - the $b$-jet efficiency estimate.

2. **Ratio of $t\bar{t}$ and $Z$-boson cross-sections**: as before, the fit is performed in all the three channels ($e\mu$, $ee$ and $\mu\mu$). The likelihood is modified to add a common NF for both $t\bar{t}$ and $Z$ processes (the same factor is applied to both). This allows to scale the contribution from $t\bar{t}$ and $Z$ events using the same parameter. Furthermore, another NF is attached only to the $t\bar{t}$ prediction. This results in $t\bar{t}$ events being scaled by two NFs, where one of is shared with the $Z$ contribution. This means that the NF that is attached only to $t\bar{t}$ events acts as a relative NF on top of the $Z$ prediction, which is the sought after ratio of the $t\bar{t}$ over $Z$ cross-section. The implementation allows to extract the ratio and its uncertainty directly from the fit, without the need of and error-propagation operation, obtaining as a result:

  - the signal strength for the ratio between cross-sections;
  - the signal strength for the $Z$-boson production;
  - the $b$-jet efficiency estimate.

   Both this fit procedure and the one described in the previous item are equivalent for the estimation of the signal strength for the $Z$-boson production and of the $b$-jet efficiency.

3. **Pure $Z$-boson cross-section**: a third fit is implemented to extract the $Z$-boson cross-section from the $ee$ and $\mu\mu$ channels only. This precautionary measure is taken to decorrelate back the $t\bar{t}$ and $Z$-boson POIs, thus maintaining consistency between the $Z$-boson cross-section presented in this thesis, and other measurements related to different processes[3]. This fit produces the estimate of a single POI: the signal strength for the $Z$-boson production.

The extrapolation of $\sigma_{t\bar{t}}$ is derived from the first fit, $R_{t\bar{t}/Z}$ is obtained from the second fit, and $\sigma^{\text{fid.}}_{Z\to\ell\ell}$ is extracted from the third fit. The $b$-jet efficiency can be taken either from the first or the second setup.

### 5.2.4 Validation of the fit procedure

Validating the outcome of a profile likelihood fit is paramount to ensure the robustness and accuracy of the derived results. A set of diagnostic tools, including pull plots, constraints, correlation matrices, and ranking plots, are employed in this thesis and are presented in the following.

---

[3] For instance, a parallel measurement of the $Z$-boson production can be obtained while studying the ratio between the $W$-boson and the $Z$-boson production cross sections.

### Nuisance parameters pulls and constraints

In profiling the likelihood to obtain estimates for the POIs and the NPs, the concepts of pulls and constraints become significantly pertinent. The "pull" of a nuisance parameter $\theta$ is defined as the normalised difference between the estimated value $\hat{\theta}$ from the fit and its prior expected value $\theta_0$ [233]:

$$\mathrm{pull}(\theta) = \frac{\hat{\theta} - \theta_0}{\sigma_\theta}, \tag{5.7}$$

where $\sigma_\theta$ is the standard deviation of the pre-fit probability distribution of $\theta$. Pulls are instrumental in quantifying how the data influences the NPs away from their prior expectations. The expected interval of the pull is $[-1, +1]$; a pull of zero denotes a good agreement between the data and the prior, while non-zero pulls warrant a deeper investigation into the systematic uncertainties or the model itself.

On the other hand, the so-called post-fit constraints quantify how much the fit is able to tell about the NPs, possibly improving upon their prior knowledge embedded in the prediction model. Indeed, the constraint terms in the likelihood function are meant to incorporate previous or "auxiliary" measurements of the NPs, so that they can be used to define what we call nuisance-parameter 'pre-fit' uncertainties. When the model is compared to the data, i.e. when the fit is performed, the NP best-fit values come with their new uncertainties, in general always equal or smaller than the pre-fit ones. The smaller a post-fit uncertainty on a NP, the stronger the constraining power of the data, so that the ratio of the post-fit over the pre-fit uncertainty, often referred as 'post-fit NP constraint', quantifies how much the data could improve the knowledge on this particular NP, or, in other words, reduce the impact of the associated source of systematic uncertainty.

### Post-fit parameter correlation matrix

As described in Section 5.2.1, the post-fit parameter correlation matrix elucidates the linear relationships between the parameters of interest and the NPs. The elements of the correlation matrix, $\rho_{ij}$ range from -1 to 1, with -1 indicating a perfect negative linear relationship, 1 indicating a perfect positive linear relationship, and 0 indicating no linear correlation.

The interpretation of the correlation matrix offers a reliable way in understanding how uncertainties in the NPs propagate to the uncertainties in the POIs, as well as how pulls and post-fit constraints of different nuisance parameters are correlated. High absolute values of correlation indicate that the uncertainties in the parameters are significantly intertwined, which might necessitate a more cautious interpretation of the fit results or further investigation into the underlying model and systematic uncertainties.

### Nuisance parameter ranking

The so-called “nuisance parameter ranking” (often presented in the form of a plot, hence the common name “ranking plot”) serves as a vital tool for discerning the impact of NPs on the parameters of interest. These plots rank the NPs based on a specified metric, often the impact of each NP on the POIs when varied within their uncertainties.

The impact of each NP, $\Delta\mu$, is computed by comparing the nominal best-fit value of $\mu/\mu_{\text{pred.}}$ with the result of the fit when fixing the considered nuisance parameter to its best-fit value, $(\theta)$, shifted by its pre-fit and post-fit uncertainties $\pm\Delta\theta(\pm\Delta\hat{\theta})$. The ranking plots thus provide a clear, visual representation of which NPs have the most substantial influence on the POIs.

Moreover, ranking plots can expose unexpected behaviours in the fit, such as NPs with unexpectedly large impacts or those whose impacts have changed significantly between different iterations of the analysis. Such insights can be instrumental in diagnosing issues with the fit or the model, and in understanding the interplay between different sources of systematic uncertainty.

## 5.2.5 Comparison with previous measurements

### Cross-sections estimation treatment in ATLAS-CONF-2022-070

For this measurement, the definition of the $Z$-boson production cross-section $\sigma^{m_{\ell\ell}>40}_{Z\to\ell\ell}$ differs with respect to $\sigma^{\text{fid.}}_{Z\to\ell\ell}$ presented at the beginning of the chapter. $\sigma^{m_{\ell\ell}>40}_{Z\to\ell\ell}$ is measured using events with reconstructed $m_{\ell\ell}$ values that satisfy $66 < m_{\ell\ell} < 116$ GeV, and is extrapolated to $m_{\ell\ell} > 40$ GeV with $Z \longrightarrow \ell^+\ell^-$, where $\ell = e$ or $\mu$.

Moreover, only two fits are used; in the first, $\sigma^{m_{\ell\ell}>40}_{Z\to\ell\ell}$, $R_{t\bar{t}/Z}$ and $\epsilon_b$ are implemented as unconstrained parameters and extracted using the $e\mu$, $ee$ and $\mu\mu$ channels. The value for $\sigma_{t\bar{t}}$ is derived from a second fit procedure, using only the $e\mu$ channel.

### Cross-sections estimation treatment in ATLAS-CONF-2023-006

The fit configuration of this analysis matches the one presented in Section 5.2.3, the only difference being that the third fit is not employed. Therefore, $\sigma_{t\bar{t}}$ is taken from the first fit, $R_{t\bar{t}/Z}$ is extracted from the second fit, and both $\epsilon_b$ and $\sigma^{\text{fid.}}_{Z\to\ell\ell}$ can be taken either from the first or the second setup.

# Chapter 6

# Signal and background modelling

In high energy physics, measurements often make use of simulation for the involved physics processes, with simulated events being compared to the experimentally observed data. The predictions of various physics models, including the SM, are typically entrusted to Monte Carlo generators.

The first stage of the simulation is the hard process, in which the constituents of the colliding particles interact at high momentum scale to produce outgoing fundamental objects as the quarks, leptons, and bosons from the SM, or potential new particles from BSM theories. The partons generated by the hard process emit gluons, forming a parton shower; these parton shower constituents then transform into stable, colour-neutral hadrons in a process called hadronisation. Many of the hadrons produced are unstable and decay. In hadron-hadron collisions, the remaining partons of the incoming hadrons further interact, producing underlying events[1]. These simulation steps are schematically shown in Figure 6.1.

After the event generation, the detector response is simulated by the toolkit Geant4 [234] with the full simulation of the ATLAS detector. The simulated samples are processed using the same software framework as the data [185]. All simulated processes that include a top quark have its mass set to $m_\mathrm{t}$ = 172.5 GeV.

The effect of multiple $pp$ interactions in the same bunch crossing (*in-time pile-up*) and neighbouring ones (*out-of-time pile-up*), is modelled by overlaying the original hard-scattering event with simulated inelastic $pp$ events generated by Pythia 8.307 [235], using the NNPDF2.3 LO set of PDFs [236] and parameter values set according to the A3 tune [237] for a particle with high $p_\mathrm{T}$. For the particles with low $p_\mathrm{T}$, the EPOS 2.0.1.4 [238] generator is used with the EPOS LHC tune.

The MC simulated samples are generated with a best estimate of the pile-up distribution of data. However, the distribution of the “actual $\mu$” variable does not agree between data and simulation,

---

[1] An underlying event is a particle production process not associated with the hardest parton-parton process.

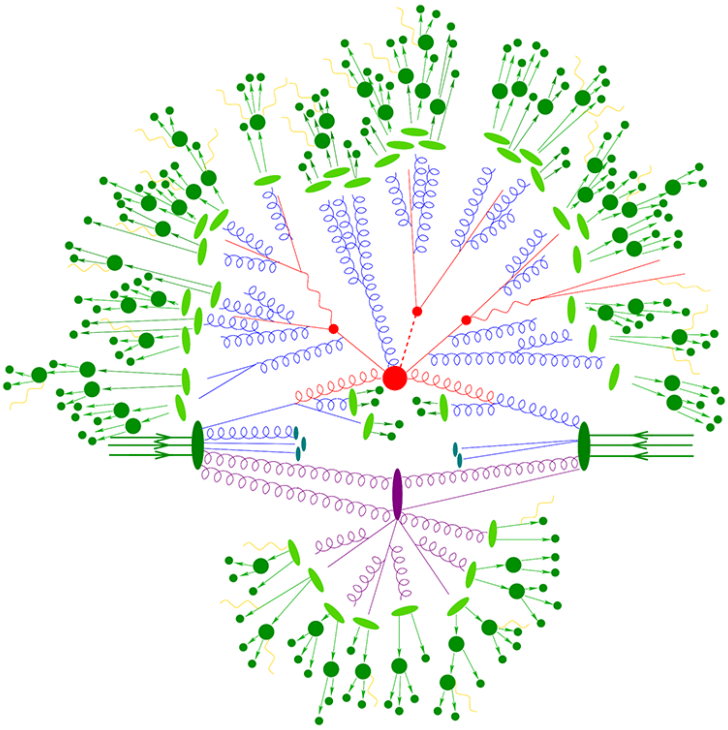

Figure 6.1: Schematic diagram of the event simulation process. The hard process simulation is indicated by red lines, while blue lines represent the parton shower. Green lines and dots depict the creation of hadrons and their subsequent decay. Purple lines correspond to the simulation of the underlying events. Figure taken from [239].

thus a dedicated weight is used to correct the discrepancy. The reweighting uses a default MC pile-up profile, which is used to generate all the MC samples. It applies a weight based on the provided list of data acquisition runs included in the analysis[2], the corresponding file containing the integrated luminosity estimate, and the actual $\mu$ file. This operation leads to the matching between the simulated and observed actual $\mu$ distributions. Figure 6.2 shows the distribution of the actual $\mu$ between data and MC, highlighting, as expected, a reasonable agreement.

---

[2] The concept of “good run list” is further inspected in Section 7.1.

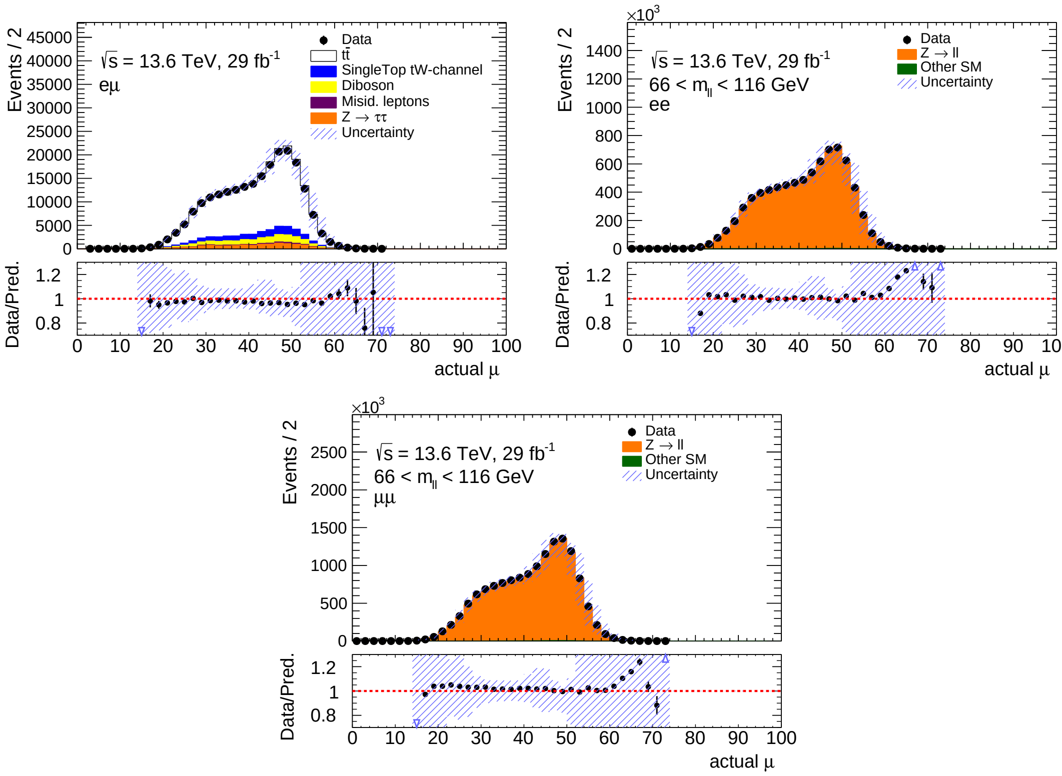

Figure 6.2: Comparison of data and prediction for the actual $\mu$ distribution between data and prediction in the three channels after the pileup reweighting is applied. The bottom panel shows the ratio of data over the prediction.

## 6.1 $t\bar{t}$ sample

The production of $t\bar{t}$ events is modelled using the Powheg Box v2 [240–243] generator at NLO in QCD with the NNPDF3.0nlo [244] PDF set and the $h_{\text{damp}}$ parameter[3] set to $1.5\,m_t$ [245]. The events are interfaced to Pythia 8.307 [246] to model the parton shower, hadronisation, and underlying event, with parameters set according to the A14 tune [247] and using the NNPDF2.3lo set of PDFs [236]. The decays of bottom and charm hadrons are performed by EvtGen 2.1.1 [248]. The $t\bar{t}$ sample is normalised to the cross-section prediction at NNLO in QCD including the resummation of NNLL soft-gluon terms calculated using Top++ 2.0 [49–55]. For proton–proton collisions at a centre-of-mass energy of $\sqrt{s} = 13.6$ TeV, this cross-section corresponds to $\sigma(t\bar{t})_{\text{NNLO+NNLL}} = 924^{+32}_{-40}$ pb using a top-quark mass of $m_t = 172.5$ GeV and the PDF4LHC21 PDF set [69]. The uncertainty includes variations in the renormalisation and factorisation scales, $\alpha_S$ and PDFs. For this calculation, the renormalisation and factorisation scales are set to match

---

[3] The $h_{\text{damp}}$ parameter is a resummation damping factor and one of the parameters that controls the matching of Powheg matrix elements to the parton shower and thus effectively regulates the high-$p_{\text{T}}$ radiation against which the $t\bar{t}$ system recoils.

the top-quark mass for the nominal result. The strong coupling constant is set to 0.118 for the nominal prediction.

## 6.2 $Z$-boson sample

Events from $Z/\gamma^* \to \ell^+\ell^-$ production are simulated with the Sherpa 2.2.12 [249] generator using NLO in QCD matrix elements (ME) for up to two partons, and leading-order (LO) matrix elements for up to four partons calculated with the Comix [250] and OpenLoops [251–253] libraries. They are matched with the Sherpa parton shower [254] using the MEPS@NLO prescription [255–258] using the tune developed by the Sherpa authors. The NNPDF3.0nnlo set of PDFs is used. Decays of $Z/\gamma^* \to e^+e^-$, $Z/\gamma^* \to \mu^+\mu^-$ and $Z/\gamma^* \to \tau^+\tau^-$ are simulated. The sample is generated with a requirement of $m_{\ell\ell} > 10$ GeV. The production is split into samples with $10 < m_{\ell\ell} < 40$ GeV and samples with $m_{\ell\ell} > 40$ GeV. The events are normalised to NNLO in QCD and NLO in EW corrections calculated using the `MATRIX` [259] program using the PDF4LHC21 PDF set. In both the MC generator requirement and in the `MATRIX` calculation, leptons before QED radiation, called Born leptons, are used. This calculation uses $m_{\ell\ell} > 40$ GeV and the same $k$-factor as for the $m_{\ell\ell} > 40$ GeV is also applied to the samples with $10 < m_{\ell\ell} < 40$ GeV for the sake of continuity. For the fiducial phase-space defined with lepton $p_{\mathrm{T}} > 27$ GeV, $|\eta| < 2.5$ and $66 < m_{\ell\ell} < 116$ GeV, the predicted cross-section at NNLO in QCD and NLO in EW is $\sigma(Z)^{\mathrm{fid.}} = 746 \pm 0.7(\mathrm{integration})^{+3}_{-5}(\mathrm{scale}) \pm 21(\mathrm{PDF})$ pb for the $Z$-boson decaying into a single lepton flavour for leptons before QED radiation. More details regarding the theoretical calculation are provided in Appendix A.

## 6.3 Background samples

### 6.3.1 Single top samples

The associated production of single top quarks with $W$ bosons ($tW$) is modelled using the Powheg Box v2 generator at NLO in QCD, employing the five-flavour scheme and the NNPDF3.0nlo set of PDFs. The diagram-removal scheme [260] is used to eliminate interference and overlap with $t\bar{t}$ production. The events are interfaced to Pythia 8.307 using the A14 tune and the NNPDF2.3lo set of PDFs. The inclusive cross-section is corrected to the theory prediction calculated at approximate N$^3$LO in QCD using the PDF4LHC21 PDF set [68]. The cross-section corresponds to $\sigma(tW)_{\mathrm{aN^3LO}} = 87.9^{+2.0}_{-1.9}(\mathrm{scale}) \pm 2.4(\mathrm{PDF})$ pb.

Single-top-quark $t$-channel production is modelled with the Powheg Box v2 [240–243, 261] generator at NLO in QCD using the four-flavour scheme and the corresponding NNPDF3.0nlo set of PDFs. The events are interfaced with Pythia 8.307 using the A14 tune and the NNPDF2.3lo set of PDFs. The inclusive cross-section is corrected to the theory prediction $\sigma_{t\text{-channel}} = 232.2^{+4,3}_{-2.9}$ pb. The cross-section is calculated with the MCFM program [67] at NNLO QCD. The quoted uncertainties include the uncertainties due to the choice of the renormalisation and factorisation scales $\mu_r$, $\mu_f$, the uncertainty in the parton distributions functions (PDFs) and in the value of the strong coupling constant $\alpha_s$.

Single-top-quark $s$-channel production is modelled using the Powheg Box v2 generator at NLO in QCD in the five-flavour scheme with the NNPDF3.0nlo PDF set. The events are interfaced with Pythia 8.307 using the A14 tune and the NNPDF2.3lo PDF set. The inclusive cross-section is corrected to the theory prediction computed at NNLO in QCD, $\sigma_{s\text{-channel}} = 7.246^{+0.059}_{-0.043}$ pb. In this analysis, the contributions from $t$-channel and $s$-channel productions only arise through fake and non-prompt leptons.

### 6.3.2 Diboson samples

Samples of diboson final states ($VV$) are simulated using the Sherpa 2.2.12 generator, which includes off-shell effects and Higgs boson contributions where appropriate. Both fully-leptonic and semileptonic final states, where one boson decays leptonically and the other hadronically, are generated using matrix elements at NLO accuracy in QCD for up to one additional parton and at LO accuracy for up to three additional parton emissions. Since no dedicated NNLO calculation for the cross-section is available at the time of writing, the same $k$-factors used in Run 2 are employed also for the $\sqrt{s}$ = 13.6 TeV normalisation.

### 6.3.3 $t\bar{t}$ +$V$ samples

Samples of associated production of the top-quark pairs with a $Z$-boson, a $W$-boson, or a Higgs boson are simulated using the Sherpa 2.2.12 generator. Events with at least two leptons in the final state are considered. The small contributions are merged into a single process labelled $t\bar{t} + V$. No dedicated $k$-factors are available at the time of writing, so a 50% uncertainty is applied to the cross-section.

### 6.3.4 Mis-identified and non-prompt lepton background

As described in Chapter 4, charged pions can be mis-reconstructed as electrons in the detector; similarly, non-prompt electrons and muons can pass the isolation selection and be misidentified as prompt leptons. Both mis-reconstructed electrons and non-prompt leptons are referred to as "fake leptons".

The majority of events with a fake lepton in the dilepton channel originate from events featuring a real, prompt single lepton. This allows to use the MC predictions to estimate this background.

For each event, the MC truth information is checked to determine if the event that passes the selection contains a fake lepton and based on this information the events are split into real and fake contributions. This is done when processing MC samples with two or more real leptons in the final state and also for processes with only one prompt lepton in the final state such as $W$+jets, simulated with Sherpa 2.2.12, or single lepton $t\bar{t}$ process, simulated with Powheg Box v2 interfaced with Pythia 8.307. The distributions classified as fake contributions represent the fake lepton background. To cover the possible mis-modelling of the MC prediction, a conservative 50-100% uncertainty is added to the prediction of this background. The conservative uncertainty does not significantly impact the measured cross-section uncertainty, owing to the low contribution of the fake lepton background in the dilepton channel[4].

## 6.4 Comparison with previous measurements

### Signal and background modelling in ATLAS-CONF-2022-070

**$Z$-boson sample:** During the early stage of Run 3, a complete estimate of the $Z$-boson fiducial cross-section was not available. Therefore, the predicted cross-section is computed with the requirement $m_{\ell\ell} > 40$GeV:

$$\sigma(Z)^{m_{\ell\ell}>40} = 2182^{+20}_{-25}(\text{scale}) \pm 37(\text{PDF})\text{ pb}$$

**Single-top samples:** The cross-section value for the $tW$ process belongs to a previous N$^3$LO estimate, corresponding to $\sigma(tW)_{\text{NLO+NNLL}} = 87.6^{+2.0}_{-1.9}(\text{scales})^{+2.1}_{-1.5}(\text{PDF})$ pb.

**$t\bar{t}$ +$V$ samples:** No $t\bar{t}$ +$V$ samples are used in this measurement.

### Signal and background modelling in ATLAS-CONF-2023-006

**$Z$-boson sample:** In this measurement, the production cross-section is extrapolated from the complete fiducial phase space, resulting in:

$$\sigma(Z)^{\text{fid.}} = 741 \pm 4(\text{integration})^{+3}_{-4}(\text{scale}) \pm 14(\text{PDF})\text{ pb}$$

The central value used in the main measurement is shifted by about 0.6% from the one quoted above, following the update of one of the PDFs used in the calculation.

**Single-top samples:** The same cross-section value used in ATLAS-CONF-2022-070 is employed.

**$t\bar{t}$ +$V$ samples:** No $t\bar{t}$ +$V$ samples are used in this measurement.

---

[4] The breakdown of the contributions can be seen in Table 7.2

# Chapter 7

# Event selection

The measurement presented in this thesis employs data collected by the ATLAS detector in $pp$ collisions at $\sqrt{s} = 13.6$ TeV, using all available 2022 data with a working muon trigger. This corresponds to an integrated luminosity of approximately 29 $\text{fb}^{-1}$, following the luminosity measurement methods described in Section 3.2.6. Section 7.1 describes the dataset used and the related data taking conditions. Events are gathered in the dilepton channel, obeying to specific criteria, as presented in Section 7.2. A more refined selection is then outlined in Section 7.3, with events categorised according to their flavour.

## 7.1 Dataset

The dataset consists of a number of *ATLAS runs* – data acquisition periods recorded within specific fills of the LHC. Each run contains numerous luminosity blocks (LBs), each of which corresponds to about one minute of data collection. As mentioned previously, not all events recorded by the ATLAS detector are used in the analyses; only events passing certain quality criteria are selected. Data quality criteria require all detector subsystems to be fully operational. The “good” LBs are stored in a *good run list* (GRL), which is available for each data-taking year separately. The GRL utilised in this thesis is valid for analyses employing muon triggers. The pile-up conditions of 2022-2023 data are shown in Figure 7.1.

## 7.2 Pre-selection

This analysis employs single-lepton triggers for electrons or muons, as listed in Table 7.1. The single-object triggers vary in their requirements concerning object identification, isolation, and $p_{\text{T}}$ thresholds. Triggers with lower $p_{\text{T}}$ requirements impose stricter identification and isolation criteria; on the other hand, triggers with higher $p_{\text{T}}$ thresholds require looser (or no) identification

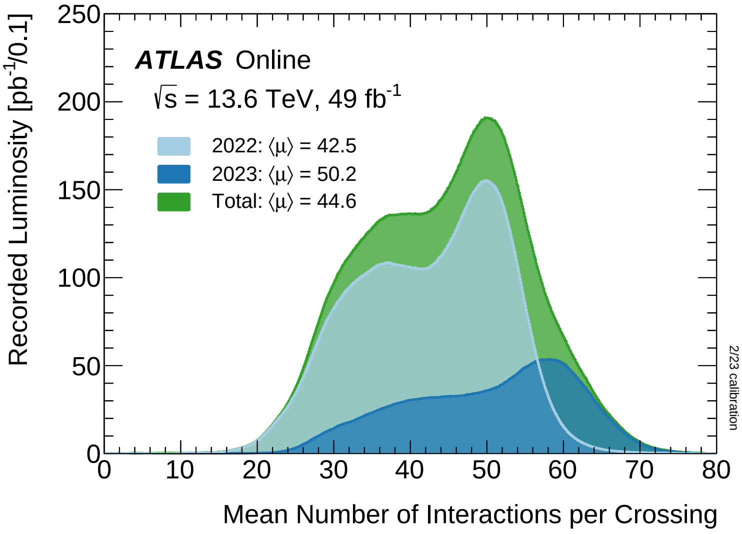

Figure 7.1: Distribution of the mean number of interactions per crossing for the 2022-23 $pp$ collision data at 13.6 TeV centre-of-mass energy. All physics data recorded by ATLAS during stable beams in Run 3 are shown (until 5 June 2023). Figure taken from [149].

and isolation criteria. A logical OR is applied between the triggers, allowing events to be selected via either the electron or the muon trigger. To operate within the plateau regime of the triggers, events must feature leptons with $p_{\mathrm{T}} > 27$ GeV. Additionally, the leptons that fired the trigger are required to be trigger-matched[1]. Only events with a primary vertex [262], reconstructed from at least two tracks with $p_{\mathrm{T}} > 500$ MeV, originating from the beam collision region in the $x$–$y$ plane, are selected.

| Electron triggers | Muon triggers |
|---|---|
| HLT_e26_lhtight_ivarloose_L1EM22VHI | HLT_mu24_ivarmedium_L1MU14FCH |
| HLT_e60_lhmedium_L1EM22VHI | HLT_mu50_L1MU14FCH |
| HLT_e140_lhloose_L1EM22VHI | |

Table 7.1: A list of triggers used in the analysis. Triggers are split between electron and muon flavours. A logical OR is applied between the triggers.

---

[1] Being trigger-matched means that the objects detected in real-time (online objects) and those analysed in detailed offline studies (offline objects) must have a small angular distance between each other.

## 7.3 Dilepton selection

As stated in the previous chapters, three sub-channels are defined based on the flavours of the leptons: $ee$, $e\mu$ and $\mu\mu$. Selected events must contain exactly two leptons (electrons or muons) of opposite electric charge. Events from the $Z$ production contribute to the $e\mu$ selection only via $Z \rightarrow \tau\tau$ with leptonic decays of the tau leptons. In the same-flavour channels, events are required to have the dilepton invariant mass, $m_{\ell\ell}$, in the $Z$-boson window, $66 < m_{\ell\ell} < 116$ GeV, to increase the purity of the events originating from a $Z$-boson. No dilepton mass criteria are imposed on the $e\mu$ channel, but the events are required to have one or two $b$-tagged jets, as described in Section 5. The $e\mu$ channel is solely utilised in the extraction of the $t\bar{t}$ cross-section, owing to its naturally small background contribution. The same-flavour channels serve both for comparison between data and prediction and for determining the ratio of the $t\bar{t}$ and the $Z$-boson cross-sections. Table 7.2 summarises the selection criteria employed in the analysis. Table 7.3 shows the event yields predicted and observed in the different channels; the $e\mu$ inclusive selection is only used in the simulation to calculate $C_b$.

### 7.3.1 $e\mu$ channel

Alongside the inclusive selection, events featuring at least one reconstructed jet with $p_{\mathrm{T}} > 30$ GeV, which is also $b$-tagged using the DL1dv01 tagger at the 77% efficiency working point, are utilised in the extraction of the $t\bar{t}$ cross-section and $b$-jet efficiency. Comparison of data and simulation is presented in Figures 7.2, 7.2, and 7.4. Given that the selection is inclusive in jets, distributions involving the leading jet necessitate that events have at least one reconstructed jet. Figures 7.5, 7.6, and 7.7 show data to MC comparison for events with at least one $b$-tagged jet.

### 7.3.2 Same-flavour channels

The same-flavour channels have a large contribution from the $Z$(+jets) events. An inclusive jet selection targets the $Z$-boson contribution, which is subsequently employed in the measurement of the cross-section ratio[2]. For the $ee$ channel, comparison of data and simulation is presented in Figures 7.8-7.9. Additionally, Figure 7.10 shows the distributions of $p_{\mathrm{T}}$ and $\eta$ for the events with at least one jet with $p_{\mathrm{T}} > 30$ GeV. Figure 7.11 shows the jet and $Z$-boson $p_{\mathrm{T}}$ balance distribution, together with the jet multiplicity. For the $p_{\mathrm{T}}$ balance distribution, only events with exactly one jet with $p_{\mathrm{T}} > 30$ GeV and $\Delta\phi(\text{jet}, \ell\ell) > 2.7$ are selected. Similarly, for the $\mu\mu$ channel, Figures 7.12-7.13 show the basic kinematic distributions. Figure 7.14 shows the leading jet $p_{\mathrm{T}}$ and $\eta$ distributions and Figure 7.15 shows the $p_{\mathrm{T}}$ balance distribution together with the jet multiplicity; in both figures the same selection criteria are applied as in the $ee$ channel.

Several distributions show significant deviations between prediction and data, especially for high $p_{\mathrm{T}}$. However, the vast majority of events populate the low $p_{\mathrm{T}}$ portions of the distributions, where

---

[2] Despite the selection being inclusive, jets are defined to ensure a consistent overlap-removal procedure with the $e\mu$ channel.

agreement between data and prediction is notably better. Moreover, the jet- and $E_{\mathrm{T}}^{\mathrm{miss}}$-related distributions are not relevant for this measurement, as the selection is inclusive in jets and no $E_{\mathrm{T}}^{\mathrm{miss}}$ requirements are imposed. An additional check, documented in Appendix B, has been performed by reweighting the dilepton $p_{\mathrm{T}}$ distribution to assess the impact on the yields.

| **Object** | **Requirements** | |
|---|---|---|
| | $e\mu$ | $ee/\mu\mu$ |
| Trigger | Single-electron OR single-muon | |
| Primary vertex | $\geq 1$ (with $\geq 2$ tracks with $p_{\mathrm{T}} \geq 500$ MeV) | |
| Leptons | == 2 | == 2 |
| Jets | $\geq 1$ | $\geq 0$ |
| $b$-tags (DL1dv01 77%) | $\geq 1$ | $\geq 0$ |
| $m_{\ell\ell}$ cut [GeV ] | - | $66 < m_{\ell\ell} < 116$ |

Table 7.2: Summary of the event selection used in the different channels of the analysis. Dash indicates that the given requirement is not applied.

| **Process** | **Channel** | | | | |
|---|---|---|---|---|---|
| | $e\mu$ inclusive | $e\mu$ 1 $b$ | $e\mu$ 2 $b$ | $ee$ | $\mu\mu$ |
| $t\bar{t}$ | 177 000 ± 5 000 | 87 400 ± 2 600 | 52 700 ± 1 600 | 22 300 ± 1 200 | 33 500 ± 1 900 |
| $Z \to ll$ | 13 100 ± 600 | 270 ± 70 | 14.2 ± 3.0 | 7 7490 000 ± 230 000 | 14 100 000 ± 400 000 |
| Single-top $tW$-channel | 19 000 ± 9 000 | 10 200 ± 700 | 1 720 ± 290 | 2 250 ± 120 | 3 410 ± 200 |
| Diboson | 17 000 ± 8 000 | 230 ± 120 | 5.3 ± 3.0 | 9 000 ± 5 000 | 18 000 ± 9 000 |
| $t\bar{t}V$ | 220 ± 110 | 100 ± 50 | 69 ± 35 | 240 ± 120 | 250 ± 130 |
| Fake/non-prompt leptons | 2 800 ± 1 400 | 1 100 ± 500 | 500 ± 500 | 6 000 ± 6 000 | 6 000 ± 6 000 |
| Total prediction | 229 000 ± 14 000 | 99 200 ± 3 000 | 55 000 ± 1 700 | 7 780 000 ± 230 000 | 14 100 000 ± 400 000 |
| Data | 222 711 | 92 385 | 50 956 | 7 812 978 | 14 242 875 |

Table 7.3: Predicted and observed event yields in the different dilepton channels after event selection. Systematic uncertainties, representing all considered sources, are shown for the predicted yields.

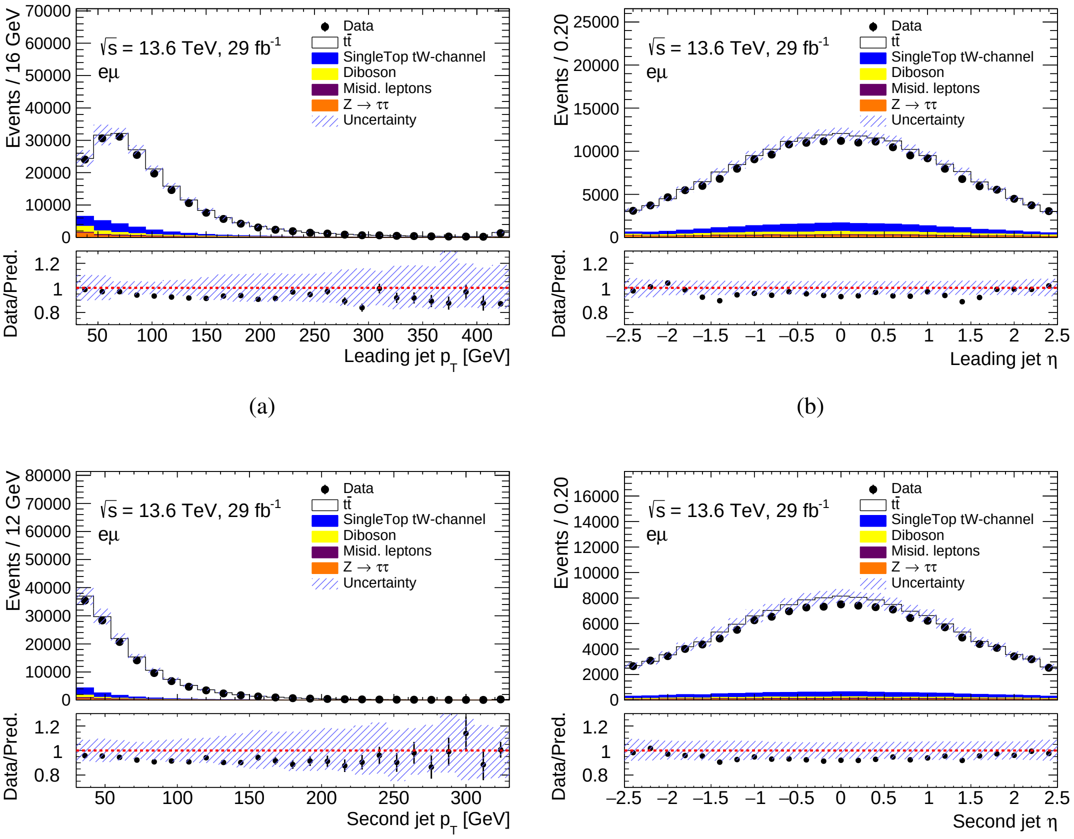

(a) (b)

(c) (d)

Figure 7.2: Comparison of data and prediction in the $e\mu$ channel for the leading jet $p_{\mathrm{T}}$ (a), the leading jet $\eta$ (b), the sub-leading jet $p_{\mathrm{T}}$ (c), and the sub-leading jet $\eta$ (d). The “Misid. leptons” label represents fake and non-prompt leptons. The last bin contains overflow events. The hashed band represents the total systematic uncertainty. The bottom panel shows the ratio of data over the prediction.

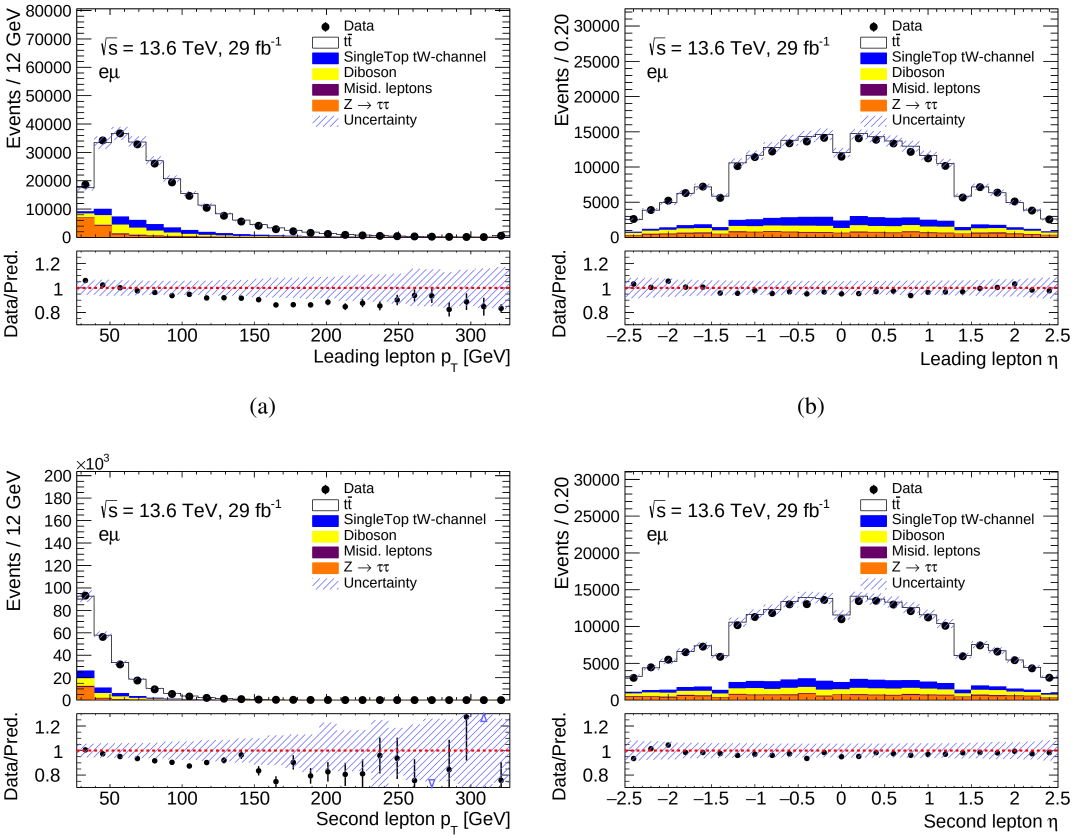

(a) (b)

(c) (d)

Figure 7.3: Comparison of data and prediction in the $e\mu$ channel for the leading lepton $p_{\mathrm{T}}$ (a), the leading lepton $\eta$ (b), the sub-leading lepton $p_{\mathrm{T}}$ (c), and the sub-leading lepton $\eta$ (d). The "Misid. leptons" label represents fake and non-prompt leptons. The last bin contains overflow events. The hashed band represents the total systematic uncertainty. The bottom panel shows the ratio of data over the prediction.

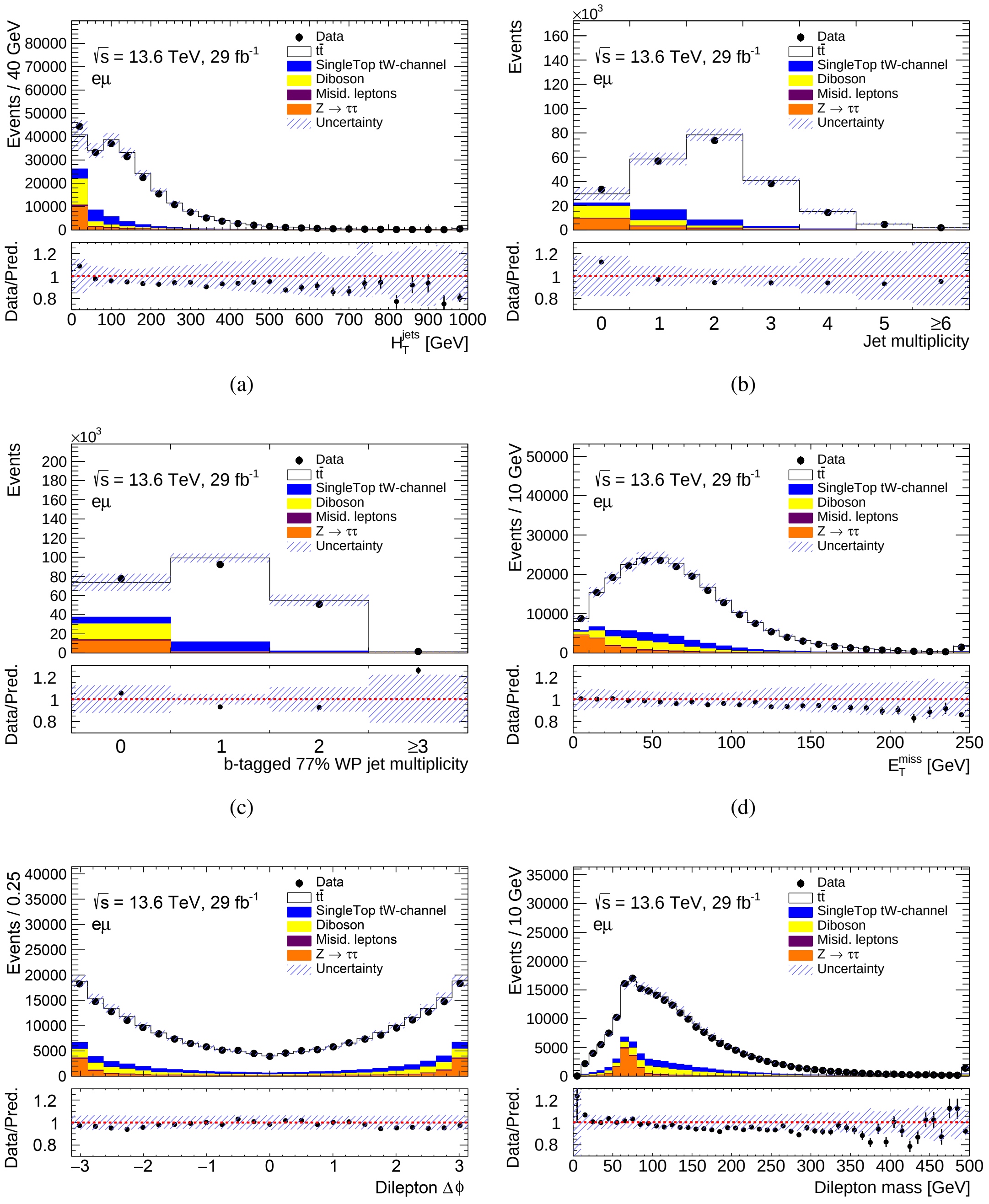

(a) (b) (c) (d) (e) (f)

Figure 7.4: Comparison of data and prediction in the $e\mu$ channel for the scalar sum of transverse momenta $H_{\mathrm{T}}^{\mathrm{jets}}$ (a), the jet multiplicity (b), the $b$-jet multiplicity (c), the missing energy $E_{\mathrm{T}}^{\mathrm{miss}}$ (d), the $\Delta\phi$ between dilepton pairs (e), and the invariant mass of the dilepton pair (f). The “Misid. leptons” label represents fake and non-prompt leptons. The last bin contains overflow events. The hashed band represents the total systematic uncertainty. The bottom panel shows the ratio of data over the prediction.

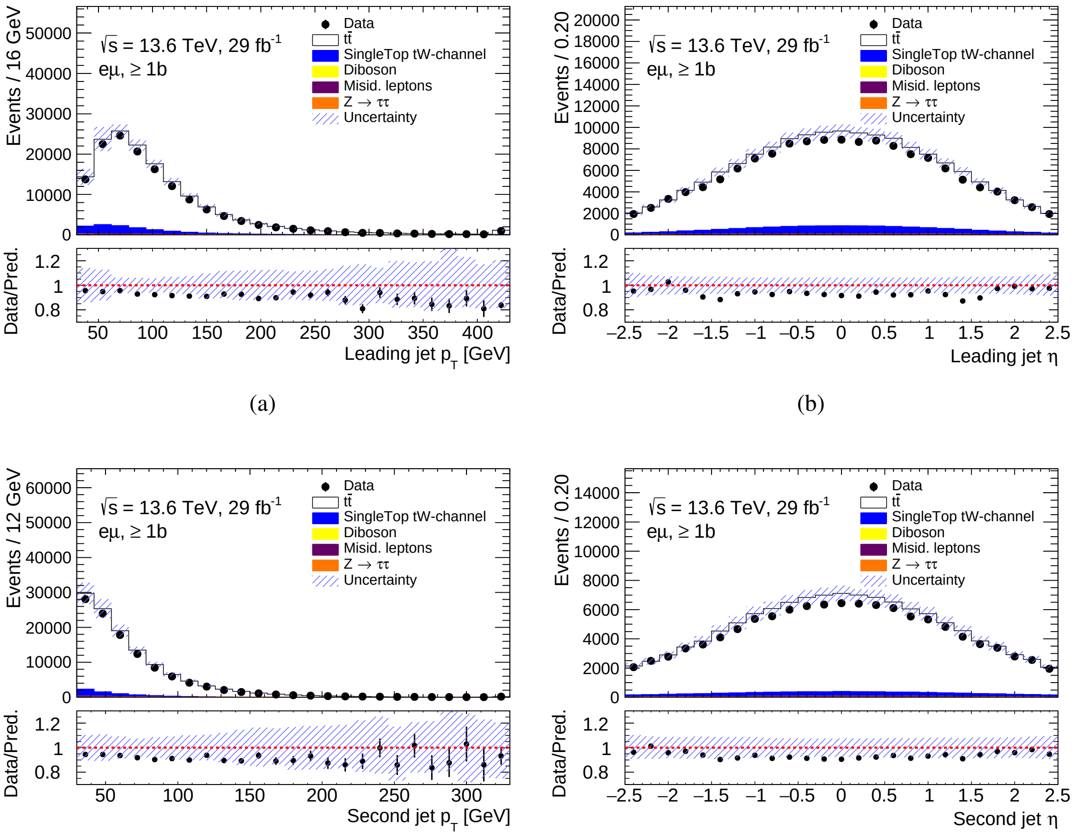

(a) (b)

(c) (d)

Figure 7.5: Comparison of data and prediction in the $e\mu$ channel for the leading jet $p_{\mathrm{T}}$ (a), the leading jet $\eta$ (b), the sub-leading jet $p_{\mathrm{T}}$ (c), and the sub-leading jet $\eta$ (d). Events with at least one $b$-tagged jet are selected. The “Misid. leptons” label represents fake and non-prompt leptons. The last bin contains overflow events. The hashed band represents the total systematic uncertainty. The bottom panel shows the ratio of data over the prediction.

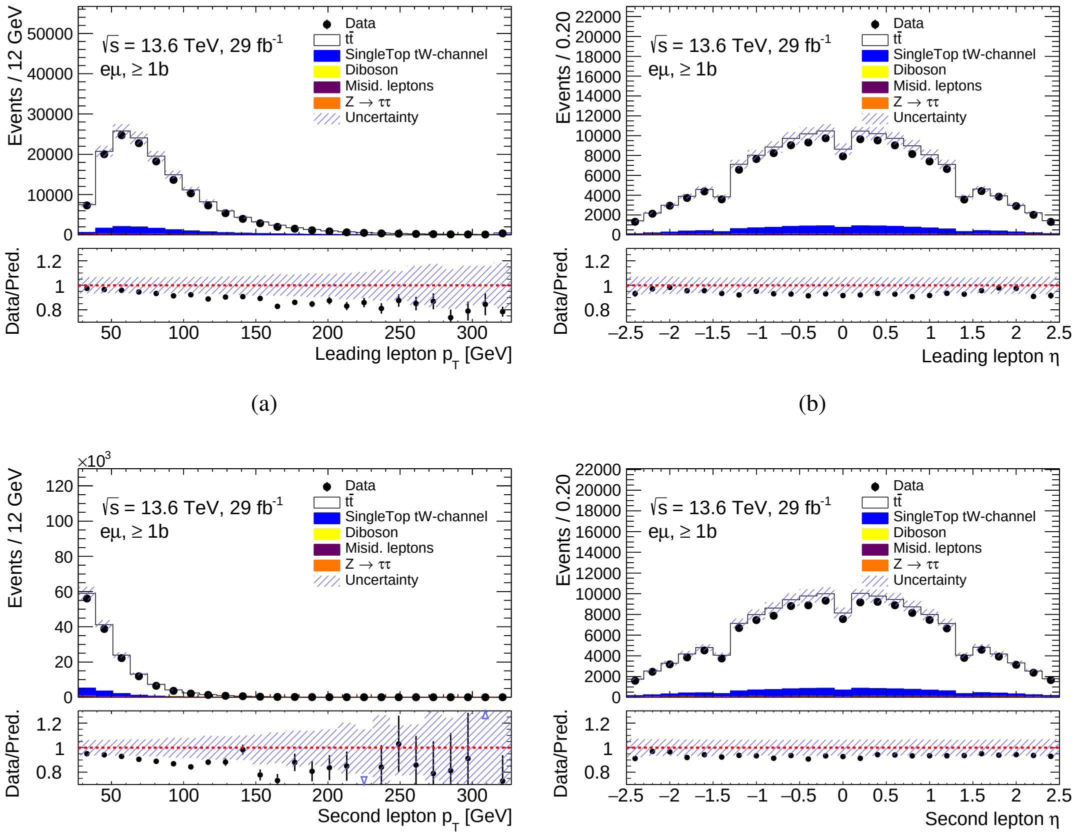

(a) (b)

(c) (d)

Figure 7.6: Comparison of data and prediction in the $e\mu$ channel for the leading lepton $p_{\mathrm{T}}$ (a), the leading lepton $\eta$ (b), the sub-leading lepton $p_{\mathrm{T}}$ (c), and the sub-leading lepton $\eta$ (d). Events with at least one $b$-tagged jet are selected. The “Misid. leptons” label represents fake and non-prompt leptons. The last bin contains overflow events. The hashed band represents the total systematic uncertainty. The bottom panel shows the ratio of data over the prediction.

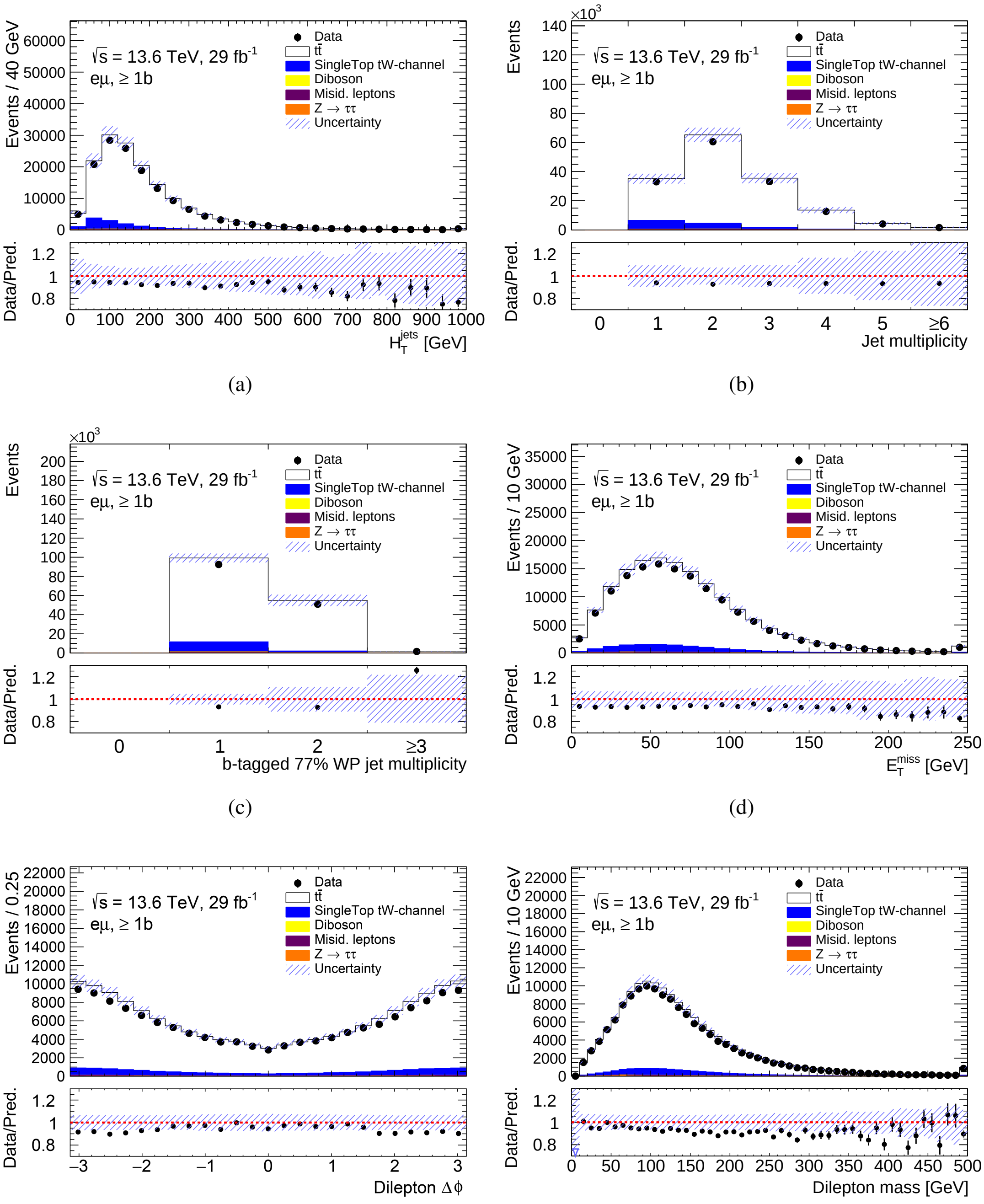

(a) (b)

(c) (d)

(e) (f)

Figure 7.7: Comparison of data and prediction in the $e\mu$ channel for the scalar sum of transverse momenta $H_{\mathrm{T}}^{\mathrm{jets}}$ (a), the jet multiplicity (b), the $b$-jet multiplicity (c), the missing energy $E_{\mathrm{T}}^{\mathrm{miss}}$ (d), the $\Delta\phi$ between dilepton pairs (e), and the invariant mass of the dilepton pair (f). Events with at least one $b$-tagged jet are selected. The “Misid. leptons” label represents fake and non-prompt leptons. The last bin contains overflow events. The hashed band represents the total systematic uncertainty. The bottom panel shows the ratio of data over the prediction.

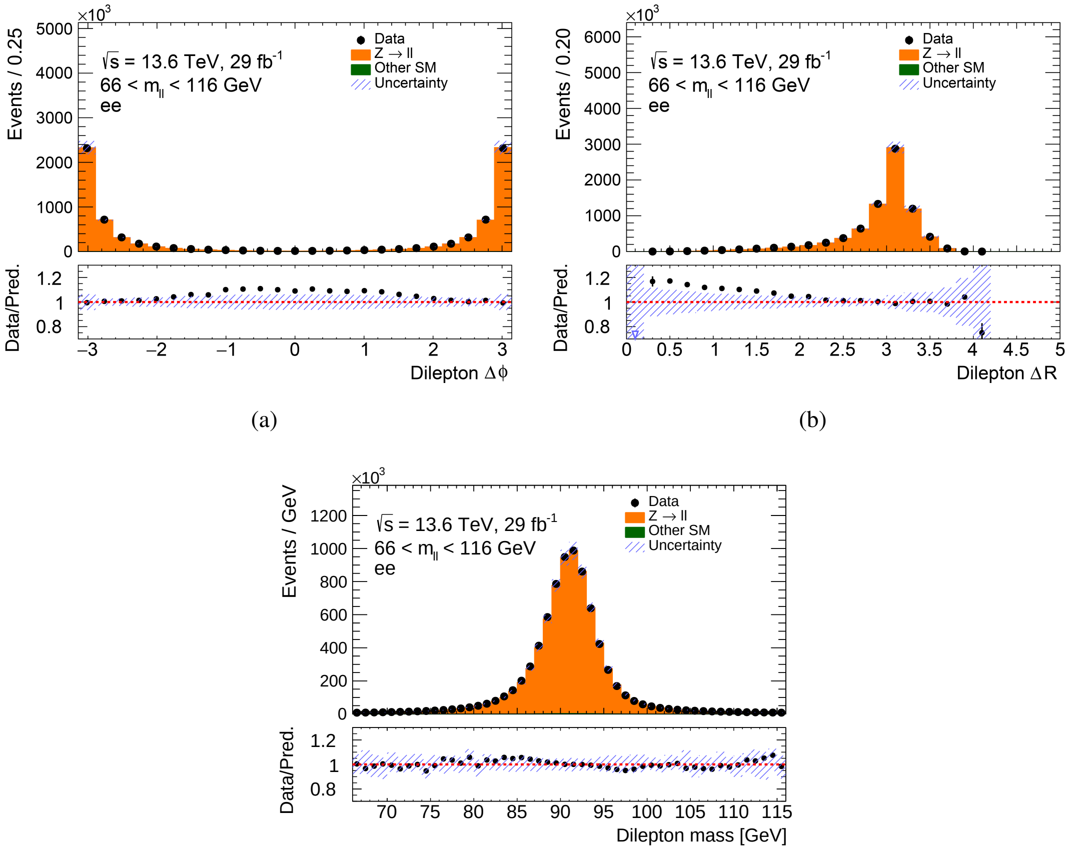

(a)

(b)

(c)

Figure 7.8: Comparison of data and prediction in the *ee* channel for various observables. The last bin contains overflow events. The "Other SM" represents all non-$Z$-boson SM processes merged into a single contribution. The hashed band represents the total systematic uncertainty. The bottom panel shows the ratio of data over the prediction.

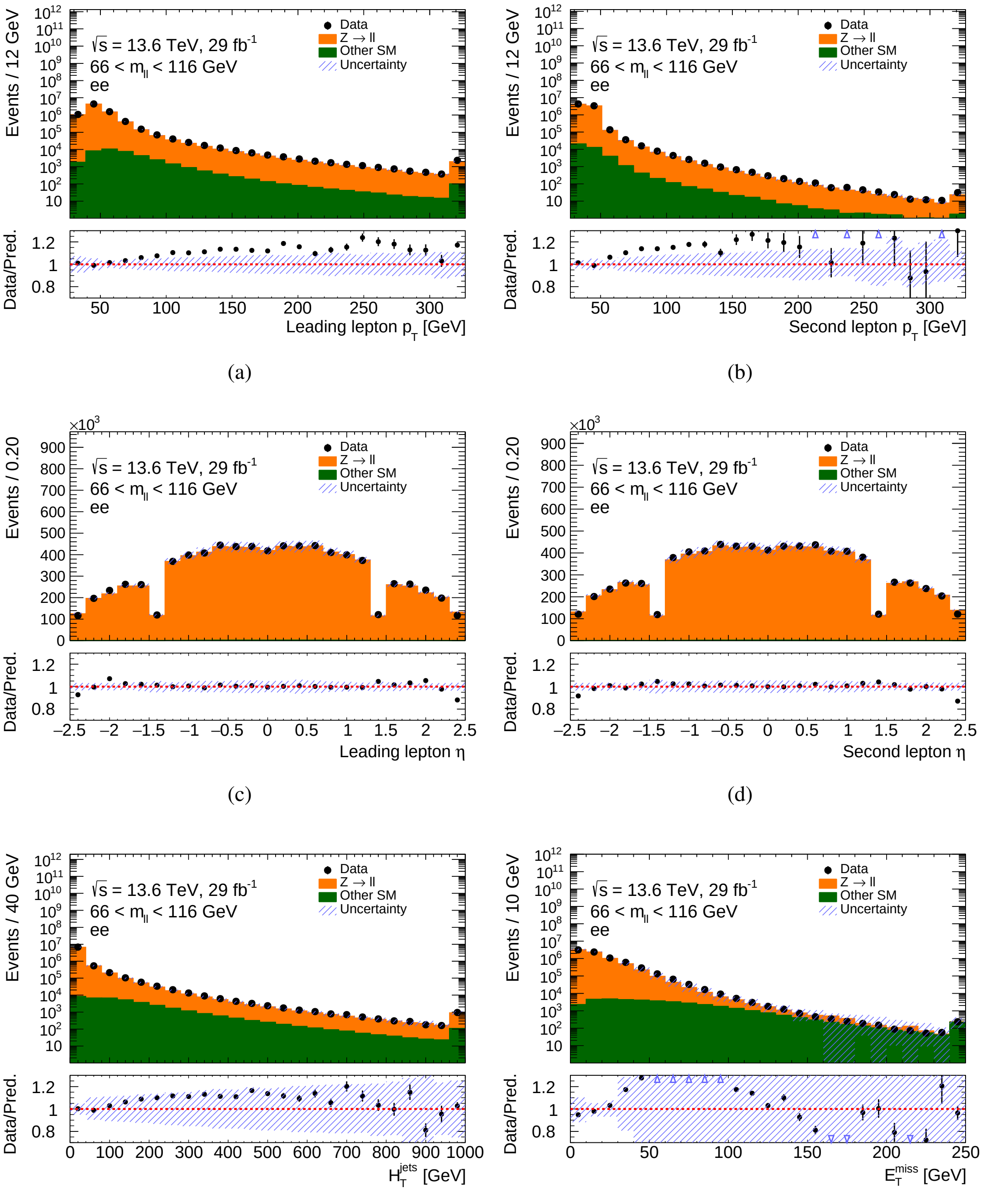

(a) (b) (c) (d) (e) (f)

Figure 7.9: Comparison of data and prediction in the *ee* channel for various observables. The last bin contains overflow events. The “Other SM” represents all non-$Z$-boson SM processes merged into a single contribution. The hashed band represents the total systematic uncertainty. The bottom panel shows the ratio of data over the prediction.

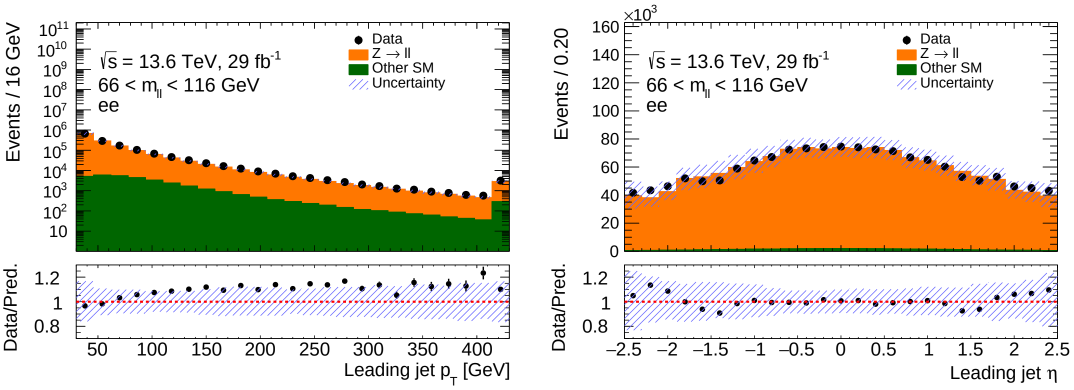

(a) (b)

Figure 7.10: Comparison of data and prediction in the *ee* channel for the leading jet distributions. Only events with at least one jet with $p_{\mathrm{T}}$ > 30 GeV are selected. The last bin contains overflow events. The "Other SM" represents all non-$Z$-boson SM processes merged into a single contribution. The hashed band represents the total systematic uncertainty. The bottom panel shows the ratio of data over the prediction.

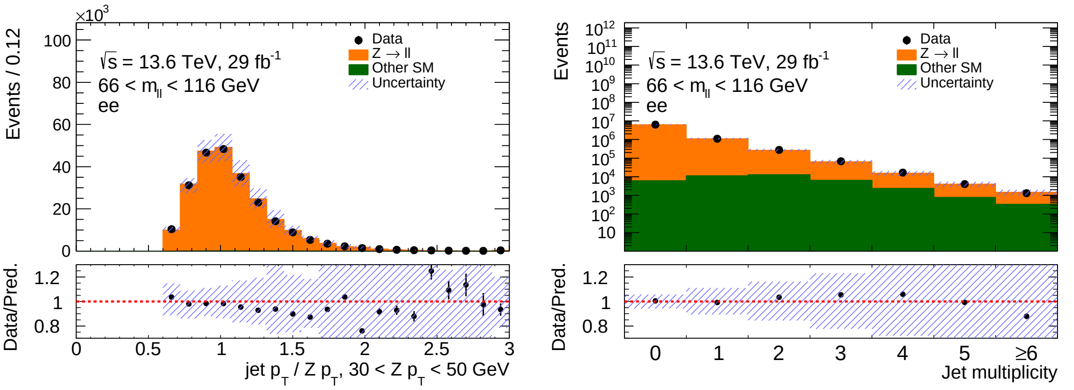

(a) (b)

Figure 7.11: Comparison of data and prediction in the *ee* channel for the jet-$Z$ $p_{\mathrm{T}}$ balance (a), and for the jet multiplicity (b). Event with exactly one jet with $p_{\mathrm{T}}$ > 30 GeV and $\Delta\phi(\text{jet}, \ell\ell)$ > 2.7 are selected. The last bin contains overflow events. The "Other SM" represents all non-$Z$-boson SM processes merged into a single contribution. The hashed band represents the total systematic uncertainty. The bottom panel shows the ratio of data over the prediction.

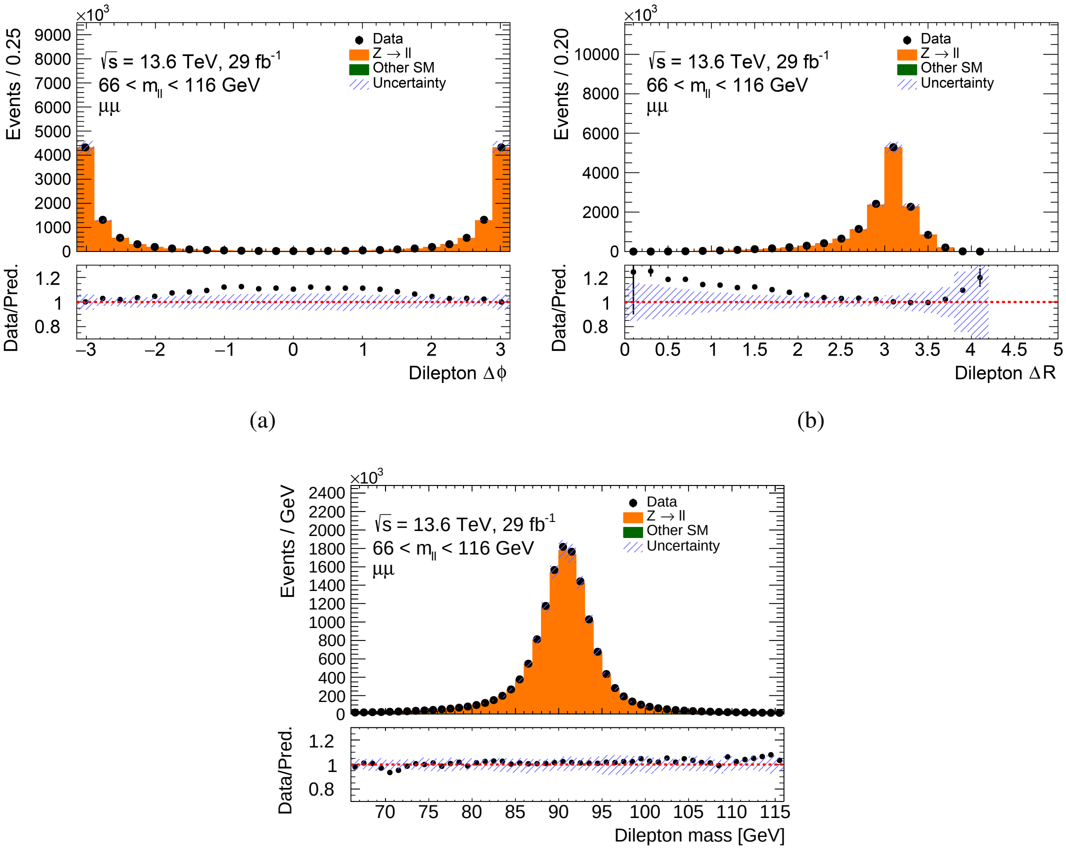

(a) (b)

(c)

Figure 7.12: Comparison of data and prediction in the $\mu\mu$ channel for various observables. The last bin contains overflow events. The “Other SM” represents all non-$Z$-boson SM processes merged into a single contribution. The hashed band represents the total systematic uncertainty. The bottom panel shows the ratio of data over the prediction.

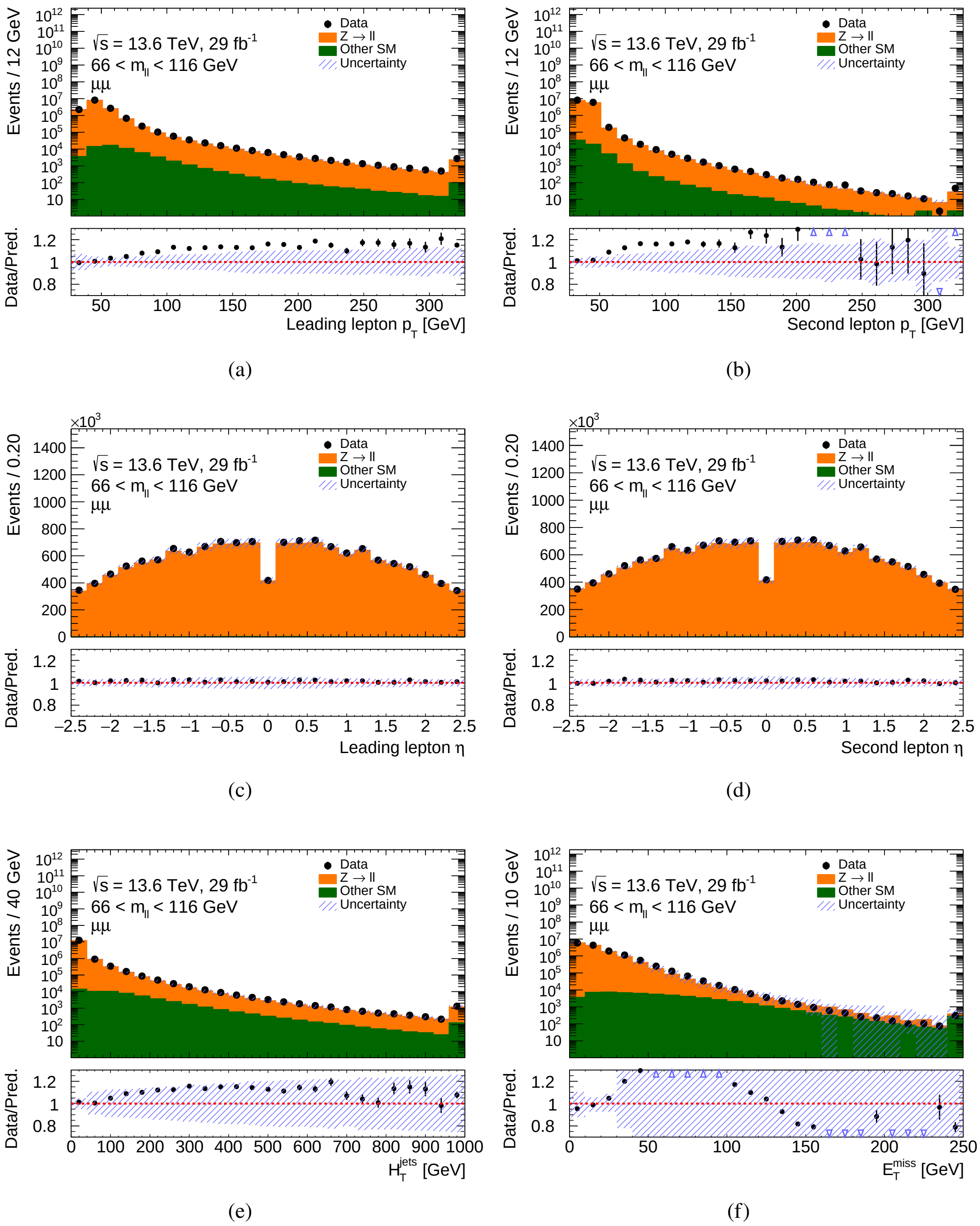

(a) (b)

(c) (d)

(e) (f)

Figure 7.13: Comparison of data and prediction in the $\mu\mu$ channel for various observables. The last bin contains overflow events. The "Other SM" represents all non-$Z$-boson SM processes merged into a single contribution. The hashed band represents the total systematic uncertainty. The bottom panel shows the ratio of data over the prediction.

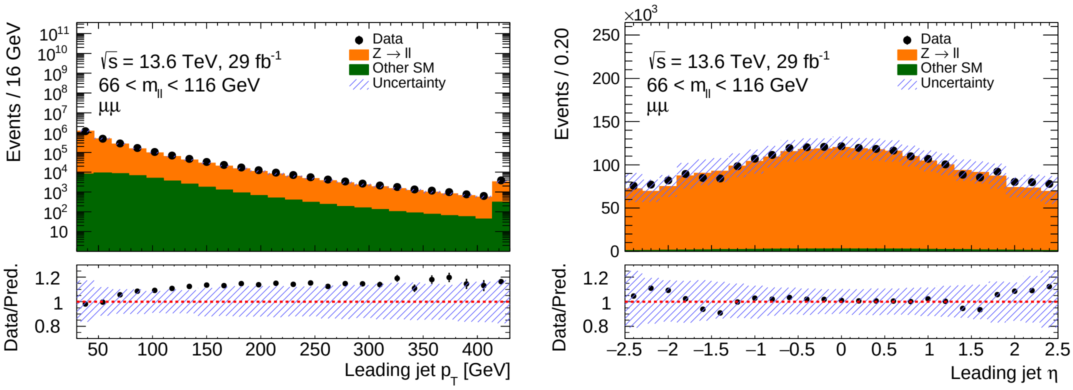

(a)

(b)

Figure 7.14: Comparison of data and prediction in the $\mu\mu$ channel for the leading jet distributions. Only events with at least one jet with $p_{\mathrm{T}} > 30$ GeV are selected. The last bin contains overflow events. The "Other SM" represents all non-$Z$-boson SM processes merged into a single contribution. The hashed band represents the total systematic uncertainty. The bottom panel shows the ratio of data over the prediction.

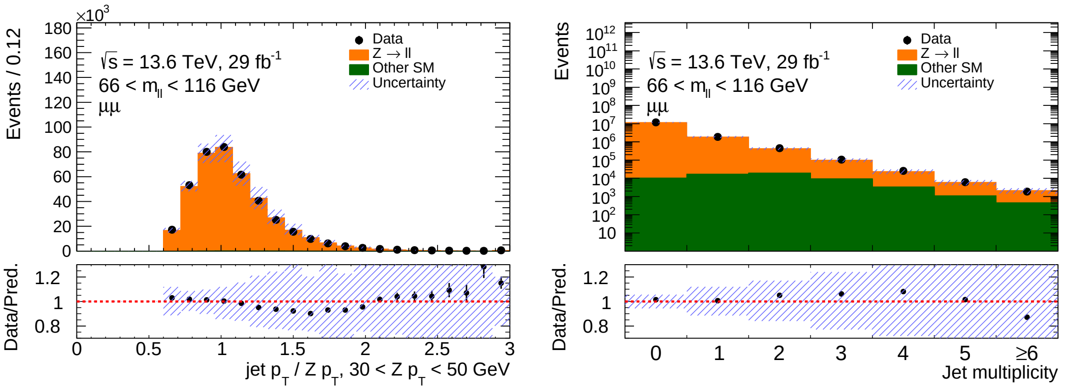

(a)

(b)

Figure 7.15: Comparison of data and prediction in the $\mu\mu$ channel for the jet-$Z$ $p_{\mathrm{T}}$ balance (a), and for the jet multiplicity (b). Event with exactly one jet with $p_{\mathrm{T}} > 30$ GeV and $\Delta\phi(\text{jet}, \ell\ell) > 2.7$ are selected. The last bin contains overflow events. The "Other SM" represents all non-$Z$-boson SM processes merged into a single contribution. The hashed band represents the total systematic uncertainty. The bottom panel shows the ratio of data over the prediction.

## 7.4 Comparison with previous measurements

### Event selection in ATLAS-CONF-2022-070

Due to the early stage of the analysis, a sizeable difference is observed between the efficiency for electron triggers in the forward region. Thus, events with electrons $|\eta| < 2.37$ are excluded in this analysis.

# Chapter 8

# Prediction for the $t\bar{t}$ over $Z$ production cross-section

This chapter describes both the theoretical prediction and the associated uncertainty for the ratio of $t\bar{t}$ over $Z$-boson production. As outlined in Chapter 6, the prediction for the $t\bar{t}$ inclusive cross-section is estimated through the Top++ 2.0 program for different masses of the top quark and different PDF sets. The calculation precision is NNLO in QCD with NNLL terms. The $Z$-boson prediction is calculated using the MATRIX program, as documented in Appendix A. Its precision is at NNLO in QCD and NLO in EW coupling. To calculate the $Z$-boson production cross-section, the fiducial phase-space is defined as follows: lepton $p_{\mathrm{T}} > 27$ GeV, lepton $|\eta| < 2.5$ and $66 < m_{\ell\ell} < 116$ GeV.

In calculating the ratio, uncertainties arising from scale variation are assumed to be uncorrelated between the processes; meanwhile, uncertainties from PDF variations are assumed fully correlated. The scale uncertainty is assessed through restricted scale variations, wherein $\mu_{\mathrm{R}}$ and $\mu_{\mathrm{F}}$ are independently varied by a factor of two, subject to the constraint that their values never diverge by more than this factor. Table 8.1 displays the predicted values for the ratio of $t\bar{t}$ to $Z$-boson fiducial production cross-sections, considering different PDF sets and, in the case of the PDF4LHC21, varying top-quark masses as well.

| PDF set | Top-quark mass [GeV] | $R_{t\bar{t}/Z}$ | Stat. | Scale unc. | PDF+$\alpha_S$ unc. | Total unc. |
|---|---|---|---|---|---|---|
| PDF4LHC21 | 171.5 | 1.2720 | ±0.0013 | $^{+0.0321}_{-0.0463}$ | ±0.0566 | $^{+0.0651}_{-0.0731}$ |
| PDF4LHC21 | 172.5 | 1.2379 | ±0.0012 | $^{+0.0312}_{-0.0450}$ | ±0.0551 | $^{+0.0634}_{-0.0712}$ |
| PDF4LHC21 | 173.5 | 1.2048 | ±0.0012 | $^{+0.0304}_{-0.0438}$ | ±0.0537 | $^{+0.0617}_{-0.0693}$ |
| CT18 | 172.5 | 1.2661 | ±0.0013 | $^{+0.0317}_{-0.0462}$ | $^{+0.1031}_{-0.0913}$ | $^{+0.1078}_{-0.1024}$ |
| CT18A | 172.5 | 1.2237 | ±0.0012 | $^{+0.0306}_{-0.0447}$ | $^{+0.0720}_{-0.0645}$ | $^{+0.0783}_{-0.0785}$ |
| MSHT20 | 172.5 | 1.2340 | ±0.0012 | $^{+0.0315}_{-0.0451}$ | $^{+0.0539}_{-0.0351}$ | $^{+0.0624}_{-0.0571}$ |
| NNPDF4.0 | 172.5 | 1.1748 | ±0.0012 | $^{+0.0294}_{-0.0426}$ | $^{+0.0209}_{-0.0256}$ | $^{+0.0361}_{-0.0498}$ |
| ATLASpdf21 | 172.5 | 1.2440 | ±0.0012 | $^{+0.0314}_{-0.0453}$ | $^{+0.0713}_{-0.0619}$ | $^{+0.0779}_{-0.0767}$ |
| ABMP16 | 172.5 | 1.1269 | ±0.0011 | $^{+0.0284}_{-0.0413}$ | ±0.0378 | $^{+0.0473}_{-0.0560}$ |

Table 8.1: Prediction and uncertainties on the ratio of $t\bar{t}$ and $Z$-boson production cross-section at centre-of-mass energy of 13.6 TeV. For the $Z$-boson prediction, a fiducial phase-space defined by: lepton $p_T > 27$ GeV, lepton $|\eta| < 2.5$ and $66 < m_{\ell\ell} < 116$ GeV is considered. The prediction for the $t\bar{t}$ inclusive cross-section is estimated using the Top++ 2.0 program. The calculation precision is NNLO in QCD with NNLL terms. The $Z$-boson prediction is calculated using the MATRIX program. Its precision is NNLO in QCD and NLO in EW coupling. Predictions for different PDF sets, and in the case of the PDF4LHC21 set also for different top-quark masses, are provided.

## 8.1 Comparison with previous measurements

### Ratio prediction estimation in ATLAS-CONF-2022-070

During the calculation of the $Z$-boson production cross-section, a requirement of $m_{\ell\ell} > 40$ GeV or $m_{\ell\ell} > 60$ GeV or a fully fiducial prediction with lepton $p_T > 27$ GeV, lepton $|\eta| < 2.5$ and $66 < m_{\ell\ell} < 116$ GeV is imposed.

The acceptances for dileptonic, same-flavour $Z$ events, either with dressed or bare leptons, in the context of the fully fiducial selection are:

$$\mathrm{acc}_{\text{nom, } e^+e^- \text{ dressed}} = 0.105 \pm 0.003 \tag{8.1}$$

$$\mathrm{acc}_{\text{nom, } e^+e^- \text{ bare}} = 0.099 \pm 0.003 \tag{8.2}$$

$$\mathrm{acc}_{\text{nom, } \mu^+\mu^- \text{ dressed}} = 0.109 \pm 0.003 \tag{8.3}$$

$$\mathrm{acc}_{\text{nom, } \mu^+\mu^- \text{ bare}} = 0.107 \pm 0.003. \tag{8.4}$$

Further details are provided in Appendix H.

In the calculation of the ratio, the uncertainty from the scale variation are assumed to be uncorrelated between the processes, whereas uncertainties from PDF variations, obtained from PDF4LHC21 eigenvector decomposition, are fully correlated. The scale uncertainty is evaluated as described in the previous section. Table 8.2 shows the predicted values for the ratio of $t\bar{t}$ over $Z$-boson production cross-section, utilising the PDF4LHC21 prediction.

| Top-quark mass [GeV] | Fiducial selection for $Z$ | $R_{t\bar{t}/Z}$ | Scale unc. | PDF unc. | Total unc. |
|---|---|---|---|---|---|
| 171.5 | $m_{\ell\ell} > 40$ GeV | 0.4349 | ±0.0117 | ±0.0106 | ±0.0158 |
| 172.5 | $m_{\ell\ell} > 40$ GeV | 0.4232 | ±0.0114 | ±0.0103 | ±0.0154 |
| 173.5 | $m_{\ell\ell} > 40$ GeV | 0.4120 | ±0.0111 | ±0.0101 | ±0.0150 |
| 172.5 | $m_{\ell\ell} > 60$ GeV | 0.4564 | ±0.0123 | ±0.0077 | ±0.0145 |

Table 8.2: Prediction and uncertainties on the ratio of $t\bar{t}$ and $Z$-boson production cross-section at centre-of-mass energy of 13.6 TeV. Predictions for different fiducial phase-space for the $Z$-boson production are presented and for the different masses of the top quark. The prediction for the $t\bar{t}$ inclusive cross-section is estimated using the Top++ 2.0 program using the top-quark mass of $m_t = 172.5$GeV and using the PDF4LHC21 PDF set. The calculation precision is NNLO in QCD with NNLL terms. The $Z$-boson prediction is calculated using the MATRIX program with PDF4LHC21 PDF set. Its precision is NNLO in QCD and NLO in EW coupling.

## Ratio prediction estimation in ATLAS-CONF-2023-006

In this measurement, an initial estimate of the ratio prediction of provided using different PDFs sets, as listed above. Similarly to the primary measurement, Table 8.3 shows the predicted values for the ratio of $t\bar{t}$ over $Z$-boson fiducial production cross-section. In this calculation, a different value for the $Z$-boson fiducial prediction is employed with respect to the main measurement, as described in Section 6.4. Morevoer, at the time of the writing of the table, the individual components of the total uncertainty were not available for all the PDF sets considered.

| PDF set | Top-quark mass [GeV] | $R_{t\bar{t}/Z}$ | Stat. | Scale unc. | PDF unc. | Total unc. |
|---|---|---|---|---|---|---|
| PDF4LHC21 | 171.5 | 1.2796 | ±0.0077 | $^{+0.0323}_{-0.0466}$ | ±0.0782 | $^{+0.0849}_{-0.0913}$ |
| PDF4LHC21 | 172.5 | 1.2453 | ±0.0075 | $^{+0.0314}_{-0.0453}$ | ±0.0761 | $^{+0.0827}_{-0.0889}$ |
| PDF4LHC21 | 173.5 | 1.2121 | ±0.0073 | $^{+0.0306}_{-0.0441}$ | ±0.0741 | $^{+0.0805}_{-0.0866}$ |
| CT18 | 172.5 | 1.2768 | — | — | — | $^{+0.0649}_{-0.0804}$ |
| CT18A | 172.5 | 1.2529 | — | — | — | $^{+0.0565}_{-0.0792}$ |
| MSHT20 | 172.5 | 1.2375 | — | — | — | $^{+0.0601}_{-0.0578}$ |
| NNPDF4.0 | 172.5 | 1.218 | ±0.0061 | $^{+0.0305}_{-0.0442}$ | ±0.0143 | $^{+0.0342}_{-0.0468}$ |
| ATLASpdf21 | 172.5 | 1.252 | — | — | — | $^{+0.0624}_{-0.0745}$ |
| ABMP16 | 172.5 | 1.1342 | ±0.0045 | $^{+0.0286}_{-0.0416}$ | ±0.0380 | $^{+0.0478}_{-0.0565}$ |

Table 8.3: Prediction and uncertainties on the ratio of $t\bar{t}$ and $Z$-boson production cross-section at centre-of-mass energy of 13.6 TeV. For the $Z$-boson prediction, a fiducial phase-space defined by: lepton $p_{\mathrm{T}} > 27$ GeV, lepton $|\eta| < 2.5$ and $66 < m_{\ell\ell} < 116$ GeV is considered. The prediction for the $t\bar{t}$ inclusive cross-section is estimated using the TOP++ 2.0 program. The calculation precision is NNLO in QCD with NNLL terms. The $Z$-boson prediction is calculated using the MATRIX program. Its precision is NNLO in QCD and NLO in EW coupling. Predictions for different PDF sets, and in the case of the PDF4LHC21 set also for different top-quark masses, are provided.

# Chapter 9

# Systematic uncertainties

As previously presented in Chapter 5.2.1, systematic uncertainties are included as NPs in the likelihood. Additional histograms are produced, corresponding to $\pm 1\sigma$ variations of each NP, calculated with respect to the nominal distribution. Each NP affects the nominal distribution by altering either its shape, its normalisation, or both. As mentioned in Chapter 5, in this thesis the fitted distributions consist of single bins, which means that the shape effects of NPs are implicitly not considered. All the systematic effects are symmetrised with respect to the nominal histogram by considering half the difference of the $\pm 1\sigma$ variations. In certain scenarios, the systematic variation leads to a unidirectional $+(-)1\sigma$ effect; this one-sided impact is mirrored against the nominal histogram to obtain the opposite variation as well.

Systematic uncertainties are categorised into detector-related or instrumental uncertainties, described in Section 9.1, and modelling-related uncertainties, presented in Section 9.2. For the modelling uncertainties affecting the $Z$-boson yields, the impact of the extrapolation from the generated phase space to the fiducial phase-space is subtracted from the absolute impact on the detector level yields in the $ee$ and $\mu\mu$ channels. This subtraction is performed for each modelling NP individually. More details about the impact of each NP are provided in Appendix C. The background normalisation uncertainties are summarised in Table 9.1, whereas Table 9.2 lists all the systematic uncertainties considered in the analysis.

## 9.1 Detector uncertainties

The detector uncertainties, or experimental uncertainties, pertain to the modelling of the physics objects, as presented in Chapter 4, including integrated luminosity and pile-up.

### 9.1.1 Electron and muon uncertainties

Uncertainties affecting charged lepton detection are subdivided into two main categories: the first encompasses lepton momentum resolution and scales, while the second includes uncertainties originating from trigger, reconstruction, isolation and identification efficiencies. For the electron energy corrections, uncertainties obtained from the Run 2 calibrations using $Z \rightarrow ee$ events, following the prescription of Ref. [164], are implemented. These uncertainties are increased to account adequately for the differences in reconstruction between Run 2 and Run 3 of the LHC, as deduced from simulations. The uncertainty in the muon momentum correction is estimated by separately varying the ID and MS components as estimated from $Z \rightarrow \mu\mu$ events, according to what is done in Ref. [194]. For both the energy and momentum correction uncertainties, the so-called *breakdown* model is used, which furnishes multiple NPs for each component – specifically, 73 for electrons and 8 for muons – while preserving the input correlations.

Regarding electron efficiencies, different strategies are used for identification, reconstruction, isolation and for trigger SFs, as described in Section 4.1. The identification SF uncertainties are implemented following the *simplified* model, consisting of 34 NPs; additional uncertainties are computed comparing simulation between Run 2 and Run 3. It was checked that the SFs in Run 3 are within the estimated uncertainties in Run 2. Identification SF for electrons with $E_{\mathrm{T}} < 15$ GeV are taken equal to 1 with conservative uncertainties.

Reconstruction and isolation SFs are deemed to be equal to 1, with conservative uncertainties assessed as the absolute value of the deviation from 1 to the corresponding SF value estimated during Run 2. The *total* model, meaning that each component is treated as a single NP in the fit, is used for electron reconstruction and isolation SF uncertainties. Uncertainties on the electron trigger SFs cover the differences between efficiencies seen in data and in simulation. These are provided as a function of electron $p_{\mathrm{T}}$ and $\eta$.

Muon SFs for identification, isolation and TTVA have been measured using the tag-and-probe method for muons with $p_{\mathrm{T}} > 10$ GeV in Run 3 data, with the related uncertainties represented respectively by 20, 9 and 7 NPs. These measurements are performed using $Z \rightarrow \mu\mu$ events and the uncertainties on these SFs have been calculated using the methods described in [195]. Similarly to electrons, a model preserving the correlations is used for the SF uncertainties. Since a dedicated MC-to-MC correction for the isolation is applied for the samples simulated with the SHERPA generator, the uncertainty covering the difference between the isolation efficiencies is excluded from the set of uncertainties.

### 9.1.2 Jet uncertainties

The JES and its uncertainty are computed as described in Section 4.3, where events featuring a vector boson and additional jets are used for the calibration of jets in the central region. Moreover, dijet events are exploited to calibrate forward jets against those in the central region of the detector, whereas multi-jet events are used to calibrate high-$p_{\mathrm{T}}$ jets. The measurements are combined and their uncertainty components decorrelated to obtain a set of eigenvectors depending on the jet $p_{\mathrm{T}}$

and $\eta$. These are split into different categories, including 1 NP related to the $b$-jet energy scale, 16 NPs for the in-situ calibration, 3 NPs dedicated to the $\eta$ intercalibration, 2 NPs for the flavour composition and response, 4 NPs arising from the uncertainty on the pile-up components, 1 NP originating from the uncertainty on the *punch-through*[1] effect, and 1 NP describing high-$p_{\mathrm{T}}$ jets. Additionally, dedicated uncertainties covering the difference between Run 2 and Run 3 based on the MC simulation, and preliminary calibrations are applied, resulting in 3 additional NPs, for a total of 31.

For the NNJvt SFs, no calibration is available at the time of writing; thus, a conservative 10% uncertainty per bin is applied. This uncertainty, however, is applied only for the backgrounds in the $e\mu$ channel as the $t\bar{t}$ uncertainty should be fully absorbed by the $\epsilon_b$ parameter. The uncertainty on the backgrounds is estimated by considering 10% uncertainty per $b$-tagged jet, as only $b$-tagged jets are relevant in this analysis.

JER uncertainties are included in the analysis as 16 NPs, coming from Run 2 based in-situ measurements, as well as early calibrations and Run 2 against Run 3 MC comparisons.

### 9.1.3 Flavour-tagging uncertainties

For the efficiency of tagging a true $b$-jet, the uncertainties from the calibration are derived using the Run 3 $t\bar{t}$ dilepton data. This uncertainty is a function of jet $p_{\mathrm{T}}$. More details about the uncertainty on the SFs are provided in Appendix I. A conservative uncertainty is considered for the efficiency of mis-tagging. Uncertainties corresponding to 20% and 40% are applied respectively on mis-tag rates of $c$- and light-flavour jets. These uncertainties are inclusive in jet $p_{\mathrm{T}}$ and $\eta$. A total of 13 NPs are considered in the analysis, split between 9, 2, and 2 NPs respectively for the $b$-, $c$-, and light-jet-tagging.

### 9.1.4 Luminosity and pile-up reweighting

The uncertainty in the integrated luminosity for data recorded in 2022 is 2.2% [175], following the methodology discussed in Ref. [263], using the LUCID-2 detector [264] for the primary luminosity measurements, complemented by measurements using the inner detector and calorimeters. The uncertainty primarily arises from two factors: the first involves effects from horizontal-vertical correlations—known as non-factorisation—in the bunch-density distributions; these effects are observed during beam-separation scans used to determine the absolute luminosity scale. The second factor contributing to the uncertainty involves the transfer from conditions in which absolute luminosity calibration data are collected, to those relevant for routine physics data-taking. Various beam-, calibration-method-, consistency-, reproducibility- and stability-related effects provide smaller contributions to the overall uncertainty. The uncertainty in the pile-up modelling is estimated by varying the average number of interactions per bunch-crossing by 4% in the simulation.

---

[1] The punch-through, or particle leakage, is the act of a shower particle to exit the calorimeter and enter the ATLAS muon spectrometer.

## 9.2 Signal and background modelling uncertainties

### 9.2.1 Modelling of the $t\bar{t}$ signal

The uncertainties on the $t\bar{t}$ sample are divided into various categories. The impact of the choice of the parton shower and hadronisation model is evaluated by comparing the nominal $t\bar{t}$ sample with another event sample produced with the Powheg Box v2 [240–243] generator using the NNPDF3.0nlo [244] parton distribution function. Events in this sample were interfaced to Herwig 7.2.3 [265, 266], using the Herwig 7.2 default set of tuned parameters [266, 267] and the MMHT2014lo PDF set [268].

Uncertainties related to the missing higher orders in the hard scattering calculation are estimated considering independent variations of the renormalisation and factorisation scales in the ME by factors of 0.5 and 2, but normalising the signal to the nominal cross-section.

A variation of the parameter *Var3c* of the A14 tune [269] is considered independently. This corresponds to a variation of the $\alpha_S$ coupling in the initial-state radiation (ISR) of the parton shower. An uncertainty due to the final-state radiation modelling is considered by independent variations of the renormalisation scale for emissions from the parton shower by a factor of two up and down. The uncertainty due to the choice of the $h_{\text{damp}}$ parameter is estimated by varying it by a factor of two up.

To account for the uncertainty due to the top quark $p_T$ distribution mismodelling [59], the nominal $t\bar{t}$ sample is compared with the same sample reweighted according to the NNLO QCD top $p_T$ prediction, computed with the `MATRIX` program. The difference between the reweighted and the nominal prediction is symmetrised and used as an uncertainty. A more detailed study on the top $p_T$ reweighting is presented in Appendix J.

### 9.2.2 Modelling of the single-top events

Similarly to the $t\bar{t}$ uncertainties, scale variations in the ME, Var3c and for the final state radiation of the parton shower are considered for the $tW$ process. Furthermore, because of the overlap with the $t\bar{t}$ process, an uncertainty is considered by comparing the *diagram removal* (DR) scheme [270], with an alternative removal technique, the *diagram subtraction* (DS) [260]. The symmetrised difference between the distributions obtained from the DS and the DR methods is implemented as a modelling uncertainty.

### 9.2.3 Modelling of the $V$+jets events

In the dilepton channel, the $W$+jets events contribute only via fake and non-prompt leptons. Several sources of systematic uncertainties in the modelling of the $Z$+jets events are considered. The independent variation of the factorisation and renormalisation scales in the ME, as well as the simultaneous variations of the parton shower by factors of 0.5 and 2, are considered. Variations that differ by a factor of four (such as $\mu_r = 2\mu_{r0}$, $\mu_f = 0.5\mu_{f0}$ and $\mu_r = 0.5\mu_{r0}$, $\mu_f = 2\mu_{f0}$) are excluded. The variation having the maximum impact on the yields is symmetrised and used in the analysis.

For the modelling uncertainties affecting the $Z$ samples, the acceptance effect coming from the difference in the simulated phase-space and the analysis phase-space is subtracted. The largest uncertainties of the scale variations in ME and PS for the $Z$ samples are the simultaneous variation of the factorisation and renormalisation scales by a factor of 0.5 in the ME and PS for $ee$, and the simultaneous variation of the factorisation and renormalisation scales by a factor of two in the ME and PS for $\mu\mu$ events. Summary of the impact of the different variations is provided in Appendix C. The difference in the modelling of $Z$-boson events coming from the usage of different MC generators is described in Appendix K; there was no sizeable effect due to the comparison between the SHERPA and POWHEG BOX v2 +PYTHIA 8 MC generators. An additional check for the modelling of the $Z$-boson events is considered by reweighting the dilepton $p_{\mathrm{T}}$ distribution to match data perfectly. This check is documented in Appendix B.

### 9.2.4 Fake and non-prompt lepton modelling

For the dilepton channel, a conservative normalisation uncertainty of 50% is assigned for the fake lepton background in the $e\mu$ channel with one $b$-tagged jet and 100% uncertainty is assigned to events with two $b$-tagged jets. Additionally, a decorrelated, 100% uncertainty is assigned to the fake lepton estimate in the $ee$ and $\mu\mu$ channels.

### 9.2.5 Other SM backgrounds

A conservative 50% uncertainty is considered for the normalisation of the diboson processes. This value is inspired by the 33% uncertainty quoted in the Run 2 measurement [59] for the two $b$-tagged region. The uncertainty is adjusted upwards to account for the imperfect calculation of the $k$-factors for the normalisation. Nevertheless, the uncertainty does not impact the precision of the measurement. Additionally, a 50% uncertainty is assigned for the combined contribution of $t\bar{t}Z$ and $t\bar{t}W$ processes.

### 9.2.6 PDF uncertainty

The PDF uncertainty for $t\bar{t}$ and $Z$ modelling is estimated by considering the internal variations of the PDF4LHC21 PDF set. The PDF sets considered in the PDF4LHC21 recommendation are CT18 [271], MSHT20 [272], and NNPDF3.1.1 [273]. A set of 42 NPs, symmetrised and uncorrelated with each other, is used in the analysis. This uncertainty is correlated between processes.

## 9.3 MC statistical uncertainty

The statistical uncertainty originating from the finite number of simulated events is considered in the analysis as a systematic uncertainty. The uncertainty results in two NPs for each bin used in the final fit. One NP combines the MC statistical uncertainty from all non-$t\bar{t}$ processes in the $e\mu$ channel, and one NP represents the MC statistical uncertainty of the $t\bar{t}$ process. This separation is needed due to the way how the $t\bar{t}$ histograms are generated as described in Section 5.2.2. In the same flavour channels, one NP per bin is used to represent the MC statistical uncertainty of all processes.

## 9.4 Pruning

Often, not all sources of systematic uncertainty are significant in an analysis. Each NP contributes to increase the complexity of maximising the multidimensional likelihood. In order to limit the formation of local maxima, which can make the procedure typically unstable and possibly dependent on the starting point of the maximisation, the so-called pruning technique is applied. This operation consists in removing any source of systematics that has an impact below a specific threshold. In this thesis, a threshold on the normalisation effect of NPs is set at 0.01%; NPs that fail to comply with the threshold requirements, are dropped.

| **Components** | **Uncert.** |
|---|---|
| Single-Top | 3.5% |
| Diboson | 50% |
| $t\bar{t}V$ | 50% |
| Fake leptons $ee$ | 100% |
| Fake leptons $\mu\mu$ | 100% |
| Fake leptons $e\mu$ $1b$ | 50% |
| Fake leptons $e\mu$ $2b$ | 100% |

Table 9.1: Uncertainties on the normalisation of background processes.

| Systematic Uncertainty | Components |
|---|---|
| **Luminosity** | |
| Luminosity | 1 |
| **Electrons** | |
| Electron ID | 38 |
| Electron isolation | 1 |
| Electron reconstruction | 1 |
| Electron energy scale | 63 |
| Electron energy resolution | 10 |
| Electron trigger | 1 |
| **Muons** | |
| Muon ID | 20 |
| Muon isolation | 9 |
| Muon TTVA | 7 |
| Muon trigger | 1 |
| Muon momentum scale | 3 |
| Muon momentum resolution | 2 |
| Muon sagitta bias | 2 |
| **Jets** | |
| Jet energy scale | 31 |
| Jet energy resolution | 16 |
| Jet vertex fraction | 1 |
| **Pile-up** | |
| Pile-up profile | 1 |
| **Flavour tagging** | |
| $b$-tagging efficiency | 9 |
| $c$-tagging efficiency | 2 |
| Light-jet-tagging efficiency | 2 |
| **Background Model** | |
| Single top $\mu_\mathrm{R}$ in ME | 1 |
| Single top $\mu_\mathrm{F}$ in ME | 1 |
| Single top $\alpha_\mathrm{s}^\mathrm{FSR}$ | 1 |
| Single top Var3c (ISR scale) | 1 |
| Single top normalisation | 1 |
| Single top and $t\bar{t}$ overlap | 1 |
| Fake leptons normalisation | 4 |
| Diboson normalisation | 1 |
| $t\bar{t}V$ normalisation | 1 |
| **$t\bar{t}$ Model** | |
| $t\bar{t}$ $\mu_\mathrm{R}$ in ME | 1 |
| $t\bar{t}$ $\mu_\mathrm{F}$ in ME | 1 |
| $t\bar{t}$ $\alpha_\mathrm{s}^\mathrm{FSR}$ | 1 |
| $t\bar{t}$ Var3c (ISR scale) | 1 |
| $t\bar{t}$ $h_\mathrm{damp}$ | 1 |
| $t\bar{t}$ shower & hadronisation | 1 |
| Top quark $p_\mathrm{T}$ reweighting | 1 |
| **$Z$+jets Model** | |
| $Z$+jets scales | 1 |
| **PDFs** | |
| PDF4LHC21 | 42 |

Table 9.2: A summary of the systematic uncertainties considered in the analysis with their corresponding number of components that enter the uncertainty calculation.

## 9.5 Comparison with previous measurements

### Systematic uncertainties treatment in ATLAS-CONF-2022-070

**Electrons and muons:** contrary to the main measurement, electron uncertainties are considered in a preliminary scheme, in which each of the categories listed in Table 9.2 corresponds to a single NP. Muon uncertainties are derived by exploiting a subset of the data collected during Run 3; these are implemented in the analysis according to a preliminary scheme. The early scheme includes 2 NPs for muon identification, 2 NPs for isolation, 2 NPs for TTVA, 2 NPs for muon trigger, and 5 NPs for muon momentum scale and resolution, and sagitta. Lepton trigger SFs are computed according to the procedure presented in Appendix F.

**Jets:** to produce the initial set of uncertainties for JES and JER, the jet response, calculated as the reconstructed jet $p_{\mathrm{T}}$ over the truth jet $p_{\mathrm{T}}$, is calculated as a function of jet $p_{\mathrm{T}}$ and jet $|\eta|$. A set of $t\bar{t}$ events is generated using 2018-like MC samples; differences between the track reconstruction and related pile-up contamination across the software releases of Run 2 and Run 3 are taken into account during the study. The obtained distributions are then fitted with a Gaussian function to determine the mean values (JES) and the width (JER). Additionally, the JVT algorithm is employed, using the uncertainties on SFs as estimated in Run 2.

**Flavour tagging:** as described in Section 4.7.4, preliminary prescriptions are applied, including SFs set to 1, with conservative uncertainties on the $b$-tagging and $c$- and light-mistagging rates, respectively, 10%, 20% and 40%.

**Top quark $p_{\mathrm{T}}$ reweighting:** this uncertainty is not considered in this analysis, since no NNLO (QCD) predictions for the top quark $p_{\mathrm{T}}$ distribution were available at the time of writing.

**$Z$-boson modelling:** given the phase space definition of $Z$ events, no additional acceptance effects are considered.

**Luminosity and pile-up:** before the result of the LUCID2 detector, based on the Van-der-Meer scans, the uncertainty on the integrated luminosity collected is estimated to be about 10%. The pile-up uncertainty is estimated by shifting the average $\mu$ value in simulation by 3% up and down. This value is motivated by using the same shift in Run 2.

**SM backgrounds uncertainties:** the normalisation uncertainty on $t\bar{t}+V$ is not included, since the $t\bar{t}+V$ sample is not used in the analysis.

## Systematic uncertainties treatment in ATLAS-CONF-2023-006

**Electrons and muons:** uncertainties for electron and muons are implemented as described in Section 9.1.1. Recommendations for electrons remain unchanged, whereas muon uncertainties are updated according to the GRL used.

**Jets:** the implementation of jet-related uncertainties follows the recipe provided in Section 9.1.2.

**Flavour tagging:** efficiency SFs are estimated using the technique mentioned in Section 4.5. Uncertainties on such SFs remain consistent with both ATLAS-CONF-2022-070 and the main measurement.

**Top quark $p_T$ reweighting:** predictions for the top quark $p_T$ distribution at the NNLO (QCD) are computed using `MATRIX`, and implemented in the analysis as described in Section 9.2.1.

**$Z$-boson modelling:** the same strategy as in the main measurement is implemented in this analysis; the estimation of the acceptance effects relies on the integrated luminosity used in the measurement.

**Luminosity and pile-up:** this analysis employs the same uncertainty on the integrated luminosity and pile-up as is used in the main measurement.

**SM backgrounds uncertainties:** the normalisation uncertainty on $t\bar{t}+V$ is not included, since the $t\bar{t}+V$ sample is not used in the analysis.

# Chapter 10

# Results

This chapter presents the results obtained from the application of the fit strategies described in Chapter 5 to data. The fitted values for $\sigma_{t\bar{t}}$, $\sigma^{\text{fid.}}_{Z\to\ell\ell}$, $R_{t\bar{t}/Z}$, and $\epsilon_b$ are presented for the primary measurement, employing 29 fb$^{-1}$ of integrated luminosity. A general comparison with the results obtained in the previous measurements is provided as well. Further details on both ATLAS-CONF-2022-070 and ATLAS-CONF-2023-006 are provided in Appendix D, according to the chronological order of the publications.

Figure 10.1 shows the distributions used in the fit to extract the results before and after performing the fit. Distributions employed in previous measurements are included as well. The expected values for the $t\bar{t}$ and $Z$-boson production cross-section, for the fiducial phase space of the $Z$-boson, and the ratio of the cross-sections are:

$$\begin{aligned} R^{\text{SM}}_{t\bar{t}/Z} &= 1.238^{+0.063}_{-0.071}\ (\text{scale+PDF+}\alpha_{\text{s}}), \\ \sigma^{\text{SM}}_{t\bar{t}} &= 924^{+32}_{-40}(\text{scale} + \text{PDF})\text{pb}, \\ \sigma^{\text{SM}}_{Z} &= 746^{+21}_{-22}\ (\text{scale+PDF+}\alpha_{\text{s}})\ \text{pb}. \end{aligned}$$

Where the term scale+PDF indicates the QCD scale variations and the PDF uncertainties. For the $\sigma^{\text{fid.}}_{Z\to\ell\ell}$ and $R_{t\bar{t}/Z}$ measurements, also the uncertainty related to $\alpha_{\text{s}}$ is considered. The $\epsilon_b$ value in the simulation is $0.5431 \pm 0.0003(\text{MCstat.})$.

The fitted values are:

$$
\begin{aligned}
R_{t\bar{t}/Z} &= 1.145 \pm 0.003(\text{stat.}) \pm 0.021(\text{syst.}) \pm 0.002(\text{lumi.}),\\
\sigma_{t\bar{t}} &= 850 \pm 3(\text{stat.}) \pm 18(\text{syst.}) \pm 20(\text{lumi.})\text{pb},\\
\sigma^{\text{fid.}}_{Z\to\ell\ell} &= 743.6 \pm 0.2\ (\text{stat.}) \pm 11\ (\text{syst.}) \pm 16\ (\text{lumi.})\ \text{pb},\\
\epsilon_b &= 0.544 \pm 0.001(\text{stat.}) \pm 0.004(\text{syst.}) \pm 0.001(\text{lumi.})\text{pb},
\end{aligned}
$$

where (stat.), (syst.), (lumi.) represent respectively the statistical, systematic, and luminosity-related uncertainties. In this measurement, as described in Section 5.2.3, only same flavour channels are used in the $Z$-only fit. This procedure is designed to account for all the correlations among systematic uncertainties while computing the $t\bar{t}$ and $Z$-boson cross sections measurements. Moreover, in the $Z$-boson cross section fit an additional normalisation uncertainty of 5.1% is applied on the $t\bar{t}$ sample, according to the theoretical uncertainty on the predicted cross section value. Table 10.1 presents the comparison of the results obtained in the three different analyses reported in this thesis.

| | | **ATLAS-CONF-2022-070** | **ATLAS-CONF-2023-006** | **Primary Measurement** |
|---|---|---|---|---|
| $\sigma_{t\bar{t}}$ [pb] | Theory | $924^{+32}_{-40}$ | $924^{+32}_{-40}$ | $924^{+32}_{-40}$ |
| | Measurement | 830 ± 12 ± 27 ± 86 | 859 ± 4 ± 22 ± 19 | 850 ± 3 ± 18 ± 20 |
| $\sigma^{\text{fid.}}_{Z\to\ell\ell}$ [pb] | Theory | $2182^{+42}_{-45}$ | 741 ± 15 | $746^{+21}_{-22}$ |
| | Measurement | 2075 ± 2 ± 98 ± 199 | 751.2 ± 0.3 ± 15 ± 17 | 743.6 ± 0.2 ± 11 ± 16 |
| $R_{t\bar{t}/Z}$ | Theory | 0.423 ± 0.015 | 1.2453 ± 0.076 | $1.238^{+0.063}_{-0.071}$ |
| | Measurement | 0.400 ± 0.006 ± 0.017 ± 0.005 | 1.144 ± 0.006 ± 0.022 ± 0.003 | 1.145 ± 0.003 ± 0.021 ± 0.002 |
| $\epsilon_b$ | MC simulation | 0.5529 ± 0.0002 | 0.5451 ± 0.0002 | 0.5431 ± 0.0003 |
| | Measurement | 0.553 ± 0.007 ± 0.005 ± 0.001 | 0.548 ± 0.002 ± 0.004 ± 0.001 | 0.544 ± 0.001 ± 0.004 ± 0.001 |

Table 10.1: Comparison between the measurements performed using different subsets of the 2022 data, and their corresponding theory predictions. As described in Section 6.4, for ATLAS-CONF-2022-070 the predicted cross-section for $Z$ is computed with the requirement $m_{\ell\ell} > 40$GeV. Theory predictions are associated with the (scale + PDF) uncertainty, except for the predictions on $\sigma^{\text{fid.}}_{Z\to\ell\ell}$ and $R_{t\bar{t}/Z}$, that in the primary measurement include also the uncertainty on $\alpha_s$. The value of $\epsilon_b$ obtained from the simulation is followed by the statistical uncertainty on the MC sample. Results from measurements are followed by statistical ± systematic ± luminosity uncertainties.

The result for $\sigma_{t\bar{t}}$ is presented for a top quark mass of 172.5 GeV. The dependence of the result from $m_t$ is $(1/\sigma_{t\bar{t}})\text{d}\sigma_{t\bar{t}}/\text{d}m_t = -0.36\%/\text{GeV}$, as estimated from a variation of the top-quark mass in the $t\bar{t}$ and $tW$ samples to 171.5 GeV and 173.5 GeV.

Table 10.2 shows the impact of the systematic uncertainties grouped by their origin. The uncertainties from the previous measurements have been added as well to facilitate the comparison.

In the $t\bar{t}$ cross section measurement, the uncertainty in the luminosity estimation yields the largest contribution, followed by electron and muon reconstruction. Uncertainties in the parton shower and hadronisation modelling also have a significant impact on the precision. For the $\sigma^{\text{fid.}}_{Z\to\ell\ell}$ result, uncertainty on luminosity, muon reconstruction, pile-up and electron reconstruction provide the largest contribution to the measurement. For the cross section ratio, several sources of the systematic uncertainties partially cancel out; nevertheless, the dominant contribution comes from $t\bar{t}$ modelling, as it does not cancel out in the ratio. Other significant sources of uncertainty include trigger and lepton reconstruction efficiencies. The reason for which the trigger efficiency uncertainty does not fully cancel out, is that $t\bar{t}$ and $Z$-boson events have different $\eta$ and $p_{\text{T}}$ distributions; moreover, different combinations of triggers are employed for the samples.

Figure 10.2 shows the measured $t\bar{t}$ cross-section as a function of the centre-of-mass energy compared to the theory prediction using the PDF4LHC21 PDF set. This primary measurement is compatible with the prediction at 1.5 standard deviations, assuming uncorrelated uncertainties between the prediction and measurement. In Fig. 10.3 the ratio of the $t\bar{t}$ and $Z$-boson production cross-sections is compared to the prediction for several sets of PDF. The ratio is slightly lower than most predictions, but compatible at 1.3 standard deviations with the SM prediction based on the PDF4LHC21 set, assuming a top-quark mass of 172.5 GeV.

As in the previous measurements, cross-checks have been performed to validate the obtained results. Firstly, some pull and constraint on nuisance parameters could be related to the $Z \to ee$ and $Z \to \mu\mu$ cross sections not being equal. The ratio of $Z \to \mu\mu$ over $Z \to ee$ has been measured to be $R_{Z\to\mu\mu/Z\to ee} = 1.003 \pm 0.034$; the two cross section measurements agree to better than 0.5 standard deviations, therefore no significant pulls are observed, except for a NP related to the isolation of muons, that is constrained to about 75% of its pre-fit uncertainty. The complete summary of ranking, pulls and constraints of the NPs, as well as correlation matrices, is shown in Appendix E. Moreover, as the $p_{\text{T}}$ of the dilepton pair is known to not be accurately modelled by the MC simulation [274], the distribution of the $p_{\text{T}}$ of the simulated dilepton pair has been reweighted to match the data in $ee$ and $\mu\mu$ events. This operation is performed assuming that the only contribution comes from $Z$-boson events. This test yields a 0.13% impact on the prediction, thus it has been considered negligible.

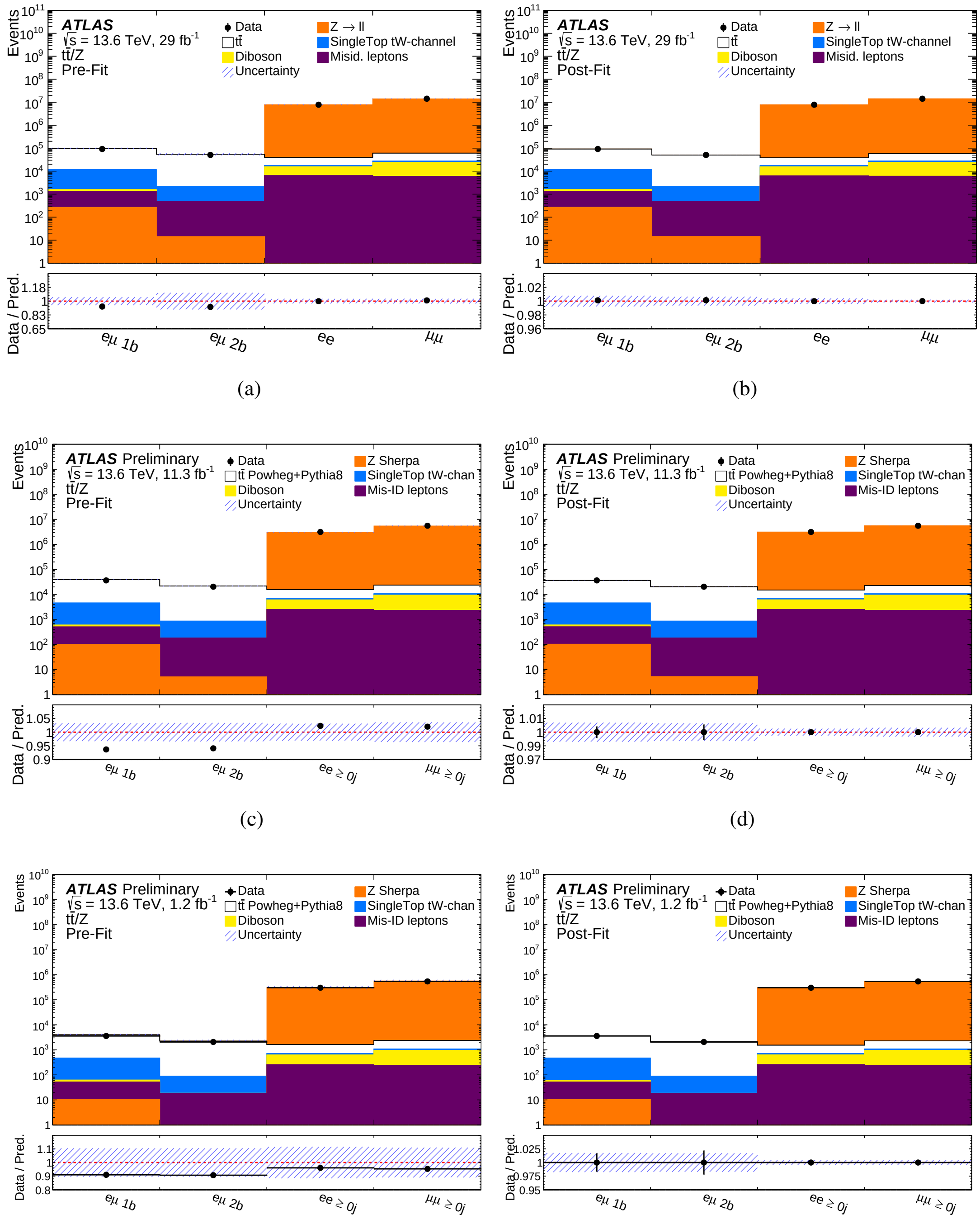

(a) (b)

(c) (d)

(e) (f)

Figure 10.1: Comparison of data and prediction for the event yields in the three lepton channels before the fit (left) and after the fit (right). Distributions used in the primary measurement (a, b), as well as in ATLAS-CONF-2022-070 (c, d) and ATLAS-CONF-2023-006 (e, f) results are reported. The $e\mu$ channel is split into events with one or two $b$-tagged jets. The bottom panel shows the ratio of data over the prediction. The hashed bands represent the total uncertainty. Correlations of the NPs as obtained from the fit are used to build the uncertainty bad in the post-fit distribution.

| Category | | ATLAS-CONF-2022-070 | | | ATLAS-CONF-2023-006 | | | Primary Measurement | | |
|---|---|---|---|---|---|---|---|---|---|---|
| | | Uncertainty [%] | | | | | | | | |
| | | $\sigma_{t\bar{t}}$ | $\sigma^{m_{\ell\ell}>40}_{Z\to\ell\ell}$ | $R_{t\bar{t}/Z}$ | $\sigma_{t\bar{t}}$ | $\sigma^{\text{fid.}}_{Z\to\ell\ell}$ | $R_{t\bar{t}/Z}$ | $\sigma_{t\bar{t}}$ | $\sigma^{\text{fid.}}_{Z\to\ell\ell}$ | $R_{t\bar{t}/Z}$ |
| $t\bar{t}$ | parton shower/hadronisation | 0.6 | 0.2 | 0.7 | 1.1 | < 0.2 | 1.0 | 0.9 | < 0.2 | 0.9 |
| | scale variations | 0.5 | < 0.2 | 0.5 | 0.2 | < 0.2 | 0.2 | 0.4 | < 0.2 | 0.4 |
| | Top quark $p_{\mathrm{T}}$ reweighting | - | - | - | 0.6 | < 0.2 | 0.5 | 0.6 | < 0.2 | 0.6 |
| $Z$ | scale variations | 0.2 | 2.9 | 2.9 | 0.2 | 0.5 | 0.3 | < 0.2 | 0.4 | 0.3 |
| Bkg. | Single top modelling | 0.6 | < 0.2 | 0.6 | 0.4 | < 0.2 | 0.4 | 0.6 | < 0.2 | 0.6 |
| | Diboson modelling | < 0.2 | < 0.2 | 0.5 | < 0.2 | < 0.2 | < 0.2 | < 0.2 | < 0.2 | 0.2 |
| | Mis-Id leptons | 0.6 | < 0.2 | 0.6 | 0.5 | < 0.2 | 0.5 | 0.6 | < 0.2 | 0.6 |
| | $t\bar{t}V$ modelling | - | - | - | - | - | - | < 0.2 | < 0.2 | < 0.2 |
| Lept. | Electron reconstruction | 1.6 | 2.3 | 1.1 | 1.0 | 1.1 | 0.5 | 1.2 | 1.0 | 0.4 |
| | Muon reconstruction | 1.3 | 2.4 | 0.3 | 1.5 | 1.2 | 0.8 | 1.4 | 1.4 | 0.3 |
| | Lepton trigger | 0.2 | 1.3 | 1.1 | 0.4 | 0.7 | 0.8 | 0.4 | 0.4 | 0.4 |
| Jets/tagging | Jet reconstruction | 0.2 | - | 0.2 | 0.4 | - | 0.3 | 0.4 | - | 0.4 |
| | Flavour tagging | 1.9 | - | 1.9 | 0.2 | - | 0.2 | 0.4 | - | 0.3 |
| | Pileup | 0.5 | 0.6 | < 0.2 | 1.1 | 1.1 | < 0.2 | 0.7 | 0.8 | < 0.2 |
| | PDFs | 0.5 | 1.4 | 1.3 | 0.4 | 0.2 | 0.4 | 0.5 | < 0.2 | 0.5 |
| | Luminosity | 10.3 | 9.6 | 1.3 | 2.3 | 2.2 | 0.3 | 2.3 | 2.2 | 0.3 |
| | Systematic Uncertainty | 10.8 | 10.7 | 4.4 | 3.5 | 3.0 | 2.0 | 3.2 | 2.8 | 1.8 |
| | Statistical Uncertainty | 1.5 | 0.1 | 1.5 | 0.5 | 0.03 | 0.5 | 0.3 | 0.02 | 0.3 |
| | Total Uncertainty | 11 | 10.7 | 4.7 | 3.5 | 3.0 | 2.0 | 3.2 | 2.8 | 1.9 |

Table 10.2: Observed impact of the different sources of uncertainty on the $t\bar{t}$ and $Z$-boson cross sections and their ratio $R$, grouped by category. The $t\bar{t}$ cross section and $R$ are obtained in a simultaneous fit to the four regions including both opposite- and same-flavour, while the $Z$-boson cross section is obtained from a fit to same-flavour events only. The impact of each category is obtained by repeating the fit after having fixed the set of nuisance parameters corresponding to that category, and subtracting that uncertainty in quadrature from the uncertainty found in the full fit. The statistical uncertainty is obtained by repeating the fit after having fixed all nuisance parameters to their fitted values. Only the acceptance effects are considered for the PDF and the modelling uncertainties.

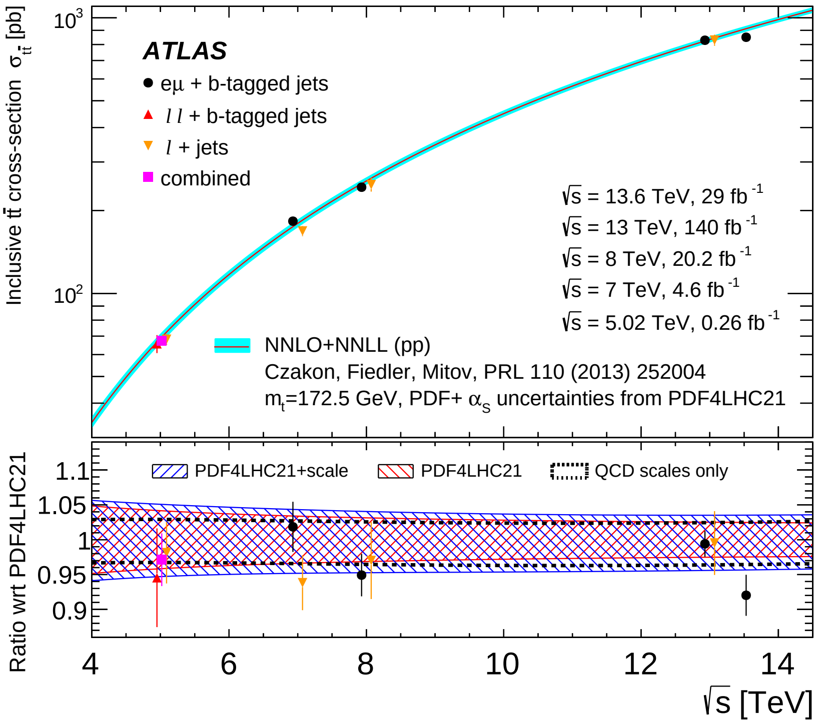

Figure 10.2: Comparison of the measures $t\bar{t}$ cross-section compared to theory predictions using the PDF4LHC21 PDF set. The measurements shown include $e\mu$ final state ($e\mu$ + $b$-tagged jets); $ee$, $\mu\mu$ and $e\mu$ final states ($ll$ + $b$-tagged jets); single lepton final states ($l$ + jets); as well as combinations of final states (combined). The bottom panel shows the ratio of the measured values and three predictions that either contain only the uncertainties originating from the QCD scale variations (black), only the variations in the PDF uncertainties (red) or the total uncertainty in the prediction (blue).

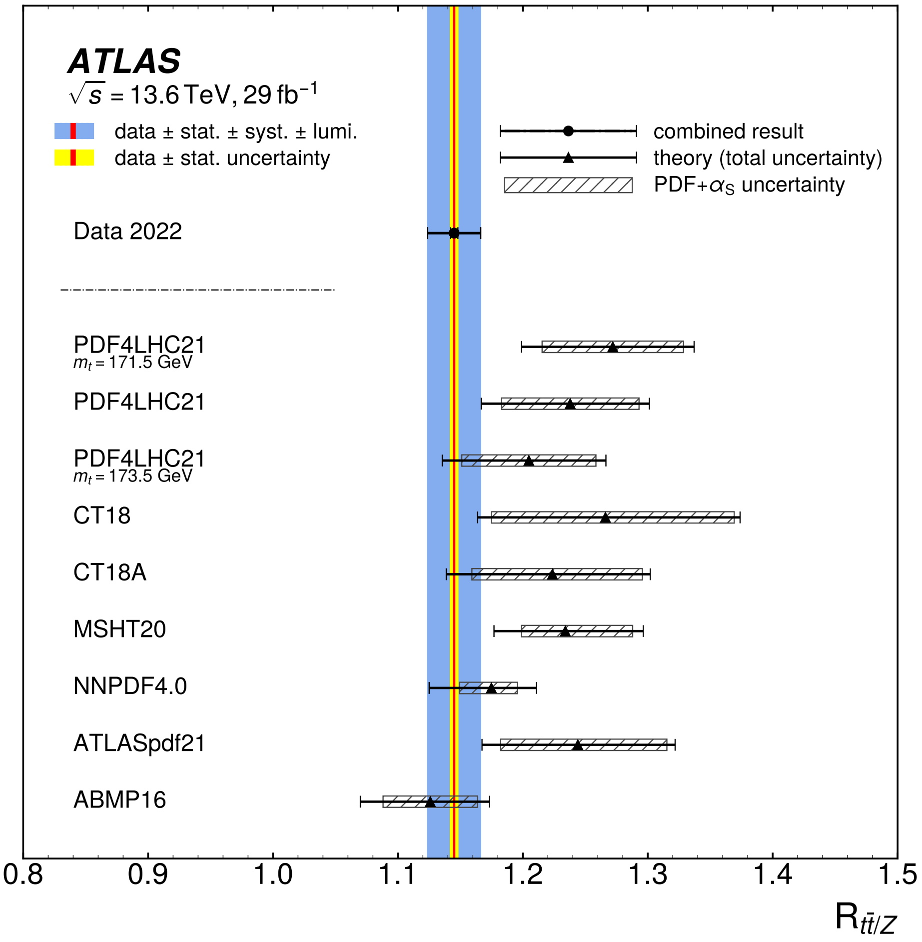

Figure 10.3: Ratio of the $t\bar{t}$ to the $Z$-boson cross-section compared to the prediction for several sets of parton distribution functions. If not explicitly mentioned, a top-quark mass of 172.5 GeV is assumed. The hatched box represents the PDF+$\alpha_S$ component of the uncertainty on the prediction. For the PDF4LH21 PDF set, predictions for different assumptions about the top-quark mass are also displayed.

# Chapter 11

# Conclusions

This thesis reports the first measurement of the top quark pair, of the $Z$-boson production cross section, and of the ratio between the two with data collected by the ATLAS experiment using proton-proton collisions at a centre-of-mass energy of 13.6 TeV. Since this measurement is among the earliest conducted during Run 3 by the collaboration, the analysis has been repeated three times, to account for different datasets, corresponding to different integrated luminosities, progressively accumulated during the whole 2022. The results presented not only constitute a significant contribution to physics, but also serve as a valuable benchmark of the detector, as well as of the computational infrastructure utilised by the collaboration in Run 3, after a series of complex upgrades and modifications.

In the latest measurement, employing a dataset corresponding to an integrated luminosity of 29 $\mathrm{fb}^{-1}$, the $t\bar{t}$ cross-section is measured to be:

$$\sigma_{t\bar{t}} = 850 \pm 3(\text{stat.}) \pm 18(\text{syst.}) \pm 20(\text{lumi. pb}).$$

The measured value is compatible with the prediction at 1.5 standard deviations using the PDF4LHC21 PDF set and assuming top-quark mass of 172.5 GeV. The measured $Z$-boson cross-section is:

$$\sigma^{\text{fid.}}_{Z\to\ell\ell} = 743.6 \pm 0.2\ (\text{stat.}) \pm 11\ (\text{syst.}) \pm 16\ (\text{lumi.})\ \text{pb}.$$

The fitted value for the ratio is:

$$R_{t\bar{t}/Z} = 1.145 \pm 0.003(\text{stat.}) \pm 0.021(\text{syst.}) \pm 0.002(\text{lumi.}).$$

The absolute cross-section measurements are limited by the uncertainty in the luminosity measurement as well as the lepton selection efficiency uncertainties. In the ratio of the $t\bar{t}$ and $Z$ cross-sections, however, the luminosity uncertainty and lepton uncertainties largely cancel out, resulting in a total uncertainty of about 1.9%. The measured values are consistent with the SM prediction using the PDF4LHC21 PDF set, assuming that the uncertainties of the measurement and prediction are uncorrelated.

As the Run 3 goes on, more and more data will be available for this measurement, allowing eventually the exploitation of the full dataset, which is expected to be around 300 $\text{fb}^{-1}$. Furthermore, several improvements are expected for the definition and calibration of the physics objects used in the analysis. Finally, by virtue of the strategy employing a profile likelihood fit, this result can be combined with a measurement in the single-lepton channel, further improving the precision on the cross section estimation.

# Appendix

# Appendix A

# $Z$-boson cross-section prediction

In this appendix, the calculation of the higher order cross sections for the $W^{\pm}$ and $Z$-bosons are reported. To perform these computations, `MATRIX` v2 [259] was used, which can compute cross sections up to NNLO QCD and NLO EW, and combine them by means of an additive prescription.

Uncertainties on the cross sections arising from missing higher orders (standard 7-points variations for the renormalisation scale $\mu_R$ and factorisation scale $\mu_F$), the variation of the strong coupling constant $\alpha_s$, and variations of the input PDFs are also assessed and provided.

## A.1 Input parameters and EW scheme

In the following, the SM input parameters used in the computation are summarised. For more details, these are also reported in Section 5.1 of the `MATRIX` documentation [259].

The $G_\mu$ scheme is employed. When considering leptonic final states produced via off-shell EW bosons, the complex-mass scheme is employed, i.e. complex $W$- and $Z$-boson masses are used and the EW mixing angle is defined as $\cos\theta_W^2 = \left(m_W^2 - i\Gamma_W m_W\right)/\left(m_Z^2 - i\Gamma_Z m_Z\right)$ and $\alpha = \sqrt{2}\,G_\mu\,m_W^2\sin^2\theta_W/\pi$. The PDG values of $G_F$, $m_W$, $\Gamma_W$, $m_Z$ and $\Gamma_Z$ are used and reported for completeness in Table A.1.

All processes considered here apply the 5 flavour scheme (FS) with a vanishing bottom mass $m_b = 0$. The top quark is treated as massive and unstable throughout with $m_t = 173.2\,\text{GeV}$ as well as $\Gamma_t = 1.44262\,\text{GeV}$

The CKM matrix is set to unity except for the production of a single $W^{\pm}$ boson. In that case the PDG SM values are used

$$\begin{bmatrix} V_{ud} & V_{us} & V_{ub} \\ V_{cd} & V_{cs} & V_{cb} \\ V_{td} & V_{ts} & V_{tb} \end{bmatrix} = \begin{bmatrix} 0.97417 & 0.2248 & 0.00409 \\ 0.22 & 0.995 & 0.0405 \\ 0.0082 & 0.04 & 1.009 \end{bmatrix}$$

## A.2 PDFs input and uncertainty

Cross section estimates for a series of different PDF sets are provided and listed in the following, as summarised in Table A.2. Each set includes an overview of the main feature and the prescription used to compute the corresponding PDF error on a given observable.

**PDF4LHC21:** presented in Ref. [69]. Only NNLO grids are provided. The Hessian set denoted as PDF4LHC21_40 is employed, which renders the central value (members 0) and the 68% probability intervals (members 1:40). Denoting as $\mathcal{F}^{(k)}$ a physical observable computed using the $k$-th eigenvector direction, the PDF uncertainty is given by

$$\delta^{\mathrm{PDF}}\mathcal{F} = \sqrt{\sum_{k=1}^{N_{\mathrm{eig}}} \left(\mathcal{F}^{(k)} - \mathcal{F}^{(0)}\right)^2}\,, \tag{A.1}$$

which gives the 68% CL uncertainty according to the symmetric Hessian prescription.

| Parameter | Value |
|---|---|
| $m_W$ | 80.385 GeV |
| $\Gamma_W$ | 2.091 GeV |
| $m_Z$ | 91.1876 GeV |
| $\Gamma_Z$ | 2.4952 GeV |
| $m_H$ | 125 GeV |
| $\Gamma_H$ | 0.00407 GeV |
| $m_t$ | 173.2 GeV |
| $\Gamma_t$ | 1.44262 GeV |
| $G_F$ | $1.16638 \times 10^{-5}$ GeV$^{-2}$ |
| $\sin^2(\theta_W)$ | 0.222897222524 |
| $1/\alpha_{\mathrm{QED}}(m_Z)$ | 132.233229791 |

Table A.1: EW input parameters used for the calculation of inclusive EW vector boson cross sections.

**CT18:** presented in Ref. [271]. NNLO grids are provided for the central fit and 58 eigenvectors sets, corresponding to 29 eigenvectors in the '+' and -' directions giving the 90% CL interval. The 90% CL PDF uncertainty is computed according to the asymmetric Hessian prescription

$$\delta^{\mathrm{PDF}}\mathcal{F} = \frac{\sqrt{\sum_{k=1}^{N_{\mathrm{eig}}} \left(\mathcal{F}^{(+)} - \mathcal{F}^{(-)}\right)^2}}{2} \, . \tag{A.2}$$

In the final results the 68% CL is quoted, obtained applying a rescale factor to Eq. (A.2). Furthermore, an alternative set (CT18A) which also includes the ATLAS precision 7 TeV $W/Z$ data [133] is considered as well.

**MSHT20:** presented in Refs. [272, 275, 276]. Also in this case NNLO grids are provided for the central fit and 64 eigenvectors sets (corresponding to 32 eigenvectors in the '+' and '-' directions) giving the 68% CL interval. The PDF uncertainty is computed according to Eq. (A.2).

**NNPDF4.0:** presented in Ref. [277], represents the latest release of the NNPDF family sets. NNLO grids are provided, for the central fit and 100 MC replicas. To compute the best value of the physical observable $\mathcal{F}$ and the corresponding PDF uncertainty it is necessary to first compute the ensemble $\mathcal{S}$ of the $\mathcal{F}$ values given the 100 replicas of the set:

$$\mathcal{S} = \{\mathcal{F}^{(1)}, \ldots, \mathcal{F}^{(100)}\} \, . \tag{A.3}$$

Next, the elements of Eq. (A.3) are sorted in ascending order, while removing the lowest and the highest 16% of the ordered replicas, keeping in this way the central 68% replicas. Denoting the resulting 68% CL interval as $[\mathcal{F}_{16}, \mathcal{F}_{84}]$ the up and down PDF error are estimated as

$$\delta^{\mathrm{PDF,up}}\mathcal{F} = \mathcal{F}_{84} - \mathcal{F}_0 \, , \qquad \delta^{\mathrm{PDF,down}}\mathcal{F} = \mathcal{F}_0 - \mathcal{F}_{16} \, . \tag{A.4}$$

The median of the ensemble $\mathcal{S}$ in Eq. (A.3) is quoted as the best value of the observable.

**ABMP16:** presented in Ref. [278]. NNLO grids are provided for the central fit (member 0) and 29 eigenvectors (member 1 to 30). The 68% CL interval can be obtained using the symmetric Hessian prescription of Eq. (A.1). For NNLO results, the ABMP16als118_5_nnlo set is employed.

**ATLASpdf21** presented in Ref. [279]. It represents the determination of a new set of PDFs using diverse measurements in $pp$ collisions at $\sqrt{s}$ =7, 8 and 13 TeV, together with deep inelastic scattering (DIS) data from $ep$ collisions at the HERA collider. NNLO grids are provided for the central fit (member 0) and 42 eigenvectors (member 1 to 43). The experimental uncertainties for this specific set have been evaluated with an enhanced $\chi^2$ tolerance, $\Delta\chi^2 = T^2$, with $T = 3$. The 68% CL interval can be obtained using the symmetric Hessian prescription of Eq. (A.1).

| | Number of members | Perturbative orders | Error type | Reference |
|---|---|---|---|---|
| PDF4LHC21 | 43 | NNLO | 68% CL symmHessian | [69] |
| CT18, CT18A | 59 | NNLO | 68% CL Hessian | [271] |
| MSHT20 | 65 | NNLO | 68% CL Hessian | [272, 275, 276] |
| NNPDF4.0 | 101 | NNLO | Montecarlo | [277] |
| ABMP16 | 30 | NNLO | 68% CL symmHessian | [278] |
| ATLASpdf21 | 43 | NNLO | 68% CL symmHessian | [279] |

Table A.2: Summary of the PDF sets used in the computation of theoretical predictions for the fiducial cross sections.

## A.3 Results

In Table A.4 NNLO QCD + NLO EW results are reported. Results are presented for each PDF set listed in the previous section, and are supplemented with PDF and scale variations error. The fiducial cuts which have been used to produce results are reported in Table A.3.
The only requirement of $66 < m_{\ell\ell} < 116$ GeV has been adopted.

In order to perform NNLO computations a cut-off $r_{\text{cut}}$ on the quantity $q_T/M$ is used, as described in details in Sections 2.1 and 2.2 of Ref. [259]. Depending on the process, the result might show a more or less marked dependence on the choice of such cut-off, and an additional extrapolation procedure is required to get the final NNLO result. The cut-off is therefore sent to 0, and the resulting extrapolated result, denoted as $\sigma^{\text{extr}}$, is taken as the best value of the computation. In the case of the process $pp \to e^+e^-$, for which the $r_{\text{cut}}$ dependence is reported to be especially strong, the `MATRIX` runs have been performed using a dedicated option available in the code, which uses smaller values of the cut-off. The details regarding the extrapolation procedure and the $r_{\text{cut}}$ dependence of the different results are described in details in Section7 of Ref. [259].

| | $pp \to \ell^+\ell^-$ |
|---|---|
| Lepton $p_{\text{T}}$ cuts | $p_{\text{T}} > 27$ GeV |
| Lepton $\eta$ cuts | $\lvert\eta\rvert < 2.5$ |
| Mass cuts | $66 < m_{\ell\ell} < 116$ GeV |

Table A.3: Fiducial cuts for single boson production processes.

## A.4 Estimate of $\alpha_s$ uncertainty

The following paragraph reports an estimate for the $\alpha_s$ uncertainty, using as input the PDF4LHC21 set. As detailed in Ref. [69], the PDF4LHC21 combination assumes

$$\alpha_s(m_Z^2) = 0.1180 \pm 0.0010\,. \tag{A.5}$$

| PDF set | $pp \to \ell^+\ell^-$ [pb] |
|---|---|
| CT18 | $733.22^{+0.5\%,+0.5\%,+5.9\%}_{-0.5\%,-0.5\%,-6.2\%}$ |
| CT18A | $750.47^{+0.4\%,+0.5\%,+3.7\%}_{-0.4\%,-0.5\%,-4.3\%}$ |
| MSHT20 | $747.48^{+0.6\%,+0.5\%,+2.2\%}_{-0.6\%,-0.7\%,-2.7\%}$ |
| NNPDF4.0 | $767.68^{+0.5\%,+0.3\%,+0.9\%}_{-0.5\%,-0.5\%,-0.9\%}$ |
| PDF4LHC21 | $746.04^{+0.6\%,+0.4\%,+4.6\%}_{-0.6\%,-0.6\%,-4.6\%}$ |
| ATLASpdf21 | $787.39^{+0.4\%,+0.4\%,+3.2\%}_{-0.4\%,-0.6\%,-4.1\%}$ |
| ABMP16 | $746.12^{+0.5\%,+0.6\%,+1.5\%}_{-0.5\%,-0.6\%,-1.5\%}$ |

Table A.4: Single boson production fiducial cross-section results for a series of different PDF sets. The first error which is quoted correspond to statistical uncertainty, the second to scale error, while the third to PDF error, estimated as described in Section A.2.

Following the prescription given in Ref. [69], for a given cross section $\sigma$ the $\alpha_s$ uncertainty is estimated as

$$\delta^{\alpha_s}\sigma = \frac{\sigma\,(\alpha_s = 0.119) - \sigma\,(\alpha_s = 0.117)}{2} \tag{A.6}$$

corresponding to an uncertainty $\delta\alpha_s = 0.0010$ at the 68% CL. In order to compute Eq. (A.6) Hessian variants which include the central fits for variations of the strong coupling constant $\alpha_s(m_Z^2)$ are provided. Results for each process considered here are reported in Table A.5.

| | PDF4LHC21 | | |
|---|---|---|---|
| | $\sigma\,(\alpha_s = 0.117)$ [pb] | $\sigma\,(\alpha_s = 0.119)$ [pb] | $\delta^{\alpha_s}\sigma$ |
| $pp \to \ell^+\ell^-$ | 740.93 | 751.40 | 0.7% |

Table A.5: Fiducial cross sections predictions for $\alpha_s$ variations obtained using PDF4LHC21.

# Appendix B

# Reweighting dilepton transverse momentum in the same flavour channels

This appendix describes a test that was performed to check the impact of mismodelling of the dilepton $p_{\mathrm{T}}$ distribution in the same flavour channels, using 29 $\mathrm{fb}^{-1}$ of data. In this test, the ratio of the observed data and prediction (assuming all events originate from the $Z$-boson production) is used to reweight the $Z$ distribution. Figure B.1 shows the distribution of the dilepton $p_{\mathrm{T}}$ between the prediction and data.

The impact on the inclusive yields, used in the fit are shown in Figure B.2. It can be seen that the impact is at maximum 0.13% on the yields, thus negligible.

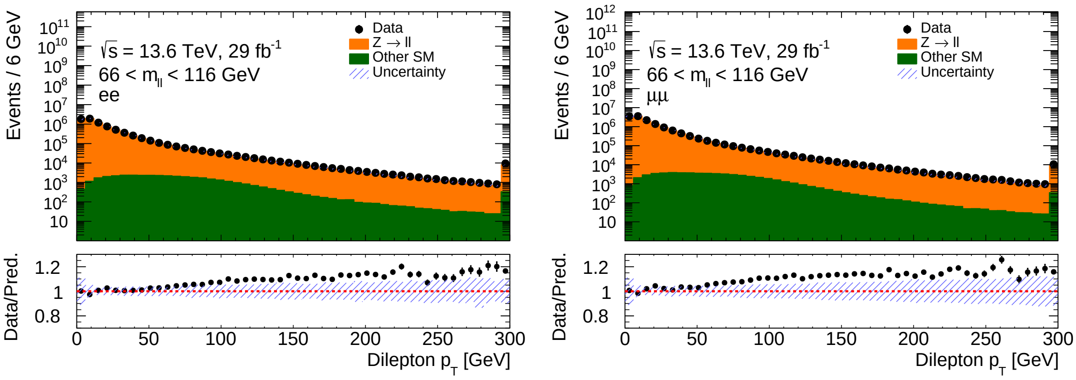

(a) (b)

Figure B.1: Comparison of data and prediction for the dilepton $p_\mathrm{T}$ distribution in the $ee$ channel (left) and $\mu\mu$ channel (right). The last bin contains overflow events. The hashed band represents the total systematic uncertainty. The bottom panel shows the ratio of data over the prediction.

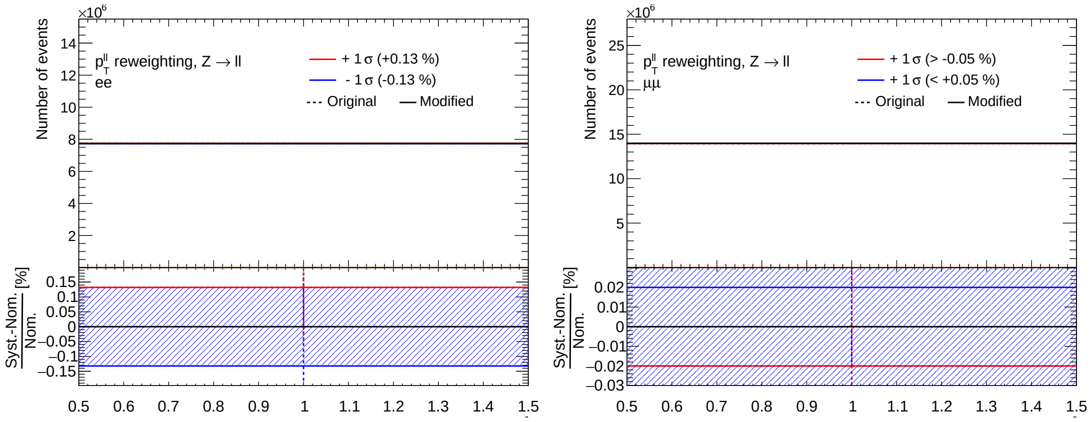

(a) (b)

Figure B.2: Impact of the variation on the inclusive yields in the $ee$ channel (left) and $\mu\mu$ channel (right), obtained by reweighting the dilepton $p_\mathrm{T}$ distribution in the $\mu\mu$ channel to match data.

# Appendix C

# Acceptances for fiducial-level $Z$

This appendix describes the acceptances calculated for the fiducial-level selection on the $Z$ dilepton, same-flavor MC samples (i.e. $ee$ and $\mu\mu$). A selection requiring all leptons to fulfill $p_{\mathrm{T}} \geq 27\,\mathrm{GeV}$ and $|\eta| < 2.5$, as well as a dilepton mass requirement of $66\,\mathrm{GeV} < m_{\ell\ell} < 116\,\mathrm{GeV}$ is applied to events on particle-level and on Born level separately. This selection matches the reco-level selection used in the analysis. For all passing events, per DSID, the individual weights are summed and finally scaled by the sum of all weights regardless of the selection, giving the acceptance

$$\mathrm{acc}_{\mathrm{var}} = \frac{\sum_{\text{events passing selection}} (\text{weight}\,(\text{var}))}{\sum_{\text{all events}} (\text{weight}\,(\text{var}))}. \tag{C.1}$$

The statistical uncertainties of the acceptances are calculated as

$$\sigma_{\text{stat, acc}_{\text{var}}} = \frac{\sqrt{\sum_{\text{events passing selection}} [\text{weight}\,(\text{var})]^2}}{\sum_{\text{all events}} [\text{weight}\,(\text{var})]}. \tag{C.2}$$

The weighted mean of the acceptances per DSID are calculated, using the filter efficiency of the DSID as weight.

These acceptances are given in Table C.1. They are derived, using about 20% of the events, ensuring that the statistical uncertainty for each DSID is smaller or in the order of magnitude of $10^{-5}$, while the acceptances have an order of magnitude of $10^{-1}$.

The statistical uncertainties of the final acceptances are maximally of the order of magnitude of $10^{-6}$ and thus negligible. The systematic uncertainty on the nominal acceptance is chosen as the largest deviation between nominal and the acceptances of the variations of ME and PS. The nominal acceptances are

$$\mathrm{acc}_{\mathrm{nom},\,ee} = 0.336 \pm 0.010 \tag{C.3}$$

$$\mathrm{acc}_{\mathrm{nom},\,\mu\mu} = 0.337 \pm 0.008. \tag{C.4}$$

| | Acceptances | |
|---|---|---|
| | $ee$ events | $\mu\mu$ events |
| Weight | 0.336 | 0.337 |
| MUR05_MUF05_PDF303200_PSMUR05_PSMUF05 | 0.335 | 0.335 |
| ME_ONLY_MUR05_MUF05_PDF303200_PSMUR05_PSMUF05 | 0.337 | 0.337 |
| MUR05_MUF1_PDF303200_PSMUR05_PSMUF1 | 0.335 | 0.336 |
| ME_ONLY_MUR05_MUF1_PDF303200_PSMUR05_PSMUF1 | 0.335 | 0.336 |
| MUR1_MUF05_PDF303200_PSMUR1_PSMUF05 | 0.335 | 0.336 |
| ME_ONLY_MUR1_MUF05_PDF303200_PSMUR1_PSMUF05 | 0.337 | 0.338 |
| MUR1_MUF2_PDF303200_PSMUR1_PSMUF2 | 0.344 | 0.343 |
| ME_ONLY_MUR1_MUF2_PDF303200_PSMUR1_PSMUF2 | 0.335 | 0.336 |
| MUR2_MUF1_PDF303200_PSMUR2_PSMUF1 | 0.337 | 0.338 |
| ME_ONLY_MUR2_MUF1_PDF303200_PSMUR2_PSMUF1 | 0.337 | 0.338 |
| MUR2_MUF2_PDF303200_PSMUR2_PSMUF2 | 0.346 | 0.345 |
| ME_ONLY_MUR2_MUF2_PDF303200_PSMUR2_PSMUF2 | 0.336 | 0.337 |

Table C.1: The particle-level acceptances for different variations are shown, separated for $ee$ and $\mu\mu$ events. The variations include the nominal (Weight) and scale variations, for both matrix element and parton shower, as well as matrix element-only (ME_ONLY).

Additionally, the acceptances for only the dilepton mass requirement of $66\,\mathrm{GeV} < m_{\ell\ell} < 116\,\mathrm{GeV}$ are calculated in the same way. These acceptances, as well as the ratio between the full fiducial-selection and only the dilepton mass selection acceptances are given in Table C.2.

From the full-fiducial acceptances, the fiducial cross-section and reco-level scale variation uncertainties can be corrected. This is done by taking the deviation from one of ratio between the acceptance of each variance and the nominal acceptance, and then shifting the reco-level uncertainty corresponding to the variation by this value. These values are given in Table C.3.

As these uncertainties just effect the yields in the singular bins in the $Z$ signal region, only the largest uncertainty of all variations is assigned as the corresponding uncertainty. The reco-level ME and PS uncertainties for the $Z$ samples are

$$\sigma_{\mathrm{ME+PS},\,Z\to ee} = 0.637\text{‰} \tag{C.5}$$

$$\sigma_{\mathrm{ME+PS},\,Z\to\mu\mu} = 0.392\text{‰}, \tag{C.6}$$

corresponding to the simultaneous variation of the factorisation and renormalisation scales by a factor of 0.5 in the ME and PS for $ee$ and the simultaneous variation of the factorisation and renormalisation scales by a factor of two in the ME and PS for $\mu\mu$.

| | Acceptances | | Ratio of Acceptances | |
|---|---|---|---|---|
| | $ee$ events | $\mu\mu$ events | $ee$ events | $\mu\mu$ events |
| Weight | 0.900 | 0.901 | 0.374 | 0.374 |
| MUR05_MUF05_PDF303200_PSMUR05_PSMUF05 | 0.903 | 0.905 | 0.370 | 0.371 |
| ME_ONLY_MUR05_MUF05_PDF303200_PSMUR05_PSMUF05 | 0.903 | 0.904 | 0.373 | 0.373 |
| MUR05_MUF1_PDF303200_PSMUR05_PSMUF1 | 0.900 | 0.901 | 0.373 | 0.372 |
| ME_ONLY_MUR05_MUF1_PDF303200_PSMUR05_PSMUF1 | 0.900 | 0.901 | 0.372 | 0.373 |
| MUR1_MUF05_PDF303200_PSMUR1_PSMUF05 | 0.904 | 0.905 | 0.370 | 0.371 |
| ME_ONLY_MUR1_MUF05_PDF303200_PSMUR1_PSMUF05 | 0.903 | 0.904 | 0.373 | 0.374 |
| MUR1_MUF2_PDF303200_PSMUR1_PSMUF2 | 0.902 | 0.901 | 0.383 | 0.381 |
| ME_ONLY_MUR1_MUF2_PDF303200_PSMUR1_PSMUF2 | 0.899 | 0.900 | 0.373 | 0.374 |
| MUR2_MUF1_PDF303200_PSMUR2_PSMUF1 | 0.901 | 0.901 | 0.375 | 0.375 |
| ME_ONLY_MUR2_MUF1_PDF303200_PSMUR2_PSMUF1 | 0.900 | 0.901 | 0.374 | 0.375 |
| MUR2_MUF2_PDF303200_PSMUR2_PSMUF2 | 0.902 | 0.902 | 0.384 | 0.382 |
| ME_ONLY_MUR2_MUF2_PDF303200_PSMUR2_PSMUF2 | 0.899 | 0.899 | 0.374 | 0.375 |

Table C.2: The particle-level acceptances for the dilepton mass selection-only for different variations are shown, separated for $ee$ and $\mu\mu$ events. The variations include the nominal (Weight) and scale variations, for both matrix element and parton shower, as well as matrix element-only (ME_ONLY). Additionally, the ratio of the full fiducial selection acceptances over the dilepton mass selection acceptances is shown.

| Variation | Uncor. unc. in % | | acc. ratio | | Cor. unc. in % | |
|---|---|---|---|---|---|---|
| | $ee$ | $\mu\mu$ | $ee$ | $\mu\mu$ | $ee$ | $\mu\mu$ |
| MUR05_MUF05_PDF303200_PSMUR05_PSMUF05 | 0.10 | 0.48 | 1.00 | 1.00 | 0.64 | 0.05 |
| ME_ONLY_MUR05_MUF05_PDF303200_PSMUR05_PSMUF05 | 0.29 | 0.00 | 1.00 | 1.00 | 0.23 | 0.00 |
| MUR05_MUF1_PDF303200_PSMUR05_PSMUF1 | −0.17 | 0.31 | 1.00 | 1.00 | 0.10 | 0.14 |
| ME_ONLY_MUR05_MUF1_PDF303200_PSMUR05_PSMUF1 | 0.13 | 0.36 | 1.00 | 1.00 | 0.45 | 0.01 |
| MUR1_MUF05_PDF303200_PSMUR1_PSMUF05 | −0.17 | 0.39 | 1.00 | 1.00 | 0.31 | 0.08 |
| ME_ONLY_MUR1_MUF05_PDF303200_PSMUR1_PSMUF05 | 0.34 | 0.30 | 1.00 | 1.00 | 0.05 | 0.06 |
| MUR1_MUF2_PDF303200_PSMUR1_PSMUF2 | 2.49 | 2.16 | 1.02 | 1.02 | 0.10 | 0.28 |
| ME_ONLY_MUR1_MUF2_PDF303200_PSMUR1_PSMUF2 | −0.27 | 0.28 | 1.00 | 1.00 | 0.01 | 0.02 |
| MUR2_MUF1_PDF303200_PSMUR2_PSMUF1 | 0.10 | 0.37 | 1.00 | 1.00 | 0.21 | 0.18 |
| ME_ONLY_MUR2_MUF1_PDF303200_PSMUR2_PSMUF1 | 0.04 | 0.27 | 1.00 | 1.00 | 0.17 | 0.08 |
| MUR2_MUF2_PDF303200_PSMUR2_PSMUF2 | 2.76 | 2.70 | 1.03 | 1.02 | 0.10 | 0.39 |
| ME_ONLY_MUR2_MUF2_PDF303200_PSMUR2_PSMUF2 | −0.18 | 0.06 | 1.00 | 1.00 | 0.19 | 0.07 |

Table C.3: The corrected and uncorrected ME and PS variation uncertainties on reco-level are shown, using the fiducial acceptances for the correction, separated for $ee$ and $\mu\mu$ events. Furthermore, the ratio of the variation's acceptance and the nominal acceptance is shown. The variations include the nominal (Weight) and scale variations, for both matrix element and parton shower, as well as matrix element-only (ME_ONLY).

The PDF systematic uncertainties are corrected according to the fiducial selection in the same way.

# Appendix D

# Results from previous measurements

## D.1 ATLAS-CONF-2022-070 - 1.2 fb$^{-1}$

Figure D.1 shows the distribution used in the fit to extract the cross-sections and the ratio, before and after performing the fit. The expected values for the $t\bar{t}$ and $Z$-boson production cross-section, for the fiducial phase space of the $Z$-boson defined by $m_{\ell\ell} > 40$ GeV and the ratio of the cross-sections are

$$\begin{aligned} R^{\text{SM}}_{t\bar{t}/Z} &= 0.423 \pm 0.015(\text{scale+PDF}), \\ \sigma^{\text{SM}}_{t\bar{t}} &= 924^{+32}_{-40}(\text{scale+PDF})\text{ pb}, \\ \sigma^{m_{\ell\ell}>40,\text{SM}}_{Z\to\ell\ell} &= 2182^{+42}_{-45}(\text{scale+PDF})\text{ pb}. \end{aligned}$$

Furthermore, the $\epsilon_b$ value in the $t\bar{t}$ simulation is 0.5529 ± 0.0002(MC stat.). The fitted values are:

$$\begin{aligned} R_{t\bar{t}/Z} &= 0.400 \pm 0.006(\text{stat.}) \pm 0.017(\text{syst.}) \pm 0.005(\text{lumi.}), \\ \sigma_{t\bar{t}} &= 830 \pm 12(\text{stat.}) \pm 27(\text{syst.}) \pm 86(\text{lumi.})\text{pb}, \\ \sigma^{m_{\ell\ell}>40}_{Z\to\ell\ell} &= 2075 \pm 2(\text{stat.}) \pm 98(\text{syst.}) \pm 199(\text{lumi.})\text{pb}, \\ \epsilon_b &= 0.553 \pm 0.007(\text{stat.}) \pm 0.005(\text{syst.}) \pm 0.001(\text{lumi.}). \end{aligned}$$

The $t\bar{t}$ cross-section is measured by repeating the fit in the $e\mu$ channel, see Section 5.2.3.

Even with the relatively low integrated luminosity, the measurement of the $t\bar{t}$ cross-sections is dominated by systematic uncertainties. The dominant source of systematic uncertainties originates from luminosity. The uncertainty on the efficiency of the $b$-tagging simulation is caused by a large impact on the $tW$ single-top contribution that is not absorbed by $\epsilon_b$ as in the case of the $t\bar{t}$ production. Other important sources of the systematic uncertainties include: lepton identification, and parton-shower and hadronisation model.

Also, the $Z$ cross section measurement is dominated by the luminosity uncertainty, followed by the matrix element and parton shower uncertainty on $Z$+jets samples, and by the electron and muon reconstruction uncertainties.

As for the ratio, Figure D.2 shows the impact of most important systematic uncertainties on the cross-section, and Table D.1 shows the impact of the systematic uncertainties grouped by their origin. The dominant source of systematic uncertainties originates from the simultaneous variation of matrix element and parton shower uncertainty in the $Z$+jets samples. The uncertainty on the luminosity has a large impact due to its effect on the backgrounds that do not have an unconstrained normalisation parameter in the fit to compensate for it. Other important sources of the systematic uncertainties include: parton-shower and hadronisation model, and the uncertainty in the simulation of the response of the muon trigger efficiency.

Several checks have been performed to validate the obtained results. Firstly, the ratio of $Z \to \mu\mu$ over $Z \to ee$ has been measured to be $R_{Z\to\mu\mu/Z\to ee} = 0.99 \pm 0.05$. This ratio is consistent with one within the uncertainties, validating the estimation of the lepton uncertainties. Secondly, the fit has been performed for each of the four LHC fills separately, to validate the data quality requirements. The ratio values obtained for different runs are consistent with each other within the measured uncertainties. Thirdly, to assess the possible impact of the top-quark $p_{\mathrm{T}}$ modelling on the acceptance, the fit has been repeated with an increased requirement on the lepton $p_{\mathrm{T}}$ of 30 and 35 GeV. The impact on $R_{t\bar{t}/Z}$ due to the tighter lepton $p_{\mathrm{T}}$ requirement is found to be up to 2%. Finally, to assess the impact coming from same-flavour regions, the fit has been repeated excluding the $ee$ and $\mu\mu$ regions.

Figure D.3 reports the fitted values of the $t\bar{t}$ over $Z$-boson production cross-section ratio, the results of the fits in the individual LHC fills, and the fits with only one flavour channel for the $Z$-boson cross-section. For the last two cross-checks, only the statistical uncertainty is shown.

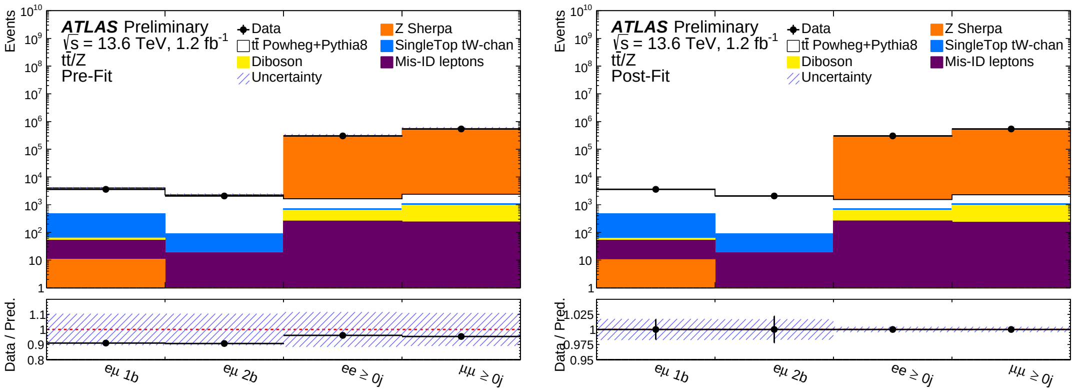

Figure D.1: Comparison of data and prediction for the event yields in the three lepton channels before the fit (left) and after the fit (right). The $e\mu$ channel is split into events with one or two $b$-tagged jets. The bottom panel shows the ratio of data over the prediction. The hashed bands represent the total uncertainty. Correlations of the NPs as obtained from the fit are used to build the uncertainty band in the post-fit distribution.

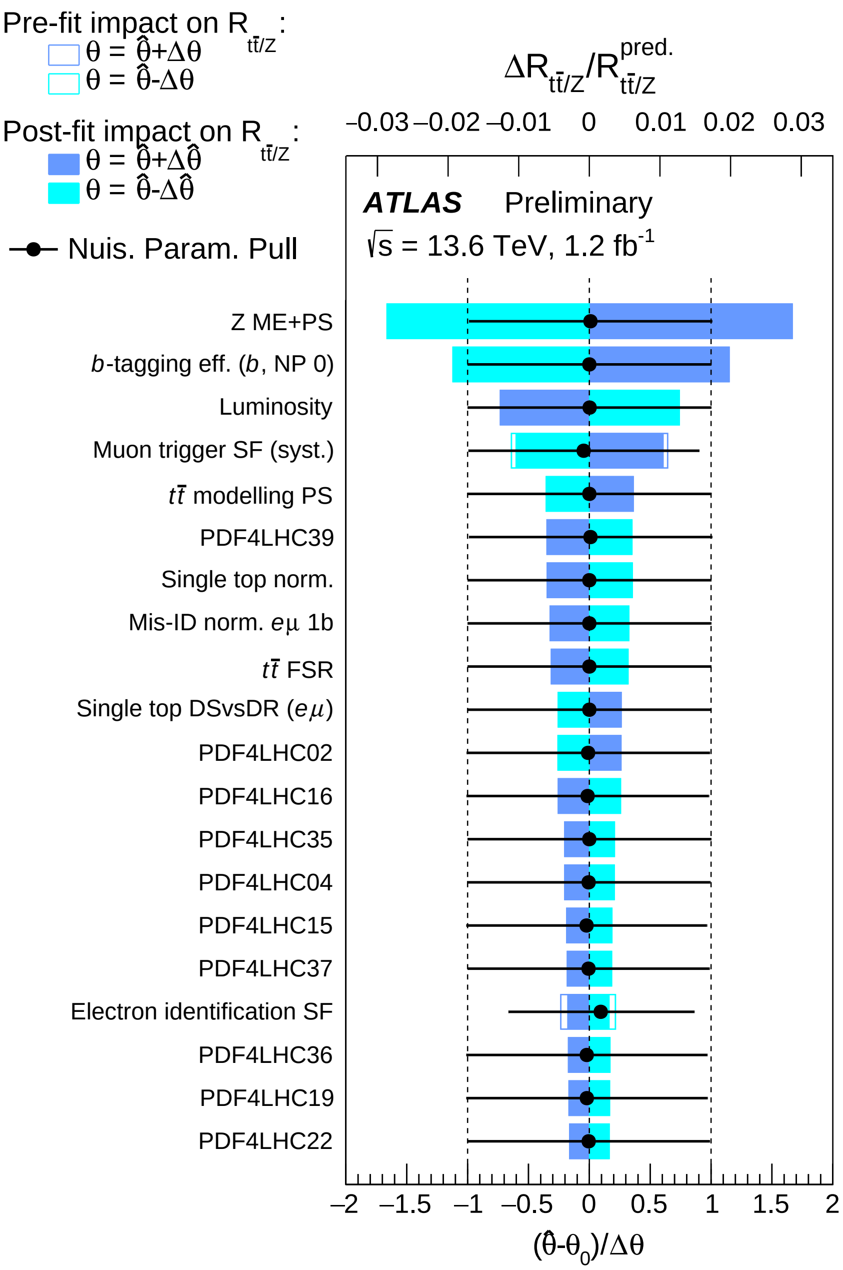

Figure D.2: Ranking plot showing the effect of the 20 most important systematic uncertainties on the measured $t\bar{t}$ cross-section, $\mu$, in the fit to data. The impact of each NP, $\Delta\mu$, is computed by comparing the nominal best-fit value of $\mu/\mu_{\text{pred.}}$ with the result of the fit when fixing the considered nuisance parameter to its best-fit value, $(\theta)$, shifted by its pre-fit and post-fit uncertainties $\pm\Delta\theta(\pm\Delta\hat{\theta})$. The empty boxes show the pre-fit impact while the filled boxes show the post-fit impact of each nuisance parameter on the result. The black dots represent the post-fit value (pull) of each NP where the pre-fit value is subtracted, while the black line represents the post-fit uncertainty normalised to the pre-fit uncertainty.

| | **Category** | **Uncert.** [%] | | |
|---|---|---|---|---|
| | | $\sigma_{t\bar{t}}$ | $\sigma^{m_{\ell\ell}>40}_{Z\to\ell\ell}$ | $R_{t\bar{t}/Z}$ |
| $t\bar{t}$ | $t\bar{t}$ parton shower/hadronisation | 0.6 | 0.2 | 0.7 |
| | $t\bar{t}$ scale variations | 0.5 | $< 0.2$ | 0.5 |
| $Z$ | $Z$ scale variations | 0.2 | 2.9 | 2.9 |
| Bkg. | Single top modelling | 0.6 | $< 0.2$ | 0.6 |
| | Diboson modelling | $< 0.2$ | $< 0.2$ | 0.5 |
| | Mis-Id leptons | 0.6 | $< 0.2$ | 0.6 |
| Lept. | Electron reconstruction | 1.6 | 2.3 | 1.1 |
| | Muon reconstruction | 1.3 | 2.4 | 0.3 |
| | Lepton trigger | 0.2 | 1.3 | 1.1 |
| Jets/tagging | Jet reconstruction | 0.2 | - | 0.2 |
| | Flavour tagging | 1.9 | - | 1.9 |
| | Pileup | 0.5 | 0.6 | $< 0.2$ |
| | PDFs | 0.5 | 1.4 | 1.3 |
| | Luminosity | 10.3 | 9.6 | 1.3 |
| | Systematic Uncertainty | 10.8 | 10.7 | 4.4 |
| | Statistical Uncertainty | 1.5 | 0.1 | 1.5 |
| | Total Uncertainty | 11 | 10.7 | 4.7 |

Table D.1: Observed impact of the different sources of uncertainty on the measured $t\bar{t}$ and $Z$-boson cross-section and on the ratio $R_{t\bar{t}/Z}$, grouped by categories. The impact of each category is obtained by repeating the fit after having fixed the set of nuisance parameters corresponding to that category, subtracting the square of the resulting uncertainty from the square of the uncertainty found in the full fit, and calculating the square root. The statistical uncertainty is obtained by repeating the fit after having fixed all nuisance parameters to their fitted values. Only the acceptance effects are considered for the PDF and the modelling uncertainties.

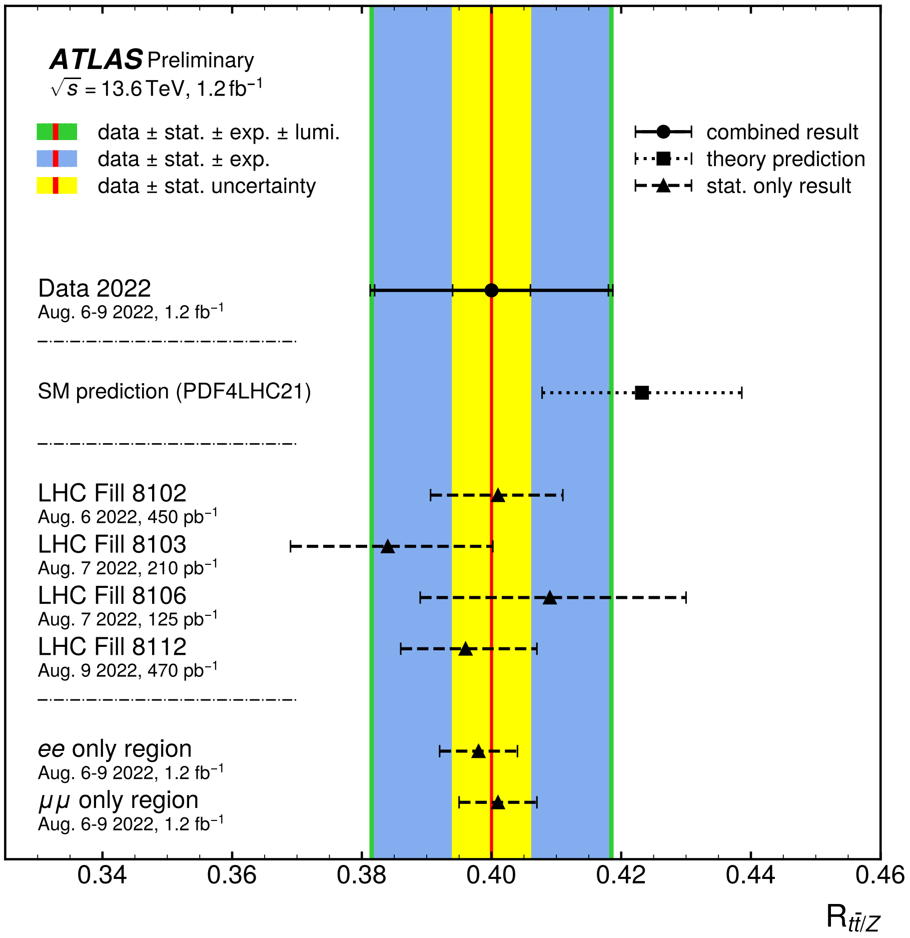

Figure D.3: Fitted values and uncertainties of the $t\bar{t}/Z$ cross-section ratio $R_{t\bar{t}/Z}$. The three shaded bands correspond to the statistical uncertainty, statistical and experimental systematic uncertainties added in quadrature, and total uncertainty, including luminosity uncertainty. The fitted values and statistical uncertainties for the fits in the individual LHC fills or from fits with only one flavour channel for the $Z$-boson cross-section (triangular marker pointing up) are marked with a dashed error bar. The Standard Model prediction based on the NNLO+NNLL calculation for $t\bar{t}$ and NNLO(QCD)+NLO EW prediction for $Z$+jets production, using the PDF4LHC21 parton distribution function, is indicated with a square marker. The corresponding total (scale+PDF) uncertainty is shown as a dotted error bar.

## D.2 ATLAS-CONF-2023-006 - 11.3 $\mathrm{fb}^{-1}$

Figure D.4 shows the distribution used in the fit to extract the cross-sections and the ratio, before and after performing the fit. The expected values for the $t\bar{t}$ and $Z$-boson production cross-section, for the fiducial phase space of the $Z$-boson and the ratio of the cross-sections are

$$\begin{aligned} R^{\mathrm{SM}}_{t\bar{t}/Z} &= 1.2453 \pm 0.076(\mathrm{scale}+\mathrm{PDF}, \mathrm{PDF4LHC21}),\\ \sigma^{\mathrm{SM}}_{t\bar{t}} &= 924^{+32}_{-40}(\mathrm{scale}+\mathrm{PDF})\mathrm{pb},\\ \sigma^{\mathrm{SM}}_{Z} &= 741 \pm 15(\mathrm{scale}+\mathrm{PDF})\mathrm{pb}. \end{aligned}$$

The $\epsilon_b$ value in the $t\bar{t}$ simulation is $0.5451 \pm 0.0004$(MCstat.)

The fitted values are:

$$\begin{aligned} R_{t\bar{t}/Z} &= 1.144 \pm 0.006(\mathrm{stat.}) \pm 0.022(\mathrm{syst.}) \pm 0.003(\mathrm{lumi.}),\\ \sigma_{t\bar{t}} &= 859 \pm 4(\mathrm{stat.}) \pm 22(\mathrm{syst.}) \pm 19(\mathrm{lumi.})\mathrm{pb},\\ \sigma^{\mathrm{fid.}}_{Z\to\ell\ell} &= 751.2 \pm 0.3(\mathrm{stat.}) \pm 15(\mathrm{syst.}) \pm 17(\mathrm{lumi.})\mathrm{pb},\\ \epsilon_b &= 0.548 \pm 0.002(\mathrm{stat.}) \pm 0.004(\mathrm{syst.}) \pm 0.001(\mathrm{lumi.})\mathrm{pb}. \end{aligned}$$

The measured $\epsilon_b$ is compatible within the per mille uncertainty with the simulated one. To estimate the impact of each systematic uncertainty on the uncertainty of the signal strength, a ranking plot is shown in Figure D.5, Figure D.6 and Figure D.7. Table D.2 shows the impact of the systematic uncertainties grouped by their origin.

In both the individual cross section measurements, the largest source of systematic uncertainty originates from the luminosity estimation, immediatly followed by leptons reconstruction. In the $t\bar{t}$ case, the uncertainty in the parton shower and hadronisation modelling has a significant impact on the precision as well. The dominant uncertainty in the ratio stems from the $t\bar{t}$ modelling, followed by trigger and lepton reconstruction efficiencies.

Figure D.8 shows the measured $t\bar{t}$ cross-section as a function of the centre-of-mass energy compared to the theory prediction using the PDF4LHC21 PDF set. This new measurement is slightly lower than the predictions but compatible at 1.3 standard deviations, assuming uncorrelated uncertainties between the prediction and measurement. In Figure D.9 the ratio of the $t\bar{t}$ and $Z$-boson production cross-sections is compared to the prediction for several sets of PDF. The ratio is slightly lower than most predictions where the level of compatibility varies between the PDF sets.

A number of checks have been performed to validate the obtained results. Firstly, the ratio of $Z \to \mu\mu$ over $Z \to ee$ has been measured to be $1.003 \pm 0.034$, in agreement with unity. Then, in order to study the impact of isolation uncertainties, these were decorrelated for $t\bar{t}$ and $Z$ samples; such treatment of the uncertainties does not impact the result. To estimate the impact of fiducial corrections in $Z$-boson events, decorrelated uncertainties were assigned to out-of-fiducial events, and did not undergo the fiducial correction. The result is found to be not sensitive to any of these effects Finally, the simulated distribution of the $p_{\mathrm{T}}$ of the dilepton pair has been reweighted to match the data perfectly in the $ee$ and $\mu\mu$ events, assuming only $Z$-boson events contributing. After the reweighting, the impact on the total predicted yields has been checked. This impact was found to be below 0.15%, thus negligible.

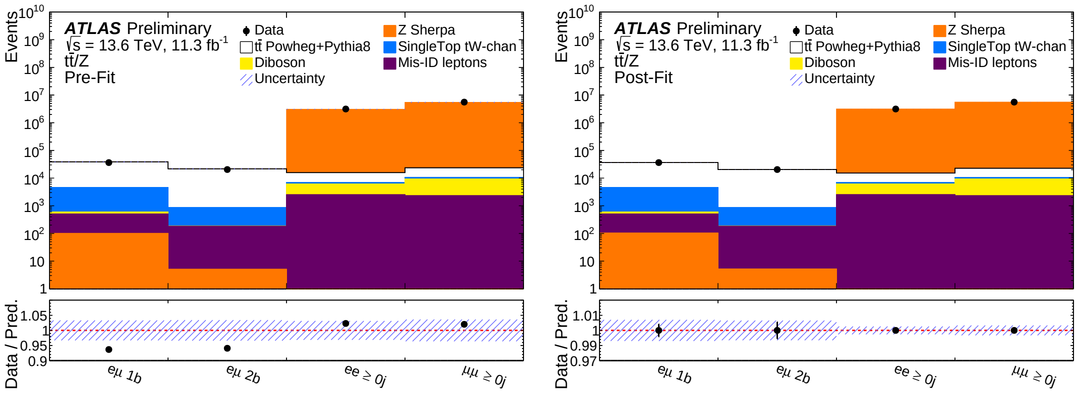

Figure D.4: Comparison of data and prediction for the event yields in the three lepton channels before the fit (left) and after the fit (right). The $e\mu$ channel is split into events with one or two $b$-tagged jets. The bottom panel shows the ratio of data over the prediction. The hashed bands represent the total uncertainty. Correlations of the NPs as obtained from the fit are used to build the uncertainty bad in the post-fit distribution.

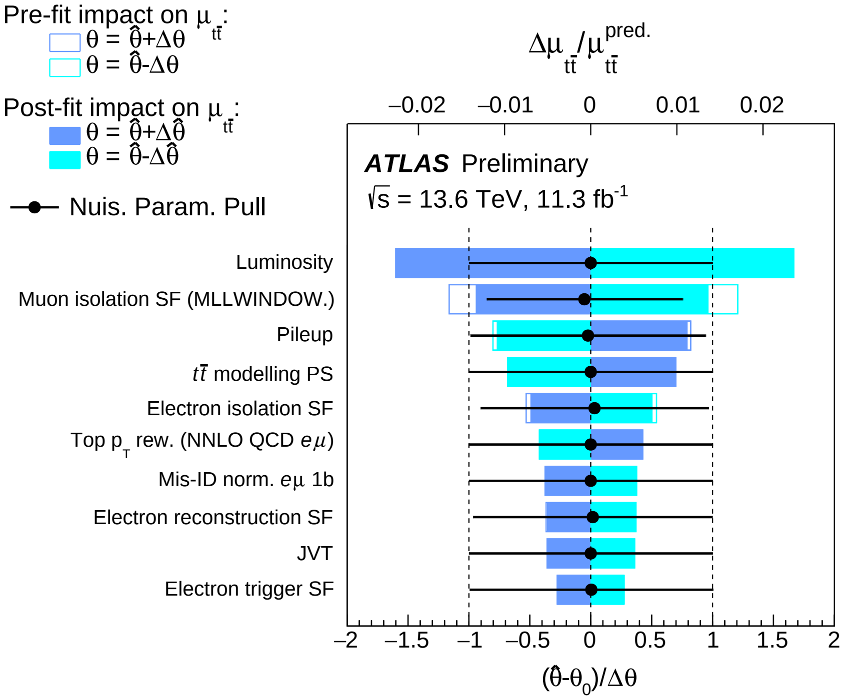

Figure D.5: Ranking plot showing the effect of the 10 most important systematic uncertainties on the measured $t\bar{t}$ cross-section, $\mu$, in the fit to data. The impact of each NP, $\Delta\mu$, is computed by comparing the nominal best-fit value of $\mu/\mu_{\text{pred.}}$ with the result of the fit when fixing the considered nuisance parameter to its best-fit value, ($\theta$), shifted by its pre-fit and post-fit uncertainties $\pm\Delta\theta(\pm\Delta\hat{\theta})$. The empty boxes show the pre-fit impact while the filled boxes show the post-fit impact of each nuisance parameter on the result. The black dots represent the post-fit value (pull) of each NP where the pre-fit value is subtracted, while the black line represents the post-fit uncertainty normalised to the pre-fit uncertainty.

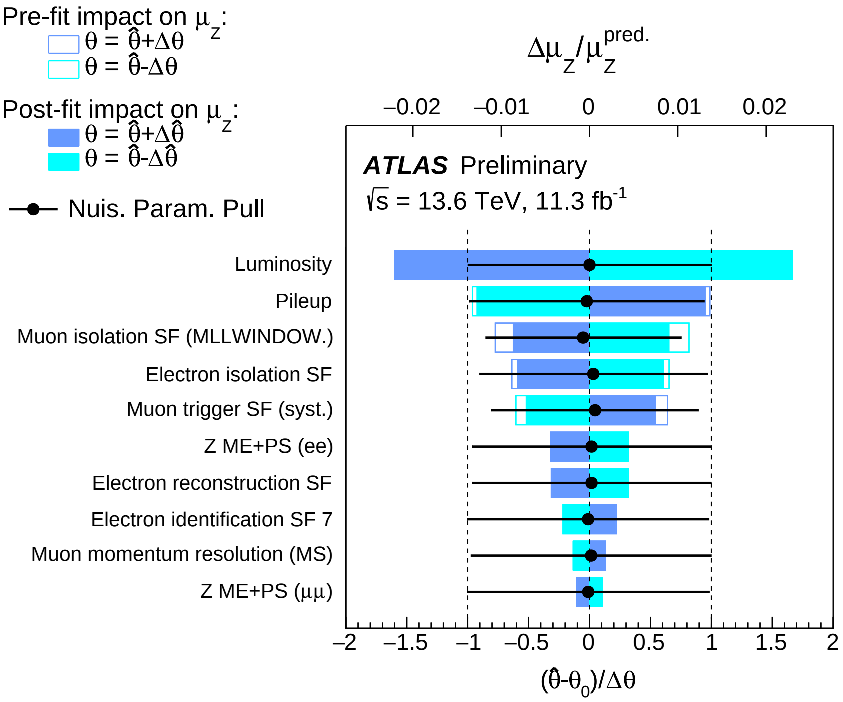

Figure D.6: Ranking plot showing the effect of the 10 most important systematic uncertainties on the measured $Z$ cross-section, $\mu$, in the fit to data. The impact of each NP, $\Delta\mu$, is computed by comparing the nominal best-fit value of $\mu/\mu_{\text{pred.}}$ with the result of the fit when fixing the considered nuisance parameter to its best-fit value, $(\theta)$, shifted by its pre-fit and post-fit uncertainties $\pm\Delta\theta(\pm\Delta\hat{\theta})$. The empty boxes show the pre-fit impact while the filled boxes show the post-fit impact of each nuisance parameter on the result. The black dots represent the post-fit value (pull) of each NP where the pre-fit value is subtracted, while the black line represents the post-fit uncertainty normalised to the pre-fit uncertainty.

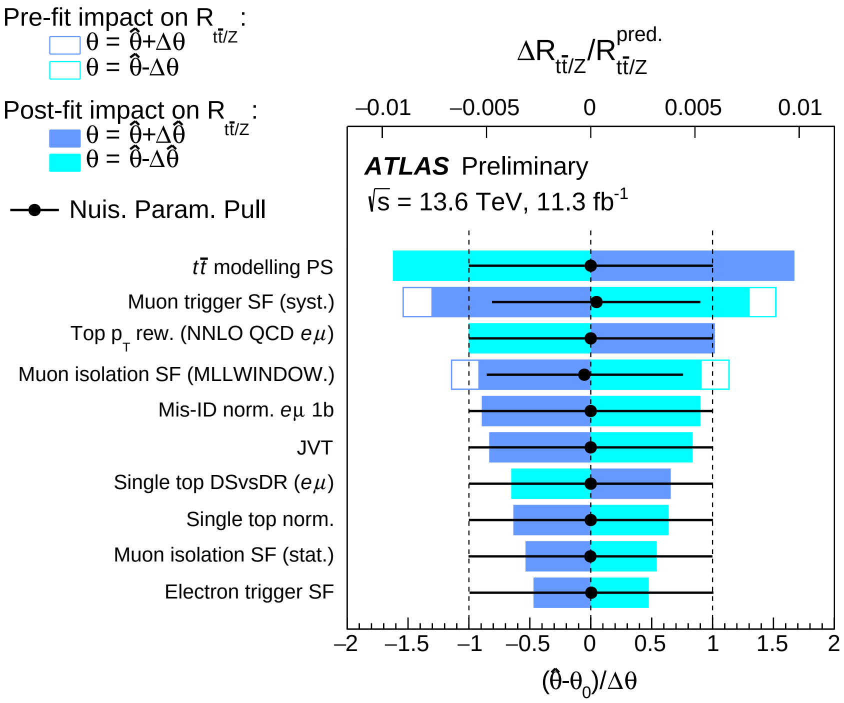

Figure D.7: Ranking plot showing the effect of the 10 most important systematic uncertainties on the measured ratio of the $t\bar{t}$ cross-section over $Z$ cross-section, $R$, in the fit to data. The impact of each NP, $\Delta R/R_{\text{pred.}}$, is computed by comparing the nominal best-fit value of $R/R_{\text{pred.}}$ with the result of the fit when fixing the considered nuisance parameter to its best-fit value, $(\theta)$, shifted by its pre-fit and post-fit uncertainties $\pm\Delta\theta(\pm\Delta\hat{\theta})$. The empty boxes show the pre-fit impact while the filled boxes show the post-fit impact of each nuisance parameter on the result. The black dots represent the post-fit value (pull) of each NP where the pre-fit value is subtracted, while the black line represents the post-fit uncertainty normalised to the pre-fit uncertainty.

|  | **Category** | **Uncert.** [%] |  |  |
|---|---|---|---|---|
|  |  | $\sigma_{t\bar{t}}$ | $\sigma^{\text{fid.}}_{Z\to\ell\ell}$ | $R_{t\bar{t}/Z}$ |
| $t\bar{t}$ | $t\bar{t}$ parton shower/hadronisation | 1.1 | < 0.2 | 1.0 |
|  | $t\bar{t}$ scale variations | 0.2 | < 0.2 | 0.2 |
|  | Top quark $p_{\mathrm{T}}$ reweighting | 0.6 | < 0.2 | 0.5 |
| $Z$ | $Z$ scale variations | 0.2 | 0.5 | 0.3 |
| Bkg. | Single top modelling | 0.4 | < 0.2 | 0.4 |
|  | Diboson modelling | < 0.2 | < 0.2 | < 0.2 |
|  | Mis-Id leptons | 0.5 | < 0.2 | 0.5 |
| Lept. | Electron reconstruction | 1.0 | 1.1 | 0.5 |
|  | Muon reconstruction | 1.5 | 1.2 | 0.8 |
|  | Lepton trigger | 0.4 | 0.7 | 0.8 |
| Jets/tagging | Jet reconstruction | 0.4 | - | 0.3 |
|  | Flavour tagging | 0.2 | - | 0.2 |
|  | PDFs | 0.4 | 0.2 | 0.4 |
|  | Pileup | 1.1 | 1.1 | < 0.2 |
|  | Luminosity | 2.3 | 2.2 | 0.3 |
|  | Systematic Uncertainty | 3.5 | 3.0 | 2.0 |
|  | Statistical Uncertainty | 0.5 | 0.03 | 0.5 |
|  | Total Uncertainty | 3.5 | 3.0 | 2.0 |

Table D.2: Observed impact of the different sources of uncertainty on the measured $t\bar{t}$ and $Z$-boson cross-section and on the ratio $R_{t\bar{t}/Z}$, grouped by categories. The impact of each category is obtained by repeating the fit after having fixed the set of nuisance parameters corresponding to that category, subtracting the square of the resulting uncertainty from the square of the uncertainty found in the full fit, and calculating the square root. The statistical uncertainty is obtained by repeating the fit after having fixed all nuisance parameters to their fitted values. Only the acceptance effects are considered for the PDF and the modelling uncertainties.

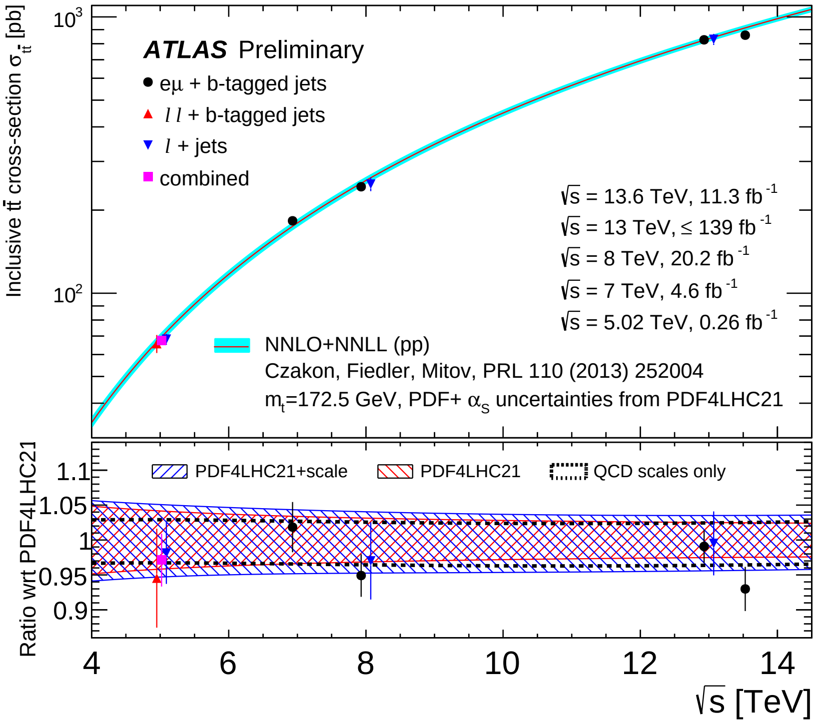

Figure D.8: Comparison of the measures $t\bar{t}$ cross-section compared to theory predictions using the PDF4LHC21 PDF set. The measurements shown include $e\mu$ final state ($e\mu$ + $b$-tagged jets); $ee$, $\mu\mu$ and $e\mu$ final states ($ll$ + $b$-tagged jets); single lepton final states ($l$ + jets); as well as combinations of final states (combined). The bottom panel shows the ratio of the measured values and three predictions that either contain only the uncertainties originating from the QCD scale variations (black), only the variations in the PDF uncertainties (red) or the total uncertainty in the prediction (blue).

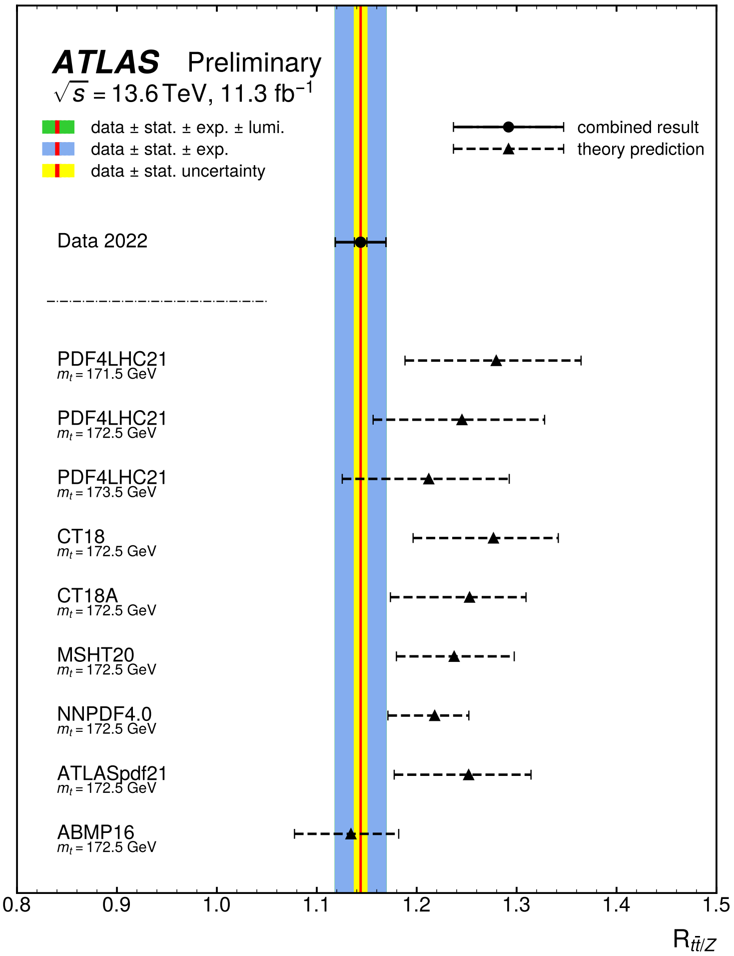

Figure D.9: Ratio of the $t\bar{t}$ to the $Z$-boson cross-section compared to the prediction for several sets of parton distribution functions. For the PDF4LH21 PDF set, predictions for different assumptions about the top-quark mass are also displayed.

# Appendix E

# Nuisance parameters: correlation matrices, pulls, and constraints

This appendix reports the correlation matrices, the pull plots and the ranking of the nuisance parameters for the systematic uncertainties included in the fit. Figures E.1, E.2, and E.3 shows the impact of most important systematic uncertainties on the cross-section ratio. Correlations for the $t\bar{t}$, $Z$ and ratio measurements are displayed respectively in Figures E.4, E.6, and E.8. The correlations are extracted using the method described in Section 5.2.1.

On the other hand, pulls and constraints of the NPs are shown in Figures E.5, E.7, and E.9.

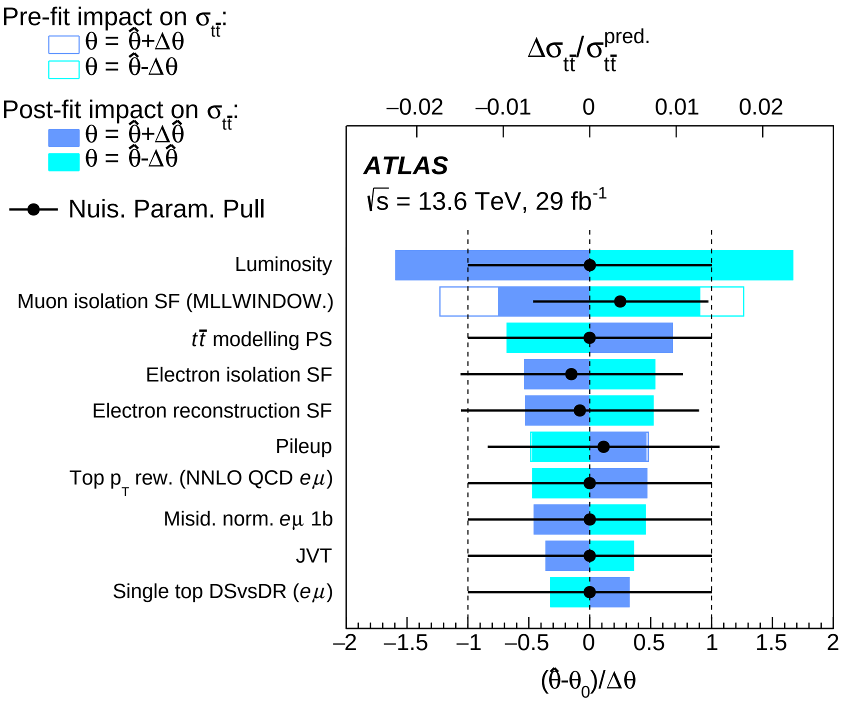

Figure E.1: Ranking of the 10 most important NPs in the simultaneous fit of $t\bar{t}$ and $Z$-boson cross sections to data. The impact of each NP on the measured $t\bar{t}$ cross section, $\Delta\sigma_{t\bar{t}}$, is defined as the shift induced in $\sigma_{t\bar{t}}$ as the NP is shifted by its pre-fit and post-fit uncertainties $\pm\Delta\theta(\pm\Delta\hat{\theta})$ from its nominal best-fit value, $\hat{\theta}$, and then fixed while all other NPs profiled. The empty boxes show the pre-fit impact while the filled boxes show the post-fit impact of each nuisance parameter on the result. The black dots represent the post-fit value (pull) of each NP where the pre-fit value is subtracted, while the black line represents the post-fit uncertainty normalised to the pre-fit uncertainty.

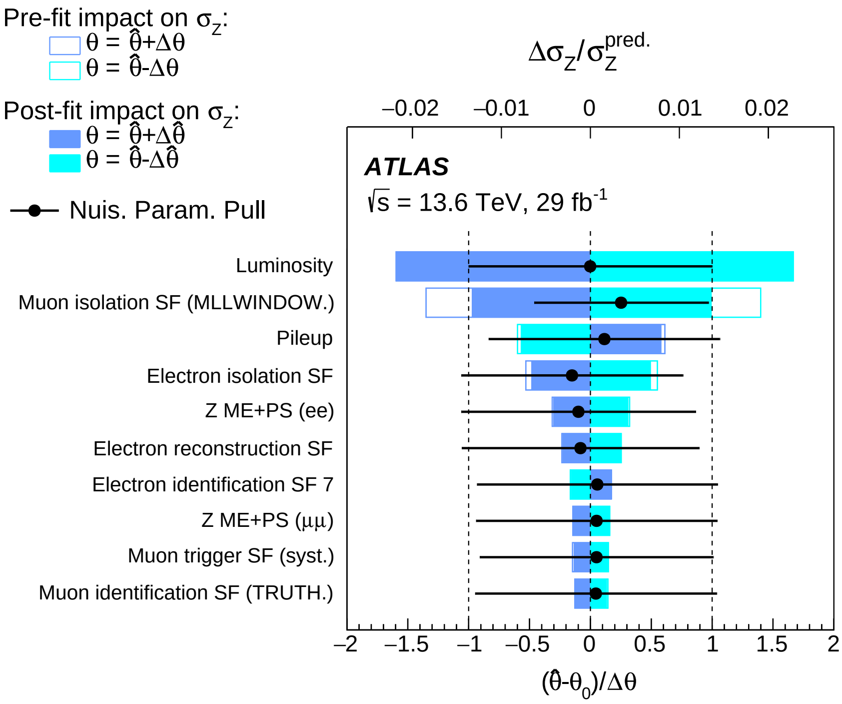

Figure E.2: Ranking plot showing the effect of the 10 most important systematic uncertainties in the fit to $ee$ and $\mu\mu$ data. The impact of each NP on the measured fiducial $Z$-boson cross section, $\Delta\sigma_Z$, is defined as the shift induced in $\sigma_Z$ as the NP is shifted by its pre-fit and post-fit uncertainties $\pm\Delta\theta(\pm\Delta\hat{\theta})$ from its nominal best-fit value, $\hat{\theta}$, and then fixed while all other NPs profiled. The empty boxes show the pre-fit impact while the filled boxes show the post-fit impact of each nuisance parameter on the result. The black dots represent the post-fit value (pull) of each NP where the pre-fit value is subtracted, while the black line represents the post-fit uncertainty normalised to the pre-fit uncertainty.

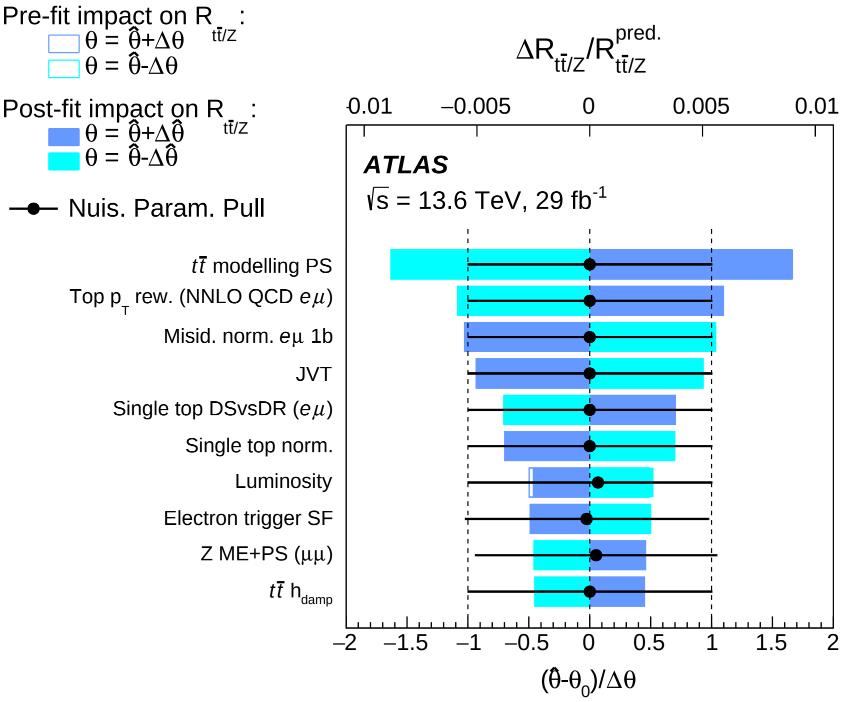

Figure E.3: Ranking plot showing the effect of the 10 most important systematic uncertainties on the measured ratio of the $t\bar{t}$ cross-section over $Z$ cross-section, $R$, in the fit to data. The impact of each NP, $\Delta R/R_{\text{pred.}}$, is computed by comparing the nominal best-fit value of $R/R_{\text{pred.}}$ with the result of the fit when fixing the considered nuisance parameter to its best-fit value, $(\theta)$, shifted by its pre-fit and post-fit uncertainties $\pm\Delta\theta(\pm\Delta\hat{\theta})$. The empty boxes show the pre-fit impact while the filled boxes show the post-fit impact of each nuisance parameter on the result. The black dots represent the post-fit value (pull) of each NP where the pre-fit value is subtracted, while the black line represents the post-fit uncertainty normalised to the pre-fit uncertainty.

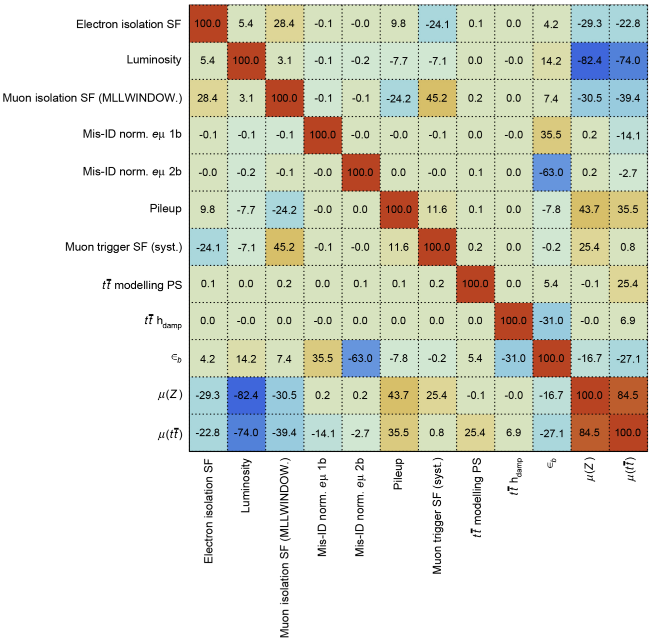

| | Electron isolation SF | Luminosity | Muon isolation SF (MLLWINDOW.) | Mis-ID norm. $e\mu$ 1b | Mis-ID norm. $e\mu$ 2b | Pileup | Muon trigger SF (syst.) | $t\bar{t}$ modelling PS | $t\bar{t}$ $h_{damp}$ | $\epsilon_b$ | $\mu(Z)$ | $\mu(t\bar{t})$ |
|---|---|---|---|---|---|---|---|---|---|---|---|---|
| Electron isolation SF | 100.0 | 5.4 | 28.4 | -0.1 | -0.0 | 9.8 | -24.1 | 0.1 | 0.0 | 4.2 | -29.3 | -22.8 |
| Luminosity | 5.4 | 100.0 | 3.1 | -0.1 | -0.2 | -7.7 | -7.1 | 0.0 | -0.0 | 14.2 | -82.4 | -74.0 |
| Muon isolation SF (MLLWINDOW.) | 28.4 | 3.1 | 100.0 | -0.1 | -0.1 | -24.2 | 45.2 | 0.2 | 0.0 | 7.4 | -30.5 | -39.4 |
| Mis-ID norm. $e\mu$ 1b | -0.1 | -0.1 | -0.1 | 100.0 | -0.0 | -0.0 | -0.1 | 0.0 | -0.0 | 35.5 | 0.2 | -14.1 |
| Mis-ID norm. $e\mu$ 2b | -0.0 | -0.2 | -0.1 | -0.0 | 100.0 | 0.0 | -0.0 | 0.1 | 0.0 | -63.0 | 0.2 | -2.7 |
| Pileup | 9.8 | -7.7 | -24.2 | -0.0 | 0.0 | 100.0 | 11.6 | 0.1 | 0.0 | -7.8 | 43.7 | 35.5 |
| Muon trigger SF (syst.) | -24.1 | -7.1 | 45.2 | -0.1 | -0.0 | 11.6 | 100.0 | 0.2 | 0.0 | -0.2 | 25.4 | 0.8 |
| $t\bar{t}$ modelling PS | 0.1 | 0.0 | 0.2 | 0.0 | 0.1 | 0.1 | 0.2 | 100.0 | 0.0 | 5.4 | -0.1 | 25.4 |
| $t\bar{t}$ $h_{damp}$ | 0.0 | -0.0 | 0.0 | -0.0 | 0.0 | 0.0 | 0.0 | 0.0 | 100.0 | -31.0 | -0.0 | 6.9 |
| $\epsilon_b$ | 4.2 | 14.2 | 7.4 | 35.5 | -63.0 | -7.8 | -0.2 | 5.4 | -31.0 | 100.0 | -16.7 | -27.1 |
| $\mu(Z)$ | -29.3 | -82.4 | -30.5 | 0.2 | 0.2 | 43.7 | 25.4 | -0.1 | -0.0 | -16.7 | 100.0 | 84.5 |
| $\mu(t\bar{t})$ | -22.8 | -74.0 | -39.4 | -14.1 | -2.7 | 35.5 | 0.8 | 25.4 | 6.9 | -27.1 | 84.5 | 100.0 |

Figure E.4: Correlations of nuisance parameters in the fit to the observed data for the $t\bar{t}$ fit. Only entries with correlation larger than 20% are shown.

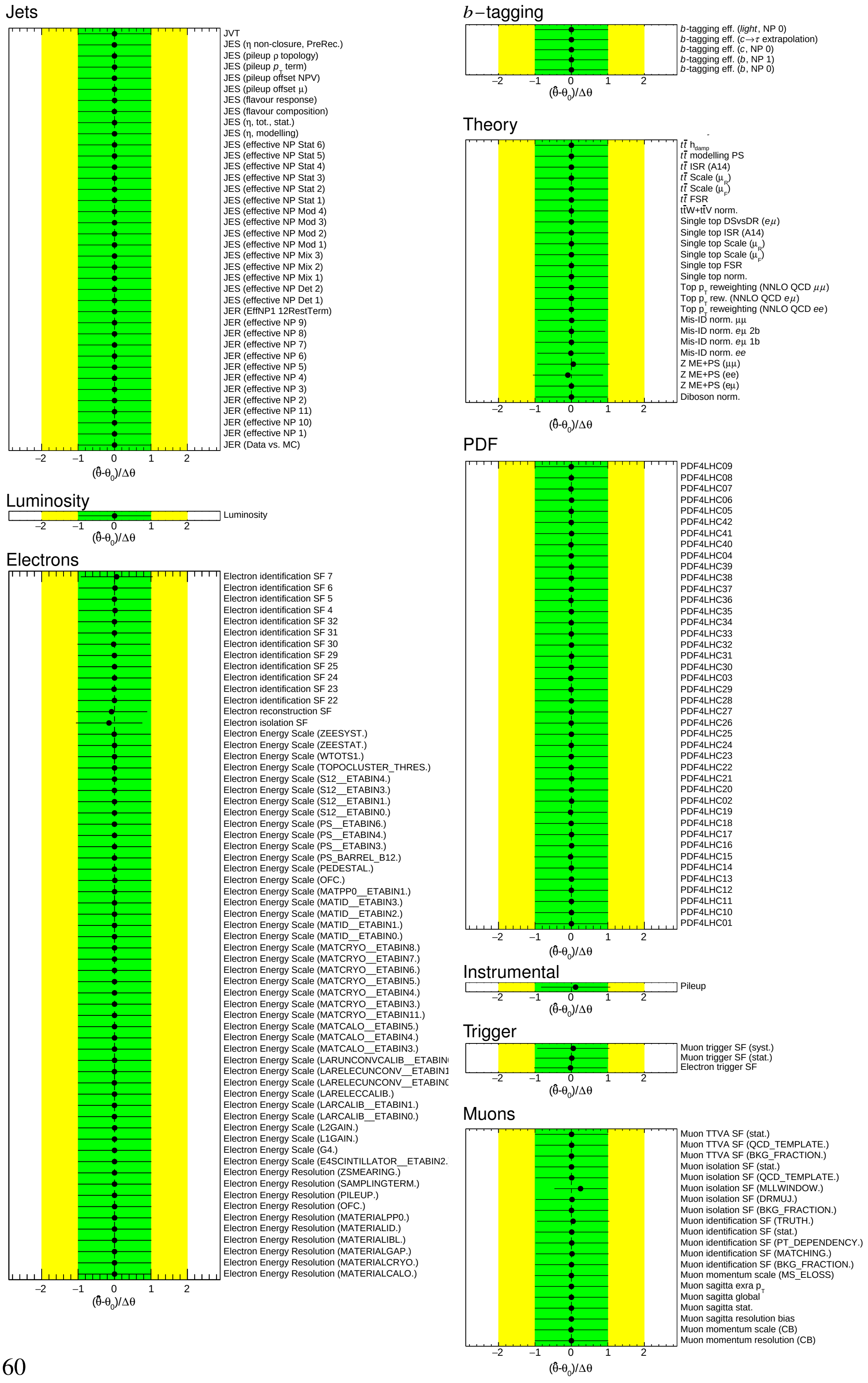

Figure E.5: Fitted nuisance parameters after a fit to the observed data for the $t\bar{t}$ fit. NPs are arranged in different groups.

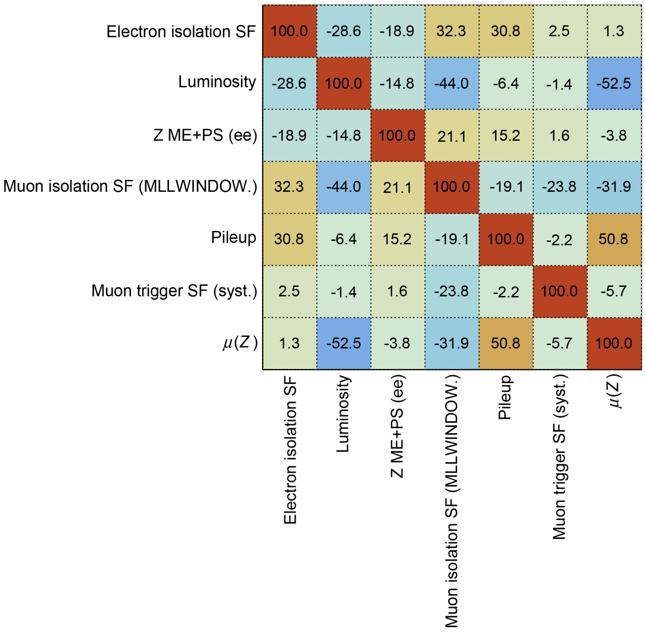

| | Electron isolation SF | Luminosity | Z ME+PS (ee) | Muon isolation SF (MLLWINDOW.) | Pileup | Muon trigger SF (syst.) | $\mu(Z)$ |
|---|---|---|---|---|---|---|---|
| Electron isolation SF | 100.0 | -28.6 | -18.9 | 32.3 | 30.8 | 2.5 | 1.3 |
| Luminosity | -28.6 | 100.0 | -14.8 | -44.0 | -6.4 | -1.4 | -52.5 |
| Z ME+PS (ee) | -18.9 | -14.8 | 100.0 | 21.1 | 15.2 | 1.6 | -3.8 |
| Muon isolation SF (MLLWINDOW.) | 32.3 | -44.0 | 21.1 | 100.0 | -19.1 | -23.8 | -31.9 |
| Pileup | 30.8 | -6.4 | 15.2 | -19.1 | 100.0 | -2.2 | 50.8 |
| Muon trigger SF (syst.) | 2.5 | -1.4 | 1.6 | -23.8 | -2.2 | 100.0 | -5.7 |
| $\mu(Z)$ | 1.3 | -52.5 | -3.8 | -31.9 | 50.8 | -5.7 | 100.0 |

Figure E.6: Correlations of nuisance parameters in the fit to the observed data for the $Z$ fit. Only entries with correlation larger than 20% are shown.

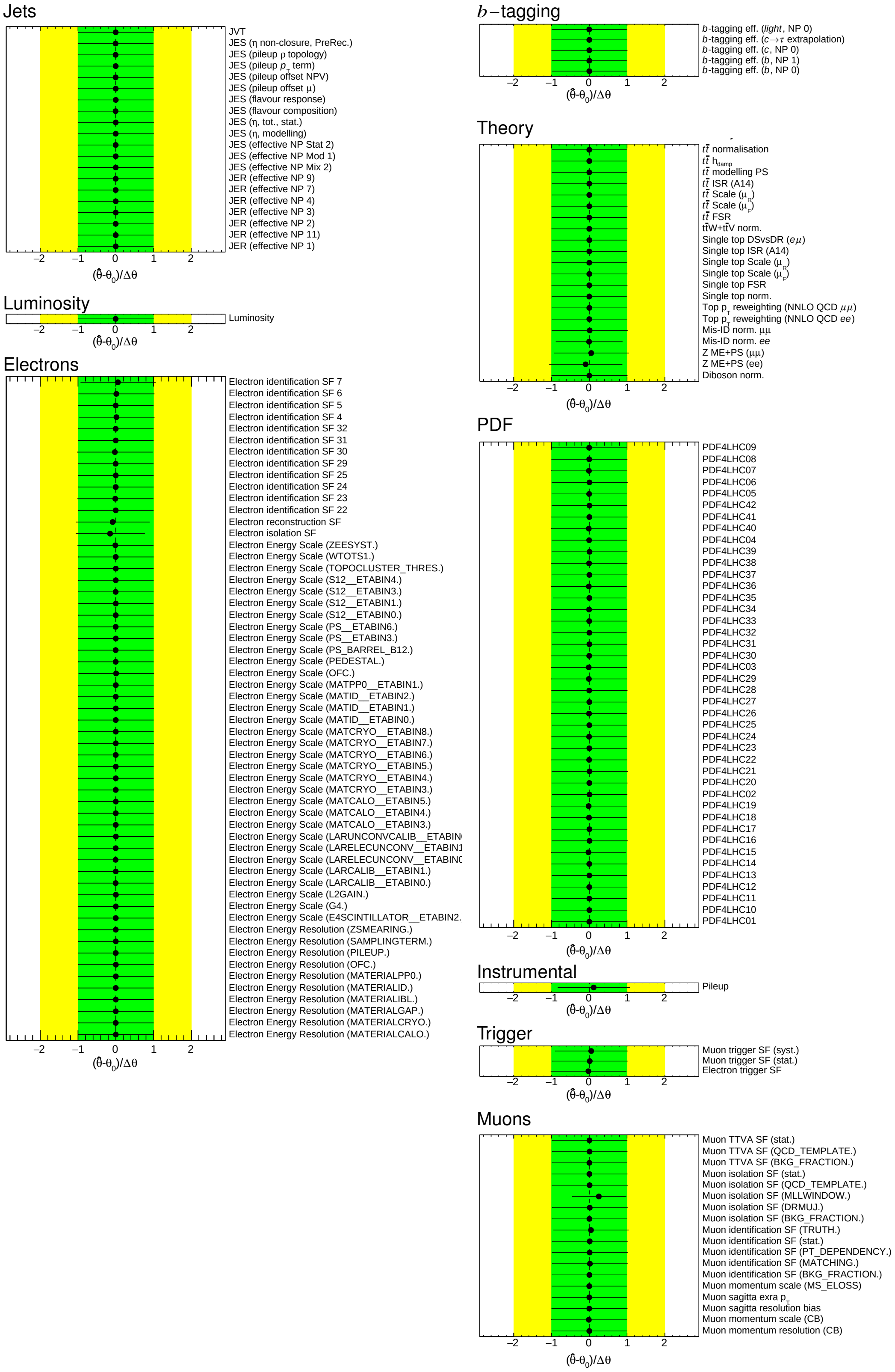

Figure E.7: Fitted nuisance parameters after a fit to the observed data for the Z fit. NPs are arranged in different groups.

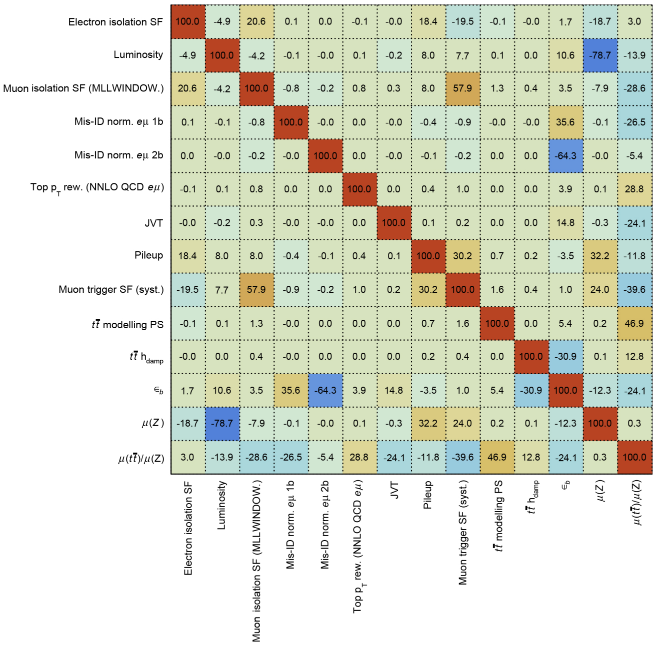

| | Electron isolation SF | Luminosity | Muon isolation SF (MLLWINDOW.) | Mis-ID norm. $e\mu$ 1b | Mis-ID norm. $e\mu$ 2b | Top $p_T$ rew. (NNLO QCD $e\mu$) | JVT | Pileup | Muon trigger SF (syst.) | $t\bar{t}$ modelling PS | $t\bar{t}$ $h_{damp}$ | $\epsilon_b$ | $\mu(Z)$ | $\mu(t\bar{t})/\mu(Z)$ |
|---|---|---|---|---|---|---|---|---|---|---|---|---|---|---|
| Electron isolation SF | 100.0 | -4.9 | 20.6 | 0.1 | 0.0 | -0.1 | -0.0 | 18.4 | -19.5 | -0.1 | -0.0 | 1.7 | -18.7 | 3.0 |
| Luminosity | -4.9 | 100.0 | -4.2 | -0.1 | -0.0 | 0.1 | -0.2 | 8.0 | 7.7 | 0.1 | 0.0 | 10.6 | -78.7 | -13.9 |
| Muon isolation SF (MLLWINDOW.) | 20.6 | -4.2 | 100.0 | -0.8 | -0.2 | 0.8 | 0.3 | 8.0 | 57.9 | 1.3 | 0.4 | 3.5 | -7.9 | -28.6 |
| Mis-ID norm. $e\mu$ 1b | 0.1 | -0.1 | -0.8 | 100.0 | -0.0 | 0.0 | -0.0 | -0.4 | -0.9 | -0.0 | -0.0 | 35.6 | -0.1 | -26.5 |
| Mis-ID norm. $e\mu$ 2b | 0.0 | -0.0 | -0.2 | -0.0 | 100.0 | 0.0 | -0.0 | -0.1 | -0.2 | 0.0 | 0.0 | -64.3 | -0.0 | -5.4 |
| Top $p_T$ rew. (NNLO QCD $e\mu$) | -0.1 | 0.1 | 0.8 | 0.0 | 0.0 | 100.0 | 0.0 | 0.4 | 1.0 | 0.0 | 0.0 | 3.9 | 0.1 | 28.8 |
| JVT | -0.0 | -0.2 | 0.3 | -0.0 | -0.0 | 0.0 | 100.0 | 0.1 | 0.2 | 0.0 | 0.0 | 14.8 | -0.3 | -24.1 |
| Pileup | 18.4 | 8.0 | 8.0 | -0.4 | -0.1 | 0.4 | 0.1 | 100.0 | 30.2 | 0.7 | 0.2 | -3.5 | 32.2 | -11.8 |
| Muon trigger SF (syst.) | -19.5 | 7.7 | 57.9 | -0.9 | -0.2 | 1.0 | 0.2 | 30.2 | 100.0 | 1.6 | 0.4 | 1.0 | 24.0 | -39.6 |
| $t\bar{t}$ modelling PS | -0.1 | 0.1 | 1.3 | -0.0 | 0.0 | 0.0 | 0.0 | 0.7 | 1.6 | 100.0 | 0.0 | 5.4 | 0.2 | 46.9 |
| $t\bar{t}$ $h_{damp}$ | -0.0 | 0.0 | 0.4 | -0.0 | 0.0 | 0.0 | 0.0 | 0.2 | 0.4 | 0.0 | 100.0 | -30.9 | 0.1 | 12.8 |
| $\epsilon_b$ | 1.7 | 10.6 | 3.5 | 35.6 | -64.3 | 3.9 | 14.8 | -3.5 | 1.0 | 5.4 | -30.9 | 100.0 | -12.3 | -24.1 |
| $\mu(Z)$ | -18.7 | -78.7 | -7.9 | -0.1 | -0.0 | 0.1 | -0.3 | 32.2 | 24.0 | 0.2 | 0.1 | -12.3 | 100.0 | 0.3 |
| $\mu(t\bar{t})/\mu(Z)$ | 3.0 | -13.9 | -28.6 | -26.5 | -5.4 | 28.8 | -24.1 | -11.8 | -39.6 | 46.9 | 12.8 | -24.1 | 0.3 | 100.0 |

Figure E.8: Correlations of nuisance parameters in the fit to the observed data for the ratio fit. Only entries with correlation larger than 20% are shown.

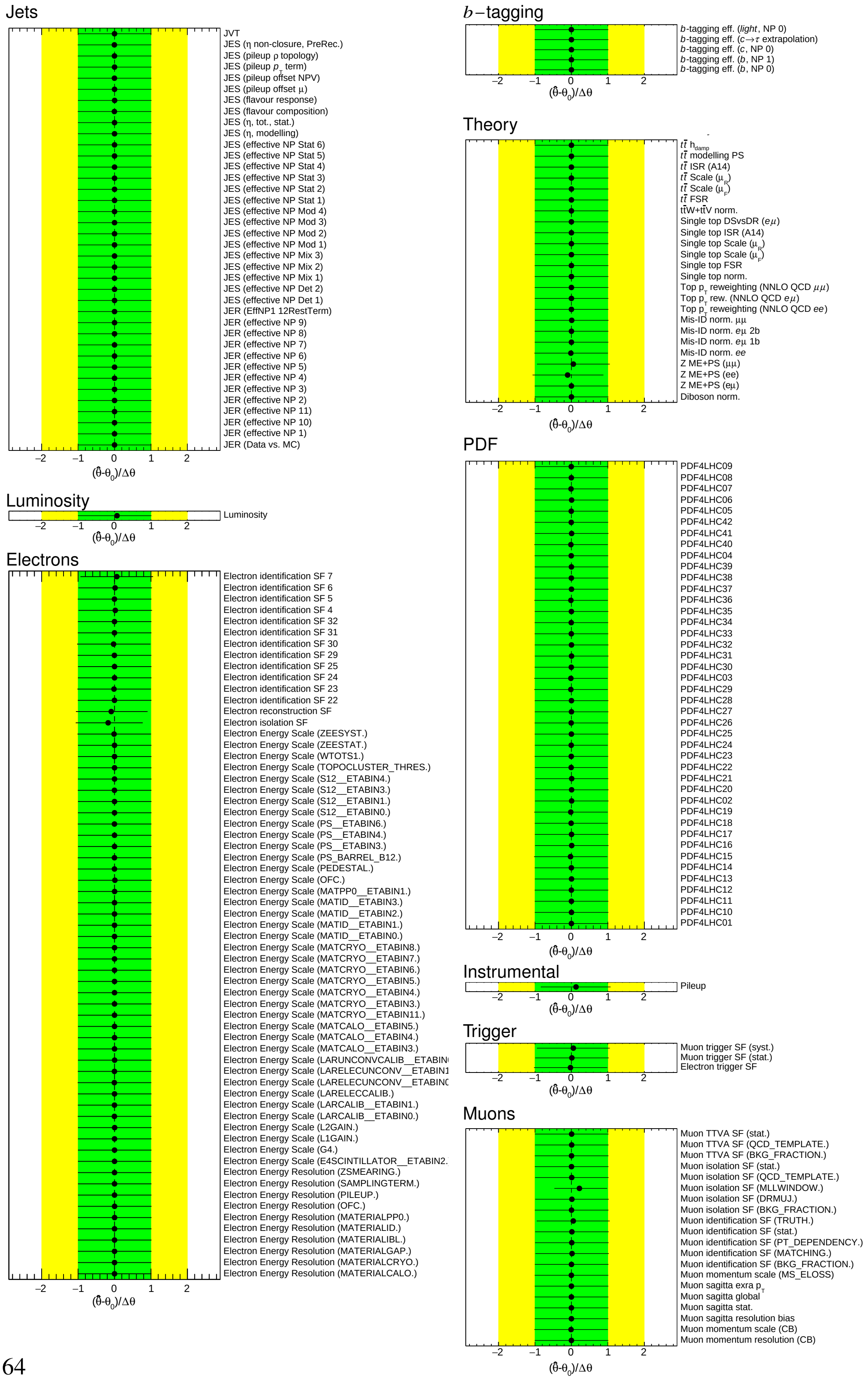

Figure E.9: Fitted nuisance parameters after a fit to the observed data for the ratio fit. NPs are arranged in different groups.

# Studies performed in ATLAS-CONF-2022-070

# Appendix F

# Trigger scale-factors calculation

Usually, centrally provided tools are used to calculate the trigger scale-factors (SFs). However, given the early stage of Run 3, a custom implementation is used, summarised in this appendix.

The inputs for the trigger SF calculations are as follows. Trigger efficiencies for the electron triggers in data and in simulation, parametrised as a function of lepton $\eta$, split into the individual triggers. Trigger efficiencies for the muon triggers in data and in simulation, parametrised as a function of lepton $\eta$ and $\phi$, split into central ($|\eta| < 1.05$) and forward $|\eta| > 1.05$ triggers, provided as a logical OR of the two muon triggers used. The provided efficiencies are valid for leptons with $p_{\mathrm{T}} > 27$ GeV.

The SFs are calculated using the following formula

$$\epsilon_{\mathrm{Data(MC)}} \equiv \epsilon_{1,\,\mathrm{Data(MC)}} + \epsilon_{2,\,\mathrm{Data(MC)}} - \epsilon_{1,\,\mathrm{Data(MC)}}\epsilon_{2,\,\mathrm{Data(MC)}} \tag{F.1}$$

$$\mathrm{SF} = \frac{\epsilon_{\mathrm{Data}}}{\epsilon_{\mathrm{MC}}}, \tag{F.2}$$

where $\epsilon_{1,\,\mathrm{Data(MC)}}$ is the trigger efficiency for the first lepton as measured in data(MC simulation) and similarly for $\epsilon_{2,\,\mathrm{Data(MC)}}$. The efficiency formula can be rewritten as

$$\epsilon_{\mathrm{Data(MC)}} = 1 - \left(1 - \epsilon_{1,\,\mathrm{Data(MC)}}\right)\left(1 - \epsilon_{2,\,\mathrm{Data(MC)}}\right). \tag{F.3}$$

Since the electron trigger efficiencies are provided only for each of the individual triggers separately and not as a logical OR, the trigger efficiency from the lowest $p_{\mathrm{T}}$ trigger is used because it is unlikely that the lowest $p_{\mathrm{T}}$ trigger is not fired and the efficiencies between the different triggers are very similar.

The systematic uncertainties for the trigger efficiencies are calculated using the provided variations for data and MC simulation for the muon triggers, split into statistical and systematic variations. Electron trigger performance has been studied through data and MC efficiencies comparisons. Run 3 data collected between 19 Jul and 15 Aug 2022 for stable beam runs with more than 600 bunches are used, together with a MC sample of $Z \to ee$ events. Single electron trigger SFs are taken equal to 1, with an uncertainty derived as the difference between 1 and the data to MC ratio. The uncertainty is computed as a function of $\eta$ for the using 5 $\eta$ bins.

# Appendix G

# MC-MC efficiency maps for flavour tagging

This appendix describes the studies performed to investigate the efficiency of flavour tagging on different Monte Carlo generators, exploiting $t\bar{t}$ samples.

Three different samples were used, corresponding to three different generators, namely Powheg Box v2 + Pythia 8, Powheg Box v2 + Herwig 7 and Sherpa 2.2.12. For each generator, a nominal 2D (jet $p_T$ vs. jet $\eta$) efficiency map is obtained by computing the ratio between the events that pass the selection criteria and the inclusive set. The selection requires at least one reconstructed jet with $p_T > 5$ GeV and $\eta < |2.5|$, using the DL1d tagger at 77% fixed efficiency working point. Efficiency maps for $b-$, $c-$, and light quarks tagging are computed and shown in Figure G.1.

In order to assess the uncertainty on flavour tagging coming from the choice of a specific generator, the ratio between the 2D efficiency maps of different generators is computed. The ratio plots are displayed in Figure G.2. Since there is no evidence of significant variations between the extracted SFs and the ones in use during Run 2, no additional flavour tagging uncertainty is added to the analysis.

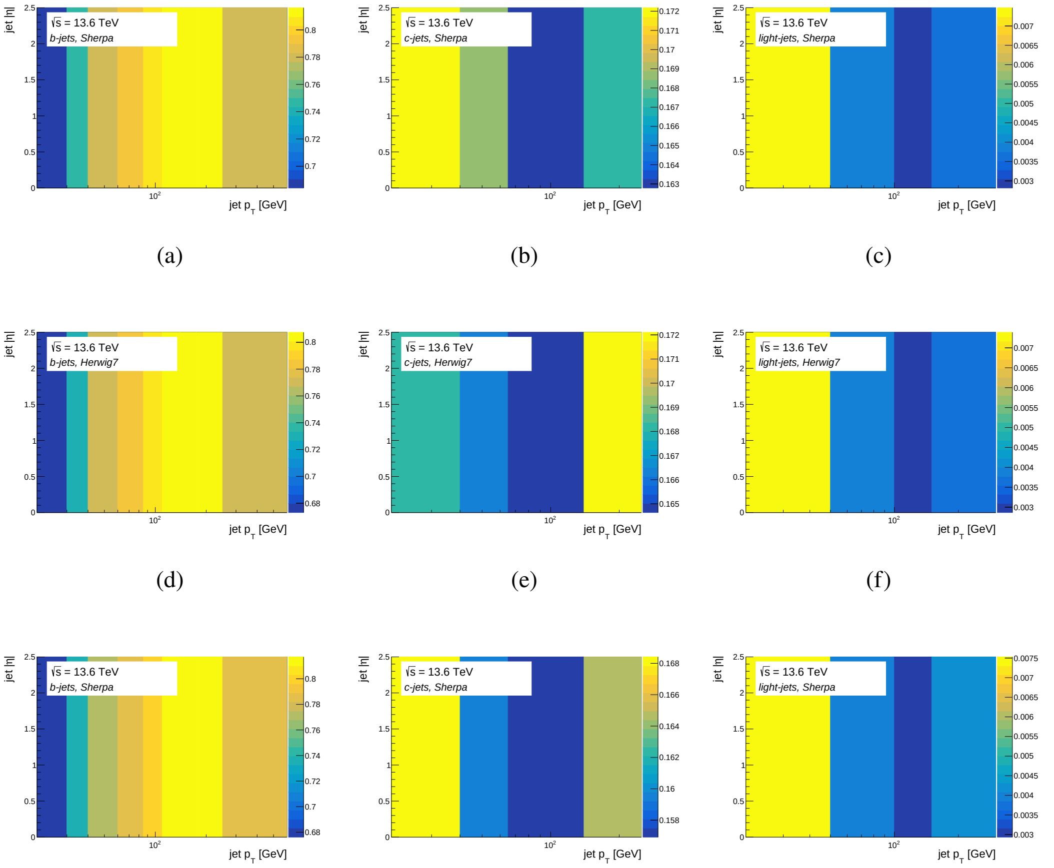

(a) (b) (c)

(d) (e) (f)

(g) (h) (i)

Figure G.1: Efficiency maps for $t\bar{t}$ sample using Powheg Box v2 +Pythia 8 displaying $b$-jets (a), $c$-jets (b), and light jets (c); Powheg Box v2 +Herwig 7 displaying $b$-jets (d), $c$-jets (e), and light jets (f); Sherpa 2.2.12 displaying $b$-jets (g), $c$-jets (h), and light jets (i).

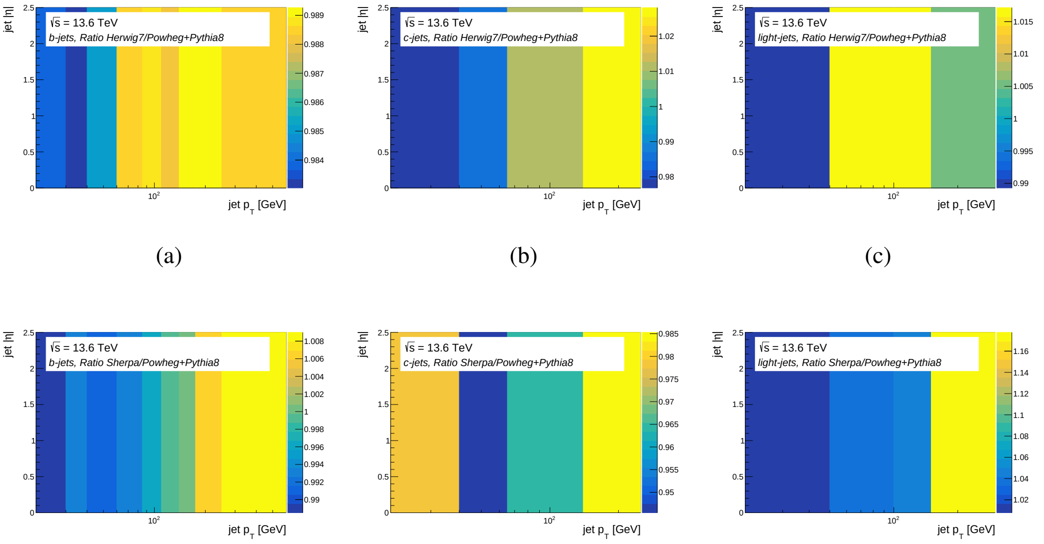

(a) (b) (c)

(d) (e) (f)

Figure G.2: Efficiency maps ratio for $t\bar{t}$ between Powheg Box v2 +Herwig 7 and Powheg Box v2 +Pythia 8, displaying $b$-jets (a), $c$-jets (b), and light jets (c) alongisde with the ratio between Sherpa 2.2.12 and Powheg Box v2 +Pythia 8, displaying $b$-jets (d), $c$-jets (e), and light jets (f).

# Appendix H

# Acceptances for fiducial-level $Z$

This appendix describes the acceptances calculated for the fiducial-level selection on the $Z$ dilepton, same-flavor MC samples (i.e. $ee$ and $\mu\mu$). A selection requiring all leptons to fulfill $p_\mathrm{T} > 27\,\mathrm{GeV}$ and $|\eta| < 2.5$, as well as a dilepton mass requirement of $66\,\mathrm{GeV} < m_{\ell\ell} < 116\,\mathrm{GeV}$ is applied on all events on particle-level, for both bare, and dressed leptons, separately. This selection matches the reco-level selection used in the analysis. For all passing events, the individual weights are summed and finally scaled by the sum of all weights regardless of the selection, giving the acceptance

$$\mathrm{acc}_\mathrm{var} = \frac{\sum_\text{events passing selection} [\text{weight}\,(\text{var})]}{\sum_\text{all events} [\text{weight}\,(\text{var})]}. \tag{H.1}$$

The acceptances for the $ee$ and $\mu\mu$ events are then calculated by building the weighted mean considering the filter efficiencies of the events. Truth-level $\tau^+\tau^-$ events are not considered. The statistical uncertainties on the acceptances are calculated as

$$\sigma_{\text{stat, acc}_\text{var}} = \frac{\sqrt{\sum_\text{events passing selection} [\text{weight}\,(\text{var})]^2}}{\sum_\text{all events} [\text{weight}\,(\text{var})]}. \tag{H.2}$$

These acceptances are given in Table H.1. The statistical uncertainties of the acceptances are of the order of magnitude of $10^{-4}$. They cover the differences between the $ee$ and $\mu\mu$ acceptance on the dressed lepton level. The systematic uncertainty on the nominal acceptance is chosen as the largest deviation between nominal and the acceptances of the variations. The nominal acceptances are

$$\mathrm{acc}_{\mathrm{nom},\, ee\ \mathrm{dressed}} = 0.105 \pm 0.003 \tag{H.3}$$

$$\mathrm{acc}_{\mathrm{nom},\, ee\ \mathrm{bare}} = 0.099 \pm 0.003 \tag{H.4}$$

$$\mathrm{acc}_{\mathrm{nom},\, \mu\mu\ \mathrm{dressed}} = 0.109 \pm 0.003 \tag{H.5}$$

$$\mathrm{acc}_{\mathrm{nom},\, \mu\mu\ \mathrm{bare}} = 0.107 \pm 0.003. \tag{H.6}$$

From the acceptances, the fiducial cross-section and reco-level scale variation uncertainties can be corrected.

| | Acceptances | | | |
|---|---|---|---|---|
| | $ee$ events | | $\mu\mu$ events | |
| Variation | dressed | bare | dressed | bare |
| Weight | 1.05298 | 9.93011 | 1.08638 | 1.06772 |
| MUR05_MUF05_PDF303200_PSMUR05_PSMUF05 | 1.04685 | 9.87414 | 1.08029 | 1.06174 |
| ME_ONLY_MUR05_MUF05_PDF303200_PSMUR05_PSMUF05 | 1.05308 | 9.93166 | 1.08672 | 1.06807 |
| MUR05_MUF1_PDF303200_PSMUR05_PSMUF1 | 1.04954 | 9.89809 | 1.08286 | 1.06431 |
| ME_ONLY_MUR05_MUF1_PDF303200_PSMUR05_PSMUF1 | 1.04908 | 9.89336 | 1.08255 | 1.06397 |
| MUR1_MUF05_PDF303200_PSMUR1_PSMUF05 | 1.04809 | 9.88502 | 1.08120 | 1.06259 |
| ME_ONLY_MUR1_MUF05_PDF303200_PSMUR1_PSMUF05 | 1.05601 | 9.95920 | 1.08920 | 1.07049 |
| MUR1_MUF1_PDF303200 | 1.05298 | 9.93011 | 1.08638 | 1.06772 |
| ME_ONLY_MUR1_MUF1_PDF303200 | 1.05298 | 9.93011 | 1.08638 | 1.06772 |
| MUR1_MUF2_PDF303200_PSMUR1_PSMUF2 | 1.07951 | 1.01822 | 1.11223 | 1.09324 |
| ME_ONLY_MUR1_MUF2_PDF303200_PSMUR1_PSMUF2 | 1.05004 | 9.90208 | 1.08322 | 1.06463 |
| MUR2_MUF1_PDF303200_PSMUR2_PSMUF1 | 1.05674 | 9.96577 | 1.08927 | 1.07059 |
| ME_ONLY_MUR2_MUF1_PDF303200_PSMUR2_PSMUF1 | 1.05558 | 9.95447 | 1.08856 | 1.06986 |
| MUR2_MUF2_PDF303200_PSMUR2_PSMUF2 | 1.08526 | 1.02364 | 1.11724 | 1.09821 |
| ME_ONLY_MUR2_MUF2_PDF303200_PSMUR2_PSMUF2 | 1.05344 | 9.93397 | 1.08645 | 1.06780 |

Table H.1: The particle-level acceptances for different variations are shown, separated for $ee$ and $\mu\mu$ events. The variations include the nominal (Weight) and scale variations, for both matrix element and parton shower, as well as matrix element-only (ME_ONLY).

# Studies performed in ATLAS-CONF-2023-006

# Appendix I

# $b$-tag calibration

This appendix briefly describes the calibration procedure employed for the calculation of the SFs used to correct the efficiency of tagging a true $b$-jet. Section I.1 presents the results of the obtained SFs with their uncertainties as a function of the jet transverse momentum.

The calibration exploits $t\bar{t}$ decays into and electron and a muon pair. Events with exactly one electron and one muon with a $p_T > 27$ GeV were selected, using the same single lepton triggers and lepton definitions used for the cross-section measurement. The jets are also defined as done in the cross-section measurement, with the main difference being that the $p_{\mathrm{T}}$ cut applied here is lowered to 20 GeV.

The scale factors and efficiencies shown below include updated jet calibration (see Section 4.7.3), while the relative uncertainties are based on the previous jet calibration. The jet uncertainties are very conservative and should cover the differences.

## I.1 Results of the calibration

For the extraction of the scale factors and uncertainties, the likelihood method described in Ref. [213] is employed. The main difference to the method described in this reference is that in the setup used here, the control regions were not yet included in the fit. The additional cuts on $m_{j_1,\ell}$ and $m_{j_2,\ell}$ were however already applied to improve the $bb$ purity in the signal region. The results shown below only correspond to the 77% efficiency working point which is used in the analysis presented in this thesis. Figure I.1 shows the $b$-tagging efficiency and corresponding scale factor for the 77% working point. At low momentum, the relative uncertainties are large and dominated by pileup-related uncertainties as well as hadronisation and parton-shower effects. The jets used in the cross-section measurement have a larger $p_{\mathrm{T}}$ cut of 30 GeV and are less affected by the uncertainties.

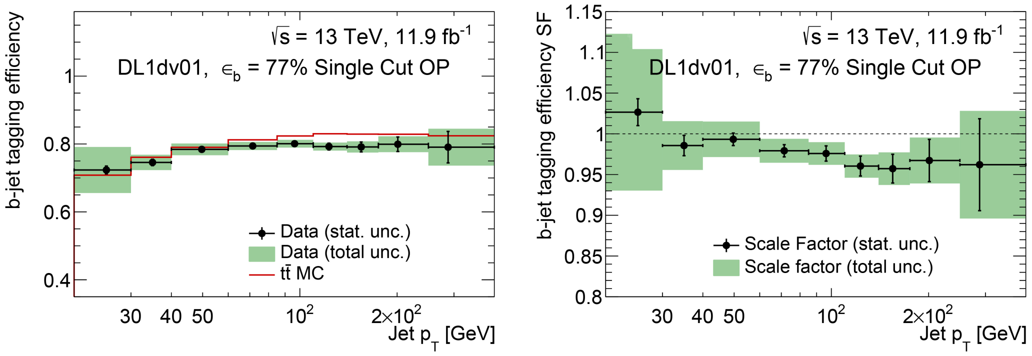

(a) (b)

Figure I.1: $b$-tagging efficiency (a) and $b$-tagging efficiency scale factors (b) for the 77% $b$-tagging working point of the DL1dv01 tagger. The luminosity was not updated yet to the new value of 11.3 fb$^{-1}$.

# Appendix J

# Top quark $p_\mathrm{T}$ NNLO QCD reweighting

This appendix describes the studies performed to investigate the impact of the top quark modelling on the agreement between data and MC.

The prediction for the top quark $p_\mathrm{T}$ distribution is computed at NNLO QCD for $\sqrt(s) = 13.6$ TeV by using the MATRIX program. Predictions based on NNLO QCD calculations are in better agreement with the measured top $p_\mathrm{T}$ spectra [98], but NNLO corrections are not yet available in full event generator programs, and reweighting approaches must be used instead. To test the effect of a softer top quark $p_\mathrm{T}$ spectrum on the lepton $p_\mathrm{T}$ spectrum, the POWHEG BOX v2 +PYTHIA 8.307 dataset 601230 was reweighted as a function of true top quark $p_\mathrm{T}$, according to the ratio shown in Figure J.1. In order to benchmark the performance of the MATRIX software at known center-of-mass energies, a comparison of the 13 TeV NNLO QCD prediction with the one previously provided by Mitov *et al.* is performed; Such comparison is displayed in Figure J.1 and shows no significant divergence between the two predictions.

The effects of this reweighting on the electron and muon $p_\mathrm{T}$ spectra, and for the $b$-jet spectra, are shown in Figure J.2, comparing the data to the POWHEG BOX v2 +PYTHIA 8.307 prediction without and with the top quark $p_\mathrm{T}$ reweighting.

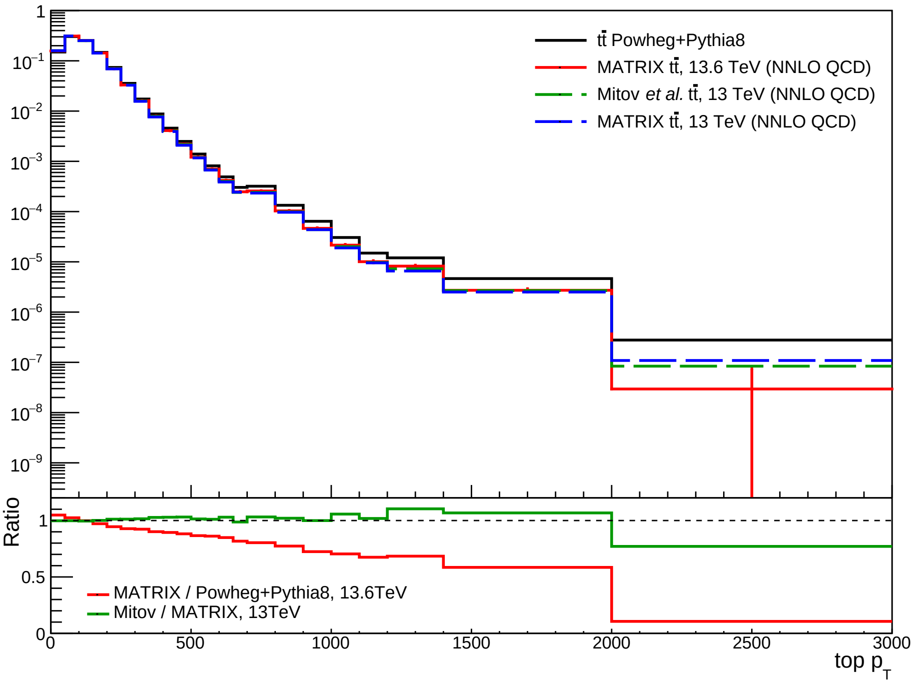

Figure J.1: Top quark $p_T$ spectrum at truth level. The upper plot displays the $p_T$ distributions for the Powheg Box v2 +Pythia 8.307 currently used $t\bar{t}$ sample (black solid line) and for the MATRIX NNLO QCD prediction (red solid line), as well as the NNLO QCD prediction for $\sqrt{(s)} = 13$ TeV as provided by the MATRIX program (blue dotted line) and by Mitov *et al.* (green dotted line). The bottom plot shows the ratio between The MATRIX NNLO QCD prediction at $\sqrt{(s)} = 13.6$ TeV and the Powheg Box v2 +Pythia 8.307 sample (red solid line), and the ratio between the two different NNLO QCD predictions at $\sqrt{(s)} = 13$ TeV (green solid line).

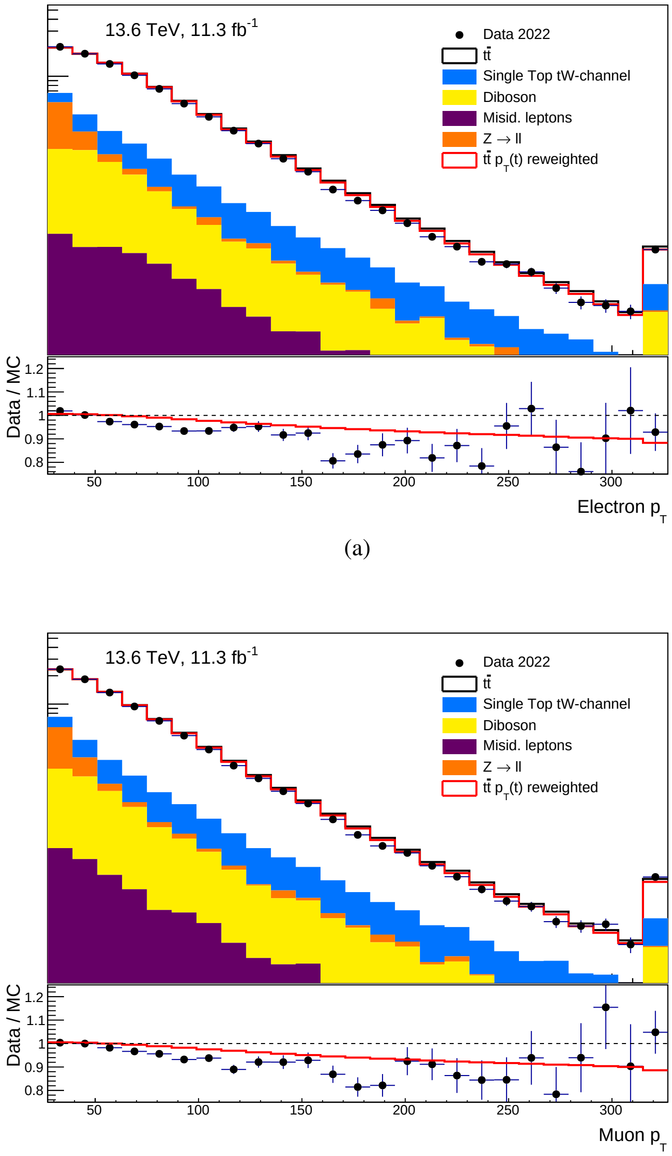

(a)

(b)

Figure J.2: Distributions of the electron (a) and muon (b) $p_{\mathrm{T}}$. The data is shown compared to the expectation from simulation, separately for $t\bar{t}$ events taken from the POWHEG BOX v2 +PYTHIA 8.307 $t\bar{t}$ signal sample, and from the same sample reweighted to improve the agreement of the top quark $p_{\mathrm{T}}$ distribution with data. The lower plots show the ratios of data to the unweighted prediction (points with error bars), and the ratio of the $p_{\mathrm{T}}$-reweighted prediction to the baseline prediction (red lines).

# Appendix K

# Comparison between different MC generators for $Z$ samples

These studies were performed with the $11.3\ \text{fb}^{-1}$ data.

This appendix describes the comparison between $Z$ events generated by Sherpa , and by Powheg Box v2 +Pythia 8 (PP8). For both generators, acceptances are calculated for the fiducial-level selection in the $ee$ and $\mu\mu$ channels. As described in C, a selection requiring all leptons to fulfill $p_{\text{T}} \geq 27\,\text{GeV}$ and $|\eta| < 2.5$, as well as a dilepton mass requirement of $66\,\text{GeV} < m_{\ell\ell} < 116\,\text{GeV}$ is applied events on particle-level on born separately.

The obtained acceptance and fiducial cross-sections are then used to compute the correction on the uncertainty due to the difference between Sherpa and PP8. Figure K.1 shows the impact of such uncertainty before the fiducial corrections. Table K.1 lists the breakdown of acceptances, cross sections and corrections for the uncertainty for the $ee$ and $\mu\mu$ channels.

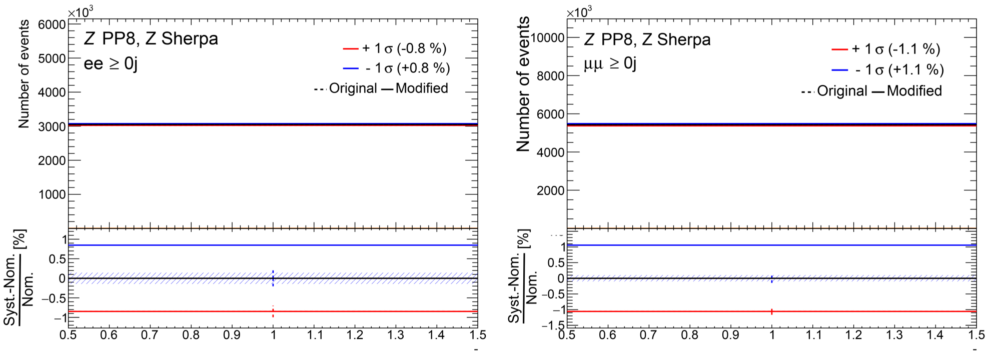

(a)

(b)

Figure K.1: Difference between Sherpa and PP8 in the $ee$ (a) and $\mu\mu$ (b) channels.

| Variation | Uncor. unc. (%) | Cross-sec. ratio | Cor. unc. (%) |
|---|---|---|---|
| SHERPA vs. PP8 ($ee$) | 0.848 | 1.0086 | 0.009 |
| SHERPA vs. PP8 ($\mu\mu$) | 1.058 | 1.0099 | -0.06 |

Table K.1: The corrected and uncorrected SHERPA vs. PP8 uncertainties on reco-level are shown, using the fiducial acceptances for the correction, separated for $ee$ and $\mu\mu$ events. Furthermore, the ratio of the fiducial cross-sections is shown.

The impact of the SHERPA vs. PP8 is smaller than $0.1\%$ for both the $ee$ and $\mu\mu$ channels, therefore it is considered negligible.

# Appendix L

# Additional work done during PhD

Throughout my PhD, I have contributed to a few activities that are not directly related to the work presented in this thesis. A brief chronological overview of the activities is presented in this appendix.

## Regression DNNs for $t\bar{t}$ resonance searches in the dilepton channel

During 2021, I contributed to the development of a Deep Neural Network (DNN) to perform a regression task on both SM $t\bar{t}$ events and $Z'$ signal events, using $m_{t\bar{t}}$ as the output parameter [280]. The datasets used for the training consist of events generated through the Monte Carlo simulation of the ATLAS detector achieved with Geant4. For each event, 22 features are considered and are listed below:

- 4-momenta $(p_T, \eta, \phi, m)$ of the 2 final-state charged leptons $(4 + 4)$
- 4-momenta $(p_T, \eta, \phi, m)$ of the 3 leading jets $(4 + 4 + 4)$
- missing $E_T$ and $\phi$ (2)

The comparison between this machine-learning approach and more traditional system reconstruction techniques highlights a tangible improvement in the ability to correctly reconstruct and resolve a TeV-scale $t\bar{t}$ resonance peak.

## ATLAS Open Data

Since 2021, I have been contributing to the coordination of the software and infrastructure deployment of the ATLAS Open Data project, within the Outreach group of the collaboration.

This open science initiative aims to make the data gathered by the ATLAS detector accessible and usable to everyone, providing at the same time the knowledge necessary to perform analyses.

In my current role, I am committed to maintaining and enhancing the computational tools that enable non-expert users to deploy complex analysis infrastructures, utilising the cloud providers available on the market [281].

## Future Circular Collider

Since 2022, I have been involved in the study of a future measurement of $Z$-boson couplings to bottom quarks at FCC-ee (Future electron-positron Circular Collider).

The FCC-ee is a novel, highest-luminosity energy frontier collider, designed to tackle the open questions of contemporary physics. It will serve as a precision instrument for ongoing in-depth exploration of nature at the smallest scales, optimized for studying the $Z$, $W$, Higgs, and top particles with high precision, and with samples of $5 \times 10^{12}$ $Z$-bosons, $10^8$ $W$ pairs, $10^6$ Higgs bosons and $10^6$ top quark pairs.

The primary purpose of this analysis is to probe such interactions through a competitive determination of $A_{0,b}^{FB}$, not only improving the precision of the measurement, but also defining future detector requirements and recommendations.

## Single-top quark $t$-channel production at $\sqrt{s}$ =5.02 TeV

Between 2022 and 2023, I have contributed to the analysis measuring the single-top quark cross-section in the $t$-channel at $\sqrt{s}$ =5.02 TeV [282]. This analysis represents the first measurement of its kind at $\sqrt{s}$ =5.02 TeV. Leveraging the expertise gathered in this thesis work, my contribution to the analysis consisted in:

- the development of the framework for the processing of MC and data;
- the development of the Boosted Decision Tree (BDT) trained to separate $t$-channel signal from the SM background;
- the development of the fit setup;
- the editing of the supporting internal note.

# Acknowledgements

None of us can make it alone. I wasn't. My PhD has been crowded with people willing to connect, to interact, and to share; for that, I am very thankful.

I am especially grateful to Michele, Marina, and Giancarlo: thank you for your wise guidance, profound passion, and for spurring me to set sights high. Most importantly, thank you for providing us (the students) with so many opportunities to grow and learn.

A special thanks to the INFN Trieste/ATLAS Udine/ICTP group for the constant support and for the chance to participate in many interesting events, conferences, and physics schools; thanks to Bobby, Gilberto, Hamzeh, Jacopo, Mapo, Mohammed, Nitika, Simone, and to my fellow students Laura, Leonardo, Lorenzo for the discussions, the debugging and the coffees together.

Thank you, $\frac{1}{\sqrt{2}}\begin{pmatrix}\text{Tomáš}\\ \text{Leonid}\end{pmatrix}$, for being an inexhaustible source of knowledge, excellent mentors, and great friends. Thank you for helping me push my limits forward.

Further, I am grateful to the whole ATLAS Top group, in particular to Andrea and Marcel, for the unwavering assistance in completing this "high speed, high pressure" measurement.

During my stay at CERN, I had the privilege to meet a number of bright, kind, and vibrant people. Ale, Betto, Carlo, Francesca, Giulia, Kevin (the transformer), Kevin (the musician), Leo, Lorenzo (the umbro), Lorenzo (the wise), Matteo, Max, Miltos (Miklos), and Noè: thank you for the cocchini, the sexy stares, the LVMINOSITY explanations, the nights out, the competition with CMS, the Italian memes, the jam sessions, the deep knowledge on Italian trash culture; thank you for the existence of tuscany, for the (responsibly consumed) alcohol, for the pervasive kindness, for the chats in R1, for the "come on, Giovanni" moments, and for the ever-present Romagna vibe.

While participating in the last physics school of my PhD, I crossed paths with many wonderful persons, and in just two weeks, extraordinarily strong ties were created. I could never believe something like this to be possible. Thank you, Ana, Arnau, Chiara, Chris, Elena, Giovanni, Grazi, Léo, Madry, Paula, and Tiziano and all of the participants. In that last school, I learnt that science is fueled not only by brilliant people, but most importantly, by amazing friendships.

A deeply heartfelt thank you to my family: Mery, Pietro, Giuliana, and Tiberio (and Poppy). Thank you for your patience, your curiosity, and for always being ready to encourage me to keep going, even when my choices brought me far from home.

Thank you, Elisa, for looking after me, and for graciously fending off skeptics needlessly pitying the distance between us. Thank you for being a team. Thank you for 8 great years. May we have many more.

# Bibliography

[1] L. Evans and P. Bryant, *LHC Machine*, JINST **3** (2008) S08001 (cit. on pp. 1, 31).

[2] ATLAS Collaboration, *Observation of a new particle in the search for the Standard Model Higgs boson with the ATLAS detector at the LHC*, Phys. Lett. B **716** (2012) 1, arXiv: `1207.7214 [hep-ex]` (cit. on pp. 1, 12).

[3] CMS Collaboration, *Observation of a new boson at a mass of 125 GeV with the CMS experiment at the LHC*, Phys. Lett. B **716** (2012) 30, arXiv: `1207.7235 [hep-ex]` (cit. on pp. 1, 12).

[4] ATLAS Collaboration, *The ATLAS Experiment at the CERN Large Hadron Collider*, JINST **3** (2008) S08003 (cit. on pp. 1, 36).

[5] CMS Collaboration, *The CMS Experiment at the CERN LHC*, JINST **3** (2008) S08004 (cit. on p. 1).

[6] CDF Collaboration, *Observation of Top Quark Production in $\bar{p}p$ Collisions with the Collider Detector at Fermilab*, Phys. Rev. Lett. **74** (14 1995) 2626 (cit. on pp. 1, 19).

[7] D0 Collaboration, *Observation of the Top Quark*, Phys. Rev. Lett. **74** (14 1995) 2632 (cit. on pp. 1, 19).

[8] ATLAS Collaboration, *Measurements of top-quark pair to Z-boson cross-section ratios at $\sqrt{s} = 13, 8, 7$ TeV with the ATLAS detector*, JHEP **02** (2017) 117, arXiv: `1612.03636 [hep-ex]` (cit. on pp. 2, 26, 29).

[9] M. Gell-Mann, *The interpretation of the new particles as displaced charge multiplets*, Il Nuovo Cimento (1955-1965) **4** (1956) 848, ISSN: 1827-6121 (cit. on p. 5).

[10] V. Gribov and B. Pontecorvo, *Neutrino astronomy and lepton charge*, Physics Letters B **28** (1969) 493, ISSN: 0370-2693 (cit. on p. 5).

[11] Q. R. Ahmad et al., *Measurement of the rate of $\nu_e + d \rightarrow p + p + e^-$ interactions produced by $^8B$ solar neutrinos at the Sudbury Neutrino Observatory*, Phys. Rev. Lett. **87** (2001) 071301, arXiv: `nucl-ex/0106015 [nucl-ex]` (cit. on p. 6).

[12] Q. R. Ahmad et al., *Direct evidence for neutrino flavor transformation from neutral current interactions in the Sudbury Neutrino Observatory*, Phys. Rev. Lett. **89** (2002) 011301, arXiv: `nucl-ex/0204008 [nucl-ex]` (cit. on p. 6).

[13] Y. Fukuda et al., *Evidence for oscillation of atmospheric neutrinos*, Phys. Rev. Lett. **81** (1998) 1562, arXiv: `hep-ex/9807003 [hep-ex]` (cit. on p. 6).

[14] M. Gell-Mann, *A schematic model of baryons and mesons*, Physics Letters **8** (1964) 214, ISSN: 0031-9163 (cit. on pp. 6, 9).

[15] CERN Bulletin, *Go on a particle quest at the first CERN webfest*, (2012), URL: `http://cds.cern.ch/journal/CERNBulletin/2012/35/News%20Articles/1473657` (cit. on p. 6).

[16] ATLAS Collaboration, *Measurement of the top quark mass in the $t\bar{t} \to$ lepton+jets channel from $\sqrt{s} = 8$ TeV ATLAS data and combination with previous results*, Eur. Phys. J. C **79** (2019) 290, arXiv: `1810.01772 [hep-ex]` (cit. on pp. 6, 25).

[17] Particle Data Group, *Review of Particle Physics*, PTEP **2022** (2022) 083C01 (cit. on pp. 6, 13, 14, 19, 24–26, 51, 61).

[18] V. Rubakov and S. S. Wilson, *Classical Theory of Gauge Fields*, Princeton University Press (2002), URL: `http://www.jstor.org/stable/j.ctt7snx1` (cit. on p. 7).

[19] S. Weinberg, *A Model of Leptons*, Phys. Rev. Lett. **19** (21 1967) 1264 (cit. on p. 8).

[20] A. Salam and J. Ward, *Electromagnetic and weak interactions*, Physics Letters **13** (1964) 168, ISSN: 0031-9163 (cit. on p. 8).

[21] S. L. Glashow, *Partial-symmetries of weak interactions*, Nuclear Physics **22** (1961) 579, ISSN: 0029-5582 (cit. on p. 8).

[22] T. D. Lee and C. N. Yang, *Question of Parity Conservation in Weak Interactions*, Phys. Rev. **104** (1956) 254 (cit. on p. 8).

[23] C. S. Wu et al., *Experimental Test of Parity Conservation in Beta Decay*, Phys. Rev. **105** (1957) 1413 (cit. on p. 8).

[24] P. W. Higgs, *Broken Symmetries and the Masses of Gauge Bosons*, Phys. Rev. Lett. **13** (16 1964) 508 (cit. on p. 9).

[25] P. Higgs, *Broken symmetries, massless particles and gauge fields*, Physics Letters **12** (1964) 132, ISSN: 0031-9163 (cit. on p. 9).

[26] F. Englert and R. Brout, *Broken Symmetry and the Mass of Gauge Vector Mesons*, Phys. Rev. Lett. **13** (9 1964) 321 (cit. on p. 9).

[27] M. Gell-Mann, *Symmetries of Baryons and Mesons*, Phys. Rev. **125** (3 1962) 1067 (cit. on p. 9).

[28] G. Zweig, ‘An SU(3) model for strong interaction symmetry and its breaking. Version 2’, *Developments in the quark theory of hadrons. VOL. 1. 1964 - 1978*, ed. by D. Lichtenberg and S. P. Rosen, 1964 22 (cit. on p. 9).

[29] ZEUS Collaboration, *Combination of measurements of inclusive deep inelastic $e^{\pm}p$ scattering cross sections and QCD analysis of HERA data*, The European Physical Journal C **75** (2015) 580, ISSN: 1434-6052 (cit. on p. 10).

[30] R. P. Feynman, *The behavior of hadron collisions at extreme energies*, Conf. Proc. **C690905** (1969) 237 (cit. on p. 10).

[31] H. Fritzsch et al., *Advantages of the color octet gluon picture*, Physics Letters B **47** (1973) 365, ISSN: 0370-2693 (cit. on p. 10).

[32] H. D. Politzer, *Asymptotic freedom: An approach to strong interactions*, Physics Reports **14** (1974) 129, ISSN: 0370-1573 (cit. on p. 10).

[33] N. Cabibbo, *Unitary Symmetry and Leptonic Decays*, Phys. Rev. Lett. **10** (1963) 531 (cit. on p. 14).

[34] M. Kobayashi and T. Maskawa, *CP Violation in the Renormalizable Theory of Weak Interaction*, Prog. Theor. Phys. **49** (1973) 652 (cit. on pp. 14, 19).

[35] B. Pontecorvo, *Neutrino Experiments and the Problem of Conservation of Leptonic Charge*, Sov. Phys. JETP **26** (1968) 984 (cit. on p. 15).

[36] D. Clowe et al., *A Direct Empirical Proof of the Existence of Dark Matter**, The Astrophysical Journal **648** (2006) L109 (cit. on p. 15).

[37] A. D. Sakharov, *Violation of CP invariance, C asymmetry, and baryon asymmetry of the universe*, Soviet Physics Uspekhi **34** (1991) 392 (cit. on p. 15).

[38] A. G. Riess et al., *Observational Evidence from Supernovae for an Accelerating Universe and a Cosmological Constant*, The Astronomical Journal **116** (1998) 1009 (cit. on p. 15).

[39] P. Ramond, *Dual Theory for Free Fermions*, Phys. Rev. D **3** (10 1971) 2415 (cit. on p. 15).

[40] Y. A. Golfand and E. P. Likhtman, *Extension of the Algebra of Poincare Group Generators and Violation of p Invariance*, JETP Lett. **13** (1971) 323 (cit. on p. 15).

[41] J. Wess and B. Zumino, *A lagrangian model invariant under supergauge transformations*, Physics Letters B **49** (1974) 52, ISSN: 0370-2693 (cit. on p. 15).

[42] J. Wess and B. Zumino, *Supergauge transformations in four dimensions*, Nuclear Physics B **70** (1974) 39, ISSN: 0550-3213 (cit. on p. 15).

[43] S. P. Martin, ‘A Supersimmetry primer’, *Advanced Series on Directions in High Energy Physics*, WORLD SCIENTIFIC, 1998 1 (cit. on p. 16).

[44] S. L. Glashow, J. Iliopoulos and L. Maiani, *Weak Interactions with Lepton-Hadron Symmetry*, Phys. Rev. D **2** (7 1970) 1285 (cit. on p. 16).

[45] ATLAS Collaboration, *ATLAS public plots: Standard Model Summary*, Accessed: 16-12-2023, URL: `https://atlas.web.cern.ch/Atlas/GROUPS/PHYSICS/PUBNOTES/ATL-PHYS-PUB-2023-039/` (cit. on p. 17).

[46] J. H. Christenson, J. W. Cronin, V. L. Fitch and R. Turlay, *Evidence for the $2\pi$ Decay of the $K_2^0$ Meson*, Phys. Rev. Lett. **13** (4 1964) 138 (cit. on p. 19).

[47] M. L. Perl et al., *Evidence for Anomalous Lepton Production in $e^+ - e^-$ Annihilation*, Phys. Rev. Lett. **35** (22 1975) 1489 (cit. on p. 19).

[48] J. C. Collins, D. E. Soper and G. Sterman, 'Factorization of hard processes in QCD', *Perturbative QCD* 1, eprint: `https://www.worldscientific.com/doi/pdf/10.1142/9789814503266_0001` (cit. on p. 20).

[49] M. Czakon and A. Mitov, *Top++: A program for the calculation of the top-pair cross-section at hadron colliders*, Comput. Phys. Commun. **185** (2014) 2930, arXiv: `1112.5675 [hep-ph]` (cit. on pp. 21, 81).

[50] M. Beneke, P. Falgari, S. Klein and C. Schwinn, *Hadronic top-quark pair production with NNLL threshold resummation*, Nucl. Phys. B **855** (2012) 695, arXiv: `1109.1536 [hep-ph]` (cit. on pp. 21, 81).

[51] M. Cacciari, M. Czakon, M. Mangano, A. Mitov and P. Nason, *Top-pair production at hadron colliders with next-to-next-to-leading logarithmic soft-gluon resummation*, Phys. Lett. B **710** (2012) 612, arXiv: `1111.5869 [hep-ph]` (cit. on pp. 21, 81).

[52] P. Bärnreuther, M. Czakon and A. Mitov, *Percent-Level-Precision Physics at the Tevatron: Next-to-Next-to-Leading Order QCD Corrections to* $q\bar{q} \to t\bar{t} + X$, Phys. Rev. Lett. **109** (2012) 132001, arXiv: `1204.5201 [hep-ph]` (cit. on pp. 21, 81).

[53] M. Czakon and A. Mitov, *NNLO corrections to top-pair production at hadron colliders: the all-fermionic scattering channels*, JHEP **12** (2012) 054, arXiv: `1207.0236 [hep-ph]` (cit. on pp. 21, 81).

[54] M. Czakon and A. Mitov, *NNLO corrections to top pair production at hadron colliders: the quark-gluon reaction*, JHEP **01** (2013) 080, arXiv: `1210.6832 [hep-ph]` (cit. on pp. 21, 81).

[55] M. Czakon, P. Fiedler and A. Mitov, *Total Top-Quark Pair-Production Cross Section at Hadron Colliders Through* $O(\alpha_S^4)$, Phys. Rev. Lett. **110** (2013) 252004, arXiv: `1303.6254 [hep-ph]` (cit. on pp. 21, 22, 81).

[56] ATLAS Collaboration, *Measurement of the* $t\bar{t}$ *production cross-section in pp collisions at* $\sqrt{s} = 5.02$ *TeV with the ATLAS detector*, JHEP **06** (2023) 138, arXiv: `2207.01354 [hep-ex]` (cit. on p. 22).

[57] CMS Collaboration, *Measurement of the inclusive* $t\bar{t}$ *production cross section in proton–proton collisions at* $\sqrt{s} = 5.02$ *TeV*, JHEP **04** (2021) 144, arXiv: `2112.09114 [hep-ex]` (cit. on p. 22).

[58] ATLAS and CMS Collaborations, *Combination of inclusive top-quark pair production cross-section measurements using ATLAS and CMS data at* $\sqrt{s} = 7$ *and* 8 *TeV*, (2022), arXiv: `2205.13830 [hep-ex]` (cit. on p. 22).

[59] ATLAS Collaboration, *Measurement of the $t\bar{t}$ production cross-section and lepton differential distributions in $e\mu$ dilepton events from $pp$ collisions at $\sqrt{s} = 13$ TeV with the ATLAS detector*, Eur. Phys. J. C **80** (2020) 528, arXiv: `1910.08819 [hep-ex]` (cit. on pp. 22, 67, 72, 110, 111).

[60] ATLAS Collaboration, *Measurement of the $t\bar{t}$ production cross-section in the lepton+jets channel at $\sqrt{s} = 13$ TeV with the ATLAS experiment*, Phys. Lett. B **810** (2020) 135797, arXiv: `2006.13076 [hep-ex]` (cit. on p. 22).

[61] CMS Collaboration, *Measurement of the cross section for $t\bar{t}$ production with additional jets and $b$ jets in $pp$ collisions at $\sqrt{s} = 13$ TeV*, JHEP **07** (2020) 125, arXiv: `2003.06467 [hep-ex]` (cit. on p. 22).

[62] ATLAS Collaboration, *Measurement of $t\bar{t}$ and $Z$-boson cross sections and their ratio using $pp$ collisions at $\sqrt{s} = 13.6$ TeV with the ATLAS detector*, (2023), URL: `https://cds.cern.ch/record/2854834` (cit. on p. 22).

[63] CMS Collaboration, *First measurement of the top quark pair production cross section in proton-proton collisions at $\sqrt{s} = 13.6$ TeV*, (2023), arXiv: `2303.10680 [hep-ex]` (cit. on p. 22).

[64] *ATLAS Top Quark summary plots*, Accessed: 01-07-2023, URL: `https://twiki.cern.ch/twiki/bin/view/AtlasPublic/TopPublicResults` (cit. on pp. 22, 23).

[65] M. Aliev et al., *HATHOR – HAdronic Top and Heavy quarks crOss section calculatoR*, Comput. Phys. Commun. **182** (2011) 1034, arXiv: `1007.1327 [hep-ph]` (cit. on p. 22).

[66] P. Kant et al., *HATHOR for single top-quark production: Updated predictions and uncertainty estimates for single top-quark production in hadronic collisions*, Comput. Phys. Commun. **191** (2015) 74, arXiv: `1406.4403 [hep-ph]` (cit. on p. 22).

[67] J. Campbell, T. Neumann and Z. Sullivan, *Single-top-quark production in the $t$-channel at NNLO*, JHEP **02** (2021) 040, arXiv: `2012.01574 [hep-ph]` (cit. on pp. 22, 82).

[68] N. Kidonakis and N. Yamanaka, *Higher-order corrections for $tW$ production at high-energy hadron colliders*, JHEP **05** (2021) 278, arXiv: `2102.11300 [hep-ph]` (cit. on pp. 22, 82).

[69] R. D. Ball et al., *The PDF4LHC21 combination of global PDF fits for the LHC Run III*, J. Phys. G **49** (2022) 080501, arXiv: `2203.05506 [hep-ph]` (cit. on pp. 22, 81, 130, 132, 133).

[70] ATLAS Collaboration, *Measurement of $t$-channel single-top-quark production in $pp$ collisions at $\sqrt{s} = 5.02$ TeV with the ATLAS detector*, (2023), URL: `http://cds.cern.ch/record/2862022` (cit. on p. 22).

[71] ATLAS Collaboration, *Comprehensive measurements of $t$-channel single top-quark production cross sections at $\sqrt{s} = 7$ TeV with the ATLAS detector*, Phys. Rev. D **90** (2014) 112006, arXiv: `1406.7844 [hep-ex]` (cit. on p. 22).

[72] ATLAS Collaboration, *Fiducial, total and differential cross-section measurements of $t$-channel single top-quark production in $pp$ collisions at 8 TeV using data collected by the ATLAS detector*, Eur. Phys. J. C **77** (2017) 531, arXiv: `1702.02859 [hep-ex]` (cit. on p. 22).

[73] ATLAS Collaboration, *Measurement of $t$-channel production of single top quarks and antiquarks in $pp$ collisions at 13 TeV using the full ATLAS Run 2 dataset*, (2023), URL: `http://cds.cern.ch/record/2860644` (cit. on p. 22).

[74] ATLAS Collaboration, *Evidence for the associated production of a $W$ boson and a top quark in ATLAS at $\sqrt{s} = 7$ TeV*, Phys. Lett. B **716** (2012) 142, arXiv: `1205.5764 [hep-ex]` (cit. on p. 22).

[75] ATLAS Collaboration, *Measurement of the production cross-section of a single top quark in association with a $W$ boson at 8 TeV with the ATLAS experiment*, JHEP **01** (2016) 064, arXiv: `1510.03752 [hep-ex]` (cit. on p. 22).

[76] ATLAS Collaboration, *Measurement of the cross-section for producing a $W$ boson in association with a single top quark in $pp$ collisions at $\sqrt{s} = 13$ TeV with ATLAS*, JHEP **01** (2018) 063, arXiv: `1612.07231 [hep-ex]` (cit. on p. 22).

[77] ATLAS Collaboration, *Evidence for single top-quark production in the $s$-channel in proton–proton collisions at $\sqrt{s} = 8$ TeV with the ATLAS detector using the Matrix Element Method*, Phys. Lett. B **756** (2016) 228, arXiv: `1511.05980 [hep-ex]` (cit. on p. 22).

[78] ATLAS Collaboration, *Measurement of single top-quark production in the $s$-channel in proton–proton collisions at $\sqrt{s} = 13$ TeV with the ATLAS detector*, (2022), arXiv: `2209.08990 [hep-ex]` (cit. on p. 22).

[79] CMS Collaboration, *Measurement of the single-top-quark $t$-channel cross section in $pp$ collisions at $\sqrt{s} = 7$ TeV*, JHEP **12** (2012) 035, arXiv: `1209.4533 [hep-ex]` (cit. on p. 22).

[80] CMS Collaboration, *Measurement of the $t$-channel single-top-quark production cross section and of the $|V_{tb}|$ CKM matrix element in $pp$ collisions at $\sqrt{s} = 8$ TeV*, JHEP **06** (2014) 090, arXiv: `1403.7366 [hep-ex]` (cit. on p. 22).

[81] CMS Collaboration, *Measurement of the single top quark and antiquark production cross sections in the $t$ channel and their ratio in proton–proton collisions at $\sqrt{s} = 13$ TeV*, Phys. Lett. B **800** (2020) 135042, arXiv: `1812.10514 [hep-ex]` (cit. on p. 22).

[82] CMS Collaboration, *Evidence for associated production of a single top quark and $W$ boson in $pp$ collisions at $\sqrt{s} = 7$ TeV*, Phys. Rev. Lett. **110** (2013) 022003, arXiv: `1209.3489 [hep-ex]` (cit. on p. 22).

[83] CMS Collaboration, *Observation of the Associated Production of a Single Top Quark and a W Boson in $pp$ Collisions at $\sqrt{s} = 8$ TeV*, Phys. Rev. Lett. **112** (2014) 231802, arXiv: `1401.2942 [hep-ex]` (cit. on p. 22).

[84] CMS Collaboration, *Measurement of inclusive and differential cross sections for single top quark production in association with a W boson in proton–proton collisions at $\sqrt{s} = 13$ TeV*, (2022), arXiv: `2208.00924 [hep-ex]` (cit. on p. 22).

[85] CMS Collaboration, *Search for $s$ channel single top quark production in $pp$ collisions at $\sqrt{s} = 7$ and 8 TeV*, JHEP **09** (2016) 027, arXiv: `1603.02555 [hep-ex]` (cit. on p. 22).

[86] CKMfitter Group, *Updated results on the CKM matrix*, 2021, URL: `http://ckmfitter.in2p3.fr/www/results/plots_spring21/ckm_res_spring21.html` (cit. on p. 23).

[87] M. Baak et al., *The global electroweak fit at NNLO and prospects for the LHC and ILC*, Eur. Phys. J. C **74** (2014) 3046, arXiv: `1407.3792 [hep-ph]` (cit. on p. 25).

[88] J. Haller et al., *Update of the global electroweak fit and constraints on two-Higgs-doublet models*, Eur. Phys. J. C **78** (2018) 675, arXiv: `1803.01853 [hep-ph]` (cit. on p. 25).

[89] J. Haller, A. Hoecker, R. Kogler, K. Mönig and J. Stelzer, *Status of the global electroweak fit with Gfitter in the light of new precision measurements*, PoS **ICHEP2022** (2022) 897, arXiv: `2211.07665 [hep-ph]` (cit. on p. 25).

[90] G. Isidori, G. Ridolfi and A. Strumia, *On the metastability of the Standard Model vacuum*, Nuclear Physics B **609** (2001) 387, ISSN: 0550-3213 (cit. on p. 25).

[91] *First combination of Tevatron and LHC measurements of the top-quark mass*, tech. rep., All figures including auxiliary figures are available at https://atlas.web.cern.ch/Atlas/GROUPS/PHYSICS/CONFNOTES/ATLAS-CONF-2014-008: CERN, 2014, arXiv: `1403.4427`, URL: `http://cds.cern.ch/record/1669819` (cit. on p. 25).

[92] ATLAS Collaboration, *Measurement of the top quark mass in the $t\bar{t} \rightarrow$ lepton+jets and $t\bar{t} \rightarrow$ dilepton channels using $\sqrt{s} = 7$ TeV ATLAS data*, Eur. Phys. J. C **75** (2015) 330, arXiv: `1503.05427 [hep-ex]` (cit. on p. 25).

[93] ATLAS Collaboration, *Measurement of the top quark mass in the $t\bar{t} \rightarrow$ dilepton channel from $\sqrt{s} = 8$ TeV ATLAS data*, Phys. Lett. B **761** (2016) 350, arXiv: `1606.02179 [hep-ex]` (cit. on p. 25).

[94] ATLAS Collaboration, *Top-quark mass measurement in the all-hadronic $t\bar{t}$ decay channel at $\sqrt{s} = 8$ TeV with the ATLAS detector*, JHEP **09** (2017) 118, arXiv: `1702.07546 [hep-ex]` (cit. on p. 25).

[95] ATLAS Collaboration, *Measurement of the top-quark mass in the fully hadronic decay channel from ATLAS data at* $\sqrt{s} = 7$ *TeV*, Eur. Phys. J. C **75** (2015) 158, arXiv: `1409.0832 [hep-ex]` (cit. on p. 25).

[96] ATLAS Collaboration, *Measurement of the top-quark mass using a leptonic invariant mass in* $pp$ *collisions at* $\sqrt{s} = 13$ *TeV with the ATLAS detector*, (2022), arXiv: `2209.00583 [hep-ex]` (cit. on p. 25).

[97] ATLAS Collaboration, *Measurement of the top-quark mass in* $t\bar{t} \rightarrow$ *dilepton events with the ATLAS experiment using the template method in 13 TeV* $pp$ *collision data.*, (2022), URL: `http://cds.cern.ch/record/2826701` (cit. on p. 25).

[98] CMS Collaboration, *Measurement of the top-quark mass in* $t\bar{t}$ *events with lepton+jets final states in* $pp$ *collisions at* $\sqrt{s} = 7$ *TeV*, JHEP **12** (2012) 105, arXiv: `1209.2319 [hep-ex]` (cit. on p. 25).

[99] CMS Collaboration, *Measurement of the top-quark mass in* $t\bar{t}$ *events with dilepton final states in* $pp$ *collisions at* $\sqrt{s} = 7$ *TeV*, Eur. Phys. J. C **72** (2012) 2202, arXiv: `1209.2393 [hep-ex]` (cit. on p. 25).

[100] CMS Collaboration, *Measurement of the top-quark mass in all-jets* $t\bar{t}$ *events in* $pp$ *collisions at* $\sqrt{s} = 7$ *TeV*, Eur. Phys. J. C **74** (2014) 2758, arXiv: `1307.4617 [hep-ex]` (cit. on p. 25).

[101] CMS Collaboration, *Measurement of the top quark mass using proton–proton data at* $\sqrt{s} = 7$ *and* 8 *TeV*, Phys. Rev. D **93** (2016) 072004, arXiv: `1509.04044 [hep-ex]` (cit. on p. 25).

[102] CMS Collaboration, *Measurement of the top quark mass using single top quark events in proton–proton collisions at* $\sqrt{s} = 8$ *TeV*, Eur. Phys. J. C **77** (2017) 354, arXiv: `1703.02530 [hep-ex]` (cit. on p. 25).

[103] CMS Collaboration, *Measurement of the top quark mass with lepton+jets final states using* $pp$ *collisions at* $\sqrt{s} = 13$ *TeV*, Eur. Phys. J. C **78** (2018) 891, arXiv: `1805.01428 [hep-ex]` (cit. on p. 25).

[104] CMS Collaboration, *Measurement of the top quark mass using events with a single reconstructed top quark in* $pp$ *collisions at* $\sqrt{s} = 13$ *TeV*, JHEP **12** (2021) 161, arXiv: `2108.10407 [hep-ex]` (cit. on p. 25).

[105] *A profile likelihood approach to measure the top quark mass in the lepton+jets channel at* $\sqrt{s} = 13$ TeV, tech. rep., CERN, 2022, URL: `https://cds.cern.ch/record/2806509` (cit. on p. 25).

[106] *Measurement of the top quark mass using a profile likelihood approach with the lepton+jets final states in proton-proton collisions at* $\sqrt{s} = 13$ *TeV*, (2023), arXiv: `2302.01967 [hep-ex]` (cit. on p. 25).

[107] ATLAS Collaboration, *Combination of measurements of the top quark mass from data collected by the ATLAS and CMS experiments at $\sqrt{s} = 7$ and 8 TeV*, ATLAS-CONF-2023-066, 2023, URL: `https://cds.cern.ch/record/2873520` (cit. on p. 25).

[108] A. L. Kataev and V. S. Molokoedov, *Notes on Interplay between the QCD and EW Perturbative Corrections to the Pole-Running-to-Top-Quark Mass Ratio*, JETP Lett. **115** (2022) 704, arXiv: `2201.12073 [hep-ph]` (cit. on p. 25).

[109] P. Marquard, A. V. Smirnov, V. A. Smirnov and M. Steinhauser, *Quark Mass Relations to Four-Loop Order in Perturbative QCD*, Phys. Rev. Lett. **114** (2015) 142002, arXiv: `1502.01030 [hep-ph]` (cit. on p. 25).

[110] M. Beneke, P. Marquard, P. Nason and M. Steinhauser, *On the ultimate uncertainty of the top quark pole mass*, Phys. Lett. B **775** (2017) 63, arXiv: `1605.03609 [hep-ph]` (cit. on p. 25).

[111] P. Nason, *The Top Mass in Hadronic Collisions*, 2018, arXiv: `1712.02796 [hep-ph]` (cit. on p. 26).

[112] ATLAS Collaboration, *Determination of the top-quark pole mass using $t\bar{t} + 1$-jet events collected with the ATLAS experiment in 7 TeV $pp$ collisions*, JHEP **10** (2015) 121, arXiv: `1507.01769 [hep-ex]` (cit. on p. 26).

[113] ATLAS Collaboration, *Measurement of the $t\bar{t}$ production cross-section using $e\mu$ events with $b$-tagged jets in $pp$ collisions at $\sqrt{s} = 7$ and 8 TeV with the ATLAS detector*, Eur. Phys. J. C **74** (2014) 3109, arXiv: `1406.5375 [hep-ex]` (cit. on p. 26), Addendum: Eur. Phys. J. C **76** (2016) 642.

[114] ATLAS Collaboration, *Measurement of the top-quark mass in $t\bar{t} + 1$-jet events collected with the ATLAS detector in $pp$ collisions at $\sqrt{s} = 8$ TeV*, JHEP **11** (2019) 150, arXiv: `1905.02302 [hep-ex]` (cit. on p. 26).

[115] CMS Collaboration, *Determination of the top-quark pole mass and strong coupling constant from the $t\bar{t}$ production cross section in $pp$ collisions at $\sqrt{s} = 7$ TeV*, Phys. Lett. B **728** (2014) 496, arXiv: `1307.1907 [hep-ex]` (cit. on p. 26).

[116] CMS Collaboration, *Measurement of $t\bar{t}$ normalised multi-differential cross sections in $pp$ collisions at $\sqrt{s} = 13$ TeV, and simultaneous determination of the strong coupling strength, top quark pole mass, and parton distribution functions*, Eur. Phys. J. C **80** (2020) 658, arXiv: `1904.05237 [hep-ex]` (cit. on p. 26).

[117] CMS Collaboration, *Measurement of the top quark pole mass using $t\bar{t}$+jet events in the dilepton final state in proton–proton collisions at $\sqrt{s} = 13$ TeV*, (2022), arXiv: `2207.02270 [hep-ex]` (cit. on p. 26).

[118] ATLAS Collaboration, *Measurement of lepton differential distributions and the top quark mass in $t\bar{t}$ production in $pp$ collisions at $\sqrt{s} = 8$ TeV with the ATLAS detector*, Eur. Phys. J. C **77** (2017) 804, arXiv: `1709.09407 [hep-ex]` (cit. on p. 26).

[119] LHC Top Physics Working Group, *LHC Top Physics Working Group public webpage*, Accessed: 20-12-2023,
URL: `https://twiki.cern.ch/twiki/bin/view/LHCPhysics/LHCTopWG`
(cit. on p. 26).

[120] ATLAS Collaboration, *Measurement of the $t\bar{t}$ production cross-section using $e\mu$ events with b-tagged jets in $pp$ collisions at $\sqrt{s}$ = 13 TeV with the ATLAS detector*, Phys. Lett. B **761** (2016) 136, arXiv: `1606.02699 [hep-ex]` (cit. on p. 26), Erratum: Phys. Lett. B **772** (2017) 879.

[121] P. Bagnaia et al., *Evidence for $Z^0 \longrightarrow e^+e^-$ at the CERN $\bar{p}p$ Collider*, Phys. Lett. B **129** (1983) 130 (cit. on p. 26).

[122] UA1 Collaboration, *Experimental observation of isolated large transverse energy electrons with associated missing energy at s=540 GeV*, Physics Letters B **122** (1983) 103, ISSN: 0370-2693 (cit. on p. 26).

[123] G. Arnison et al., *Observation of muonic $Z^0$-decay at the $\bar{p}p$ collider*, Physics Letters B **147** (1984) 241, ISSN: 0370-2693 (cit. on p. 26).

[124] B. Richter,
*Very high energy electron-positron colliding beams for the study of weak interactions*, Nuclear Instruments and Methods **136** (1976) 47, ISSN: 0029-554X (cit. on p. 26).

[125] R. Erickson, *SLC Design handbook*, (1984) (cit. on p. 26).

[126] ALEPH, DELPHI, L3, OPAL, and SLD Collaborations, The LEP EW Working Group, The SLD EW and Heavy Flavour Group,
*Precision electroweak measurements on the Z resonance*,
Physics Reports **427** (2006) 257, ISSN: 0370-1573 (cit. on p. 27).

[127] G. Voutsinas, E. Perez, M. Dam and P. Janot, *Beam-beam effects on the luminosity measurement at LEP and the number of light neutrino species*, Physics Letters B **800** (2020) 135068, ISSN: 0370-2693 (cit. on p. 27).

[128] P. Janot and S. Jadach,
*Improved Bhabha cross section at LEP and the number of light neutrino species*, Physics Letters B **803** (2020) 135319, ISSN: 0370-2693 (cit. on p. 27).

[129] S. D. Drell and T.-M. Yan,
*Massive Lepton-Pair Production in Hadron-Hadron Collisions at High Energies*, Phys. Rev. Lett. **25** (5 1970) 316 (cit. on p. 27).

[130] J. D. Degenhardt, ‘Recent electroweak results from D∅ experiment.’,
*21st Lake Louise Winter Institute: Fundamental Interactions*, 2006 177 (cit. on p. 28).

[131] CDF Collaboration,
*Measurements of inclusive W and Z cross sections in $p\bar{p}$ collisions at $\sqrt{s}$ = 1.96 TeV*, J. Phys. G **34** (2007) 2457, ISSN: 1361-6471 (cit. on p. 28).

[132] ATLAS Collaboration, *Measurement of the inclusive $W^{\pm}$ and $Z/\gamma^{*}$ cross sections in the $e$ and $\mu$ decay channels in $pp$ collisions at $\sqrt{s} = 7$ TeV with the ATLAS detector*, Phys. Rev. D **85** (2012) 072004, arXiv: `1109.5141 [hep-ex]` (cit. on p. 28).

[133] ATLAS Collaboration, *Precision measurement and interpretation of inclusive $W^{+}$, $W^{-}$ and $Z/\gamma^{*}$ production cross sections with the ATLAS detector*, Eur. Phys. J. C **77** (2017) 367, arXiv: `1612.03016 [hep-ex]` (cit. on pp. 28, 131).

[134] ATLAS Collaboration, *Measurement of the transverse momentum and $\phi^{*}_{\eta}$ distributions of Drell-Yan lepton pairs in proton–proton collisions at $\sqrt{s} = 8$ TeV with the ATLAS detector*, Eur. Phys. J. C **76** (2016) 291, arXiv: `1512.02192 [hep-ex]` (cit. on p. 28).

[135] ATLAS Collaboration, *Measurement of $W^{\pm}$ and Z-boson production cross sections in $pp$ collisions at $\sqrt{s} = 13$ TeV with the ATLAS detector*, Phys. Lett. B **759** (2016) 601, arXiv: `1603.09222 [hep-ex]` (cit. on p. 28).

[136] ATLAS Collaboration, *Measurement of $W^{\pm}$-boson and Z-boson production cross-sections in $pp$ collisions at $\sqrt{s} = 2.76$ TeV with the ATLAS detector*, Eur. Phys. J. C **79** (2019) 901, arXiv: `1907.03567 [hep-ex]` (cit. on p. 28).

[137] CMS Collaboration, *Measurement of the inclusive W and Z production cross sections in $pp$ collisions at $\sqrt{s} = 7$ TeV with the CMS experiment*, JHEP **10** (2011) 132, arXiv: `1107.4789 [hep-ex]` (cit. on p. 28).

[138] CMS Collaboration, *Measurement of inclusive W and Z boson production cross sections in $pp$ collisions at $\sqrt{s} = 8$ TeV*, Phys. Rev. Lett. **112** (2014) 191802, arXiv: `1402.0923 [hep-ex]` (cit. on p. 28).

[139] CMS Collaboration, *Measurement of the differential and double-differential Drell-Yan cross sections in proton–proton collisions at $\sqrt{s} = 7$ TeV*, JHEP **12** (2013) 030, arXiv: `1310.7291 [hep-ex]` (cit. on p. 28).

[140] CMS Collaboration, *Measurements of differential and double-differential Drell-Yan cross sections in proton–proton collisions at 8 TeV*, Eur. Phys. J. C **75** (2015) 147, arXiv: `1412.1115 [hep-ex]` (cit. on p. 28).

[141] CMS Collaboration, *Measurement of W and Z boson inclusive cross sections in pp collisions at 5.02 and 13 TeV*, tech. rep., 2023, URL: `https://cds.cern.ch/record/2868090` (cit. on p. 28).

[142] CMS Collaboration, *Measurement of the inclusive cross section of Z boson production in pp collisions at $\sqrt{s} = 13.6$ TeV*, tech. rep., 2023, URL: `https://cds.cern.ch/record/2868001` (cit. on p. 28).

[143] ATLAS Collaboration, *Measurements of the production cross section of a Z boson in association with jets in $pp$ collisions at $\sqrt{s} = 13$ TeV with the ATLAS detector*, Eur. Phys. J. C **77** (2017) 361, arXiv: `1702.05725 [hep-ex]` (cit. on p. 29).

[144] ATLAS Collaboration,
*Luminosity monitoring using* $Z \rightarrow \ell^+\ell^-$ *events at* $\sqrt{s} = 13$ *TeV with the ATLAS detector*, ATL-DAPR-PUB-2021-001, 2021, URL: `https://cds.cern.ch/record/2752951` (cit. on p. 29).

[145] ALICE Collaboration, *The ALICE experiment at the CERN LHC*, Journal of Instrumentation **3** (2008) S08002 (cit. on p. 31).

[146] LHCb Collaboration, *The LHCb Detector at the LHC*, Journal of Instrumentation **3** (2008) S08005 (cit. on p. 31).

[147] M. Benedikt, P. Collier, V. Mertens, J. Poole and K. Schindl, *LHC Design Report*, CERN Yellow Reports: Monographs, Geneva: CERN, 2004, URL: `https://cds.cern.ch/record/823808` (cit. on p. 31).

[148] W. Herr and B. Muratori, *Concept of luminosity*, (2006) (cit. on p. 33).

[149] *Public ATLAS Luminosity Results for Run-3 of the LHC*, Accessed: 10-07-2023, URL: `https://twiki.cern.ch/twiki/bin/view/AtlasPublic/LuminosityPublicResultsRun3` (cit. on pp. 34, 86).

[150] ATLAS Collaboration, *The ATLAS Experiment at the CERN Large Hadron Collider: A Description of the Detector Configuration for Run 3*, (2023), arXiv: `2305.16623 [physics.ins-det]` (cit. on pp. 35, 36, 38–40, 42, 45, 46, 50).

[151] ATLAS Collaboration, *ATLAS pixel detector electronics and sensors*, Journal of Instrumentation **3** (2008) P07007 (cit. on p. 37).

[152] ATLAS Collaboration, *Operation and performance of the ATLAS semiconductor tracker*, JINST **9** (2014) P08009, arXiv: `1404.7473 [hep-ex]` (cit. on p. 37).

[153] ATLAS Collaboration, *The ATLAS Transition Radiation Tracker (TRT) proportional drift tube: design and performance*, Journal of Instrumentation **3** (2008) P02013 (cit. on p. 37).

[154] ATLAS Collaboration, *ATLAS Insertable B-Layer: Technical Design Report*, ATLAS-TDR-19; CERN-LHCC-2010-013, 2010, URL: `https://cds.cern.ch/record/1291633` (cit. on p. 38), Addendum: ATLAS-TDR-19-ADD-1; CERN-LHCC-2012-009, 2012, URL: `https://cds.cern.ch/record/1451888`.

[155] B. Abbott et al., *Production and integration of the ATLAS Insertable B-Layer*, JINST **13** (2018) T05008, arXiv: `1803.00844 [physics.ins-det]` (cit. on p. 38).

[156] ATLAS Collaboration, *ATLAS Insertable B-Layer Technical Design Report*, ATLAS-TDR-19; CERN-LHCC-2010-013, 2010, URL: `https://cds.cern.ch/record/1291633` (cit. on p. 38), Addendum: ATLAS-TDR-19-ADD-1; CERN-LHCC-2012-009, 2012, URL: `https://cds.cern.ch/record/1451888`.

[157] M. Bindi, *Operational Experience and Performance with the ATLAS Pixel detector at the Large Hadron Collider at CERN*, tech. rep., ICHEP2022; Talk on 08/07/2022: CERN, 2022, URL: `https://cds.cern.ch/record/2813456` (cit. on p. 39).

[158] ATLAS Collaboration, *Operation and performance of the ATLAS semiconductor tracker in LHC Run 2*, JINST **17** (2021) P01013, arXiv: `2109.02591 [physics.ins-det]` (cit. on p. 40).

[159] A. Vogel, *ATLAS Transition Radiation Tracker (TRT): Straw Tube Gaseous Detectors at High Rates*, tech. rep., CERN, 2013, URL: `https://cds.cern.ch/record/1537991` (cit. on p. 40).

[160] ATLAS Collaboration, *Performance of ATLAS Pixel Detector and Track Reconstruction at the start of Run 3 in LHC Collisions at* $\sqrt{s} = 900\,GeV$, ATL-PHYS-PUB-2022-033, 2022, URL: `https://cds.cern.ch/record/2814766` (cit. on p. 41).

[161] ATLAS Collaboration, *SCT Run 3 Plots for TIPP 2023*, 2023, URL: `https://atlas.web.cern.ch/Atlas/GROUPS/PHYSICS/PLOTS/SCT-2023-001/` (cit. on p. 41).

[162] ATLAS Collaboration, *ATLAS Liquid Argon Calorimeter: Technical Design Report*, ATLAS-TDR-2; CERN-LHCC-96-041, 1996, URL: `https://cds.cern.ch/record/331061` (cit. on p. 41).

[163] ATLAS Collaboration, *ATLAS Tile Calorimeter: Technical Design Report*, ATLAS-TDR-3; CERN-LHCC-96-042, 1996, URL: `https://cds.cern.ch/record/331062` (cit. on p. 41).

[164] ATLAS Collaboration, *Electron and photon performance measurements with the ATLAS detector using the 2015–2017 LHC proton–proton collision data*, JINST **14** (2019) P12006, arXiv: `1908.00005 [hep-ex]` (cit. on pp. 41, 43, 54, 108).

[165] D. Mahon, *ATLAS LAr calorimeter performance in LHC Run 2*, Journal of Instrumentation **15** (2020) C06045 (cit. on p. 41).

[166] J. Abdallah et al., *Study of energy response and resolution of the ATLAS Tile Calorimeter to hadrons of energies from 16 to 30 GeV*, The European Physical Journal C **81** (2021), ISSN: 1434-6052 (cit. on p. 43).

[167] ATLAS Collaboration, *ATLAS LAr Calorimeter Phase-II Upgrade: Technical Design Report*, ATLAS-TDR-027; CERN-LHCC-2017-018, 2017, URL: `https://cds.cern.ch/record/2285582` (cit. on p. 44).

[168] ATLAS Collaboration, *ATLAS Muon Spectrometer: Technical Design Report*, ATLAS-TDR-10; CERN-LHCC-97-022, CERN, 1997, URL: `https://cds.cern.ch/record/331068` (cit. on p. 44).

[169] ATLAS Collaboration, *ATLAS Level-1 Trigger: Technical Design Report*, ATLAS-TDR-12; CERN-LHCC-98-014, 1998, URL: `https://cds.cern.ch/record/381429` (cit. on pp. 46, 49).

[170] ATLAS Collaboration,
*ATLAS Magnet System: Magnet Project Technical Design Report, Volume 1*,
ATLAS-TDR-6; CERN-LHCC-97-018, 1997,
URL: https://cds.cern.ch/record/338080 (cit. on p. 47).

[171] ATLAS Collaboration,
*ATLAS Central Solenoid: Magnet Project Technical Design Report, Volume 4*,
ATLAS-TDR-9; CERN-LHCC-97-021, CERN, 1997,
URL: https://cds.cern.ch/record/331067 (cit. on p. 47).

[172] ATLAS Collaboration,
*ATLAS Barrel Toroid: Magnet Project Technical Design Report, Volume 2*,
ATLAS-TDR-7; CERN-LHCC-97-019, 1997,
URL: https://cds.cern.ch/record/331065 (cit. on p. 47).

[173] ATLAS Collaboration,
*ATLAS End-Cap Toroids: Magnet Project Technical Design Report, Volume 3*,
ATLAS-TDR-8; CERN-LHCC-97-020, CERN, 1997,
URL: https://cds.cern.ch/record/331066 (cit. on p. 48).

[174] ATLAS Collaboration, *ATLAS Forward Detectors for Measurement of Elastic Scattering and Luminosity: Technical Design Report*, ATLAS-TDR-18; CERN-LHCC-2008-004, 2008, URL: https://cds.cern.ch/record/1095847 (cit. on p. 48).

[175] ATLAS Collaboration, *Preliminary analysis of the luminosity calibration of the ATLAS 13.6 TeV data recorded in 2022*, tech. rep., CERN, 2023,
URL: http://cds.cern.ch/record/2853525 (cit. on pp. 48, 109).

[176] G. Alberghi et al.,
*Choice and characterization of photomultipliers for the new ATLAS LUCID detector*,
Journal of Instrumentation **11** (2016) P05014 (cit. on p. 48).

[177] G. Avoni et al.,
*The new LUCID-2 detector for luminosity measurement and monitoring in ATLAS*,
Journal of Instrumentation **13** (2018) P07017 (cit. on p. 48).

[178] K. Wille, *The Physics of Particle Accelerators: An Introduction*,
The Physics of Particle Accelerators: An Introduction, Oxford University Press, 2000,
ISBN: 9780198505495, URL: https://books.google.it/books?id=k1STXLP4lkgC
(cit. on p. 48).

[179] S. van der Meer, *Calibration of the effective beam height in the ISR*, tech. rep.,
CERN, 1968, URL: https://cds.cern.ch/record/296752 (cit. on p. 49).

[180] ATLAS TDAQ Collaboration, *Minimum Bias Trigger Scintillators in ATLAS Run II*,
JINST **9** (2014) C10020 (cit. on p. 49).

[181] ATLAS Collaboration,
*ATLAS High-Level Trigger, Data Acquisition and Controls: Technical Design Report*,
ATLAS-TDR-16; CERN-LHCC-2003-022, 2003,
URL: https://cds.cern.ch/record/616089 (cit. on p. 49).

[182] J. G. Panduro-Vasquez, *FELIX and the SW ROD: commissioning the new detector interface for the ATLAS trigger and readout system*, PoS **EPS-HEP2021** (2022) 825 (cit. on p. 50).

[183] *LHC computing Grid. Technical design report*, (2005), ed. by I. Bird et al. (cit. on p. 50).

[184] ATLAS Collaboration, *ATLAS Computing: Technical Design Report*, ATLAS-TDR-17; CERN-LHCC-2005-022, 2005, URL: `https://cds.cern.ch/record/837738` (cit. on p. 50).

[185] ATLAS Collaboration, *The ATLAS Simulation Infrastructure*, Eur. Phys. J. C **70** (2010) 823, arXiv: `1005.4568 [physics.ins-det]` (cit. on pp. 52, 79).

[186] ATLAS Collaboration, *The ATLAS Collaboration Software and Firmware*, ATL-SOFT-PUB-2021-001, 2021, URL: `https://cds.cern.ch/record/2767187` (cit. on p. 52).

[187] ATLAS Collaboration, *Electron reconstruction and identification efficiency measurements with the ATLAS detector using the 2011 LHC proton–proton collision data*, Eur. Phys. J. C **74** (2014) 2941, arXiv: `1404.2240 [hep-ex]` (cit. on p. 52).

[188] ATLAS Collaboration, *Electron reconstruction and identification in the ATLAS experiment using the 2015 and 2016 LHC proton–proton collision data at* $\sqrt{s} = 13\,TeV$, Eur. Phys. J. C **79** (2019) 639, arXiv: `1902.04655 [hep-ex]` (cit. on pp. 52–54).

[189] ATLAS Collaboration, *Electron and photon energy calibration with the ATLAS detector using 2015–2016 LHC proton–proton collision data*, JINST **14** (2019) P03017, arXiv: `1812.03848 [hep-ex]` (cit. on p. 53).

[190] ATLAS Collaboration, *Proposal for particle-level object and observable definitions for use in physics measurements at the LHC*, ATL-PHYS-PUB-2015-013, 2015, URL: `https://cds.cern.ch/record/2022743` (cit. on p. 54).

[191] ATLAS Collaboration, *Electron and photon efficiencies in LHC Run 2 with the ATLAS experiment*, (2023), arXiv: `2308.13362 [hep-ex]` (cit. on p. 54).

[192] ATLAS Collaboration, *ATLAS public plots: Electron identification efficiency with Run3 early data*, Accessed: 17-07-2023, URL: `https://atlas.web.cern.ch/Atlas/GROUPS/PHYSICS/PLOTS/EGAM-2022-04/index.html` (cit. on p. 55).

[193] ATLAS Collaboration, *ATLAS public plots: Electron efficiency with full Run2*, Accessed: 17-07-2023, URL: `https://atlas.web.cern.ch/Atlas/GROUPS/PHYSICS/PLOTS/EGAM-2022-02/index.html` (cit. on p. 56).

[194] ATLAS Collaboration, *Muon reconstruction performance of the ATLAS detector in proton–proton collision data at* $\sqrt{s} = 13$ *TeV*, Eur. Phys. J. C **76** (2016) 292, arXiv: `1603.05598 [hep-ex]` (cit. on pp. 56, 108).

[195] ATLAS Collaboration, *Muon reconstruction and identification efficiency in ATLAS using the full Run 2* $pp$ *collision data set at* $\sqrt{s} = 13$ *TeV*, Eur. Phys. J. C **81** (2021) 578, arXiv: `2012.00578 [hep-ex]` (cit. on pp. 56, 108).

[196] ATLAS Collaboration, *Muon reconstruction performance of the ATLAS detector in 2022*, 2023, URL: `https://atlas.web.cern.ch/Atlas/GROUPS/PHYSICS/PLOTS/MUON-2023-01/` (cit. on p. 57).

[197] ATLAS Collaboration, *Topological cell clustering in the ATLAS calorimeters and its performance in LHC Run 1*, Eur. Phys. J. C **77** (2017) 490, arXiv: `1603.02934 [hep-ex]` (cit. on p. 58).

[198] M. Cacciari, G. P. Salam and G. Soyez, *The anti-*$k_t$ *jet clustering algorithm*, JHEP **04** (2008) 063, arXiv: `0802.1189 [hep-ph]` (cit. on p. 58).

[199] M. Cacciari, G. P. Salam and G. Soyez, *FastJet user manual*, Eur. Phys. J. C **72** (2012) 1896, arXiv: `1111.6097 [hep-ph]` (cit. on p. 58).

[200] M. Cacciari and G. P. Salam, *Dispelling the N3 myth for the kt jet-finder*, Physics Letters B **641** (2006) 57, ISSN: 0370-2693 (cit. on p. 58).

[201] S. Catani, Y. Dokshitzer, M. Olsson, G. Turnock and B. Webber, *New clustering algorithm for multijet cross sections in e+e- annihilation*, Physics Letters B **269** (1991) 432, ISSN: 0370-2693 (cit. on p. 58).

[202] Y. Dokshitzer, G. Leder, S. Moretti and B. Webber, *Better jet clustering algorithms*, Journal of High Energy Physics **1997** (1997) 001 (cit. on p. 58).

[203] G. P. Salam, *Towards Jetography*, Eur. Phys. J. C **67** (2010) 637, arXiv: `0906.1833 [hep-ph]` (cit. on p. 58).

[204] P. Berta, *ATLAS jet and missing-ET reconstruction, calibration, and performance*, Nuclear and Particle Physics Proceedings **273-275** (2016) 1121 (cit. on p. 59).

[205] ATLAS Collaboration, *Jet reconstruction and performance using particle flow with the ATLAS Detector*, Eur. Phys. J. C **77** (2017) 466, arXiv: `1703.10485 [hep-ex]` (cit. on p. 59).

[206] ATLAS Collaboration, *Jet energy scale and resolution measured in proton–proton collisions at* $\sqrt{s} = 13$ *TeV with the ATLAS detector*, Eur. Phys. J. C **81** (2020) 689, arXiv: `2007.02645 [hep-ex]` (cit. on p. 59).

[207] ATLAS Collaboration, *Jet energy resolution in proton–proton collisions at* $\sqrt{s} = 7$ *TeV recorded in 2010 with the ATLAS detector*, Eur. Phys. J. C **73** (2013) 2306, arXiv: `1210.6210 [hep-ex]` (cit. on p. 59).

[208] ATLAS Collaboration, *Performance of pile-up mitigation techniques for jets in $pp$ collisions at $\sqrt{s} = 8$ TeV using the ATLAS detector*, Eur. Phys. J. C **76** (2016) 581, arXiv: `1510.03823 [hep-ex]` (cit. on p. 60).

[209] ATLAS Collaboration, *Expected performance of missing transverse momentum reconstruction for the ATLAS detector at $\sqrt{s} = 13$ TeV*, ATL-PHYS-PUB-2015-023, 2015, URL: `https://cds.cern.ch/record/2037700` (cit. on p. 60).

[210] ATLAS Collaboration, $E_T^{miss}$ *performance in the ATLAS detector using 2015–2016 LHC $pp$ collisions*, ATLAS-CONF-2018-023, 2018, URL: `https://cds.cern.ch/record/2625233` (cit. on p. 60).

[211] ATLAS Collaboration, *Performance of missing transverse momentum reconstruction with the ATLAS detector using proton–proton collisions at $\sqrt{s} = 13$ TeV*, Eur. Phys. J. C **78** (2018) 903, arXiv: `1802.08168 [hep-ex]` (cit. on p. 61).

[212] ATLAS Collaboration, *Performance and Calibration of the JetFitterCharm Algorithm for $c$-Jet Identification*, ATL-PHYS-PUB-2015-001, 2015, URL: `https://cds.cern.ch/record/1980463` (cit. on p. 61).

[213] ATLAS Collaboration, *ATLAS $b$-jet identification performance and efficiency measurement with $t\bar{t}$ events in $pp$ collisions at $\sqrt{s} = 13$ TeV*, Eur. Phys. J. C **79** (2019) 970, arXiv: `1907.05120 [hep-ex]` (cit. on pp. 61, 177).

[214] ATLAS Collaboration, *Neural Network Jet Flavour Tagging with the Upgraded ATLAS Inner Tracker Detector at the High-Luminosity LHC*, ATL-PHYS-PUB-2022-047, 2022, URL: `https://cds.cern.ch/record/2839913` (cit. on p. 61).

[215] I. J. Goodfellow, D. Warde-Farley, M. Mirza, A. Courville and Y. Bengio, *Maxout Networks*, 2013, arXiv: `1302.4389 [stat.ML]` (cit. on p. 62).

[216] ATLAS Collaboration, *Optimisation and performance studies of the ATLAS $b$-tagging algorithms for the 2017-18 LHC run*, ATL-PHYS-PUB-2017-013, 2017, URL: `https://cds.cern.ch/record/2273281` (cit. on p. 62).

[217] ATLAS Collaboration, *Secondary vertex finding for jet flavour identification with the ATLAS detector*, ATL-PHYS-PUB-2017-011, 2017, URL: `https://cds.cern.ch/record/2270366` (cit. on p. 62).

[218] ATLAS Collaboration, *Topological $b$-hadron decay reconstruction and identification of $b$-jets with the JetFitter package in the ATLAS experiment at the LHC*, ATL-PHYS-PUB-2018-025, 2018, URL: `https://cds.cern.ch/record/2645405` (cit. on p. 62).

[219] ATLAS Collaboration, *ATLAS flavour-tagging algorithms for the LHC Run 2 $pp$ collision dataset*, (2022), arXiv: `2211.16345 [physics.data-an]` (cit. on p. 62).

[220] ATLAS Collaboration, *ATLAS public plots: Performance of the Run 3 ATLAS b-tagging algorithms*, Accessed: 21-07-2023, URL: https://atlas.web.cern.ch/Atlas/GROUPS/PHYSICS/PLOTS/FTAG-2022-004 (cit. on p. 63).

[221] ATLAS Collaboration, *Measurements of b-jet tagging efficiency with the ATLAS detector using $t\bar{t}$ events at $\sqrt{s} = 13$ TeV*, JHEP **08** (2018) 089, arXiv: 1805.01845 [hep-ex] (cit. on p. 62).

[222] ATLAS Collaboration, *Graph Neural Network Jet Flavour Tagging with the ATLAS Detector*, ATL-PHYS-PUB-2022-027, 2022, URL: https://cds.cern.ch/record/2811135 (cit. on p. 62).

[223] D. Adams et al., *Recommendations of the Physics Objects and Analysis Harmonisation Study Groups 2014*, tech. rep., CERN, 2014, URL: https://cds.cern.ch/record/1743654 (cit. on p. 62).

[224] M. Cacciari, G. P. Salam and G. Soyez, *The catchment area of jets*, JHEP **04** (2008) 005 (cit. on p. 64).

[225] J. Rojo et al., *The PDF4LHC report on PDFs and LHC data: Results from Run I and preparation for Run II*, J. Phys. G **42** (2015) 103103, arXiv: 1507.00556 [hep-ph] (cit. on p. 67).

[226] M. L. Mangano and J. Rojo, *Cross Section Ratios between different CM energies at the LHC: opportunities for precision measurements and BSM sensitivity*, JHEP **08** (2012) 010, arXiv: 1206.3557 [hep-ph] (cit. on p. 67).

[227] G. Guerrieri, *First Run 3 data/MC plots for the measurement of the top-quark pair production cross-section in pp collisions at centre-of-mass energy of 13.6 TeV with the ATLAS experiment at the LHC*, 2022, arXiv: 2211.09414 [hep-ex] (cit. on p. 68).

[228] ATLAS Collaboration, *Measurement of the $t\bar{t}$ cross-section and $t\bar{t}/Z$ cross-section ratio using LHC Run 3 $pp$ collision data at a centre-of-mass energy of $\sqrt{s} = 13.6$ TeV*, ATLAS-CONF-2022-070, 2022, URL: https://cds.cern.ch/record/2842916 (cit. on p. 68).

[229] ATLAS Collaboration, *Measurement of $t\bar{t}$ and Z-boson cross sections and their ratio using $pp$ collisions at $\sqrt{s} = 13.6$ TeV with the ATLAS detector*, tech. rep., CERN, 2023, URL: http://cds.cern.ch/record/2854834 (cit. on p. 68).

[230] ATLAS Collaboration, *Measurement of the $t\bar{t}$ cross section and its ratio to the Z production cross section using $pp$ collisions at $\sqrt{s} = 13.6$ TeV with the ATLAS detector*, Physics Letters B **848** (2024) 138376, ISSN: 0370-2693 (cit. on p. 69).

[231] K. Cranmer, G. Lewis, L. Moneta, A. Shibata and W. Verkerke, *HistFactory: A tool for creating statistical models foruse with RooFit and RooStats*, tech. rep. CERN-OPEN-2012-016, New York U., 2012, URL: https://cds.cern.ch/record/1456844 (cit. on p. 71).

[232] F. James and M. Roos, *MINUIT: a system for function minimization and analysis of the parameter errors and corrections*, Comput. Phys. Commun. **10** (1975) 343, URL: `https://cds.cern.ch/record/310399` (cit. on p. 72).

[233] E. Gross, *Practical Statistics for High Energy Physics*, CERN Yellow Rep. School Proc. **3** (2018) 199, ed. by M. Mulders and G. Zanderighi (cit. on p. 76).

[234] S. Agostinelli et al., *Geant4 – a simulation toolkit*, Nucl. Instrum. Meth. A **506** (2003) 250 (cit. on p. 79).

[235] T. Sjöstrand, S. Mrenna and P. Skands, *A brief introduction to PYTHIA 8.1*, Comput. Phys. Commun. **178** (2008) 852, arXiv: `0710.3820 [hep-ph]` (cit. on p. 79).

[236] NNPDF Collaboration, R. D. Ball et al., *Parton distributions with LHC data*, Nucl. Phys. B **867** (2013) 244, arXiv: `1207.1303 [hep-ph]` (cit. on pp. 79, 81).

[237] ATLAS Collaboration, *The Pythia 8 A3 tune description of ATLAS minimum bias and inelastic measurements incorporating the Donnachie–Landshoff diffractive model*, ATL-PHYS-PUB-2016-017, 2016, URL: `https://cds.cern.ch/record/2206965` (cit. on p. 79).

[238] S. Porteboeuf, T. Pierog and K. Werner, 'Producing Hard Processes Regarding the Complete Event: The EPOS Event Generator', *45th Rencontres de Moriond on QCD and High Energy Interactions*, Gioi Publishers, 2010 135, arXiv: `1006.2967 [hep-ph]` (cit. on p. 79).

[239] *Simulations*, URL: `https://theory.slac.stanford.edu/our-research/simulations` (cit. on p. 80).

[240] S. Frixione, G. Ridolfi and P. Nason, *A positive-weight next-to-leading-order Monte Carlo for heavy flavour hadroproduction*, JHEP **09** (2007) 126, arXiv: `0707.3088 [hep-ph]` (cit. on pp. 81, 82, 110).

[241] P. Nason, *A new method for combining NLO QCD with shower Monte Carlo algorithms*, JHEP **11** (2004) 040, arXiv: `hep-ph/0409146` (cit. on pp. 81, 82, 110).

[242] S. Frixione, P. Nason and C. Oleari, *Matching NLO QCD computations with parton shower simulations: the POWHEG method*, JHEP **11** (2007) 070, arXiv: `0709.2092 [hep-ph]` (cit. on pp. 81, 82, 110).

[243] S. Alioli, P. Nason, C. Oleari and E. Re, *A general framework for implementing NLO calculations in shower Monte Carlo programs: the POWHEG BOX*, JHEP **06** (2010) 043, arXiv: `1002.2581 [hep-ph]` (cit. on pp. 81, 82, 110).

[244] The NNPDF Collaboration, R. D. Ball et al., *Parton distributions for the LHC run II*, JHEP **04** (2015) 040, arXiv: `1410.8849 [hep-ph]` (cit. on pp. 81, 110).

[245] ATLAS Collaboration, *Studies on top-quark Monte Carlo modelling for Top2016*, ATL-PHYS-PUB-2016-020, 2016, URL: `https://cds.cern.ch/record/2216168` (cit. on p. 81).

[246] T. Sjöstrand et al., *An introduction to PYTHIA 8.2*, Comput. Phys. Commun. **191** (2015) 159, arXiv: `1410.3012 [hep-ph]` (cit. on p. 81).

[247] ATLAS Collaboration, *ATLAS Pythia 8 tunes to 7 TeV data*, ATL-PHYS-PUB-2014-021, 2014, URL: `https://cds.cern.ch/record/1966419` (cit. on p. 81).

[248] D. J. Lange, *The EvtGen particle decay simulation package*, Nucl. Instrum. Meth. A **462** (2001) 152 (cit. on p. 81).

[249] E. Bothmann et al., *Event generation with Sherpa 2.2*, SciPost Phys. **7** (2019) 034, arXiv: `1905.09127 [hep-ph]` (cit. on p. 82).

[250] T. Gleisberg and S. Höche, *Comix, a new matrix element generator*, JHEP **12** (2008) 039, arXiv: `0808.3674 [hep-ph]` (cit. on p. 82).

[251] F. Buccioni et al., *OpenLoops 2*, Eur. Phys. J. C **79** (2019) 866, arXiv: `1907.13071 [hep-ph]` (cit. on p. 82).

[252] F. Cascioli, P. Maierhöfer and S. Pozzorini, *Scattering Amplitudes with Open Loops*, Phys. Rev. Lett. **108** (2012) 111601, arXiv: `1111.5206 [hep-ph]` (cit. on p. 82).

[253] A. Denner, S. Dittmaier and L. Hofer, *COLLIER: A fortran-based complex one-loop library in extended regularizations*, Comput. Phys. Commun. **212** (2017) 220, arXiv: `1604.06792 [hep-ph]` (cit. on p. 82).

[254] S. Schumann and F. Krauss, *A parton shower algorithm based on Catani–Seymour dipole factorisation*, JHEP **03** (2008) 038, arXiv: `0709.1027 [hep-ph]` (cit. on p. 82).

[255] S. Höche, F. Krauss, M. Schönherr and F. Siegert, *A critical appraisal of NLO+PS matching methods*, JHEP **09** (2012) 049, arXiv: `1111.1220 [hep-ph]` (cit. on p. 82).

[256] S. Höche, F. Krauss, M. Schönherr and F. Siegert, *QCD matrix elements + parton showers. The NLO case*, JHEP **04** (2013) 027, arXiv: `1207.5030 [hep-ph]` (cit. on p. 82).

[257] S. Catani, F. Krauss, B. R. Webber and R. Kuhn, *QCD Matrix Elements + Parton Showers*, JHEP **11** (2001) 063, arXiv: `hep-ph/0109231` (cit. on p. 82).

[258] S. Höche, F. Krauss, S. Schumann and F. Siegert, *QCD matrix elements and truncated showers*, JHEP **05** (2009) 053, arXiv: `0903.1219 [hep-ph]` (cit. on p. 82).

[259] M. Grazzini, S. Kallweit and M. Wiesemann, *Fully differential NNLO computations with MATRIX*, Eur. Phys. J. C **78** (2018) 537, arXiv: `1711.06631 [hep-ph]` (cit. on pp. 82, 129, 132).

[260] S. Frixione, E. Laenen, P. Motylinski, C. White and B. R. Webber, *Single-top hadroproduction in association with a W boson*, JHEP **07** (2008) 029, arXiv: `0805.3067 [hep-ph]` (cit. on pp. 82, 110).

[261] S. Alioli, P. Nason, C. Oleari and E. Re, *NLO single-top production matched with shower in POWHEG: s- and t-channel contributions*, JHEP **09** (2009) 111, arXiv: `0907.4076 [hep-ph]` (cit. on p. 82), Erratum: JHEP **02** (2010) 011.

[262] ATLAS Collaboration, *Vertex Reconstruction Performance of the ATLAS Detector at* $\sqrt{s} = 13$ *TeV*, ATL-PHYS-PUB-2015-026, 2015, URL: `https://cds.cern.ch/record/2037717` (cit. on p. 86).

[263] ATLAS Collaboration, *Luminosity determination in* $pp$ *collisions at* $\sqrt{s} = 13$ *TeV using the ATLAS detector at the LHC*, (2022), arXiv: `2212.09379 [hep-ex]` (cit. on p. 109).

[264] G. Avoni et al., *The new LUCID-2 detector for luminosity measurement and monitoring in ATLAS*, JINST **13** (2018) P07017 (cit. on p. 109).

[265] M. Bähr et al., *Herwig++ physics and manual*, Eur. Phys. J. C **58** (2008) 639, arXiv: `0803.0883 [hep-ph]` (cit. on p. 110).

[266] J. Bellm et al., *Herwig 7.0/Herwig++ 3.0 release note*, Eur. Phys. J. C **76** (2016) 196, arXiv: `1512.01178 [hep-ph]` (cit. on p. 110).

[267] J. Bellm et al., *Herwig 7.1 Release Note*, (2017), arXiv: `1705.06919 [hep-ph]` (cit. on p. 110).

[268] L. A. Harland-Lang, A. D. Martin, P. Motylinski and R. S. Thorne, *Parton distributions in the LHC era: MMHT 2014 PDFs*, Eur. Phys. J. C **75** (2015) 204, arXiv: `1412.3989 [hep-ph]` (cit. on p. 110).

[269] ATLAS Collaboration, *Studies on top-quark Monte Carlo modelling with Sherpa and MG5_aMC@NLO*, ATL-PHYS-PUB-2017-007, 2017, URL: `https://cds.cern.ch/record/2261938` (cit. on p. 110).

[270] E. Re, *Single-top Wt-channel production matched with parton showers using the POWHEG method*, The European Physical Journal C **71** (2011) (cit. on p. 110).

[271] T.-J. Hou et al., *New CTEQ global analysis of quantum chromodynamics with high-precision data from the LHC*, Phys. Rev. D **103** (2021) 014013, arXiv: `1912.10053 [hep-ph]` (cit. on pp. 111, 131, 132).

[272] S. Bailey, T. Cridge, L. A. Harland-Lang, A. D. Martin and R. S. Thorne, *Parton distributions from LHC, HERA, Tevatron and fixed target data: MSHT20 PDFs*, Eur. Phys. J. C **81** (2021) 341, arXiv: `2012.04684 [hep-ph]` (cit. on pp. 111, 131, 132).

[273] R. D. Ball et al., *Parton distributions from high-precision collider data*, The European Physical Journal C **77** (2017) (cit. on p. 111).

[274] ATLAS Collaboration, *Modelling and computational improvements to the simulation of single vector-boson plus jet processes for the ATLAS experiment*, JHEP **08** (2021) 089, arXiv: `2112.09588 [hep-ex]` (cit. on p. 119).

[275] T. Cridge, L. A. Harland-Lang, A. D. Martin and R. S. Thorne, *An investigation of the $\alpha_S$ and heavy quark mass dependence in the MSHT20 global PDF analysis*, Eur. Phys. J. C **81** (2021) 744, arXiv: `2106.10289 [hep-ph]` (cit. on pp. 131, 132).

[276] T. Cridge, L. A. Harland-Lang, A. D. Martin and R. S. Thorne, *QED parton distribution functions in the MSHT20 fit*, Eur. Phys. J. C **82** (2022) 90, arXiv: `2111.05357 [hep-ph]` (cit. on pp. 131, 132).

[277] R. D. Ball et al., *The path to proton structure at 1% accuracy: NNPDF Collaboration*, Eur. Phys. J. C **82** (2022) 428, arXiv: `2109.02653 [hep-ph]` (cit. on pp. 131, 132).

[278] S. Alekhin, J. Blümlein, S. Moch and R. Placakyte, *Parton distribution functions, $\alpha_s$, and heavy-quark masses for LHC Run II*, Phys. Rev. D **96** (2017) 014011, arXiv: `1701.05838 [hep-ph]` (cit. on pp. 131, 132).

[279] ATLAS Collaboration, *Determination of the parton distribution functions of the proton using diverse ATLAS data from $pp$ collisions at $\sqrt{s} = 7, 8$ and 13 TeV*, Eur. Phys. J. C **82** (2021) 438, arXiv: `2112.11266 [hep-ex]` (cit. on pp. 131, 132).

[280] Guerrieri, Giovanni and on behalf of the ATLAS collaboration, *Regression Deep Neural Networks for top-quark-pair resonance searches in the dilepton channel*, Nuovo Cimento C **45** (2022) 110 (cit. on p. 185).

[281] Sánchez Pineda, Arturo, Guerrieri, Giovanni and on behalf of ATLAS Software and Computing, *A proposal for Open Access data and tools multi-user deployment using ATLAS Open Data for Education*, EPJ Web Conf. **251** (2021) 01008 (cit. on p. 186).

[282] ATLAS Collaboration, *Measurement of $t$-channel single-top-quark production in $pp$ collisions at $\sqrt{s} = 5.02$ TeV with the ATLAS detector*, 2023, arXiv: `2310.01518 [hep-ex]` (cit. on p. 186).